547092

Development of an Innovative Algorithm for Aerodynamics-Structure Interaction Using Lattice Boltzmann Method

Renwei Mei[1*], Wei Shyy[1‡], Dazhi Yu[1¥],

[1]Department of Aerospace Engineering, Mechanics & Engineering Science

University of Florida, Gainesville, FL 32611-6250

*rwm@aero.ufl.edu, ‡wei-shyy@ufl.edu, ¥ydz@aero.ufl.edu

Ph: (352) 392-0961; Fax: (352) 392-7303

& Li-Shi Luo[2]

[2]ICASE, MS 132C, NASA Langley Research Center

3 West Reid Street, Building 1152, Hampton, VA 23681-2199

luo@icase.edu, Ph: (757) 864-8006; Fax: (757) 864-6134

Final Report

To NASA Langley Research Center

Grant Monitor: Dr. David Rudy

Content

Development of an Innovative Algorithm for Aerodynamics-Structure Interaction Using Lattice Boltzmann Method

EXECUTIVE SUMMARY

The lattice Boltzmann equation (LBE) is a kinetic formulation which offers an alternative computational method capable of solving fluid dynamics for various systems. Major advantages of the method are owing to the fact that the solution for the particle distribution functions is explicit, easy to implement, and the algorithm is natural to parallelize. In this final report, we summarize the works accomplished in the past three years. Since most works have been published, the technical details can be found in the literature. Brief summary will be provided in this report.

In this project, a second-order accurate treatment of boundary condition in the LBE method is developed for a curved boundary and tested successfully in various 2-D and 3-D configurations. To evaluate the aerodynamic force on a body in the context of LBE method, several force evaluation schemes have been investigated. A simple momentum exchange method is shown to give reliable and accurate values for the force on a body in both 2-D and 3-D cases. Various 3-D LBE models have been assessed in terms of efficiency, accuracy, and robustness. In general, accurate 3-D results can be obtained using LBE methods. The 3-D 19-bit model is found to be the best one among the 15-bit, 19-bit, and 27-bit LBE models. To achieve desired grid resolution and to accommodate the far field boundary conditions in aerodynamics computations, a multi-block LBE method is developed by dividing the flow field into various blocks each having constant lattice spacing. Substantial contribution to the LBE method is also made through the development of a new, generalized lattice Boltzmann equation constructed in the moment space in order to improve the computational stability, detailed theoretical analysis on the stability, dispersion, and dissipation characteristics of the LBE method, and computational studies of high Reynolds number flows with singular gradients. Finally, a finite difference-based lattice Boltzmann method is developed for inviscid compressible flows.

Part 1
An Accurate Curved Boundary Treatment in the Lattice Boltzmann Method

Renwei Mei[1], Li-Shi Luo[2], & Wei Shyy[1]

[1]Department of Aerospace Engineering, Mechanics & Engineering Science

University of Florida, Gainesville, FL 32611-6250

[2]ICASE

NASA Langley Research Center, Hampton, VA 23681-2199

Summary

The lattice Boltzmann equation (LBE) is an alternative kinetic method capable of solving hydrodynamics for various systems. Major advantages of the method are owing to the fact that the solution for the particle distribution functions is explicit, easy to implement, and natural to parallelize. Because the method often uses uniform regular Cartesian lattices in space, curved boundaries are often approximated by a series of stairs that leads to reduction in computational accuracy. In this work, a second-order accurate treatment of boundary condition in the LBE method is developed for a curved boundary. The proposed treatment of the curved boundaries is an improvement of a scheme due to Filippova & Hänel [J. Comp. Phys. **143**, 426 (1998)]. The proposed treatment for curved boundaries is tested against several flow problems: 2-D channel flows with constant and oscillating pressure gradients for which analytic solutions are known, flow due to an impulsively started wall, lid-driven square cavity flow, and uniform flow over a column of circular cylinders. The second-order accuracy is observed with solid boundary arbitrarily placed between lattice nodes. The proposed boundary condition has well behaved stability characteristics when the relaxation time is close to ½, the zero limit of viscosity. The improvement can make a substantial contribution toward simulating practical fluid flow problems using the lattice Boltzmann method.

Paper published in: *J. Computational Physics*, **155**, 307-330, 1999.

Part 2
Lattice Boltzmann Method for 3-D Flows with Curved Boundary

Renwei Mei, Wei Shyy, Dazhi Yu
Department of Aerospace Engineering, Mechanics & Engineering Science
University of Florida, Gainesville, FL 32611-6250
& Li-Shi Luo
ICASE, MS 132C, NASA Langley Research Center
3 West Reid Street, Building 1152, Hampton, VA 23681-2199

Summary

In this work, we investigate two issues that are important to computational efficiency and reliability in fluid dynamic applications of the lattice Boltzmann equation (LBE): (1) Computational stability and accuracy of different lattice Boltzmann models and (2) the treatment of the boundary conditions on curved solid boundaries and their 3-D implementations. Three athermal 3-D LBE models (Q15D3, Q19D3, and Q27D3) are studied and compared in terms of efficiency, accuracy, and robustness. The boundary treatment recently developed by Filippova and Hänel (1998, *J. Comp. Phys.* **147**, 219) and Mei *et al.* (1999, *J. Comp. Phys.* **155**, 307) in 2-D is extended to and implemented for 3-D. The convergence, stability, and computational efficiency of the 3-D LBE models with the boundary treatment for curved boundaries were tested in simulations of four 3-D flows: (1) Fully developed flows in a square duct, (2) flow in a 3-D lid-driven cavity, (3) fully developed flows in a circular pipe, and (4) a uniform flow over a sphere. We found that while the 15-velocity 3-D (Q15D3) model is more prone to numerical instability and the Q27D3 is more computationally intensive, the Q19D3 model provides a balance between computational reliability and efficiency. Through numerical simulations, we demonstrated that the boundary treatment for 3-D arbitrary curved geometry has second-order accuracy and possesses satisfactory stability characteristics.

Paper published in: *J. Computational Phys.*, vol. 161, 680-699, 2000.

Part 3

Force Evaluation in the Lattice Boltzmann Method Involving Curved Geometry

Renwei Mei, Dazhi Yu, Wei Shyy

Department of Aerospace Engineering, Mechanics & Engineering Science
University of Florida, Gainesville, FL 32611-6250
& Li-Shi Luo

ICASE, MS 132C, NASA Langley Research Center
3 West Reid Street, Building 1152, Hampton, VA 23681-2199

Summary

Accurate evaluation of the hydrodynamic force on a curved body is an important issue in the method of lattice Boltzmann equation for fluid flow problems. This issue has not been systematically studied so far. The present work investigates two approaches for force evaluation: the method of momentum exchange and the method of stress integration. The boundary condition for the particle distribution functions on curved geometries is handled with second order accuracy based on our recent works [Mei *et al.* (1999, *J. Comp. Phys.* **155**, 307), & Mei *et al.* (2000, *J. Comp. Phys.* **161**, 680)]. The stress integration method is tedious in 2-D flow and difficult to implement in 3-D flow in general; in comparison, the momentum exchange method is reliable, accurate, and easy to implement in both 2-D and 3-D flows. Several test cases are selected to evaluate the present methods, including: 1) 2-D pressure-driven channel flow; 2) 2-D uniform flow over a columns of circular cylinder; 3) a channel flow over an asymmetrically placed circular cylinder with vortex shedding; 4) pressure-driven flow in a circular pipe; and 5) 3-D flow over a sphere. The drag evaluated by using the momentum exchange method in the LBE agrees well with the exact or other published results.

Paper currently under review for publication at *Physical Review E.*

Part 4

A Multi-block Lattice Boltzmann Method for Fluid Flows

Dazhi Yu, Renwei Mei, & Wei Shyy

Department of Aerospace engineering, Mechanics and Engineering Science,

University of Florida, Gainesville, FL 32611-6250

Summary

Compared to the Navier-Stokes equation-based approach, the method of lattice Boltzmann Equation (LBE) offers an alternative treatment for fluid dynamics. The LBE method often employs uniform lattices to maintain a compact and efficient computational procedure, which makes it less efficient to perform flow simulations when there is a need for high resolution near the body and/or there is a far-field boundary. To resolve these difficulties, a multi-block method is developed. In this method, the flow field is divided into blocks. In each block, the grid is uniform with desired resolution. In this paper, an accurate interface treatment between neighboring blocks is derived to ensure the continuity of mass, momentum, and stresses across the interface. Several test cases are employed to demonstrate that the present multi-block method can substantially improve the accuracy and computational efficiency.

Paper published as *AIAA 2000-2614*, Fluids 2000 , Denver, Colorado, 6/19-22, 2000.

Paper is also currently under review for publication in *Int. J. of Num. Method for Fluid Flows.*

Part 5

Theory of the lattice Boltzmann method: Dispersion, dissipation, isotropy, Galilean invariance, and stability

Pierre Lallemand [1] and Li-Shi Luo [2]
[1]Laboratoire ASCI
Bâtiment 506, Universit_e Paris-Sud (Paris XI Orsay)
91405 Orsay Cedex, France
[1] ICASE, MS 132C, NASA Langley Research Center
3 West Reid Street, Building 1152, Hampton, Virginia 23681-2199, USA

Summary

The generalized hydrodynamics (the wave vector dependence of the transport coefficients) of a generalized lattice Boltzmann equation (LBE) is studied in detail. The generalized lattice Boltzmann equation is constructed in moment space rather than in discrete velocity space. The generalized hydrodynamics of the model is obtained by solving the dispersion equation of the linearized LBE either analytically by using perturbation technique or numerically. The proposed LBE model has a maximum number of adjustable parameters for the given set of discrete velocities. Generalized hydrodynamics characterizes dispersion, dissipation (hyperviscosities), anisotropy, and lack of Galilean invariance of the model, and can be applied to select the values of the adjustable parameters that optimize the properties of the model. The proposed generalized hydrodynamic analysis also provides some insights into stability and proper initial conditions for LBE simulations. The stability properties of some two-dimensional LBE models are analyzed and compared with each other in the parameter space of the mean streaming velocity and the viscous relaxation time. The procedure described in this work can be applied to analyze other LBE models. As examples, LBE models with various interpolation schemes are analyzed. Numerical results on shear ow with an initially discontinuous velocity pro_le (shock) with or without a constant streaming velocity are shown to demonstrate the dispersion e_ects in the LBE model; the results compare favorably with our theoretical analysis. We also show that whereas linear analysis of the LBE evolution operator is equivalent to Chapman-Enskog analysis in the long-wavelength limit (wave vector $k = 0$), it can also provide results for large values of k . Such results are important for the stability and other hydrodynamic properties of the LBE method and cannot be obtained through Chapman-Enskog analysis.

Paper published in *Physical Review E.* Vo. 61, No. 6, 6546-6562, June 2000.

Part 7
Finite Difference-Based Lattice Boltzmann Method for Inviscid Compressible Flows

Weiping Shi[1], Wei Shyy[2] and Renwei Mei[2]

[1]Department of Mathematics, Jilin University, Changchun 130023, China 130023

[2]Department of Aerospace Engineering, Mechanics & Engineering Science, University of Florida, Gainesville, Florida 32611-6250

Summary

A finite difference-based lattice Boltzmann model, employing the 2-D, 9-speed square (D2Q9) lattice for the compressible Euler equations, is presented. The model is constructed by allowing the particles to possess both kinetic and thermal energies. Such a lattice structure can represent both incompressible and compressible flow regimes. In the numerical treatment, to attain desirable accuracy, the total-variation-diminishing (TVD) scheme is adopted with either the minmod function or a second-order corrector as the flux limiter. The model can treat shock/expansion waves as well as contact discontinuity. Both one- and two-dimensional test cases are computed, and the results are compared with the exact as well as other reported numerical solutions, demonstrating that there is consistency between macroscopic and kinetic computations for the compressible flow.

Paper is accepted for publication in *Int. J. of Heat and Mass Transfer*

Journal of Computational Physics 155, 307–330 (1999)
Article ID jcph.1999.6334, available online at http://www.idealibrary.com on IDEAL®

An Accurate Curved Boundary Treatment in the Lattice Boltzmann Method

Renwei Mei,* Li-Shi Luo,† and Wei Shyy*

*Department of Aerospace Engineering, Mechanics and Engineering Science, University of Florida, Gainesville, Florida 32611-6250; †ICASE, NASA Langley Research Center, Hampton, Virginia 23681-2199
E-mail: rwm@aero.ufl.edu, luo@icase.edu, wei-shyy@ufl.edu

Received February 2, 1999; revised June 29, 1999

The lattice Boltzmann equation (LBE) is an alternative kinetic method capable of solving hydrodynamics for various systems. Major advantages of the method are due to the fact that the solution for the particle distribution functions is explicit, easy to implement, and natural to parallelize. Because the method often uses uniform regular Cartesian lattices in space, curved boundaries are often approximated by a series of stairs that leads to reduction in computational accuracy. In this work, a second-order accurate treatment of the boundary condition in the LBE method is developed for a curved boundary. The proposed treatment of the curved boundaries is an improvement of a scheme due to O. Filippova and D. Hänel (1998, *J. Comput. Phys.* **147**, 219). The proposed treatment for curved boundaries is tested against several flow problems: 2-D channel flows with constant and oscillating pressure gradients for which analytic solutions are known, flow due to an impulsively started wall, lid-driven square cavity flow, and uniform flow over a column of circular cylinders. The second-order accuracy is observed with a solid boundary arbitrarily placed between lattice nodes. The proposed boundary condition has well-behaved stability characteristics when the relaxation time is close to 1/2, the zero limit of viscosity. The improvement can make a substantial contribution toward simulating practical fluid flow problems using the lattice Boltzmann method.

I. INTRODUCTION

There has been a rapid progress in developing and employing the method of the lattice Boltzmann equation (LBE) [1–3] as an alternative computational technique for solving complex fluid dynamic problems (see the comprehensive reviews in [4, 5]). In a traditional method for computational fluid dynamics (CFD), the macroscopic variables, such as velocity $\boldsymbol{u}$ and pressure p, are obtained by solving the Navier–Stokes (NS) equations [6–8]. The lattice Boltzmann equation approximates the kinetic equation for the particle mass

0021-9991/99 $30.00

distribution function $f(\boldsymbol{x}, \boldsymbol{\xi}, t)$ on the mesoscopic level, such as the Boltzmann equation with the single relaxation time approximation [9],

$$\frac{\partial f}{\partial t} + \boldsymbol{\xi} \cdot \nabla f = -\frac{1}{\lambda}(f - f^{(0)}), \tag{1}$$

where $\boldsymbol{\xi}$ is the particle velocity, $f^{(0)}$ is the equilibrium distribution function (the Maxwell–Boltzmann distribution function), and λ is the relaxation time. The right hand side (RHS) term models the effect of the fluid viscosity on the molecular level through the collision (relaxation) process. The macroscopic quantities (such as mass density ρ and momentum density $\rho \boldsymbol{u}$) are the hydrodynamic moments of the distribution function f,

$$\rho = \int f(\boldsymbol{x}, \boldsymbol{\xi}, t)\, d^3\boldsymbol{\xi} \tag{2a}$$

$$\rho \boldsymbol{u} = \int \boldsymbol{\xi} f(\boldsymbol{x}, \boldsymbol{\xi}, t)\, d^3\boldsymbol{\xi}. \tag{2b}$$

It has been shown that the velocity space $\boldsymbol{\xi}$ can be discretized into a finite set of points $\{\boldsymbol{\xi}_\alpha\}$ without affecting the conservation laws [10–12]. In the discretized velocity space the Boltzmann equation (1) becomes

$$\frac{\partial f_\alpha}{\partial t} + \boldsymbol{\xi}_\alpha \cdot \nabla f_\alpha = -\frac{1}{\lambda}(f_\alpha - f_\alpha^{(eq)}) \qquad (\alpha = 0, 1, 2, \ldots, 8 \text{ for 2-D}) \tag{3}$$

for the distribution function of discrete velocities $f_\alpha(\boldsymbol{x}, t) \equiv f(\boldsymbol{x}, \boldsymbol{\xi}_\alpha, t)$. The equilibrium distribution function, $f_\alpha^{(eq)}$, and the discrete velocity set $\{\boldsymbol{\xi}_\alpha\}$ can be derived explicitly [10–12].

For the 2-D square lattice shown in Fig. 1, we use $\boldsymbol{e}_\alpha$ to denote the discrete velocity set, and we have [13]

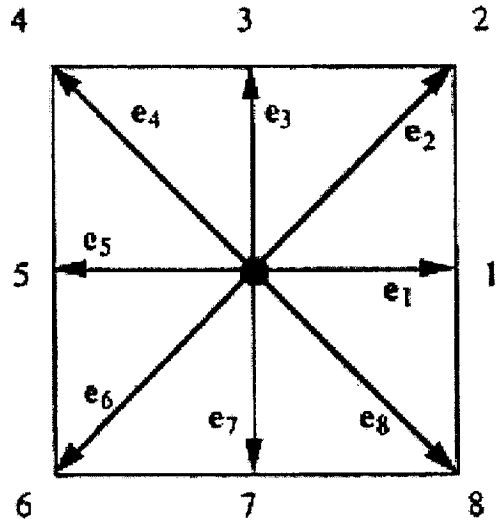

FIG. 1. A 2-D, 9-bit (or 9-velocity) lattice.

$$\begin{aligned} \boldsymbol{e}_\alpha &= 0, \qquad \text{for } \alpha = 0, \\ \boldsymbol{e}_\alpha &= (\cos((\alpha-1)\pi/4), \sin((\alpha-1)\pi/4)) \qquad \text{for } \alpha = 1,3,5,7, \\ \boldsymbol{e}_\alpha &= \sqrt{2}(\cos((\alpha-1)\pi/4), \sin((\alpha-1)\pi/4)) \qquad \text{for } \alpha = 2,4,6,8, \end{aligned} \tag{4}$$

where $c = \delta x/\delta t$, δx, and δt are the lattice constant and the time step size, respectively, and

$$f_\alpha^{(eq)} = \rho w_\alpha \left[1 + \frac{3}{c^2}\boldsymbol{e}_\alpha \cdot \boldsymbol{u} + \frac{9}{2c^4}(\boldsymbol{e}_\alpha \cdot \boldsymbol{u})^2 - \frac{3}{2c^2}\boldsymbol{u}\cdot\boldsymbol{u}\right], \tag{5}$$

where

$$w_\alpha = \begin{cases} 4/9, & \alpha = 0 \\ 1/9, & \alpha = 1,3,5,7 \\ 1/36, & \alpha = 2,4,6,8. \end{cases} \tag{6}$$

With the discretized velocity space, the hydrodynamic moments are given by

$$\rho = \sum_{\alpha=0}^{8} f_\alpha = \sum_{\alpha=0}^{8} f_\alpha^{(eq)} \tag{7a}$$

and

$$\rho \boldsymbol{u} = \sum_{\alpha=1}^{8} \boldsymbol{e}_\alpha f_\alpha = \sum_{\alpha=1}^{8} \boldsymbol{e}_\alpha f_\alpha^{(eq)}. \tag{7b}$$

The speed of sound of this model is $c_s = c/\sqrt{3}$, and the equation of state is that of an ideal gas,

$$p = \rho c_s^2. \tag{8}$$

Equation (3) is one of numerous ways to model the transport equation of f, Eq. (1).

Based on the Chapman–Enskog analysis, the solution for $f_\alpha(\boldsymbol{x}, t)$ may be expanded in the form of

$$f_\alpha(\boldsymbol{x}, t) = f_\alpha^{(eq)}(\boldsymbol{x}, t) + f_\alpha^{(1)}(\boldsymbol{x}, t) + \cdots, \tag{9}$$

where $f_\alpha^{(1)}$ in Eq. (9) is formally smaller than $f_\alpha^{(eq)}$ in the expansion. Substitution of Eq. (9) into Eq. (3) leads to

$$f_\alpha^{(1)}(\boldsymbol{x}, t) = -\lambda\left[\frac{\partial f_\alpha^{(eq)}}{\partial t} + \boldsymbol{e}_\alpha \cdot \nabla f_\alpha^{(eq)}\right]. \tag{10}$$

Proceeding with the Chapman–Enskog analysis, it can be shown that the Euler equations can be recovered from the solution for $f_\alpha^{(eq)}$ and the NS equations are recovered in the near incompressible limit (i.e., the Mach number $M = |\boldsymbol{u}|/c_s \ll 1$) by the first two terms in Eq. (9). The viscosity of the fluid is

$$\nu = \lambda c_s^2. \tag{11}$$

Equation (3) can be further discretized in space and time. The completely discretized form of Eq. (1), with the time step δt and space step $\boldsymbol{e}_\alpha \delta t$, is

$$f_\alpha(\boldsymbol{x}_i + \boldsymbol{e}_\alpha \delta t, t + \delta t) - f_\alpha(\boldsymbol{x}_i, t) = -\frac{1}{\tau}\left[f_\alpha(\boldsymbol{x}_i, t) - f_\alpha^{(eq)}(\boldsymbol{x}_i, t)\right], \tag{12}$$

where $\tau = \lambda/\delta t$, and $\boldsymbol{x}_i$ is a point in the discretized physical space. The above equation is the lattice Boltzmann equation [1–3] with Bhatnagar–Gross–Krook (BGK) approximation [9]. The left-hand side (LHS) of Eq. (12) is physically a streaming process for particles while the RHS models the collisions through relaxation.

Although the lattice Boltzmann equation historically originates from the lattice gas cellular automata [14, 15], it is indeed a special finite difference form of the continuous Boltzmann kinetic equation, i.e., the LHS of Eq. (3) is discretized along the direction of the characteristic line with discretization of phase space and time tied together [10, 11]. The leading order truncation error of such a discretization is then taken into account exactly by modifying the viscosity in the NS equation derived from Eq. (12) to

$$\nu = \left(\tau - \frac{1}{2}\right) c_s^2 \delta t. \tag{13}$$

The positivity of the viscosity thus requires that $\tau > 1/2$. The lattice Boltzmann scheme consists of two computational steps,

$$\text{collision step} \qquad \tilde{f}_\alpha(\boldsymbol{x}_i, \mathrm{t}) - f_\alpha(\boldsymbol{x}_i, \mathrm{t}) = -\frac{1}{\tau}\left[f_\alpha(\boldsymbol{x}_i, \mathrm{t}) - f_\alpha^{(eq)}(\boldsymbol{x}_i, \mathrm{t})\right] \tag{14a}$$

$$\text{streaming step} \qquad f_\alpha(\boldsymbol{x}_i + \boldsymbol{e}_\alpha \delta t, t + \delta t) = \tilde{f}_\alpha(\boldsymbol{x}_i, t), \tag{14b}$$

where f_α and $\tilde{f}_\alpha$ denote the pre- and post-collision state of the distribution function, respectively. The advantages of solving the lattice Boltzmann equation over the NS equations can now be seen. In the kinetic equation for f_α given by Eq. (3), the advection operator is linear in the phase space whereas the convection term is nonlinear in the NS equation. In traditional CFD methods, the pressure is typically obtained by solving the Poisson or Poisson-like equation derived from the incompressible NS equations that can be time consuming. In the LBE method, the pressure is obtained through an extremely simple equation of state $p = \rho c_s^2$. This is an appealing feature of the LBE method. The discretized Eq. (14) for f_α is explicit in form, easy to implement, and natural to parallelize. The collision step is completely local. The streaming step takes very little computational effort at every time step.

However, unlike solving the NS equations for which the non-slip condition for $\boldsymbol{u}$ on a solid wall is satisfied at the macroscopic level, there is no corresponding, physically based boundary condition for f_α on a solid wall at the mesoscopic level. For a lattice node located on the fluid side at $\boldsymbol{x}_f$, as illustrated in Fig. 2, Eq. (14b) clearly indicates a need for the information of $\tilde{f}_\alpha$ at $\boldsymbol{x}_b$ on the solid side. Therefore all the effort in the previous treatment of the boundary conditions in the LBE models is mainly focused on the calculation of $\tilde{f}_\alpha$ moving from the wall into the fluid region. In previous works of the LBE, the most often used boundary condition on the wall is the so-called bounce-back scheme [16–18]. In the bounce-back scheme, after a particle distribution f_α streams from a fluid node at $\boldsymbol{x}_f$ to a boundary node at $\boldsymbol{x}_b$ along the direction of $\boldsymbol{e}_\alpha$, the particle distribution f_α scatters back to

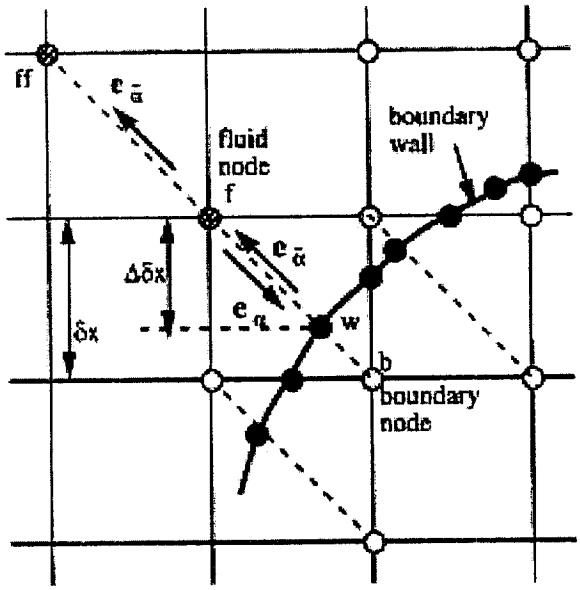

FIG. 2. Layout of the regularly spaced lattices and curved wall boundary.

the node x_f along the direction of $e_{\bar{\alpha}}(=-e_\alpha)$ as $\tilde{f}_\alpha$. Since the wall position x_w was forced to be located at x_b, this is referred to as bounce-back on the node (BBN) [19]. However, a finite slip velocity at the stationary wall exists [20, 18] and the accuracy for the flow field is thus degraded due to the inaccuracy of the boundary conditions [17]. In simulating suspension flows using the LBE, Ladd placed the solid walls in the middle between the lattice nodes [21]. This is referred to as bounce-back on the link (BBL). It has been shown that the BBL scheme gives a second-order accurate result for straight walls [24, 18]. Noble *et al.* developed a second-order accurate boundary condition to compute $\tilde{f}_\alpha$ but it is only applicable to straight walls in triangular lattice space [22]. He *et al.* generalized the scheme of Noble *et al.* to arbitrary lattice [18]. Chen *et al.* placed the wall on the lattice node so that x_b is one lattice inside the wall [23]. They used an extrapolation of f_α on the fluid side (including the wall node) to obtain f_α at x_b. Zou and He proposed to apply the BBL scheme only for the non-equilibrium part of f_α at the wall [24].

For a curved geometry, the use of BBL requires approximation of the curved solid boundary by a series of stair steps. The geometric integrity cannot be preserved by such an approximation. For high Reynolds number flows, the integrity of geometry is important since the vorticity generation and stress distributions are sensitive to the geometrical resolution. To this end, He and Luo proposed to use the LBE with nonuniform grid with second order interpolations [10, 25, 26]. He and Doolen further applied the interpolation to the LBE with curvilinear coordinates or body-fitted coordinates [27]. Mei and Shyy solved Eq. (3) in curvilinear coordinates using the finite difference method [28]. While the wall geometry is accurately preserved in body-fitted coordinates, the flexibility to handle complex geometries is maintained by using the numerical grid generation techniques common to the Navier–Stokes solvers. It should be noted that perhaps the most profound and rigorous theoretical treatment of the boundary condition along the wall is given by Ginzbourg and d'Humières [29]. The scheme proposed by Ginzbourg and d'Humières is local and accurate up to second order in Chapman–Enskog expansion. However, this work has not

attracted sufficient attention because its implementation is not as easy as the bounce-back scheme.

In this work, a robust, second-order accurate treatment for the distribution function f_α near a curved boundary is developed based on the method recently proposed by Filippova and Hänel (hereinafter referred to as FH) [30]. In Ref. [30], the boundary condition for f_α on the solid side is evaluated using Eq. (3) for f_α, and the Taylor series expansion in both space and time for f_α near the wall. FH reported numerical results for a uniform flow over a cylinder [30]. However, it is found in this work that when tested in a pressure driven channel flow (see implementation and discussions in Section II) there is a strong boundary-condition-induced instability when the distance from the wall to the first lattice on the fluid side is less than half of the lattice size.

Using the Taylor series expansion for the velocity $\boldsymbol{u}$ near the wall, a new treatment for f_α near a curved wall is proposed in this work. While maintaining a second-order accuracy of the solution in handling curved walls, the computational stability is improved so that lower viscosity, or higher Reynolds number, can be attained in the LBE simulations. The new boundary condition treatment is tested systematically to assess the temporal and spatial accuracy and robustness in 2-D channel flow with constant and oscillating pressure gradients, flow due to an impulsively started wall, lid-driven square cavity flow, and flow over a column of circular cylinders. Detailed comparisons for the flow field are made with either analytic solutions or well-resolved numerical solutions of the Navier–Stokes equations by using a finite difference method. The improved boundary treatment represents a significant step towards solving practically relevant flow problems using the LBE method.

II. FORMULATION FOR THE IMPROVED BOUNDARY CONDITION

Filippova and Hänel [30] considered a curved boundary lying between the lattice nodes of spacing δx, as illustrated in Fig. 2, and briefly presented the derivation of their scheme for the treatment of a curved boundary. However, they did not offer explanation to justify the theoretical basis of their method. It is instructive to first reexamine their derivation thoroughly. Based on the insight gained, an improved boundary treatment is then proposed.

A. *Reexamination of and Comments on the Filippova–Hänel Treatment*

The macroscopic flow has a characteristic length of L. The lattice nodes on the solid and fluid side are denoted as $\boldsymbol{x}_b$ and $\boldsymbol{x}_f$, respectively, in Fig. 2. The filled small circles on the boundary, $\boldsymbol{x}_w$, denote the intersections of the wall with various lattice links. The boundary velocity at $\boldsymbol{x}_w$, the intersection with the wall on the link between $\boldsymbol{x}_b$ and $\boldsymbol{x}_f$, is $\boldsymbol{u}_w$. The fraction of an intersected link in the fluid region is Δ, that is,

$$\Delta = \frac{|\boldsymbol{x}_f - \boldsymbol{x}_w|}{|\boldsymbol{x}_f - \boldsymbol{x}_b|}. \tag{15}$$

Obviously, $0 \leq \Delta \leq 1$ and the horizontal or vertical distance between $\boldsymbol{x}_b$ and $\boldsymbol{x}_w$ is $\Delta \cdot \delta x$ on the square lattice. Suppose the particle momentum moving from $\boldsymbol{x}_f$ to $\boldsymbol{x}_b$ is $\boldsymbol{e}_\alpha$ and the reversed one from $\boldsymbol{x}_b$ to $\boldsymbol{x}_f$ is $\boldsymbol{e}_{\bar{\alpha}} = -\boldsymbol{e}_\alpha$. After the collision step, $\tilde{f}_\alpha$ on the fluid side is known, but not on the solid side. (Hereafter we shall use $\boldsymbol{e}_{\bar{\alpha}}$ and $f_{\bar{\alpha}}$ to denote the velocity and the distribution function coming from a solid node to a fluid node, and $f_{\bar{\alpha}}$ is the unknown

to be computed.) To finish the streaming step,

$$f_{\bar{\alpha}}(x_f = x_b + e_{\bar{\alpha}}\delta t, t + \delta t) = \tilde{f}_{\bar{\alpha}}(x_b, t), \tag{16}$$

it is clear that $\tilde{f}_{\bar{\alpha}}(x_b, t)$ is needed. To construct $\tilde{f}_{\bar{\alpha}}(x_b, t)$ based upon some known information in the surrounding, Filippova and Hänel essentially proposed using the linear interpolation [30],

$$\tilde{f}_{\bar{\alpha}}(x_b, t) = (1 - \chi)\tilde{f}_{\alpha}(x_f, t) + \chi f_{\alpha}^{(*)}(x_b, t) + 2w_{\alpha}\rho\frac{3}{c^2}e_{\bar{\alpha}} \cdot u_w, \tag{17}$$

where $u_w \equiv u(x_w, t)$ is the velocity at the wall and χ is the weighting factor (to be determined) that controls the linear interpolation (or extrapolation) between $\tilde{f}_{\alpha}(x_f, t)$ and $f_{\alpha}^{*}(x_b, t)$, a fictitious equilibrium distribution function given by

$$f_{\alpha}^{(*)}(x_b, t) = w_{\alpha}\rho(x_f, t)\left[1 + \frac{3}{c^2}e_{\alpha} \cdot u_{bf} + \frac{9}{2c^4}(e_{\alpha} \cdot u_f)^2 - \frac{3}{2c^2}u_f \cdot u_f\right]. \tag{18}$$

In the above, $u_f \equiv u(x_f, t)$ is the fluid velocity near the wall and u_{bf} is to be chosen. It is emphasized here that the weighting factor χ depends on how u_{bf} is chosen. However, the choice of u_{bf} is not unique. For example, either $u_{bf} = u_f$ or a linear extrapolation using $u_{bf} = (\Delta - 1)u_f/\Delta + u_w/\Delta$ appears reasonable.

To determine χ in Eq. (17), FH considered flows under the condition

$$L/(cT) \ll 1, \tag{19}$$

i.e., the flow has an intrinsic characteristic time scale T that is much larger than the advection time on the lattice scale, L/c. This "slow-flow" condition enabled FH to approximate $f_{\bar{\alpha}}(x_f, t + \delta t)$ in Eq. (16) by $f_{\bar{\alpha}}(x_f, t)$,

$$f_{\bar{\alpha}}(x_f = x_b + e_{\bar{\alpha}}\delta t, t + \delta t) = f_{\bar{\alpha}}(x_f, t) + \delta t\frac{\partial f_{\bar{\alpha}}}{\partial t} + \cdots.$$

For the purpose of the order-of-magnitude estimate, it is seen that $O(\partial f_{\bar{\alpha}}/\partial t) = O(f_{\bar{\alpha}}/T)$ so that

$$f_{\bar{\alpha}}(x_f, t+\delta t) = f_{\bar{\alpha}}(x_f, t)\left[1+O\left(\frac{\delta t}{T}\right)\right] = f_{\bar{\alpha}}(x_f, t)\left[1+O\left(\frac{\delta x}{L}\frac{L}{cT}\right)\right] \approx f_{\bar{\alpha}}(x_f, t). \tag{20}$$

It is noted that under condition (19) the neglected terms are of $O(\frac{\delta x}{L}\frac{L}{cT})$ which are much smaller than the $O(\frac{\delta x}{L})$ terms of present interest (in deriving an accurate boundary condition for $\tilde{f}_{\bar{\alpha}}(x_b, t)$). Applying the Chapman–Enskog expansion in the form given by Eqs. (9)–(10) and invoking the "slow flow" approximation, one obtains

$$\begin{aligned} f_{\bar{\alpha}}(x_f, t) &= f_{\bar{\alpha}}^{(eq)}(x_f, t) - \lambda\left[\frac{\partial f_{\bar{\alpha}}^{eq}}{\partial t} + e_{\bar{\alpha}} \cdot \nabla f_{\bar{\alpha}}^{eq}\right] + \cdots \\ &\approx f_{\bar{\alpha}}^{(eq)}(x_f, t) - \lambda e_{\bar{\alpha}} \cdot \nabla f_{\bar{\alpha}}^{eq} + \cdots. \end{aligned} \tag{21}$$

For $f_{\bar{\alpha}}^{(eq)}$ given by Eq. (5), the leading order term in $\nabla f_{\bar{\alpha}}^{eq}$ is given by $\rho w_{\alpha}(3/c^2)e_{\bar{\alpha}} \cdot \nabla u$ since the rest are higher order terms in the near incompressible flow limit. Noticing that

$\lambda = \tau\delta t$, Eq. (21) becomes

$$f_{\bar{\alpha}}(\boldsymbol{x}_f, t) \approx f_{\bar{\alpha}}^{(eq)}(\boldsymbol{x}_f, t) - \tau\delta t\rho w_\alpha \frac{3}{c^2}\boldsymbol{e}_{\bar{\alpha}} \cdot \nabla\boldsymbol{u} \cdot \boldsymbol{e}_{\bar{\alpha}}$$
$$= f_\alpha^{(eq)}(\boldsymbol{x}_f, t) - 2\rho w_\alpha \frac{3}{c^2}\boldsymbol{u}_f \cdot \boldsymbol{e}_\alpha - \tau\delta t\rho w_\alpha \frac{3}{c^2}\boldsymbol{e}_\alpha \cdot \nabla\boldsymbol{u} \cdot \boldsymbol{e}_\alpha \tag{22}$$

which approximates the LHS of Eq. (16). To expand the RHS of Eq. (16) in terms of the small computational parameter

$$\frac{\delta x}{L} = \frac{c\delta t}{L} \ll 1, \tag{23}$$

it is first noted that $f_\alpha^{(*)}(\boldsymbol{x}_b, t)$ in Eq. (18) can be expressed as

$$f_\alpha^{(*)}(\boldsymbol{x}_b, t) = f_\alpha^{(eq)}(\boldsymbol{x}_f, t) + w_\alpha\rho\frac{3}{c^2}\boldsymbol{e}_\alpha \cdot (\boldsymbol{u}_{bf} - \boldsymbol{u}_f) \tag{24}$$

so that the RHS of Eq. (16), or Eq. (17), can be rewritten as

$$\tilde{f}_{\bar{\alpha}}(\boldsymbol{x}_b, t)$$
$$\approx f_\alpha^{(eq)}(\boldsymbol{x}_f, t) + (1-\chi)(1-1/\tau)f_\alpha^{(1)}(\boldsymbol{x}_f, t) + w_\alpha\rho\frac{3}{c^2}\boldsymbol{e}_\alpha \cdot (\chi\boldsymbol{u}_{bf} - \chi\boldsymbol{u}_f - 2\boldsymbol{u}_w)$$
$$= f_\alpha^{(eq)}(\boldsymbol{x}_f, t) - (1-\chi)(\tau-1)\delta t w_\alpha\rho\frac{3}{c^2}\boldsymbol{e}_\alpha \cdot \nabla\boldsymbol{u} \cdot \boldsymbol{e}_\alpha$$
$$+ w_\alpha\rho\frac{3}{c^2}\boldsymbol{e}_\alpha \cdot (\chi\boldsymbol{u}_{bf} - \chi\boldsymbol{u}_f - 2\boldsymbol{u}_w). \tag{25}$$

Based on linear interpolation, $\boldsymbol{u}_{bf} \approx (\Delta-1)\boldsymbol{u}_f/\Delta + \boldsymbol{u}_w/\Delta$, expanding the velocity $\boldsymbol{u}_f$ near the wall ($\boldsymbol{x}_w$) using Taylor series, and noticing that $\boldsymbol{x}_b - \boldsymbol{x}_f = \delta t\boldsymbol{e}_\alpha$, one obtains $\boldsymbol{u}_{bf} - \boldsymbol{u}_f \approx \delta t\nabla\boldsymbol{u} \cdot \boldsymbol{e}_\alpha$. Equating Eqs. (22) and (25) and matching terms linear in δt results in $\chi = (2\Delta - 1)/\tau$. For $\boldsymbol{u}_{bf} = \boldsymbol{u}_f$, we have $\boldsymbol{u}_{bf} - \boldsymbol{u}_f = 0$ in Eq. (25). Matching to $O(\delta t)$ then requires $\chi = (2\Delta-1)/\tau = (2\Delta-1)/(\tau-1)$. FH found that $\boldsymbol{u}_{bf} = (\Delta-1)\boldsymbol{u}_f/\Delta + \boldsymbol{u}_w/\Delta$ gives computationally stable results only for $\Delta > 1/2$. Hence, they proposed that

$$\boldsymbol{u}_{bf} = (\Delta-1)\boldsymbol{u}_f/\Delta + \boldsymbol{u}_w/\Delta \quad \text{and} \quad \chi = (2\Delta-1)/\tau \quad \text{for } \Delta \geq \frac{1}{2} \tag{26}$$

and

$$\boldsymbol{u}_{bf} = \boldsymbol{u}_f \quad \text{and} \quad \chi = (2\Delta-1)/(\tau-1) \quad \text{for } \Delta < \frac{1}{2}. \tag{27}$$

To recapitulate, there are three independent assumptions that have been made in the foregoing derivation. These are: (i) the Chapman–Enskog expansion in the form given by Eqs. (9)–(10) is valid; (ii) the intrinsic time of the unsteady flow must be large compared with the advection time on the lattice scale given by Eq. (19); (iii) the lattice space must be small compared with the characteristic length scale of the flow as given by Eq. (23) so that the Taylor series expansion for the velocity field near the wall is valid. There have been a large number of papers in the existing literature regarding the validity and usefulness of Chapman–Enskog expansion for the solution to the Boltzmann equation. The "slow flow"

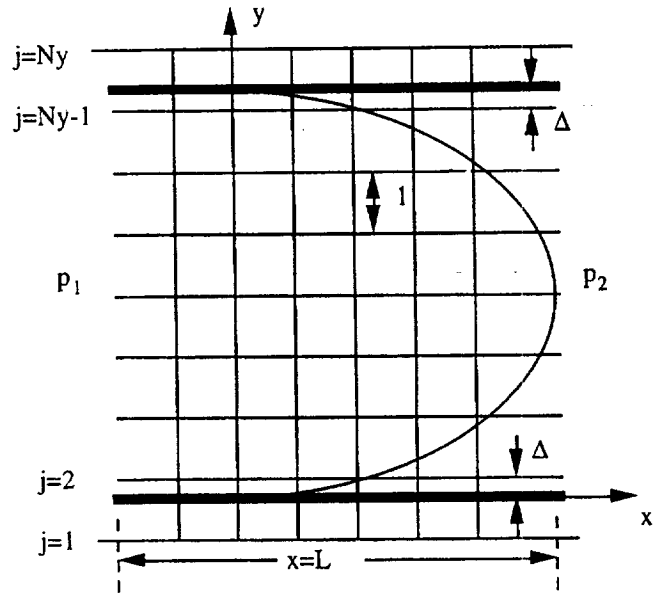

FIG. 3. Lattice distribution in channel flow simulations with arbitrary Δ.

condition is introduced to simplify the derivation of the boundary condition for f_α; the implication of this assumption will be briefly addressed later in comparing the computational results with that based on the conventional bounce-back scheme. The last assumption is a typical computational resolution requirement.

Equation (17) is essentially a linear interpolation (or extrapolation) and is used continuously in the computation. When the weighting factor χ becomes too large, instability may develop. For $\Delta \geq 1/2$, $|\chi| = |2\Delta - 1|/\tau$ is always less than 2 since the positivity of the viscosity in the LBE scheme requires $\tau > 1/2$. For $\Delta < 1/2$, $|\chi| = |(2\Delta - 1)/(\tau - 1)|$ and it may become too large when τ is near 1. To illustrate this point, a fully developed pressure driven 2-D channel flow is considered. The grid arrangement is shown in Fig. 3. For steady flow, a constant pressure gradient ∇p along the x-direction is applied and can be treated as a body force. This is included [32] after the collision step by

$$\tilde{f}_\alpha(\boldsymbol{x}_i, t) = \tilde{f}_\alpha(\boldsymbol{x}_i, t) - w_\alpha \frac{3}{c^2}\frac{dp}{dx}\boldsymbol{e}_\alpha \cdot \hat{\boldsymbol{x}}, \tag{28}$$

where $\hat{\boldsymbol{x}}$ is the unit vector along the x-axis. The boundary condition for $\tilde{f}_\alpha(\boldsymbol{x}_i, t)$ on the wall follows those given by Eqs. (17), (18), (26), and (27). At the inlet ($i = 1$) and exit ($i = N_x$, in which N_x is the number of lattices in the x-direction) the following is imposed,

$$f_\alpha(i = 1, j) = f_\alpha(i = 2, j), \tag{29}$$

$$f_\alpha(i = N_x, j) = f_\alpha(i = N_x - 1, j). \tag{30}$$

With Eq. (29), the velocity profile at the inlet, $u_x(i = 2, j)$, is not needed. Instead, the fully developed velocity profile is sought as part of the solutions. In this part of the investigation, $N_y = 35$ is used. The exact solution for the velocity profile (given by Eq. (36)) is used as the velocity initial condition which differs from the final steady state solution due to numerical errors. The equilibrium distribution function $f_\alpha^{(eq)}$ based on the exact solution

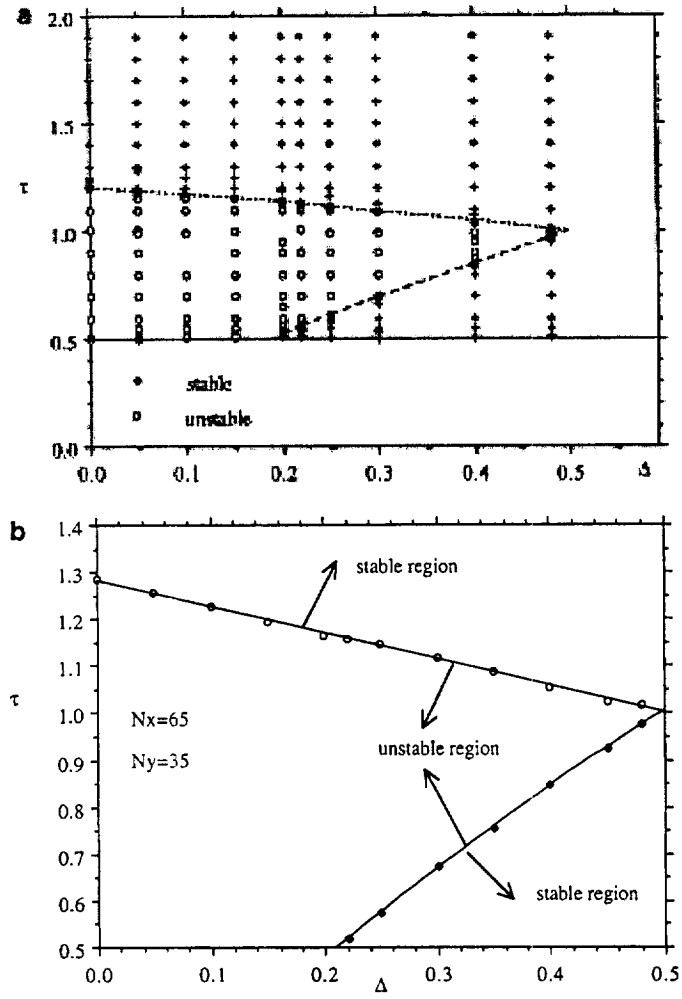

FIG. 4. (a) Regions of stability and instability in the LBE computation for fully developed 2-D channel flow using FH's boundary condition, Eqs. (17), (18), (26), (27), for $\Delta < 1/2$. (b) Regions of stability and instability in the LBE computation for 2-D channel flow entrance problem using FH's boundary condition, Eqs. (17), (18), (26), (27), for $\Delta < 1/2$.

for the velocity profile is used as the initial condition for f_α. The pressure gradient is set to $\frac{dp}{dx} = -1.0 \times 10^{-6}$. All computations are carried out using double precision.

For $\Delta < 1/2$, it is found that the computation is unstable for certain range of values of τ. Figure 4a shows the stability–instability boundaries in the (τ, Δ) space obtained from a large number of computations. For $\Delta < 0.2$, the computation becomes unstable when $\tau < 1$. The large instability region is an apparent source of concern for FH's scheme when $\Delta < 1/2$ since lower viscosity can only be achieved when τ is close to $1/2$.

One may speculate that the instability in the above example results from the lack of specifying an inlet velocity profile, $u_x(y)$, or due to the extrapolation of f_α at the inlet given by Eq. (29). To examine this possibility, a channel flow entrance problem is considered. Uniform velocity profiles, $u_x(y) = -(H^2/12\rho\nu)(dp/dx)$ and $u_y(y) = 0$ in which H is the channel height, are specified at $i = 1.5$ (half-way between the first and second lattices) and the distribution functions $f_\alpha(i = 1, j)$ for $\alpha = 1, 2$, and 8 are obtained using Eq. (17) with

$\chi = 0$ in accordance with $\Delta = 1/2$ at $i = 1.5$. The boundary conditions on the wall are based on Eqs. (17), (18), (26), and (27). The exit boundary condition for the f_α's is given by Eq. (30). Hence the extrapolation for f_α at the inlet is completely eliminated and the velocity profiles at the inlet are exactly given. Two types of initial conditions are used. Whenever possible, the equilibrium distribution functions corresponding to the uniform inlet velocity are specified at $t = 0$ throughout the flow field. This works for relatively larger values of τ. However, instability can be encountered when τ is considerably larger than the upper dash curve shown in Fig. 4a for the same value of Δ ($<1/2$). A second type of initial condition is thus implemented. A converged solution at a relatively large value of τ is used as the initial condition for a smaller value of τ. The value of τ is incrementally decreased to obtain the converged solutions for the new, smaller values of τ. When the actual instability region is approached, the increment in τ is maintained as small as 0.01 or 0.005. In the computation, $\frac{dp}{dx} = -1.0 \times 10^{-6}$, $N_y = 35$, and $N_x = 65$ are used. When the Reynolds number is low (due to the use of the small pressure gradient and larger τ), the exit velocity profile is very close to the exact solution corresponding to the fully developed channel flow which validates the solution procedure.

The stability–instability boundaries obtained through a large number of computations are shown in Fig. 4b. It is noted that the stability–instability boundaries are very similar to that shown in Fig. 4a for the fully developed channel flow despite the dramatic difference in the inlet boundary condition. Thus the source of the instability must result from the implementation of the solid wall condition. An alternative scheme must be developed to overcome this shortcoming.

B. *Improved Treatment for a Curved Boundary*

We realize that the flexibility in the construction of $f_\alpha^{(*)}(\boldsymbol{x}_b, t)$ is the key to achieving an improved computational stability as well as accuracy. Since $\chi = (2\Delta - 1)/(\tau - 1)$ given by Eq. (27) leads to a larger value of χ when τ is close to 1, it is desirable to reduce the magnitude of χ by increasing the magnitude of the denominator in the expression for χ. For $\Delta \geq 1/2$, $\boldsymbol{u}_{bf}$ is the fictitious fluid velocity inside the solid and the denominator for χ is τ. For $\Delta < 1/2$, $\boldsymbol{u}_{bf}$ was chosen by FH to be $\boldsymbol{u}_f$ which is the fluid velocity at $\boldsymbol{x}_f$ and it leads to $(\tau - 1)$ in the denominator for χ. Thus, we propose to use Eq. (26) for $\Delta \geq 1/2$ and use

$$\boldsymbol{u}_{bf} = \boldsymbol{u}_{ff} = \boldsymbol{u}_f(\boldsymbol{x}_f + \boldsymbol{e}_{\bar{\alpha}}\delta t, t) \qquad \text{for } \Delta < \frac{1}{2}. \tag{31}$$

Thus

$$\boldsymbol{u}_{bf} - \boldsymbol{u}_f = \boldsymbol{u}_f(\boldsymbol{x}_f + \boldsymbol{e}_{\bar{\alpha}}\delta t, t) - \boldsymbol{u}_f(\boldsymbol{x}_f, t) = -\delta t \nabla \boldsymbol{u} \cdot \boldsymbol{e}_\alpha. \tag{32}$$

This requires

$$-\tau(1 - \chi)(1 - 1/\tau) - \chi = 2\Delta - \tau \tag{33}$$

to match the $O(\delta t)$ terms in equating Eqs. (22) and (25). Hence

$$\chi = (2\Delta - 1)/(\tau - 2) \qquad \text{for } \Delta < \frac{1}{2}. \tag{34}$$

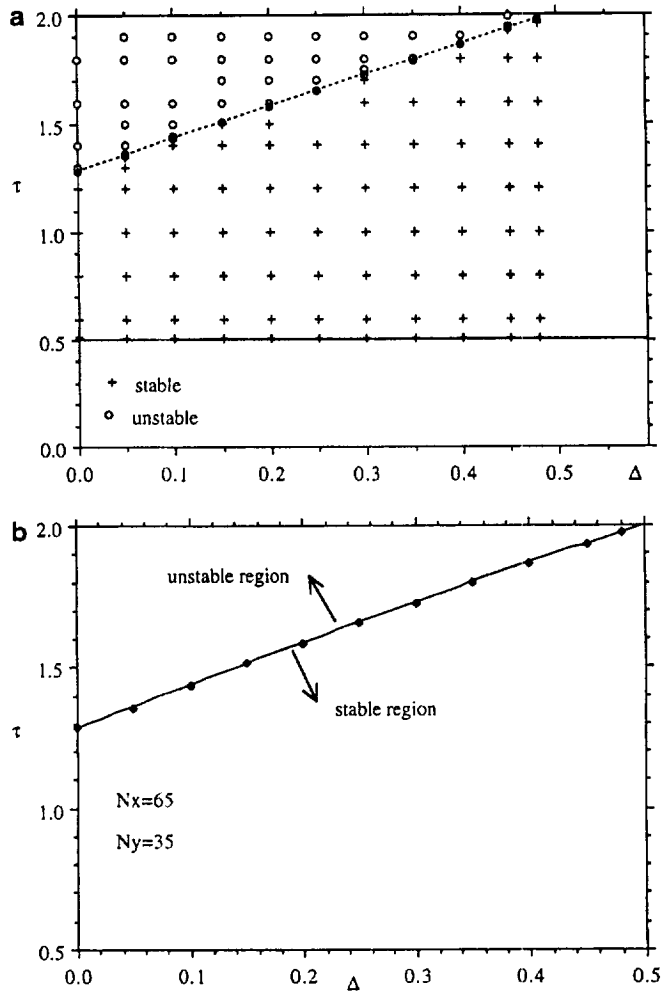

FIG. 5. (a) Regions of stability and instability in the LBE computation for fully developed 2-D channel flow using the present boundary condition, Eqs. (17), (18), (26), (31), (34), for $\Delta < 1/2$. (b) Regions of stability and instability in the LBE computation for the 2-D channel flow entrance problem using the present boundary condition, Eqs. (17), (18), (26), (31), (34), for $\Delta < 1/2$.

To test the improvement in the stability, the steady state, fully developed, pressure driven 2-D channel flow is again considered. Equations (31), (34) are used in lieu of Eq. (27). The rest of the implementation is exactly the same as described in the last section. Figure 5a shows the stability–instability boundary in the (τ, Δ) space for the fully developed channel flow. By comparing Fig. 5a with Fig. 4a, the improvement in the stability of the present treatment for this simple geometry case is clearly seen.

For the channel flow entrance problem, boundary conditions at the inlet and exit and the procedure for specifying the initial conditions are the same as described in the last section. Equations (31), (34) are used to replace Eq. (27) for the solid wall. The stability–instability boundary in the (τ, Δ) space for the entrance flow problem is shown in Fig. 5b. Close agreement in the stability–instability boundaries between Figs. 5a and 5b suggests that the improvement in the computational stability is not related to the treatment of the inlet boundary conditions. The improvement results rather from the different treatment in

the solid wall boundary condition. A direct consequence of this improvement is that lower values of τ, or lower viscosity ν, can now be used.

One may speculate at this point that $\boldsymbol{u}_f(\boldsymbol{x}_f + 2\boldsymbol{e}_{\bar{\alpha}}\delta t, t)$ can also be used for $\boldsymbol{u}_{bf}$ when $\Delta < 1/2$. This would further improve the stability since $\chi = (2\Delta - 1)/(\tau - 3)$. This is correct in principle. However, since the use of $\boldsymbol{u}_f(\boldsymbol{x}_f + \boldsymbol{e}_{\bar{\alpha}}\delta t, t)$ as $\boldsymbol{u}_{bf}$ already allows the use of τ whose value is close to $1/2$, there is little practical need to use $\boldsymbol{u}_f$ that is too far away from the wall.

For transient flows, a second-order extrapolation can be used for

$$\boldsymbol{u}_{bf} = \frac{\Delta - 1}{\Delta}\boldsymbol{u}(\boldsymbol{x}_f, t) + \frac{1}{\Delta}\boldsymbol{u}(\boldsymbol{x}_w, t) + \frac{1 - \Delta}{\Delta(1 + \Delta)}[\boldsymbol{u}(\boldsymbol{x}_w, t) - (1 + \Delta)\boldsymbol{u}(\boldsymbol{x}_f, t) + \Delta\boldsymbol{u}(\boldsymbol{x}_f + \boldsymbol{e}_{\bar{\alpha}}\delta t, t)] \qquad \text{for } \Delta > \frac{1}{2}. \tag{35}$$

This treatment helps to improve the accuracy in the velocity approximation when $\boldsymbol{u}(\boldsymbol{x}, t)$ is not well resolved near the wall. Finally, it is easily seen that the present boundary condition treatment can be extended to 3-D flow problems involving curved geometry. The efficacy of such an extension will be examined in another paper.

III. RESULTS AND DISCUSSIONS

For the proposed boundary condition treatment to be useful, several issues need to be addressed: spatial and temporal accuracy, ability to handle geometric singularity, and the flexibility to handle complex geometry. Channel flows with constant and sinusoidally oscillating pressure gradients with analytic solutions are used to assess the spatial and temporal accuracy. The Stokes first problem (i.e., the flow due to an impulsively started wall) allows one to examine the response of the computed flow field to an imposed singular acceleration. The standard lid-driven cavity flow has a bounded domain but possesses stress or vorticity singularities near the corners between the moving and stationary walls. Finally, flow over a column of circular cylinders is the case used to assess the impact of the boundary treatment on the accuracy of the flow field around a curved boundary.

A. *Pressure Driven Channel Flows*

At steady flow, the exact solution for the x-velocity profile is given by

$$u_{exact}(y) = -\frac{1}{2}\frac{dp}{dx}\frac{H^2}{\rho\nu}(\eta^2 - \eta), \tag{36}$$

where $H = N_y - 3 + 2\Delta$ and $\eta = y/H = (j - 2 + \Delta)/H$. To assess the computational error of the LBE solution of the velocity, $u_{LBE}(y)$, the following relative L_2-norm error is defined

$$E_2 = \frac{\left\{\int_0^H [u_{LBE}(y) - u_{exact}(y)]^2\, dy\right\}^{1/2}}{\left[\int_0^H u_{exact}^2(y)\, dy\right]^{1/2}}. \tag{37}$$

With the oscillating pressure gradient, $\frac{dp}{dx} = Be^{-i\omega t}$, the exact solution can be easily expressed in complex variables. An important parameter in this flow is the Stokes number

St defined as

$$St = \sqrt{\frac{H^2\omega}{\nu}}. \tag{38}$$

The Stokes number is the ratio of the channel height H to the thickness of the Stokes layer $\sqrt{\nu/\omega}$. Since the error can vary with time, a time average over one period ($T = 2\pi/\omega$) is needed and the relative error is

$$E_2 = \frac{\left\{\int_0^T \int_0^H [u_{LBE}(y,t) - u_{exact}(y,t)]^2 \, dy \, dt\right\}^{1/2}}{\left[\int_0^T \int_0^H u_{exact}^2(y,t) \, dy \, dt\right]^{1/2}}. \tag{39}$$

In the BGK model, $\Delta t = \Delta x = \Delta y = 1$. Comparing with the channel height $H = N_y - 3 + 2\Delta$, the dimensionless grid size (or grid resolution) is H^{-1}.

Figure 6a shows the dependence of the relative L_2-norm error on the channel height H for $\tau = 0.55$ and $\Delta = 0.0$, 0.25, and 0.5. A maximum value of $N_y = 131$ is used. The second-order accuracy is demonstrated in the range of H investigated. It has been well established that the accuracy of the LBE method for the interior points is of second order. The fact that the overall accuracy is of second order in the present case means that the accuracy in the boundary condition is at least of second order. It is worth noticing that the derivation given in Section II ensures that f_α is second-order accurate near the wall. It does not guarantee the second-order accuracy of the velocity field near the wall. To address this issue, the wall slip velocity, $u_w = u_x(y = 0)$, is evaluated using a second-order extrapolation based on $u_x(y = \Delta)$, $u_x(y = 1 + \Delta)$, and $u_x(y = 2 + \Delta)$. Since the true wall velocity in the pressure driven channel flow is zero, the wall slip velocity u_w provides a measure of the accuracy for the treatment of the wall velocity. Figure 6b shows the dependence of u_w, normalized by the centerline velocity $u_{max} = -(H^2/8\rho\nu)(dp/dx)$, on H for $\Delta = 0.0$, 0.25, and 0.5 with $\tau = 0.55$. Quadratic convergence is clearly observed in all three cases which demonstrates the second-order accuracy of the velocity field near the solid wall. This is entirely consistent with the results shown in Fig. 6a which involves global convergence rather than the local ($y = 0$) convergence. Figure 6c shows the relative error as a function of Δ using the present boundary treatment (Eqs. (17), (18), (26), (31), (34)) for $0 \le \Delta \le 1$. The error in the range of $0 \le \Delta \le 1/2$ is comparable to that in the range of $1/2 < \Delta \le 1$. The present boundary condition treatment does not induce larger computational error and is substantially more robust. Furthermore the second-order accuracy is achieved in general by the present treatment for $\Delta \le 1/2$.

Figure 7 shows the dependence of the relative L_2-norm error on the channel height H in the oscillating pressure driven channel flow for Stokes number $St = H\sqrt{\omega/\nu} = 1$ and 8. For $St = 1$, the Stokes layer is as thick as the channel height H. For $\Delta = 0.25$, 0.5, and 0.75, second-order accuracy in space is clearly demonstrated. Since the time step δt in LBE is equal to the spatial resolution δx, the accuracy in time must also be of second-order in order for the time-averaged L_2-norm error to have a slope of 2 in Fig. 7. For $St = 8$, the Stokes layer thickness is about 1/8 of the channel height so that the computational error due to the insufficient resolution of the Stokes layer is a significant part of the error. For $\Delta = 0.25$, the first lattice in the flow field is only a quarter of the lattice size away from the wall. The Stokes layer is thus better resolved for $\Delta = 0.25$ (denoted by solid circles in Fig. 7) than for $\Delta = 0.5$ and 0.75. However, as H increases, the difference between $\Delta = 0.25$ and $\Delta = 0.5$ and 0.75 becomes smaller since all have reasonable resolutions in the Stokes

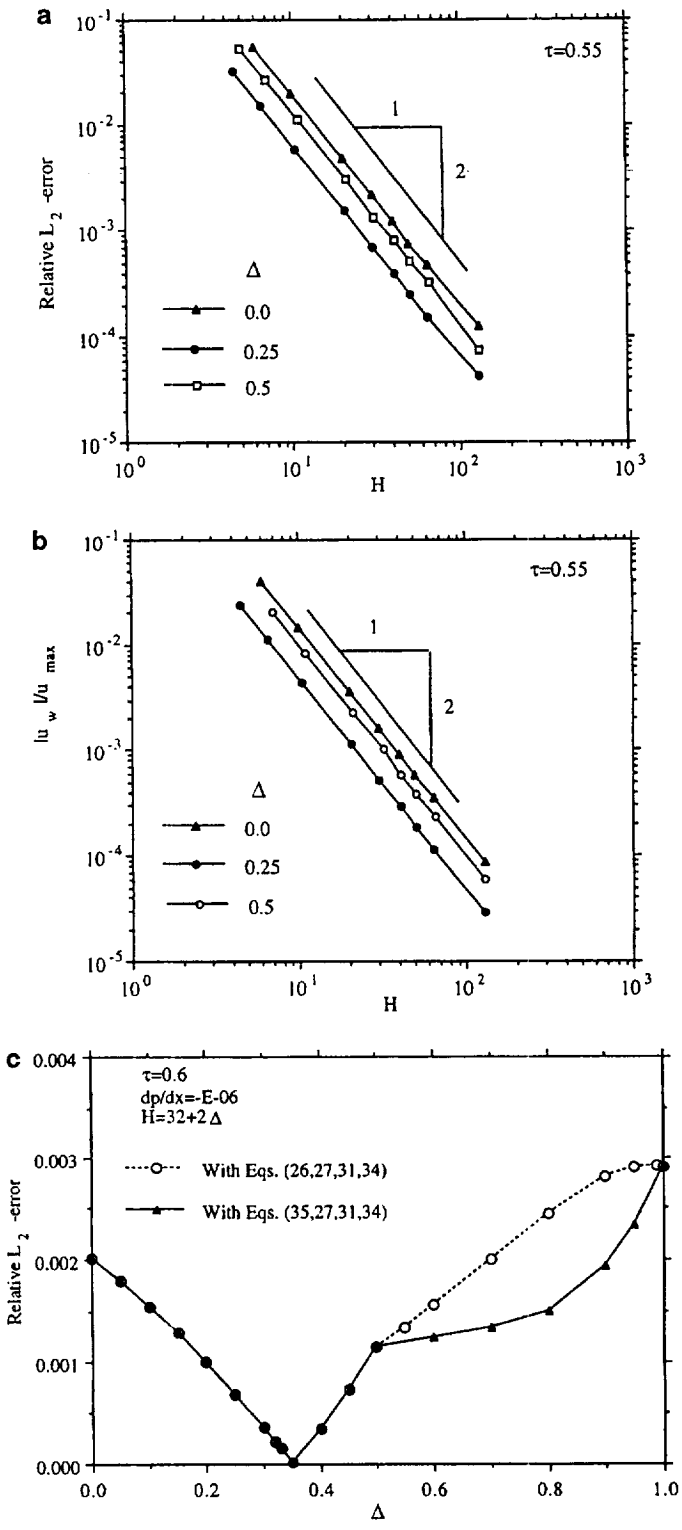

FIG. 6. (a) Dependence of relative L_2-norm error on the lattice resolution $H = N_y - 3 + 2\Delta$, in steady state pressure-driven channel flow simulations. (b) Quadratic convergence of the wall slip velocity in steady state pressure-driven channel flow simulations. (c) Relative L_2-norm error as a function of Δ in steady state pressure-driven channel flow simulations.

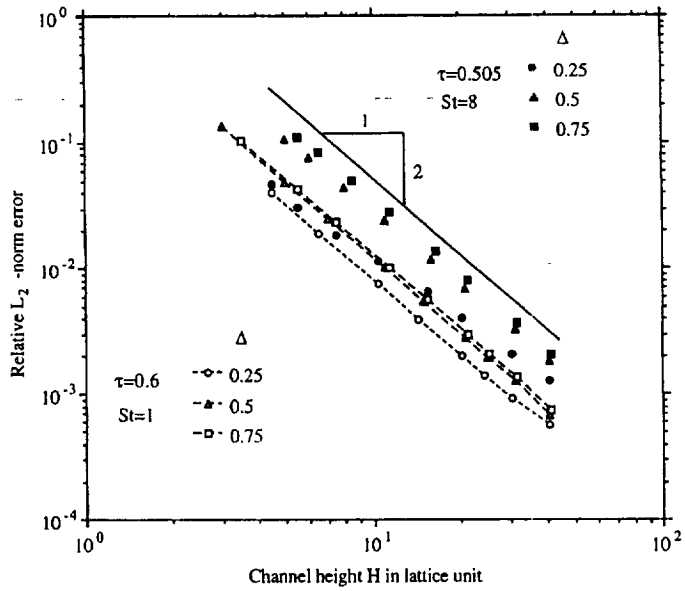

FIG. 7. Dependence of the L_2-norm error on the lattice resolution $H = N_y - 3 + 2\Delta$ in oscillating pressure driven channel flow. Stokes number $St = H\sqrt{\omega/\nu}$.

layer. Although the slope for the error curve for $\Delta = 0.25$ is observed to be about 1.5 that is less than 2, it is an indication of the better-than-expected accuracy at the low resolution end.

B. *Stokes First Problem: Flow Due to an Impulsively Started Wall*

For a wall located at $y = 0$ that is impulsively started, an unsteady Stokes layer of thickness $O(\sqrt{\nu t})$ develops near the wall. For a fixed-grid computation, the error at small time is expected to be large due to insufficient spatial resolution. In the LBE method, this is also compounded by the use of fixed δt $(= \delta x = \delta y = 1)$. Figure 8 shows the velocity profiles at $t = 100$ (in lattice unit). The wall velocity is $V = 0.1$ in lattice unit. The relaxation time $\tau = 0.52$ gives kinematic viscosity $\nu = 0.0067$. Similar to the oscillating pressure driven channel flow, the error is smaller for $\Delta = 0.25$ than for $\Delta = 0.5$ and 0.75 due to a better spatial resolution near the wall. Figure 9 shows the temporal variation of the relative L_2-norm error defined as

$$E_2 = \frac{\left\{\int_0^\infty [u_{LBE}(y,t) - u_{exact}(y,t)]^2\, dy\right\}^{1/2}}{\left[\int_0^\infty u_{exact}^2(y,t)\, dy\right]^{1/2}} \tag{40}$$

for $\Delta = 0.25$, 0.5, and 0.75. The result using the standard *bounce-back on the link* (BBL) scheme, which always sets $\Delta = 0.5$, is also shown. The large relative errors in the beginning are due to the smaller values of the denominator in the above equation. It should be emphasized that this flow at small time is difficult to deal with for any computational technique due to the singular acceleration and large spatial gradient. For an impulsively started Couette flow, the long-time solution approaches the exact linear velocity profile because the LBE method is a second-order accurate one. It is interesting to note that the present boundary

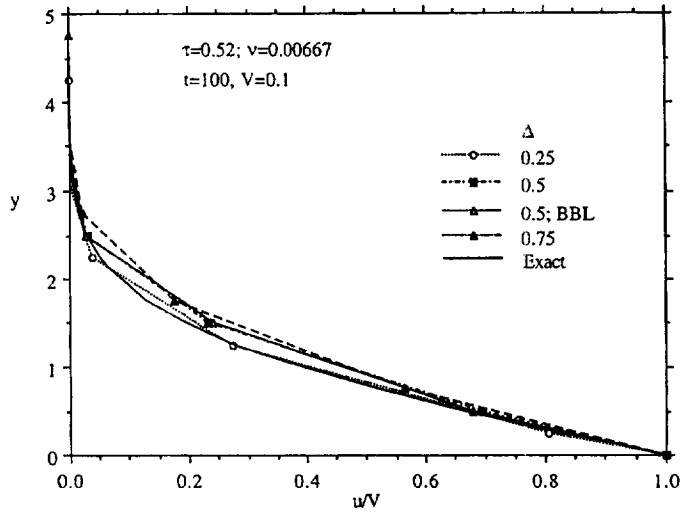

FIG. 8. Velocity profiles at $t = 100$ (lattice unit) of an impulsively started plate with various values of Δ. The bounce back on the link (BBL) always sets $\Delta = 1/2$.

condition treatment for $\Delta = 0.5$ gives a slightly smaller error than the BBL scheme in this highly transient case. In such a transient flow, the computational accuracy in the near-wall region is typically dictated by the near-wall spatial resolution which must be smaller than the Stokes layer thickness in order to resolve the local flow field. In a finite difference calculation for such a flow, δt and δx can be independently chosen. If δx is not sufficiently small, further reduction in δt will not lead to improvement in accuracy. At small t, neither the BBL scheme nor the present treatment resolved the Stokes layer so that the error is large. After the Stokes layer grows to a certain thickness, the spatial resolution becomes adequate

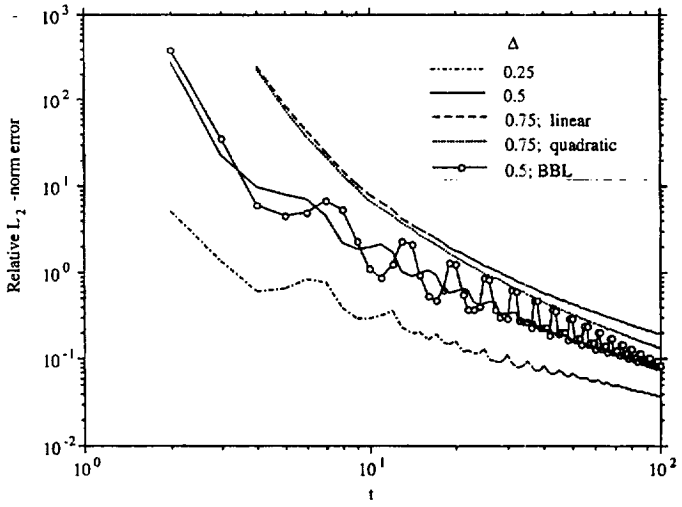

FIG. 9. Relative L_2-norm error of the velocity profile $u_x(y)$ during the initial transient of the impulsively started plate with various values of Δ. The "linear" version of the boundary condition corresponds to Eq. (26). The "quadratic" version corresponds to Eq. (35). The BBL is limited to $\Delta = 0.5$ only.

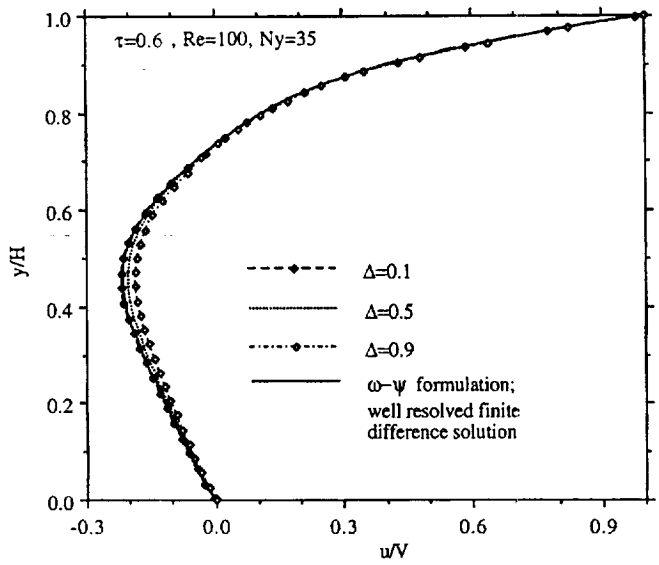

FIG. 10. Velocity profiles at the center ($x/H = 1/2$) in lid-driven cavity flow with various values of Δ at $\mathrm{Re} = 100$.

and the accuracy then improves. In view of the "slow flow" condition (19) introduced in the derivation, the performance of the current boundary treatment is comparable or better than the conventional bounce-back on the link scheme.

C. *Flow in a Lid-Driven Square Cavity*

Figure 10 shows the velocity profiles at the center ($x/H = 1/2$) of the cavity of width H at $Re = 100$ with $\tau = 0.6$. Only 35×35 lattices are used and the cavity width is $H = N_x - 3 + 2\Delta = 32 + \Delta$. This requires the lid velocity to be $V = \nu Re/H = 3.33/H$ in the lattice unit. It has a negligible compressibility effect for $H \sim 32$. A well-resolved finite difference solution for the velocity field based on the stream function-vorticity formulation is also shown for comparison. The velocity profile with $\Delta = 0.1$ agrees well with the finite difference solution. For $\Delta = 0.5$, the result is rather reasonable with such a resolution. The difference is slightly larger on the negative velocity part for $\Delta = 0.9$. The corner singularity in stress (or vorticity) is well handled for $\tau = 0.6$ and $N_x = 35$. However, for τ close to 0.5 and with $N_x = 35$, the corner singularity induces wiggles in the velocity field. This issue will be examined elsewhere. The flow field for $Re = 1000$ is obtained with 67×67 lattices using $\Delta = 0.1$, 0.5, and 0.9. Similar behavior in the velocity profiles is observed.

D. *Uniform Flow over a Column of Circular Cylinders*

To simulate the external flow over a single cylinder would require placing the outer boundary far away from the cylinder. In order to keep the computational effort at a reasonable level in using constant space lattices, a column of circular cylinders of radius r and center-to-center distance H is considered instead. The flow field that needs to be computed is thus limited to $-H \leq y \leq H$. At $y = -H$, the lattice is $j = 2$. The boundary conditions

at $j = 1$ for the f_α's are given by the following symmetry properties,

$$\begin{aligned} f_0(i,1) &= f_0(i,3), \quad & f_1(i,1) &= f_1(i,3), \quad & f_2(i,1) &= f_8(i,3), \\ f_3(i,1) &= f_7(i,3), \quad & f_4(i,1) &= f_6(i,3), \quad & f_5(i,1) &= f_5(i,3), \\ f_6(i,1) &= f_4(i,3), \quad & f_7(i,1) &= f_3(i,3), \quad & f_8(i,1) &= f_2(i,3). \end{aligned} \tag{41}$$

Similar conditions hold at $y = H$ for $j = N_y$. At the inlet, the uniform velocity, $u = V$, is specified at $i = 1.5$. Using $\Delta = 0.5$, $\chi = 0$, Eq. (17) is applied to obtain the f_α's at $i = 1$. At the exit, a simple extrapolation is used,

$$f_\alpha(N_x, j) = 2f_\alpha(N_x - 1, j) - f_\alpha(N_x - 2, j) \qquad \text{for } \alpha = 4, 5, \text{ and } 6. \tag{42}$$

On the surface of the circular cylinder, Eqs. (17), (18), (26), (31), and (34) proposed in this paper are used to update the boundary conditions for the f_α's.

Figure 11 shows the velocity profile $u(x = 0, y)/V$ for $H/r = 20$ at $Re = 2Vr/\nu = 10$ using $r = 3.5$. Two values of relaxation time τ (=0.505 and 0.525) are used. For $r = 3.5$, there are only 7 lattices from the front to the back stagnation points. The finite difference solution is obtained using body-fitted coordinates [33] and over 200 grid points are distributed along the upper surface of the circle. These two solution with $\tau = 0.505$ and $\tau = 0.525$ are virtually identical to each other and they are both close to the finite difference solution. Figure 12 shows the centerline ($y = 0$) velocity variations, upstream and downstream, respectively, at $Re = 10$ and 40. The sharp gradient near the front stagnation point, the length of the separation bubble, the maximum of the separation bubble velocity, and the recovery of the wake velocity are all in excellent agreement with the well resolved finite difference solution.

As can be seen now, an important improvement of the present boundary condition treatment over the bounce-back scheme is that it can preserve the accuracy of the geometry

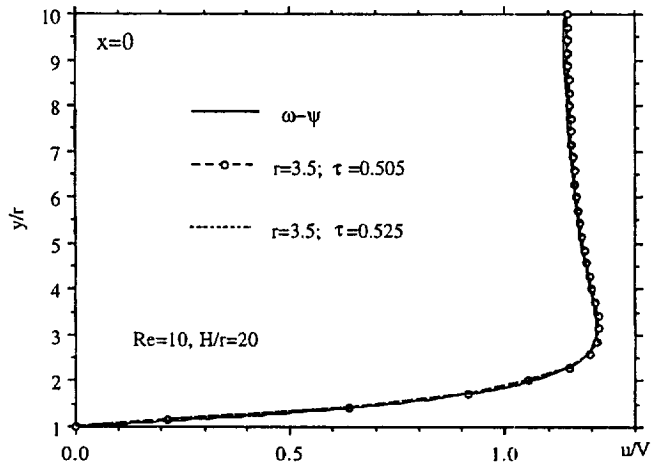

FIG. 11. Velocity profiles at $x = 0$ for uniform flow over a column of cylinders. The cylinder has a diameter ($2r$) of 7 lattice units. The cylinder center-to-center distance $H = 70$ lattice units.

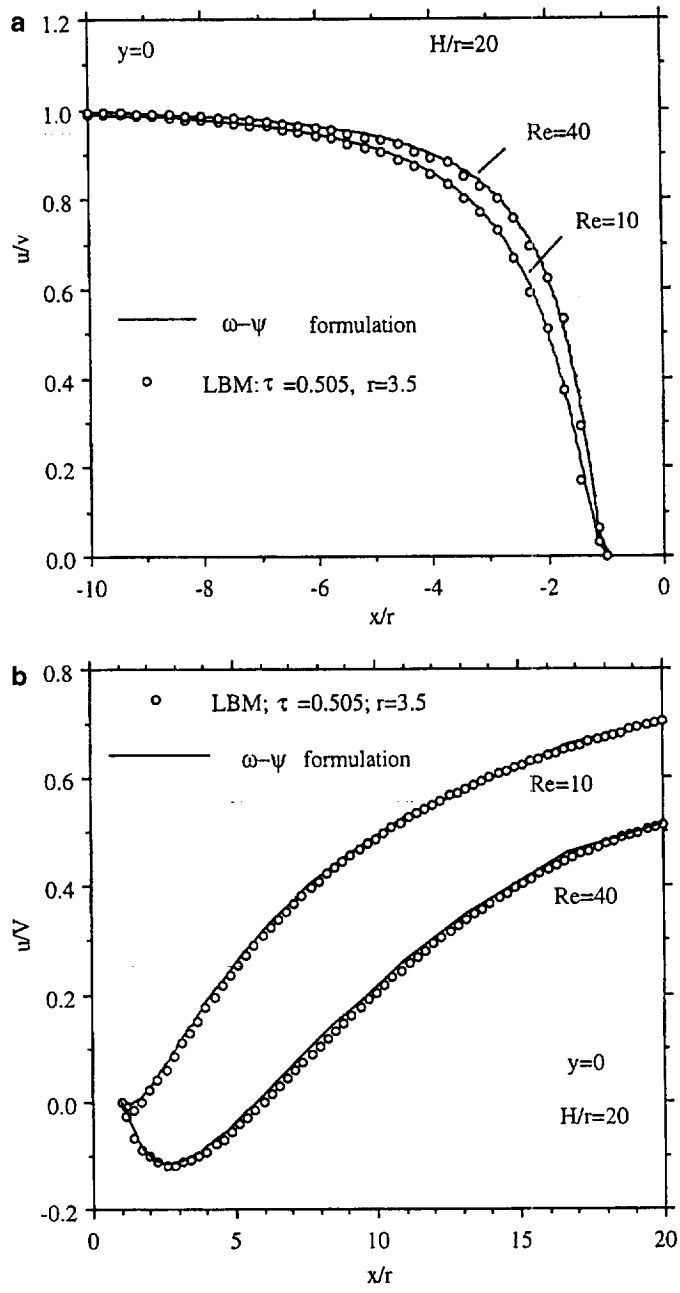

FIG. 12. Centerline ($y = 0$) velocity variation for a uniform flow over a column of cylinders. Finite difference results are based on $\omega - \psi$ formulation and are well resolved. (a) Upstream; (b) downstream.

under consideration. To further demonstrate this point, consider flow over a circular cylinder of radius (r) with the coordinate centered at the center of the cylinder. For $r = 3.4$ and 3.8, the front stagnation points are located at $x = -3.4$ and 3.8, respectively. With the bounce-back on the link (BBL) scheme, the front stagnation points in both cases will be placed at $x = -3.5$ which is half-way between the lattice at $x = -4$ and $x = -3$ on the centerline. In the present method, $\Delta = 0.6$ and 0.2 for r = 3.4 and 3.8, respectively. The

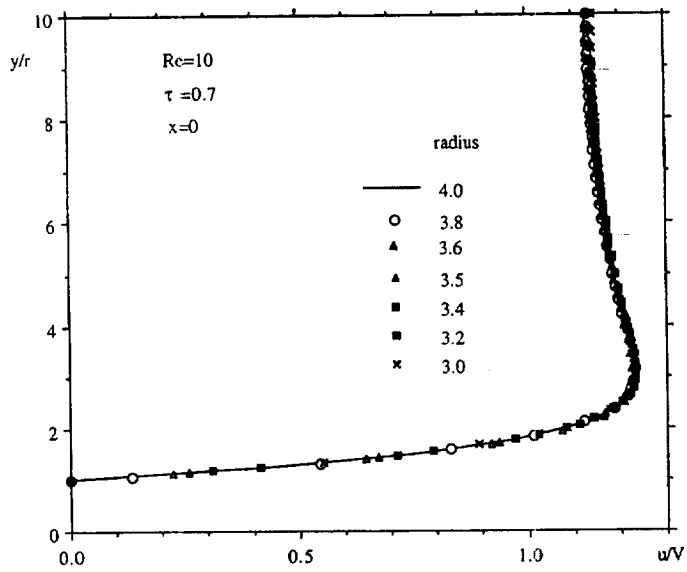

FIG. 13. Comparison of the velocity profiles at $x = 0$ for $r = 3.0, 3.2, 3.4, 3.5, 3.6, 3.8$, and 4.0 for $\mathrm{Re} = 10$ and $H/r = 20$.

difference in Δ can be accurately incorporated in the evaluation of $\tilde{f}_{\bar{\alpha}}(x_b, t)$. This implies that although the boundary links for $r = 3.4$ will be different from those for $r = 3.8$, the flow fields based on $r = 3.4$ and $r = 3.8$ should be nearly the same when the coordinates are normalized by the radius r. To validate this point, a series of computations are carried out for $r = 3.0, 3.2, 3.4, 3.5, 3.6, 3.8$, and 4.0 for $H/r = 20$ at $Re = 10$. The profiles of the dimensionless x-component velocity u_x/U as a function of y/r at $x = 0$ are compared for these seven different radii r in Fig. 13. Excellent agreement is observed. Figure 14 compares the u_x/U as a function of x/r at $y = 0$ for both the downstream and upstream regions for these seven different radii. Again, all seven cases compare very well even in the near wall region. This clearly demonstrates that the present boundary condition treatment has maintained geometric fidelity even with coarse grid resolutions.

It is noted that the interpolation for $\tilde{f}_{\bar{\alpha}}(x_b, t)$ given by Eq. (17) is carried along the line in the direction of e_α. The results for flow over a cylinder are quite satisfactory. Other interpolation procedures can certainly be devised to use more information on neighboring lattices in the flow field. However, this will result in a lot more complications in the implementation. It is not clear if such an attempt will necessarily lead to further improvement over the present approach.

IV. CONCLUSION

In this work a second-order accurate boundary condition treatment for the lattice Boltzmann equation is proposed. A series of studies are conducted to systematically validate the accuracy and examine the robustness of the proposed boundary condition in steady and unsteady flows involving flat and curved walls. Compared with the existing method for treating boundary condition in the lattice Boltzmann method, the proposed treatment has the following advantages: (i) It can preserve the geometry of interest without truncating

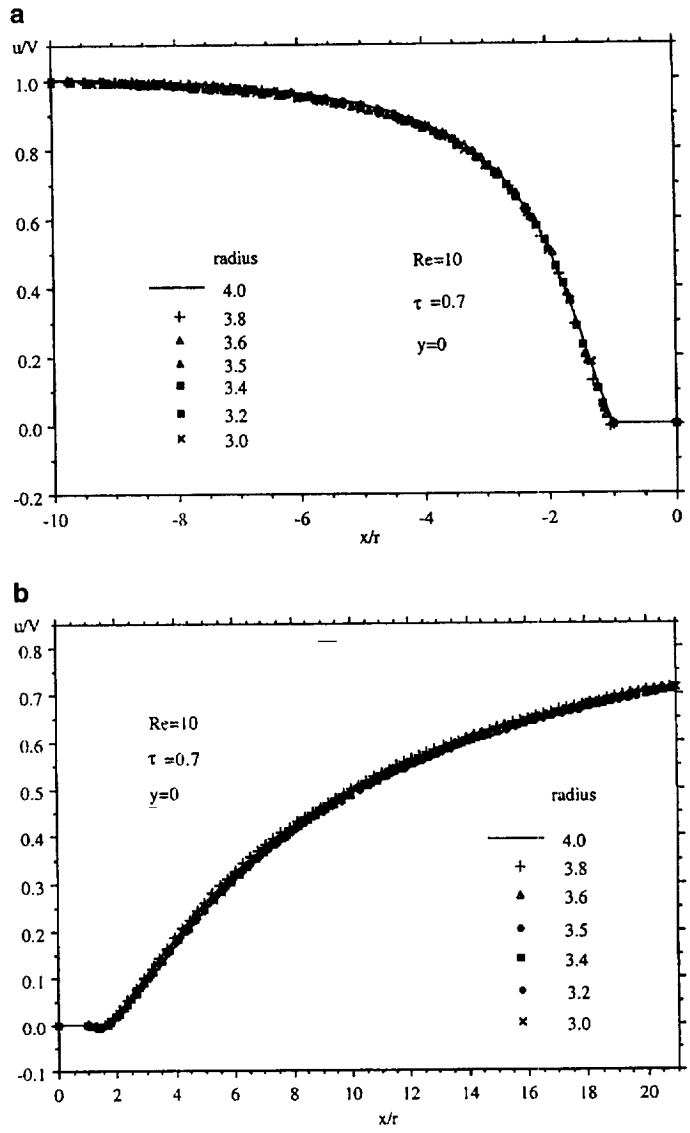

FIG. 14. Comparison of the centerline velocity for $r = 3.0$, 3.2, 3.4, 3.5, 3.6, 3.8, and 4.0 for $\mathrm{Re} = 10$ and $H/r = 20$. (a) Upstream region; (b) downstream region.

it into a series of stair steps. (ii) The boundary treatment generally results in solutions of second-order accuracy for the velocity field in space, and in time for some cases. (iii) Compared with the widely used bounce-back on the link scheme, the present treatment gives comparable or better results for the flow field under otherwise identical computational parameters.

ACKNOWLEDGMENTS

This work is supported by the NASA Langley Research Center. R. Mei also acknowledges partial support of the Alcoa Foundation, the Engineering Research Center (ERC) for Particle Science and Technology at the

University of Florida, the National Science Foundation (EEC-9402989), and Industrial partners of the ERC. W. Shyy acknowledges partial support of AFOSR and Eglin AFB. The authors are grateful to Dr. Filippova and Professor Hänel for helpful discussions.

REFERENCES

1. G. McNamara and G. Zanetti, Use of the Boltzmann equation to simulate lattice-gas automata, *Phys. Rev. Lett.* **61**, 2332 (1988).
2. F. Higuera, S. Succi, and R. Benzi, Lattice gas dynamics with enhanced collisions, *Europhys. Lett.* **9**, 345 (1989).
3. H. Chen, S. Chen, and W. H. Matthaeus, Recovery of the Navier–Stokes equations using a lattice-gas Boltzmann method, *Phys. Rev. A* **45**, R5339 (1992).
4. R. Benzi, S. Succi, and M. Vergassola, The lattice Boltzmann equation: Theory and applications, *Phys. Rep.* **222**, 145 (1992).
5. S. Chen and G. D. Doolen, Lattice Boltzmann method for fluid flows, *Ann. Rev. Fluid Mech.* **30**, 329 (1998).
6. R. Peyret and T. D. Taylor, *Computational Technique for Fluid Dynamics* (Springer-Verlag, New York, 1983), Vol. II.
7. C. A. J. Fletch, *Computational Techniques for Fluid Dynamics* (Springer-Verlag, New York, 1988), Vols. I, II.
8. W. Shyy, *Computational Modeling for Fluid Flow and Interfacial Transport*, corrected printing (Elsevier, Amsterdam, 1997).
9. P. L. Bhatnagar, E. P. Gross, and M. Krook, A model for collision processes in gases. I. Small amplitude processes in charged and neutral one-component system, *Phys. Rev. A* **94**, 511 (1954).
10. X. He and L.-S. Luo, A priori derivation of the lattice Boltzmann equation, *Phys. Rev. E* **55**, R6333 (1997).
11. X. He and L.-S. Luo, Theory of the lattice Boltzmann equation: From Boltzmann equation to lattice Boltzmann equation, *Phys. Rev. E* **56**, 6811 (1997).
12. T. Abe, Derivation of the lattice Boltzmann method by means of the discrete ordinate method for the Boltzmann equation, *J. Comput. Phys.* **131**, 241 (1997).
13. Y. H. Qian, D. d'Humières, and P. Lallemand, Lattice BGK models for Navier–Stokes equation, *Europhys. Lett.* **17**, 479 (1992).
14. U. Frisch, B. Hasslacher, and Y. Pomeau, Lattice-gas automata for the Navier–Stokes equation, *Phys. Rev. Lett.* **56**, 1505 (1986).
15. D. H. Rothman and S. Zaleski, *Lattice-Gas Cellular Automata: Simple Models of Complex Hydrodynamics* (Cambridge Univ. Press, New York, 1997).
16. D. P. Ziegler, Boundary conditions for lattice Boltzmann simulations, *J. Stat. Phys.* **71**, 1171 (1993).
17. I. Ginzbourg and P. M. Alder, Boundary flow condition analysis for the three-dimensional lattice Boltzmann model, *J. Phys. II France* **4**, 191 (1994).
18. X. He, Q. Zou, L.-S. Luo, and M. Dembo, Analytic solutions and analysis on non-slip boundary condition for the lattice Boltzmann BGK model, *J. Stat. Phys.* **87**, 115 (1997).
19. O. Behrend, Solid boundaries in particle suspension simulations via lattice Boltzmann method, *Phys. Rev. E* **52**, 1164 (1995).
20. L.-S. Luo, Analytic solutions of linearized lattice Boltzmann equation for simple flows, *J. Stat. Phys.* **88**, 913 (1997).
21. A. J. C. Ladd, Numerical simulation of particular suspensions via a discretized Boltzmann equation. Part 2. Numerical results, *J. Fluid Mech.* **271**, 311 (1994).
22. D. R. Noble, S. Chen, J. G. Georgiadis, and R. O. Buckius, A consistent hydrodynamic boundary condition for the lattice Boltzmann method, *Phys. Fluid* **7**, 203 (1995).
23. S. Chen, D. Martinez, and R. Mei, On boundary conditions in lattice Boltzmann method, *Phys. Fluids* **8**, 2527 (1996).

24. Q. Zou and X. He, On pressure and velocity boundary conditions for the lattice Boltzmann BGK model, *Phys. Fluids* **9**, 1591 (1997).

25. X. He, L.-S. Luo, and M. Dembo, Some progress in lattice Boltzmann method. Part I. Nonuniform mesh grids, *J. Comput. Phys.* **129**, 357 (1996).

26. X. He, L.-S. Luo, and M. Dembo, Some progress in lattice Boltzmann method: High Reynolds mesh grids, *Phys. A* **239**, 276 (1997).

27. X. He and G. Doolen, Lattice Boltzmann method on curvilinear coordinates system: Flow around a circular cylinder, *J. Comput. Phys.* **134**, 306 (1997).

28. R. Mei and W. Shyy, On the finite difference-based lattice Boltzmann method in curvilinear coordinates, *J. Comput. Phys.* **143**, 426 (1998).

29. I. Ginzbourg and D. d'Humières, Local second-order boundary methods for lattice Boltzmann models, *J. Stat. Phys.* **84**, 927 (1996).

30. O. Filippova and D. Hänel, Grid refinement for lattice-BGK models, *J. Comput. Phys.* **147**, 219 (1998).

31. X. He and L.-S. Luo, Lattice Boltzmann model for the incompressible Navier–Stokes equation, *J. Stat. Phys.* **88**, 927 (1997).

32. L.-S. Luo, Unified theory of the lattice Boltzmann models for non-ideal gases, *Phys. Rev. Lett.* 81, 1618 (1998).

33. R. Mei, J. Xiong, and R. Tran-Son-Tay, Motion of a sphere oscillating at low Reynolds numbers in a viscoelastic-fluid-filled cylindrical tube, *J. Non-Newtonian Fluid Mech.* **66**, 169 (1996).

Journal of Computational Physics 161, 680–699 (2000)
doi:10.1006/jcph.2000.6522, available online at http://www.idealibrary.com on IDEAL®

Lattice Boltzmann Method for 3-D Flows with Curved Boundary

Renwei Mei,* Wei Shyy,* Dazhi Yu,* and Li-Shi Luo†

*Department of Aerospace Engineering, Mechanics & Engineering Science, University of Florida, Gainesville, Florida 32611-6250; and †ICASE, MS 132C, NASA Langley Research Center, 3 West Reid Street, Building 1152, Hampton, Virginia 23681-2199
E-mail: rwm@aero.ufl.edu, wei-shyy@ufl.edu, ydz@aero.ufl.edu, luo@icase.edu

Received September 20, 1999; revised March 13, 2000

In this work, we investigate two issues that are important to computational efficiency and reliability in fluid dynamic applications of the lattice Boltzmann equation (LBE): (1) Computational stability and accuracy of different lattice Boltzmann models and (2) the treatment of the boundary conditions on curved solid boundaries and their 3-D implementations. Three athermal 3-D LBE models (Q15D3, Q19D3, and Q27D3) are studied and compared in terms of efficiency, accuracy, and robustness. The boundary treatment recently developed by Filippova and Hänel (1998, *J. Comp. Phys.* **147**, 219) and Mei *et al.* (1999, *J. Comp. Phys.* **155**, 307) in 2-D is extended to and implemented for 3-D. The convergence, stability, and computational efficiency of the 3-D LBE models with the boundary treatment for curved boundaries were tested in simulations of four 3-D flows: (1) Fully developed flows in a square duct, (2) flow in a 3-D lid-driven cavity, (3) fully developed flows in a circular pipe, and (4) a uniform flow over a sphere. We found that while the 15-velocity 3-D (Q15D3) model is more prone to numerical instability and the Q27D3 is more computationally intensive, the Q19D3 model provides a balance between computational reliability and efficiency. Through numerical simulations, we demonstrated that the boundary treatment for 3-D arbitrary curved geometry has second-order accuracy and possesses satisfactory stability characteristics.

Key Words: lattice Boltzmann equation; boundary condition for curved geometries; accuracy; 3-D flows.

I. INTRODUCTION

1.1. *Basic Notion of the Lattice Boltzmann Equation*

In one fashion or another, conventional methods of computational fluid dynamics (CFD) compute pertinent flow fields, such as velocity $\boldsymbol{u}$ and pressure p, by numerically solving the

0021-9991/00 $35.00

Navier–Stokes equations in space $\boldsymbol{x}$ and time t [1–3]. In contrast, various kinetic methods use the transport equation, or the Boltzmann equation in particular, for various problems in fluid dynamics. The Boltzmann equation deals with the single particle distribution function $f(\boldsymbol{x}, \xi, t)$, where ξ is the particle velocity, in phase space $(\boldsymbol{x}, \xi)$ and time t. Recently, the method of the lattice Boltzmann equation (LBE) [4–7] has become an alternative to the conventional CFD methods employing Navier–Stokes equations. The theoretical premises of the LBE method are that (1) hydrodynamics is insensitive to the details of microscopic physics, and (2) hydrodynamics can be preserved so long as the conservation laws and associated symmetries are respected in the microscopic or mesoscopic level. Therefore, the computational advantages of the LBE method are attained by drastically reducing the particle velocity space ξ to only a very few discrete points without seriously degrading hydrodynamics. This is possible because the LBE method rigorously preserves the hydrodynamic moments of the distribution function f, such as mass density and momentum fluxes, and the necessary symmetries [8–10].

One popular kinetic model is the Boltzmann equation with the single relaxation time approximation [11],

$$\frac{\partial f}{\partial t} + \xi \cdot \nabla f = -\frac{1}{\lambda}\left[f - f^{(0)}\right], \tag{1}$$

where ξ is the particle velocity, $f^{(0)}$ is the equilibrium distribution function (the Maxwell–Boltzmann distribution function), and λ is the relaxation time. The mass density ρ and momentum density $\rho \boldsymbol{u}$ are the first $(D+1)$ hydrodynamic moments of the distribution function f and $f^{(0)}$, where D is the dimension of velocity space.

To solve for f numerically, Eq. (1) is first discretized in the velocity space ξ using a finite set of velocities $\{\xi_\alpha\}$ without affecting the conserved hydrodynamic moments [9–11],

$$\frac{\partial f_\alpha}{\partial t} + \xi_\alpha \cdot \nabla f_\alpha = -\frac{1}{\lambda}\left[f_\alpha - f_\alpha^{(\mathrm{eq})}\right]. \tag{2}$$

In the above equation, $f_\alpha(\boldsymbol{x}, t) \equiv f(\boldsymbol{x}, \xi_\alpha, t)$ and $f_\alpha^{(\mathrm{eq})} = f^{(0)}(\boldsymbol{x}, \xi_\alpha, t)$ are the distribution function and the equilibrium distribution function of the αth discrete velocity ξ_α, respectively. The 9-velocity (or 9-bit) LBE model on the 2-D square lattice, denoted as the Q9D2 model, has been widely used for simulating 2-D flows. For 3-D flows, there are several cubic lattice models, such as the 15-bit (Q15D3), 19-bit (Q19D3), and 27-bit (Q27D3) models [12], which have been used in the literature. All three models have a rest particle (with zero velocity) in the discretized velocity set $\{\xi_\alpha\}$. A minor variation of those models is to remove the rest particles from the discrete velocity set; the resulting models are known as the Q14D3, Q18D3, and Q26D3 models, respectively. The LBE models with a rest particle generally have better computational stability. For athermal fluids, the equilibrium distributions for the Q9D2, Q15D3, Q19D3, and Q27D3 models are all of the form [9]

$$f_\alpha^{(\mathrm{eq})} = \rho w_\alpha \left[1 + \frac{3}{c^2}\boldsymbol{e}_\alpha \cdot \boldsymbol{u} + \frac{9}{2c^4}(\boldsymbol{e}_\alpha \cdot \boldsymbol{u})^2 - \frac{3}{2c^2}\boldsymbol{u} \cdot \boldsymbol{u}\right], \tag{3}$$

where w_α is a weighting factor and $\boldsymbol{e}_\alpha$ is a discrete velocity, $c = \delta x / \delta t$ is the lattice speed, and δx and δt are the lattice constant and the time step, respectively. (The values of the weighting factor w_α for the Q15D3, Q19D3, and Q27D3 models and the diagrams illustrating the lattice structures for the Q15D3 and Q19D3 models are given in the Appendix.) It can be shown that

$f_\alpha^{(eq)}$ is in fact a Taylor series expansion of the Maxwellian $f^{(0)}$ [8, 9]. This approximation of $f^{(0)}$ by the above $f_\alpha^{(eq)}$ makes the method valid only in the incompressible limit $u/c \to 0$.

With the velocity space discretized, the hydrodynamic moments of f and $f^{(0)}$ are evaluated by the following quadrature formulas:

$$\rho = \sum_\alpha f_\alpha = \sum_\alpha f_\alpha^{(eq)}, \tag{4a}$$

$$\rho \boldsymbol{u} = \sum_\alpha \boldsymbol{e}_\alpha f_\alpha = \sum_\alpha \boldsymbol{e}_\alpha f_\alpha^{(eq)}. \tag{4b}$$

The speed of sound of the above 3-D LBE models is $c_s = c/\sqrt{3}$ and the equation of state is that of an ideal gas $p = \rho c_s^2$. The viscosity of the fluid is $\nu = \lambda c_s^2$.

Equation (2) is often discretized in space, $\boldsymbol{x}$, and time, t, into

$$f_\alpha(\boldsymbol{x}_i + \boldsymbol{e}_\alpha \delta t, t + \delta t) - f_\alpha(\boldsymbol{x}_i, t) = -\frac{1}{\tau}\left[f_\alpha(\boldsymbol{x}_i, t) - f_\alpha^{(eq)}(\boldsymbol{x}_i, t)\right], \tag{5}$$

where $\tau = \lambda/\delta t$. This is the lattice Boltzmann equation with the Bhatnagar–Gross–Krook (BGK) approximation [11] and is often referred to as the LBGK model [4, 5]. The viscosity in the NS equation derived from Eq. (5) is

$$\nu = (\tau - 1/2)c_s^2 \delta t. \tag{6}$$

This choice for the viscosity makes the LBGK scheme formally a second order method for solving incompressible flows [9]. The positivity of the viscosity requires that $\tau > 1/2$. Equation (6) can be solved in the following two steps:

$$\text{collision step:} \quad \tilde{f}_\alpha(\boldsymbol{x}_i, t) = f_\alpha(\boldsymbol{x}_i, t) - \frac{1}{\tau}\left[f_\alpha(\boldsymbol{x}_i, t) - f_\alpha^{(eq)}(\boldsymbol{x}_i, t)\right], \tag{7a}$$

$$\text{streaming step:} \quad f_\alpha(\boldsymbol{x}_i + \boldsymbol{e}_\alpha \delta t, t + \delta t) = \tilde{f}_\alpha(\boldsymbol{x}_i, t), \tag{7b}$$

where $\tilde{f}_\alpha$ denotes the post-collision state of the distribution function. It is noted that the collision step is completely local, and the streaming step is uniform and requires little computational effort. Equation (7) is explicit, easy to implement, and straightforward to parallelize.

1.2. *Boundary Condition on a Solid Surface*

To date, most Neumann-type boundary conditions for a solid boundary used in the LBE method are based upon the bounce-back boundary condition: A particle colliding with a stationary wall simply reverses its momentum. Much of the previous work on LBE boundary conditions is devoted to the analysis and improvement of the bounce-back boundary condition [13–21, 27]. The bounce-back boundary condition can attain second-order accuracy if the boundary is fictictiously placed halfway between two nodes. That is, the second-order accuracy of the bounce-back boundary condition can only be achieved when the boundaries are located right in the middle of two neighboring lattices [$\Delta = 0.5$; see Eq. (8)]. (Readers are referred to our recent work [22] for a summary of the previous work.) This prevents the direct application of the bounce-back–type boundary conditions to simulate a solid

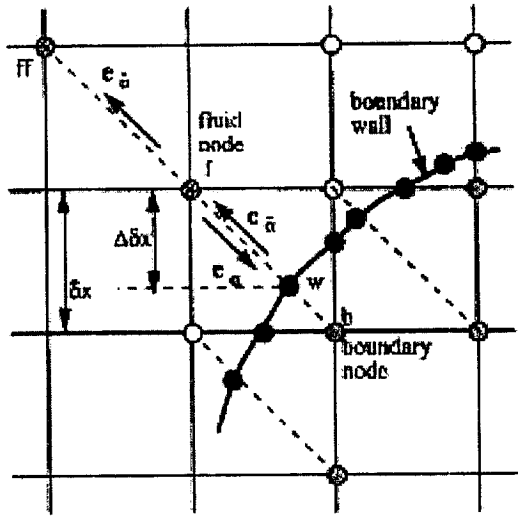

FIG. 1. 2-D projection of the layout of the regularly spaced lattices and curved wall boundary.

body with smooth curvature. To circumvent this difficulty, Mei and Shyy solved Eq. (2) in curvilinear coordinates using a finite difference method to solve for $\tilde{f}_\alpha$ [28]. One can also use body-fitted curvilinear coordinates with interpolation throughout the entire mesh, except at the boundaries where the bounce-back boundary condition is used [29]. In more recent works [22, 23], Cartesian coordinates are adopted with interpolation used only at the boundaries. These techniques rely on the freedom of using interpolation techniques. We used the latter technique in the present work.

As shown in Fig. 1 for a 2-D projection involving a 3-D body, the streaming step requires the knowledge of $\tilde{f}_{\bar{\alpha}}(\boldsymbol{x}_b, t)$, in which $\boldsymbol{e}_{\bar{\alpha}} = -\boldsymbol{e}_\alpha$, at $\boldsymbol{x}_b$ on the solid side in order to obtain $f_{\bar{\alpha}}(\boldsymbol{x}_f, \delta t)$ for the lattice node located on the fluid side at $\boldsymbol{x}_f = \boldsymbol{x}_b + \boldsymbol{e}_{\bar{\alpha}}\delta t$. Defining

$$\Delta = \frac{|\boldsymbol{x}_f - \boldsymbol{x}_w|}{|\boldsymbol{x}_f - \boldsymbol{x}_b|} \tag{8}$$

as the fraction of an intersected link in the fluid region, it is seen that $0 \leq \Delta \leq 1$ and the horizontal or vertical distance between $\boldsymbol{x}_b$ and $\boldsymbol{x}_w$ is $(1 - \Delta)\delta x$ on the cubic lattice.

Based on the work of Filippova and Hänel [23], hereinafter referred to as FH, Mei *et al.* [22] proposed the following treatment for $\tilde{f}_{\bar{\alpha}}(\boldsymbol{x}_b, t)$ on curved boundaries:

$$\tilde{f}_{\bar{\alpha}}(\boldsymbol{x}_b, t) = (1 - \chi)\tilde{f}_\alpha(\boldsymbol{x}_f, t) + \chi f_\alpha^{(*)}(\boldsymbol{x}_b, t) + 2w_\alpha \rho \frac{3}{c^2}\boldsymbol{e}_{\bar{\alpha}} \cdot \boldsymbol{u}_w \tag{9}$$

with

$$f_\alpha^{(*)}(\boldsymbol{x}_b, t) = w_\alpha \rho(\boldsymbol{x}_f, t)\left[1 + \frac{3}{c^2}\boldsymbol{e}_\alpha \cdot \boldsymbol{u}_{bf} + \frac{9}{2c^4}(\boldsymbol{e}_\alpha \cdot \boldsymbol{u}_f)^2 - \frac{3}{2c^2}\boldsymbol{u}_f \cdot \boldsymbol{u}_f\right] \tag{10}$$

and

$$\boldsymbol{u}_{bf} = (\Delta - 1)\boldsymbol{u}_f/\Delta + \boldsymbol{u}_w/\Delta \quad \text{and} \quad \chi = (2\Delta - 1)/\tau \qquad \text{for } \Delta \geq 1/2 \tag{11}$$

$$\boldsymbol{u}_{bf} = \boldsymbol{u}_{ff} = \boldsymbol{u}_f(\boldsymbol{x}_f + \boldsymbol{e}_{\bar{\alpha}}\delta t, t) \quad \text{and} \quad \chi = (2\Delta - 1)/(\tau - 2) \qquad \text{for } \Delta < 1/2. \tag{12}$$

It is noted that Eq. (12) for $\boldsymbol{u}_{bf}$ and χ differs from that originally proposed by FH. The choice for $\boldsymbol{u}_{bf}$ given by Eq. (12) improves the computational stability for $\tau < 1$ and $\Delta < 1/2$ [22]. Since Eqs. (9)–(12) are in vector form, they can be directly extended to 3-D flows with curved boundaries.

1.3. *Scope of the Present Work*

The present study examines two issues in 3-D incompressible fluid dynamics simulations with arbitrary boundaries using the LBE method: (i) The performance of various 3-D athermal LBE models for viscous flows, and (ii) the efficacy and reliability of the extension of the curved boundary treatment from 2-D to 3-D flows. We focus on the stability and accuracy of the computation and the robustness in handling an arbitrary curved geometry. In Section II, a modification of the choice of $\boldsymbol{u}_{bf}$ and the expression for χ when $\Delta \geq 1/2$ is proposed in order to further improve the computational stability of the boundary treatment. In Section III, numerical results for four 3-D steady flows are examined and various computational issues are addressed. These four cases are: (i) pressure driven fully developed flow in a square duct; (ii) 3-D lid-driven cavity flow; (iii) pressure driven fully developed flow in a circular pipe; and (iv) uniform flow over a sphere. In cases (i) and (iii), the LBE-based numerical solutions can be compared with known exact solutions so that the accuracy of the LBE solutions can be determined. The difference in these two cases is that Δ is a constant in the square duct while Δ varies around the solid boundary in the circular pipe. In the lid-driven cavity flow, the singularities at corners between the moving and stationary walls allows for a performance assessment of various LBE schemes. The flow past a sphere is an external flow around a 3-D blunt body. In all four cases, detailed assessments are made in terms of error norms and velocity profiles. It will be demonstrated that accurate and robust solutions are obtained using the newly proposed boundary conditions along with the selected LBE models.

II. MODIFICATION OF THE BOUNDARY CONDITION FOR $\Delta > 1/2$

Equations (9)–(12) are first applied to a fully developed pressure driven 2-D channel flow by using the 3-D LBE model Q19D3. At the inlet ($i = 1$) and exit ($i = N_x$, in which N_x is the number of lattices in the x-direction) the following zero derivative condition is imposed after the collision step:

$$\tilde{f}_\alpha(i = 1, j, k) = \tilde{f}_\alpha(i = 2, j, k), \tag{13}$$

$$\tilde{f}_\alpha(i = N_x, j, k) = \tilde{f}_\alpha(i = N_x - 1, j, k). \tag{14}$$

At $k = 1$ and $k = N_z$, the same is imposed:

$$\tilde{f}_\alpha(i, j, k = 1) = \tilde{f}_\alpha(i, j, k = 2), \tag{15}$$

$$\tilde{f}_\alpha(i, j, k = N_z) = \tilde{f}_\alpha(i, j, k = N_z - 1). \tag{16}$$

The constant pressure gradient ∇p along the x-direction is treated as a body force and is included in the solution procedure after the collision step and the enforcement of the above

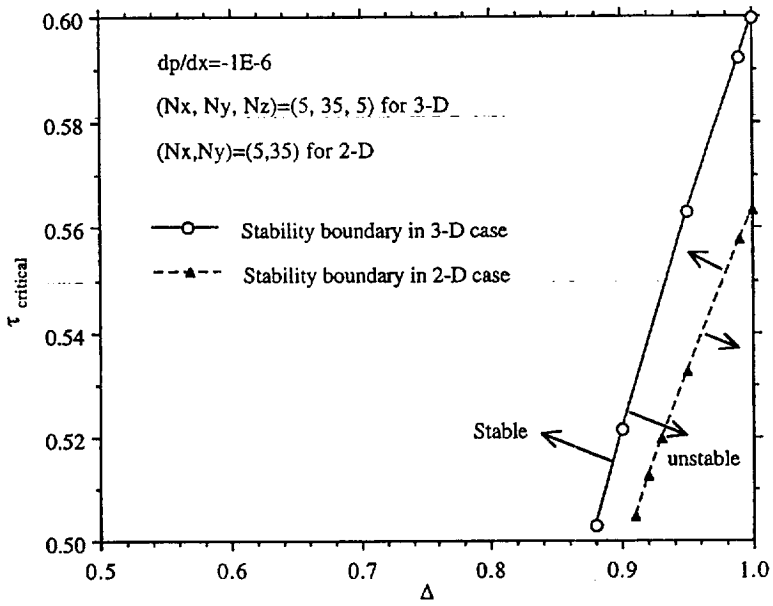

FIG. 2. Stability boundary of FHs scheme in a square duct flow for Δ near 1.

zero-derivative conditions as

$$\tilde{f}_\alpha(x_i, t) = \tilde{f}_\alpha(x_i, t) - w_\alpha \frac{3}{c^2}\frac{dp}{dx} e_\alpha \cdot \hat{x}, \tag{17}$$

where $\hat{x}$ is the unit vector along the x-axis. On the solid walls ($y = 0$ and $y = H$), Eqs. (9)–(12) are used. The exact solution for the velocity is used as the velocity initial condition. The equilibrium distribution function $f_\alpha^{(\mathrm{eq})}$ based on the exact solution for the velocity profile is used as the initial condition for f_α. The pressure gradient is set to $\frac{dp}{dx} = -1.0 \times 10^{-6}$. All computations are carried out using double precision.

It was found that the computations are stable for τ close to 0.5 (for example, $\tau = 0.505$) as long as Δ is not too close to unity (for example, $\Delta \leq 0.87$). When Δ is equal to 1, stable computation can only be carried out for τ no smaller than 0.6. Figure 2 shows the stability-instability boundary for the channel flow simulation with a system size $N_x \times N_y \times N_z = 5 \times 35 \times 5$, near $\Delta = 1$. Also shown by the dashed line is the stability–instability boundary for the channel flow simulation using the Q9D2 model and with a system size $N_x \times N_y = 5 \times 35$, near $\Delta = 1$. It is clear that similar behavior exists in both 2-D and 3-D channel flow simulations. When the computation for the pressure driven flow in a square duct was carried out using the Q19D3 formulation, a similar stability-instability boundary was encountered.

Ideally, one would like to use a fixed value of τ for the entire range of $0 \leq \Delta \leq 1$ in a simulation. Computational stability would then require the use of τ around 0.6, instead of a value that is close to 0.5, which makes it difficult to simulate a lower viscosity or higher Reynolds number flow. To overcome the restriction imposed by the numerical stability requirement due to interpolation, it would be useful if one could decrease the value of $\chi = (2\Delta - 1)/\tau$ given by Eq. (11). This can be accomplished by using

$$\boldsymbol{u}_{bf} = [1 - 3/(2\Delta)]\boldsymbol{u}_f + 3/(2\Delta)\boldsymbol{u}_w \quad \text{and} \quad \chi = (2\Delta - 1)/(\tau + 1/2) \qquad \text{for } \Delta \geq 1/2. \tag{18}$$

That is, the velocity $\boldsymbol{u}_{bf}$ is evaluated at $(\boldsymbol{x}_b + 1/2\,\boldsymbol{e}_\alpha)$, instead of at $\boldsymbol{x}_b$, using the information at $\boldsymbol{x}_f$ and $\boldsymbol{x}_w$ through linear extrapolation.

With Eq. (18) replacing Eq. (11), the channel flow simulations using the Q19D3 lattice model are carried out again for Δ from 0.85 to 1. Satisfactory results for the velocity profiles are obtained for $\tau = 0.505$ with $N_x \times N_y \times N_z = 5 \times 35 \times 5$ in terms of computational stability. For $\Delta < 0.85$, the accuracy of the solutions using Eqs. (11) and (18) is the same when the computations are stable.

III. RESULTS AND DISCUSSIONS

3.1. *Fully Developed Flow in a Square Duct*

For fully developed flow inside a square duct of height H defined by the region $-a \le y \le a$ and $-a \le z \le a$, where $a = H/2$, the axial velocity profile can be found in Ref. [24, p. 123]:

$$u_x(y, z) = -\frac{16a^2}{\mu\pi^3}\frac{dp}{dx}\sum_{n=1,3,5,\ldots}^{\infty}\left[1 - \frac{\cosh(n\pi z/2a)}{\cosh(n\pi/2)}\right]\frac{\cos(n\pi y/2a)}{n^3}. \tag{19}$$

Figure 3 compares the exact axial velocity profiles at $z = 0$ and the LBE-based solution with $\Delta = 0.2$ and $H = 2a = 32.4$. A total of $N_x \times N_y \times N_z = 13 \times 35 \times 35$ grid points are used. The pressure gradient is $\frac{dp}{dx} = -1.0 \times 10^{-6}$ and $\tau = 0.52$. The 19-bit model is used in the simulations. Excellent agreement was obtained.

Figure 4a shows the dependence of relative L_2-norm error,

$$E_2 = \frac{\left\{\int_0^H \int_0^H [u_{\mathrm{LBE}}(y, z) - u_{\mathrm{exact}}(y, z)]^2\, dy\, dz\right\}^{1/2}}{\left[\int_0^H \int_0^H u_{\mathrm{exact}}^2(y, z)\, dy\, dz\right]^{1/2}}, \tag{20}$$

on the duct height or the lattice resolution $H = N_y - 3 + 2\Delta$. The integral is evaluated by

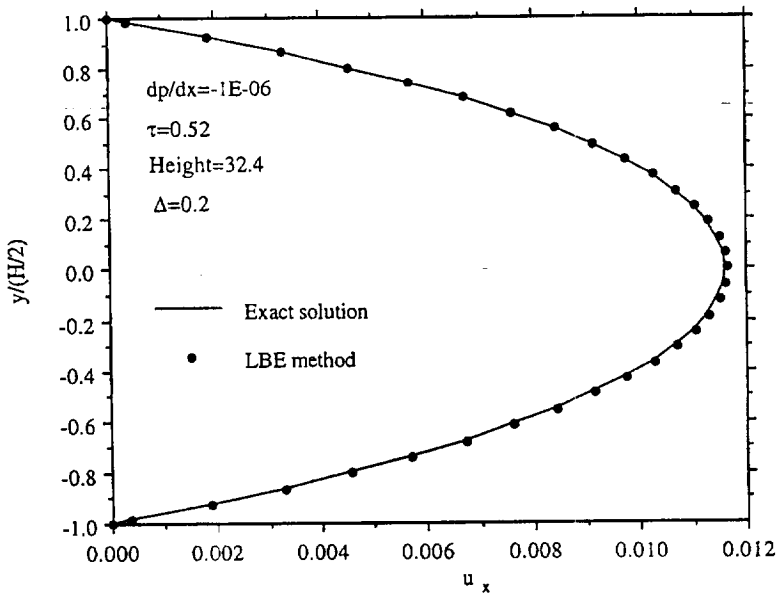

FIG. 3. Comparison of axial velocity profiles in a pressure driven square duct flow at $z = 0$ between the exact solution and the LBE-based solution with $\Delta = 0.2$.

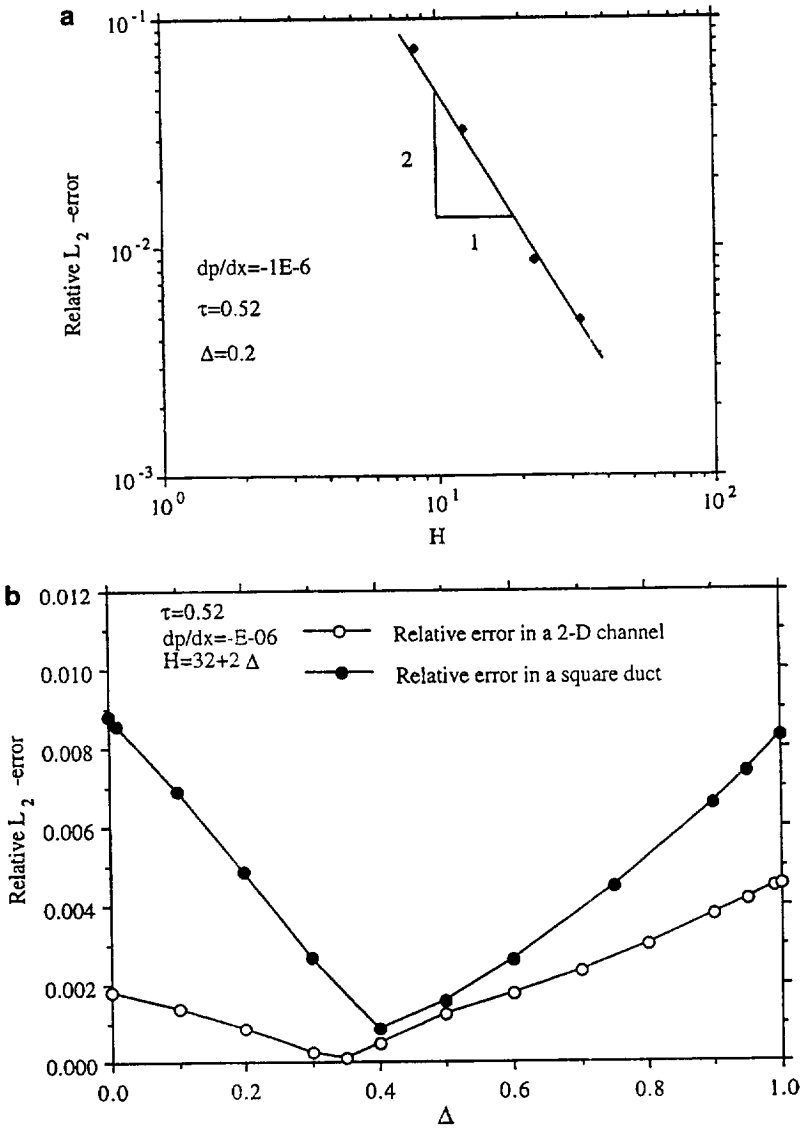

FIG. 4. (a) Dependence of relative L_2-norm error on the lattice resolution $H = N_y - 3 + 2\Delta$ in steady state pressure-driven duct flow simulations. (b) Relative L_2-norm error as a function of Δ in steady-state pressure-driven duct and channel flow simulations.

the trapezoidal rule. As was demonstrated by Mei *et al.* [22], the boundary treatment results in second order convergence for 2-D channel flow. Figure 4a clearly shows that the total error (from both the flow field and the boundary condition) of the LBE solution in 3-D flow decays quadratically.

Figure 4b shows the relative L_2-norm error E_2 as a function of Δ in the duct flow using $13 \times 35 \times 35$ grid points and $\tau = 0.52$. For the purpose of comparison, the relative L_2-norm error in the 2-D channel flow simulation using the Q9D2 model with $N_y = 35$ and $\tau = 0.52$ is also shown. The relative error is larger in 3-D duct flow than in the 2-D channel flow. Nevertheless, the error exhibits the same qualitative behavior in both 2-D and 3-D as a function of Δ.

It should be noted that the accuracy of the Q9D2 model and the Q19D3 model is different in the sense that beyond the conserved moments (density and momentum in athermal fluids), these two models have different accuracy in preserving higher order moments (fluxes) [9, 10]. The Q9D2 model preserves all the moments up to second order in momentum space, which include momentum fluxes, and maintains the isotropy of these moments, whereas the Q19D3 model can preserve density and momentum, but cannot maintain the same accuracy and isotropy of the fluxes like the Q9D2 model does. The only 3-D equivalent of the Q9D2 model in terms of accuracy of the moments is the Q27D3 model [9, 10].

3.2. *Simulation Results for 3-D Lid-Driven Cavity Flows*

Lid-driven cavity flow has been studied extensively in the CFD community. Most research has been focused on 2-D problems. Limited numbers of reliable numerical results for steady state 3-D cavity flows have been obtained in the past several years. In this study, the multiblock finite difference solution of the NS equations obtained recently by Salom [25] is used to compare with the present LBE-based results.

The size of the cavity is H^3, the number of grids is $N_x \times N_y \times N_z$, and $N_x = N_y = N_z$. The driving lid is placed at $y = H$, moving along the direction of x-axis with a speed $U = 0.1$ in lattice units. Figure 5a compares profiles of horizontal velocity $u_x(y)$ obtained using $33 \times 33 \times 33$ lattices with the solution to the NS equations at $x/H = z/H = 0.5$ for $Re = 400$. All three LBE models (15-, 19-, and 27-bit) are used. For the 15-bit model, the computation becomes unstable and blows up at this Reynolds number with 33^3 lattice resolution and $\Delta = 0.5$. For $\Delta = 0.5$, the 19- and the 27-bit models give very similar $u_x(y)$ profiles and both underpredict slightly the magnitude of the minimum in the profiles. The 19-bit model is also used with $\Delta = 0.25$; there is a slight overshoot in the velocity profiles in comparison to the results in Ref. [25]. Figure 5b compares $u_x(y)$ profiles obtained using the 15- and 19-bit lattice models on the 67^3 lattice grids and $\Delta = 0.5$ with the NS solution [25] at $x/H = z/H = 0.5$ for $Re = 400$. Excellent agreement is observed. Clearly, the 19-bit model is superior to the 15-bit model. Although the 15-bit model requires 21% less CPU time and storage than the 19-bit model per lattice, it is not as robust as the 19-bit model and may actually require more CPU time and memory to obtain a reasonable solution since more lattice points are clearly needed.

It should be noted that the stability property of the 19- and the 15-bit models is significantly different. All LBE models have inherent spurious invariants because of their simple dynamics [30]. However, the stability of the LBE models, which is very much affected by these spurious invariants, differs from one model to another and also depends on other factors such as boundary conditions and the local Reynolds number [30]. Among the three 3-D LBE models (Q15D3, Q19D3, and D27D3), the Q15D3 model is the least isotropic and therefore is more prone to numerical instability. This is independently verified in a recent work by Kandhai *et al.* [26]. It was observed that the Q15D3 model may induce artificial checkerboard invariants which are the eigenmodes of the linearized LBGK collision operator at wave vector $k = \pi$; this can cause spatial oscillations to develop in the flow field at high Reynolds number [30]. Although it was pointed out that the presence of solid walls can suppress the oscillation in certain cases, the solid walls in the present case actually excite the oscillation by producing shear stress singularities at the corners between the moving and the stationary walls. Clearly, the Q19D3 model is better suited to handle flow singularities than the Q15D3 model in this case.

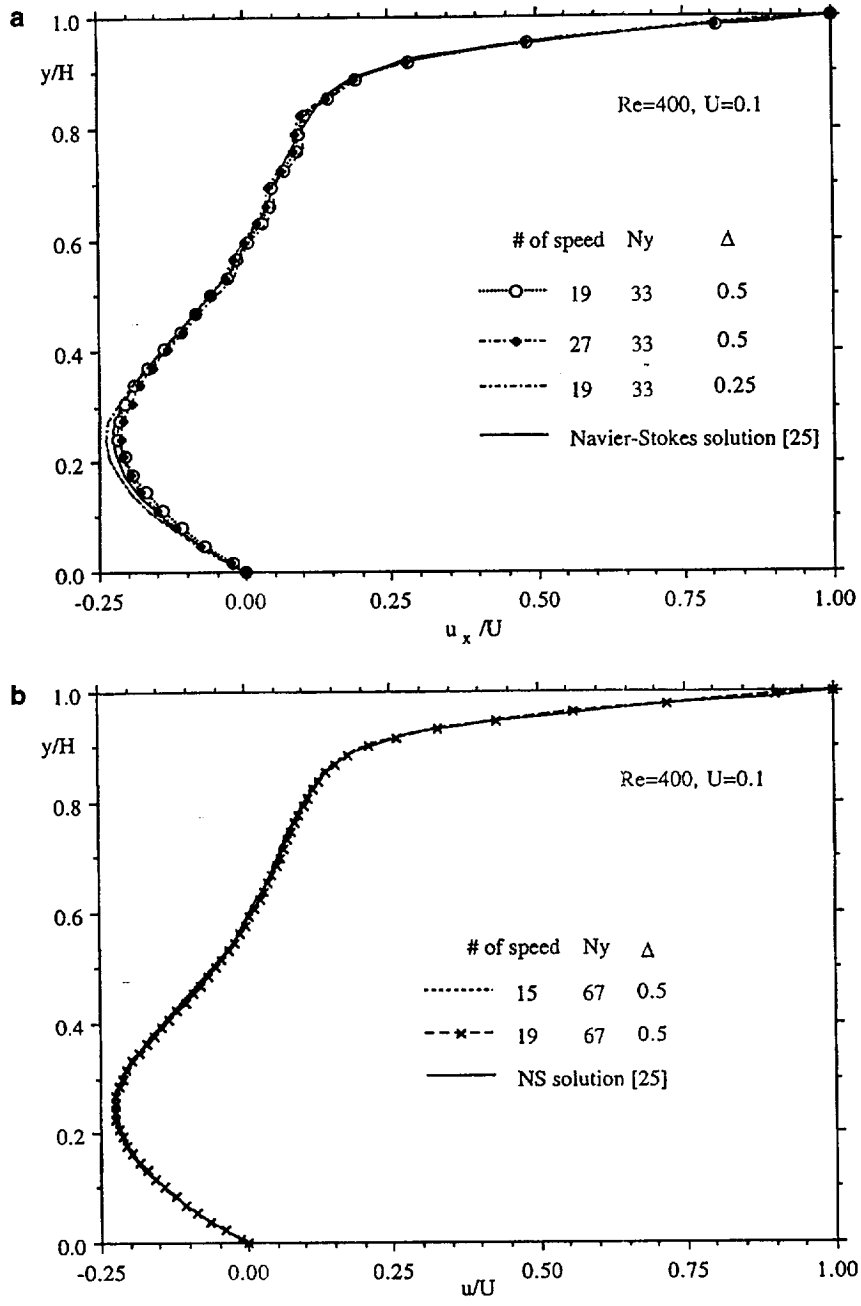

FIG. 5. Comparison of u_x profiles using (a) $33 \times 33 \times 33$ and (b) $67 \times 67 \times 67$ lattices with a Navier–Stokes (NS) solution at $x/H = z/H = 0.5$ for $Re = 400$ in a lid-driven cavity flow.

Figure 6a compares the profiles of transversal velocity $u_y(x)$ obtained from various 3-D LBE models using 33^3 lattices (grids) with the NS solution at $y/H = z/H = 0.5$ for $Re = 400$. For $\Delta = 0.5$, we found that the results from the 27-bit model deviate more from the NS results of Ref. [25] than the results of the 19-bit model with the same resolution in the spatial region $0.1 < x/H < 0.6$. Both models underpredict the extrema of the velocity profile compared to the NS solution of Ref. [25]. For $\Delta = 0.25$, the results of the 19-bit

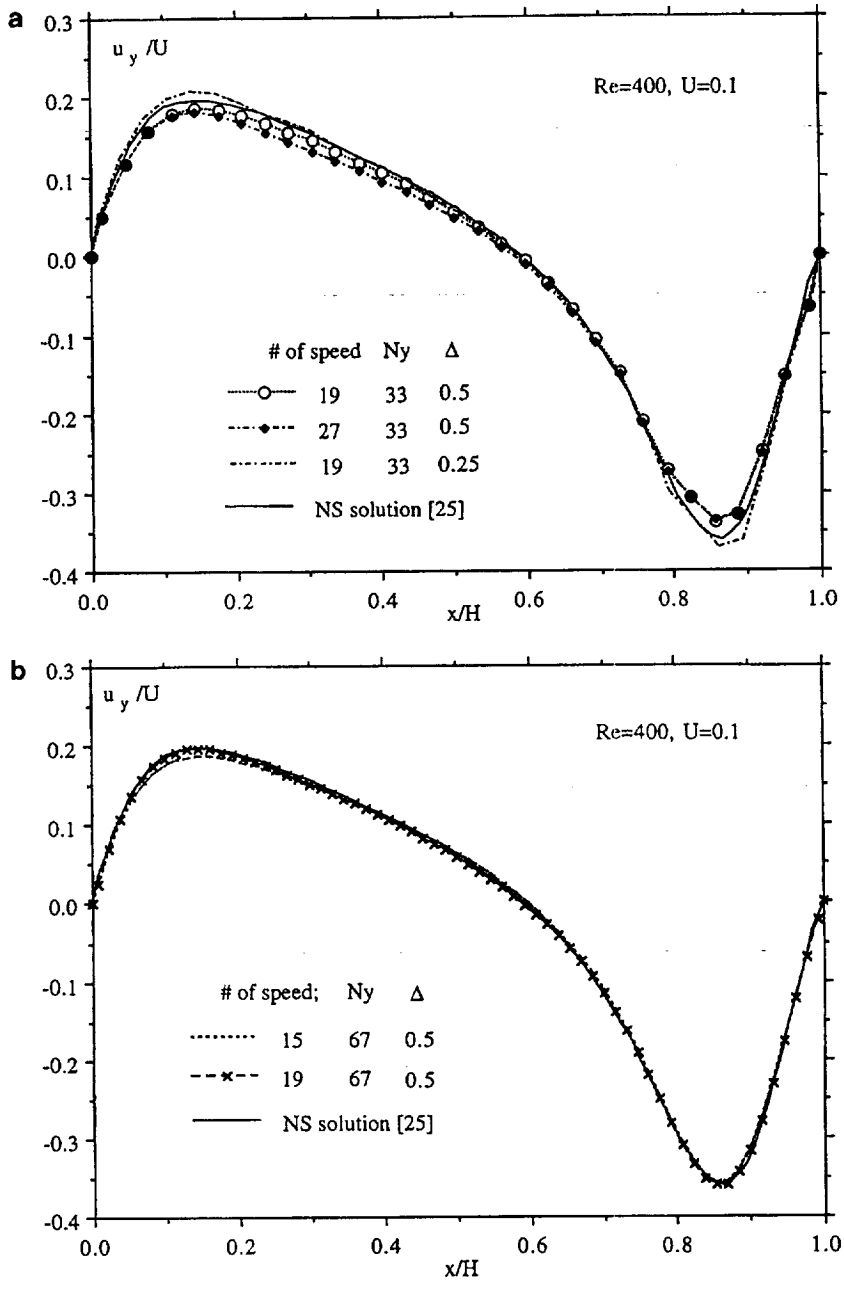

FIG. 6. Comparison of u_y profiles using (a) $33 \times 33 \times 33$ and (b) $67 \times 67 \times 67$ lattices with an NS solution at $y/H = z/H = 0.5$ for $Re = 400$ in a lid-driven cavity flow.

model slightly overpredict the extrema, also shown in Fig. 6a. However, the difference is relatively smaller in both cases. Figure 6b shows velocity profiles with a resolution of 67^3 grid points and the same Reynolds number $Re = 400$. With 67^3 lattice resolution, the result of the 15-bit model significantly differs from the results of the 19-bit model and that of the NS solution in Ref. [25]. These comparisons further suggest that the 19-bit model is better than the 15-bit model in terms of accuracy and stability and better than the 27-bit in terms

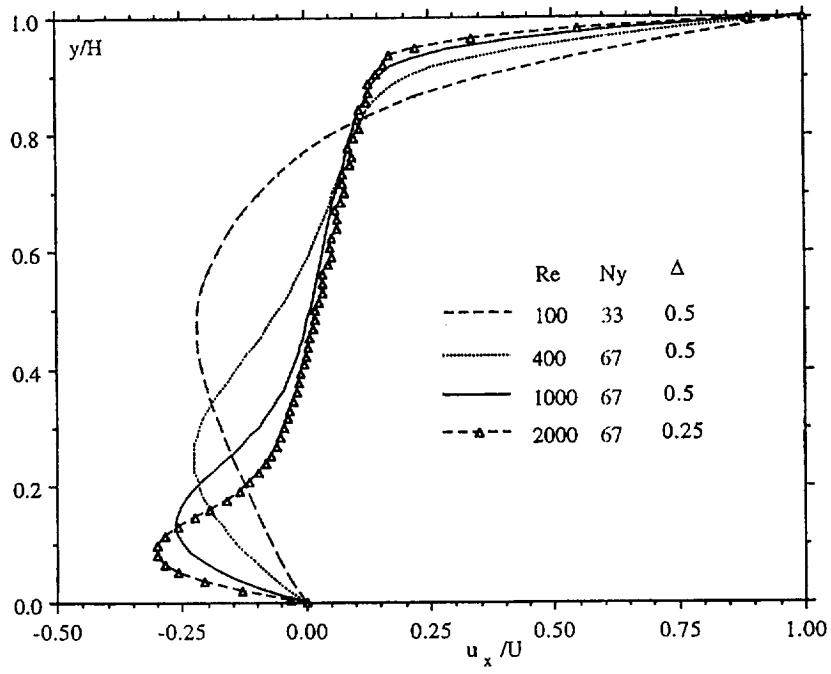

FIG. 7. Effect of Reynolds number on the centerline ($x/H = z/H = 1/2$) velocity profiles, u_x/U, based on the 19-bit LBE solutions in a lid-driven cavity flow.

of computational efficiency. The 19-bit model represents a good compromise in terms of both computational efficiency and reliability.

Figures 7 and 8 show the effect of Reynolds number (from 100 to 2000) on the profiles of horizontal velocity $u_x(y)$ at $x/H = z/H = 0.5$ and transversal velocity $u_y(x)$ at $y/H = z/H = 0.5$ based on the Q19D3 model. For $Re = 100$, 400, and 1000, $\Delta = 0.5$ is used. It is worth noting that for $Re = 2000$, the system size of 67^3, $U = 0.1$, and $\tau = 0.50325$, the LBE simulation with $\Delta = 0.5$ eventually becomes unstable, although the steady-state result of $Re = 1000$ is used as the initial condition for $Re = 2000$. When $\Delta = 0.25$ is used on the 67^3 lattice system, no computational instability occurs and the steady-state solution is obtained. Weak spatial oscillations in the $u_x(y)$ and $u_y(x)$ velocity profiles were observed for $Re = 2000$, which indicates that further increase in Re would require better spatial resolution. It is also worth pointing out that when FH's boundary condition [23] is used for $Re = 2000$ with $\Delta = 0.25$, the solution eventually blows up even when converged results (based on the present boundary condition for $\Delta = 0.25$) at $Re = 2000$ are used as the initial condition.

3.3. *Fully Developed Flows inside a Circular Pipe*

Figure 9 shows the 2-D projection of the discretized domain and the boundary nodes x_b (denoted by solid symbols) on the yz plane for flow inside a circular pipe of radius $R = 9.5$ lattice units. Geometrically, the LBE simulation of the pipe flow differs from that of the duct flow in that the fraction of the intersected link Δ is not constant over the entire boundary. As seen in Fig. 4b, computational error can vary with Δ in the duct flow and the difference in the error can easily be as large as a factor of four for $0 \leq \Delta \leq 1$. Furthermore, the error is the smallest when Δ is between 0.3 to 0.6. Hence, it is reasonable to expect that the overall error in the solution will depend on the distribution of Δ in the entire set of Δ.

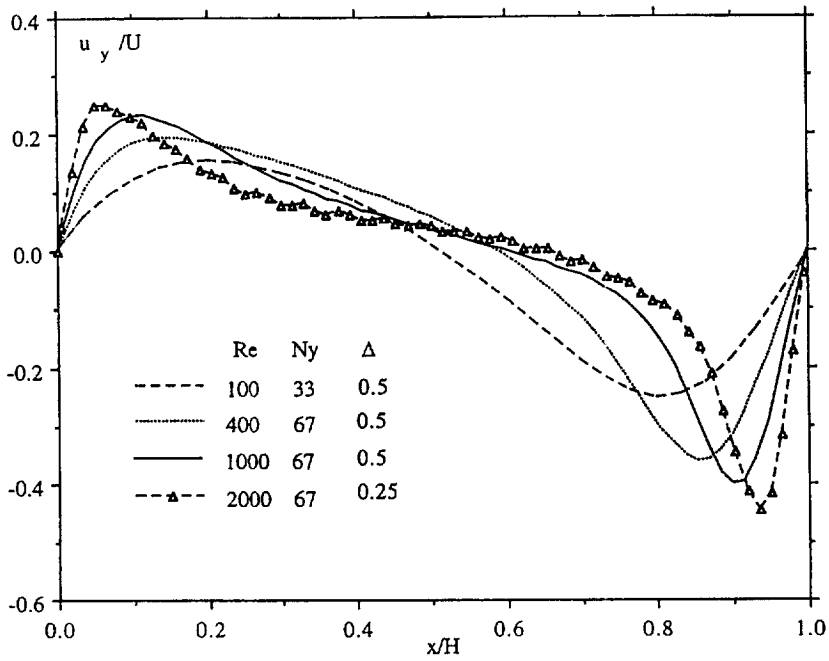

FIG. 8. Effect of Reynolds number on the y-component velocity profiles at $y/H = z/H = 1/2$ based on the 19-bit LBE solutions in a lid-driven cavity flow.

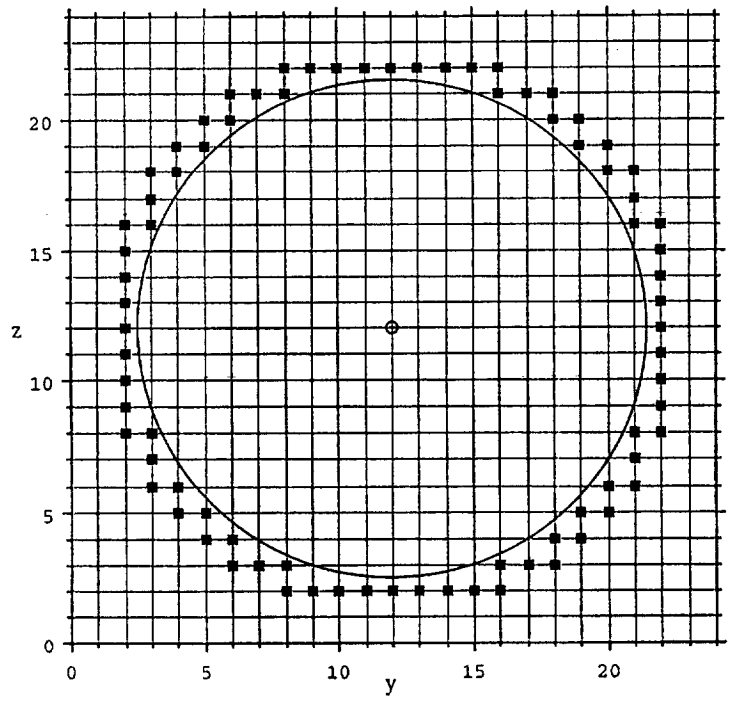

FIG. 9. Boundary nodes $\mathbf{x}_b$ (solid symbols) for flow in a pipe of radius 9.5 lattice units.

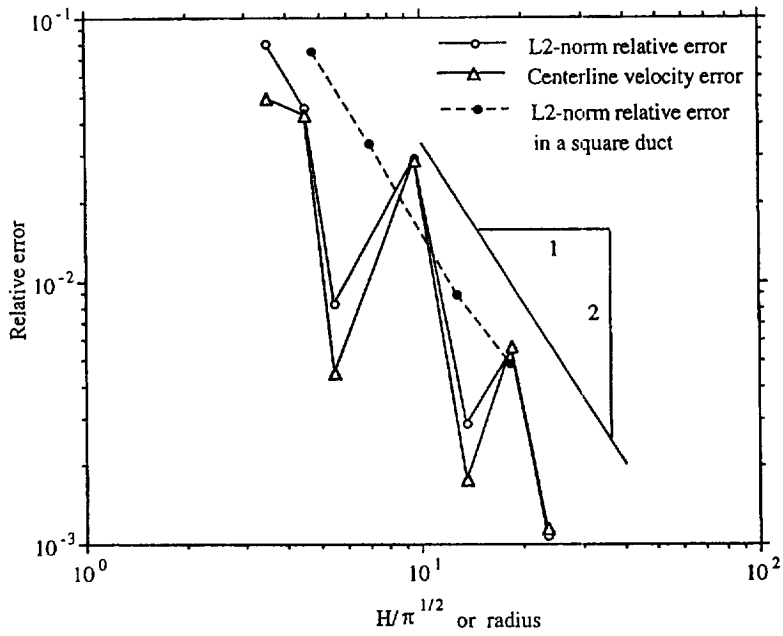

FIG. 10. Variation of relative errors in the velocity profiles as a function of pipe radius.

Figure 10 shows the relative L_2-norm error for the axial velocity profile defined as

$$E_2 = \frac{\left\{\sum_{(y_j,z_k)\in\Omega}[u_{\mathrm{LBE}}(y_j, z_k) - u_{\mathrm{exact}}(y_j, z_k)]^2\right\}^{1/2}}{\left[\sum_{(y_j,z_k)\in\Omega} u^2_{\mathrm{exact}}(y_j, z_k)\right]^{1/2}}, \tag{21}$$

where Ω is the set of the discrete lattice grids inside the pipe, as a function of radius R for $R = 3.5, 4.5, 5.5, 9.5, 13.5, 18.5$, and 23.5. The pressure gradient is $\frac{dp}{dx} = -1.0 \times 10^{-6}$ and $\tau = 0.52$. It is noted that each simple summation in Eq. (21) is slightly less than the exact integration over the entire circle due to the discretization. To ensure that such a treatment does not affect the qualitative behavior of the error measurement, the centerline axial velocity, u_c, is also compared with the exact solution and the error is defined as:

$$E_c = \frac{|u_{c,\mathrm{LBE}} - u_{c,\mathrm{exact}}|}{|u_{c,\mathrm{exact}}|}. \tag{22}$$

It is seen that E_c behaves very similarly to E_2 and both are nonmonotonic. This oscillatory behavior could be due to the difference in the distribution of Δ, which in turn results in the difference of the dissipation due to the interpolation around the boundary. Shown also in Fig. 10 is the error E_2 of the square duct flow solution (with $\Delta = 0.2$) as a function of equivalent radius $H/\pi^{1/2}$, which exhibits a quadratic convergence. Despite the nonmonotonic behavior, it can still be seen that on average, E_2 and E_c decay quadratically with increasing radius and the accuracy in the pipe flow simulation is comparable to that in the square duct flow simulation.

Figure 11 shows the axial velocity profiles in the pipe for $R = 3.5, 5.5, 9.5$, and 13.5 in comparison with the exact solution. Even for a very small radius $R = 3.5$, the LBE solution agrees with the exact solution remarkably well. A noticeable discrepancy in the velocity profile at $R = 9.5$ is also observed in E_2 and E_c shown in Fig. 10.

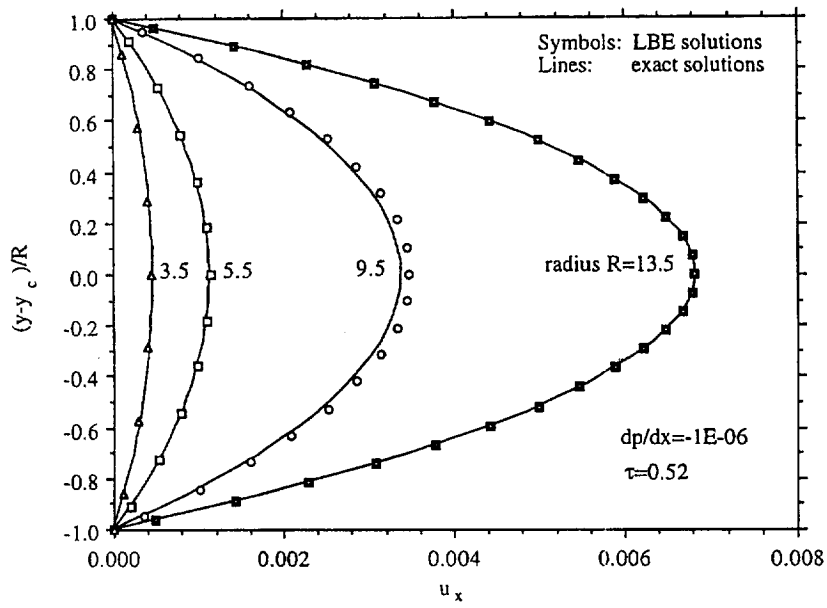

FIG. 11. Comparison of the axial velocity profiles between the LBE-based and the exact solutions for flow inside a cicular pipe.

3.4. *Simulation Results for a Uniform Flow over a Sphere*

The conventional LBE scheme uses uniform meshes. Without local mesh refinement, it is difficult to compute the external flow over a blunt body efficiently since a large number of grid points in the far field will be wasted. As a first attempt, the flow over a sphere is computed within a finite region in the transversal directions.

As shown in Fig. 12, the outer boundary is placed at $y = \pm H/2$ and $z = \pm H/2$. At $y = -H/2$, the lattice is $j = 2$. The boundary conditions at $j = 1$ for f_α's are given by the following linear extrapolation:

$$f_\alpha(i, 1, k) = 2f_\alpha(i, 2, k) - f_\alpha(i, 3, k). \tag{23}$$

The velocity at $j = 2$ is set as

$$u(i, 2, k) = u(i, 3, k). \tag{24}$$

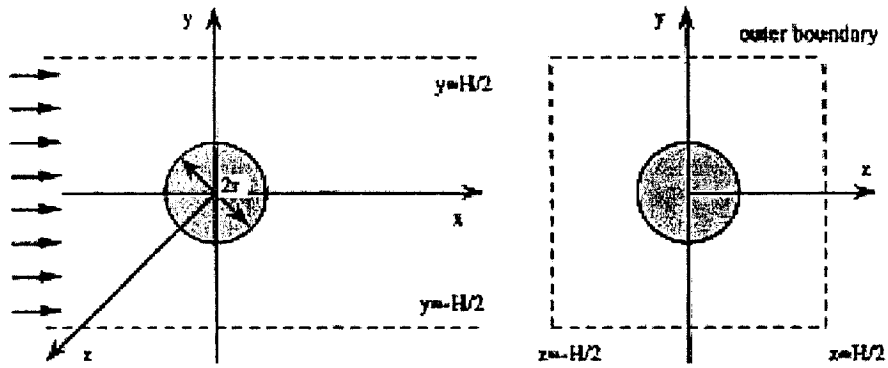

FIG. 12. Schematic for uniform flow over a sphere.

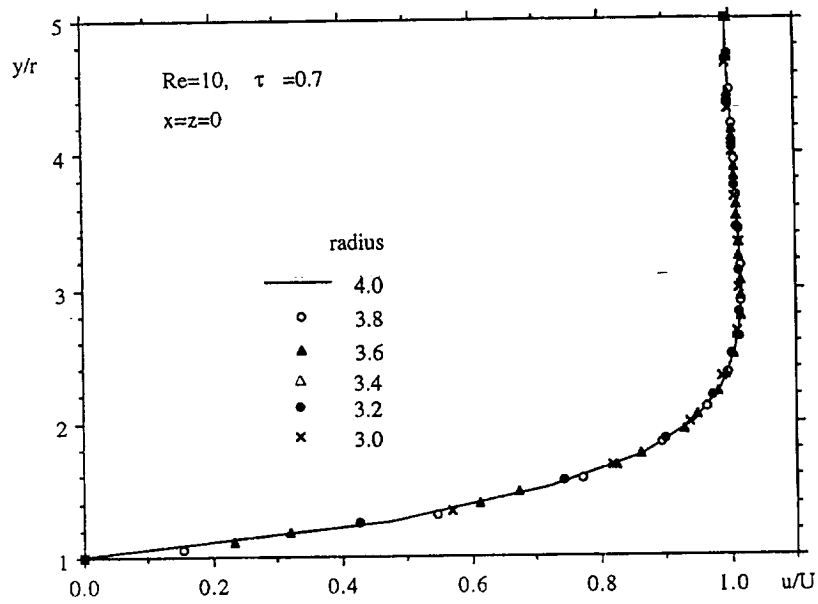

FIG. 13. Comparison of the velocity profiles at $x = 0$ for $r = 3.0, 3.2, 3.4, 3.6, 3.8$, and 4.0 for $Re = 10$ and $H/r = 5$.

Similar treatment is applied at $y = H/2$ and $z = \pm H/2$. The extrapolation condition given by Eqs. (23) and (24) allow the flow to leave the outer boundary. This helps to reduce the effect of the outer boundary on the flow field and on the drag force. At the inlet, a uniform velocity profile is imposed at $i = 1.5$ (halfway between the first and second lattice points) and Eq. (9) is applied to obtain the condition for $f_\alpha(1, j, k)$ with $\chi = 0$. At the exit, a simple extrapolation is used:

$$f_\alpha(N_x, j, k) = 2f_\alpha(N_x - 1, j, k) - f_\alpha(N_x - 2, j, k). \tag{25}$$

On the surface of the sphere, Eqs. (9), (10), (12), and (18) proposed in this work are used to update the boundary conditions for f_α's. Only the 19-bit LBE model is used to simulate the flow over a sphere.

Figure 13 shows the velocity profile $u_x(y)$ based on a series of computations carried out for several values of the radius $R = 3.0, 3.2, 3.4, 3.6, 3.8$, and 4.0 for $H/R = 10$ at $Re = 10$. The results are obtained with $\tau = 0.7$. Figure 14 compares the axial velocity profile (at $y = z = 0$) for the same set of parameters. It is worth noting that the present LBE computation does not have sufficient resolution for the given Reynolds number. Yet the velocity profiles agree with each other accurately. The fact that we have obtained a spatially accurate solution over a range of radii strongly suggests that the present boundary condition treatment for curved geometry in the LBE method is capable of handling more complex geometries while maintaining good accuracy.

VI. CONCLUDING REMARKS

Three 3-D LBE models, including the 15-, 19-, and 27-bit models, have been assessed in terms of efficiency, accuracy, and robustness in lid-driven cavity flow. While accurate 3-D results can be obtained by using various LBE models, the 19-bit model is found to be the

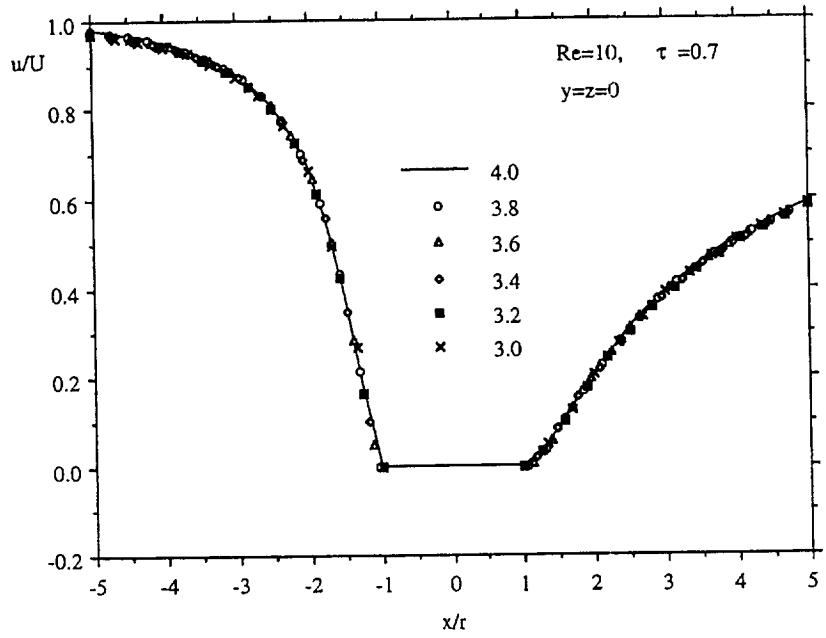

FIG. 14. Comparison of the centerline velocity ($y = 0$) for $r = 3.0, 3.2, 3.4, 3.6, 3.8$, and 4.0 for $Re = 10$ and $H/r = 5$.

best for the cases investigated. The 15-bit model exhibits velocity oscillations and is prone to computational instability. The more complicated 27-bit model does not necessarily give more accurate results than the 19-bit model with the same spatial resolution.

In this study, we have also modified the boundary condition treatment for the LBE method proposed by Filippova and Hänel [23] and Mei *et al.* [22] when the fraction of the intersected link on the boundary Δ is greater than one half. This improves the computational stability when Δ is close to 1 and τ close to 1/2.

The simulations for flows in a square duct and in a circular pipe indicate that the current boundary condition treatment for curved geometries results in second-order accuracy in 3-D flows. The velocity profiles for flow over a sphere show good self-consistency of the solution over a range of sphere radii used.

APPENDIX

The Q15D3 model has the following set of discrete velocities:

$$e_\alpha = \begin{cases} (0,0,0), & \alpha = 0; \text{ rest particle} \\ (\pm 1,0,0)c, (0,\pm 1,0)c, (0,0,\pm 1)c, & \alpha = 1,2,\ldots,6; \text{ group I} \\ (\pm 1,\pm 1,\pm 1)c, & \alpha = 7,8,\ldots,14; \text{ group III} \end{cases} \tag{A1}$$

and the weighting factor w_α is [12]

$$w_\alpha = \begin{cases} 2/9, & \alpha = 0; \text{ rest particle} \\ 1/9, & \alpha = 1,2,\ldots,6; \text{ group I} \\ 1/72, & \alpha = 7,8,\ldots,14; \text{ group III.} \end{cases} \tag{A2}$$

The Q19D3 model has the following set of discrete velocities:

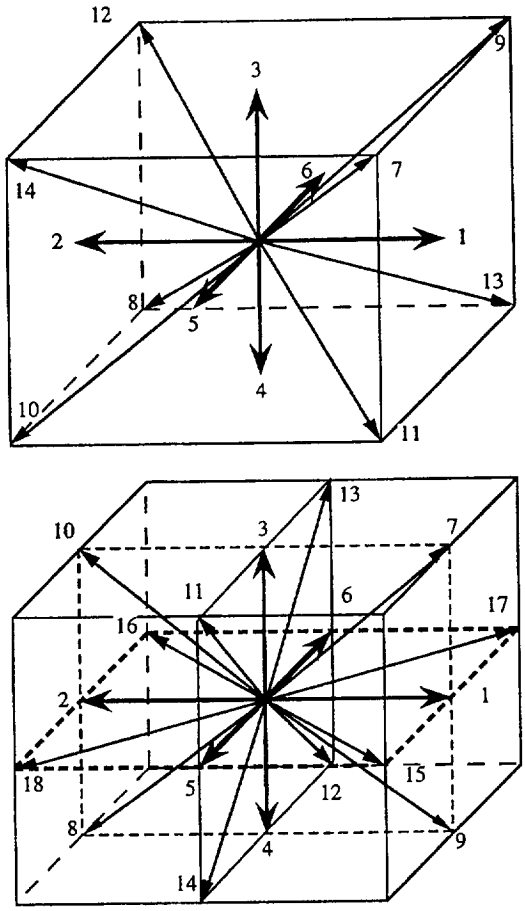

FIG. A1. Discrete velocity vectors for the Q15D3 and Q19D3 lattices.

$$e_\alpha = \begin{cases} (0,0,0), & \alpha = 0, \text{ rest particle} \\ (\pm 1,0,0)c, (0,\pm 1,0)c, (0,0,\pm 1)c, & \alpha = 1,2,\ldots,6; \text{ group I} \\ (\pm 1,\pm 1,0)c, (\pm 1,0,\pm 1)c, (0,\pm 1,\pm 1)c, & \alpha = 7,8,\ldots,18; \text{ group II} \end{cases} \tag{A3}$$

and the weighting factor w_α is [9]

$$w_\alpha = \begin{cases} 1/3, & \alpha = 0; \text{ rest particle} \\ 1/18, & \alpha = 1,2,\ldots,6; \text{ group I} \\ 1/36, & \alpha = 7,8,\ldots,18; \text{ group II.} \end{cases} \tag{A4}$$

The Q27D3 model has the following discrete velocities:

$$e_\alpha = \begin{cases} (0,0,0), & \alpha = 0; \text{ rest particle} \\ (\pm 1,0,0)c, (0,\pm 1,0)c, (0,0,\pm 1)c, & \alpha = 1,2,\ldots,6; \text{ group I} \\ (\pm 1,\pm 1,0)c, (\pm 1,0,\pm 1)c, (0,\pm 1,\pm 1)c, & \alpha = 7,8,\ldots,18; \text{ group II} \\ (\pm 1,\pm 1,\pm 1)c, & \alpha = 19,20,\ldots,26; \text{ group III} \end{cases} \tag{A5}$$

and the weighting factor w_α is [9]

$$w_\alpha = \begin{cases} 8/27, & \alpha = 0, \text{ rest particle} \\ 2/27, & \alpha = 1, 2, \ldots, 6; \text{ group I} \\ 1/54, & \alpha = 7, 8, \ldots, 18; \text{ group II} \\ 1/216, & \alpha = 19, 20, \ldots, 26; \text{ group III.} \end{cases} \tag{A6}$$

In the above, $c = \delta x/\delta t$, δx and δt are the lattice constant and the time step size, respectively. The lattice structures for the Q15D3 and Q19D3 models are shown in Fig. A1.

ACKNOWLEDGMENTS

This work is partially supported by NASA Langley Research Center under the program of Innovative Algorithms for Aerospace Engineering Analysis and Optimization. R. Mei also acknowledges partial support of the Engineering Research Center (ERC) for Particle Science & Technology at the University of Florida, the National Science Foundation (EEC-9402989), and Industrial partners of the ERC. W. Shyy acknowledges partial support of AFOSR and Eglin AFB. We thank Dr. O. Filippova and Prof. D. Hänel for helpful discussions and are grateful to Dr. R. Rubinstein for his careful reading of the manuscript.

REFERENCES

1. R. Peyret and T. D. Taylor, *Computational Technique for Fluid Dynamics*, Vol. II (Springer-Verlag, New York, 1983).
2. C. A. J. Fletcher, *Computational Techniques for Fluid Dynamics*, Vols. I & II (Springer-Verlag, New York, 1988).
3. W. Shyy, *Computational Modeling for Fluid Flow and Interfacial Transport*, Corrected printing (Elsevier, Amsterdam, 1997).
4. H. Chen, S. Chen, and W. H. Matthaeus, Recovery of the Navier–Stokes equations using a lattice–gas Boltzmann method, *Phys. Rev. A* **45**, R5339 (1992).
5. Y. H. Qian, D. d'Humières, and P. Lallemand, Lattice BGK models for Navier–Stokes equation, *Europhys. Lett.* **17**, 479 (1992).
6. R. Benzi, S. Succi, and M. Vergassola, The lattice Boltzmann equation: Theory and applications, *Phys. Rep.* **222**, 145 (1992).
7. S. Chen and G. D. Doolen, Lattice Boltzmann method for fluid flows, *Ann. Rev. Fluid Mech.* **30**, 329 (1998).
8. X. He and L.-S. Luo, *A priori* derivation of the lattice Boltzmann equation, *Phys. Rev. E* **55**, R6333 (1997).
9. X. He and L.-S. Luo, Theory of the lattice Boltzmann method: From the Boltzmann equation to the lattice Boltzmann equation, *Phys. Rev. E* **56**, 6811 (1997).
10. T. Abe, Derivation of the lattice Boltzmann method by means of the discrete ordinate method for the Boltzmann equation, *J. Comput. Phys.* **131**, 241 (1997).
11. P. L. Bhatnagar, E. P. Gross, and M. Krook, A model for collision processes in gases. I. Small amplitude processes in charged and neutral one-component system, *Phys. Rev. A* **94**, 511 (1954).
12. Y. H. Qian, S. Succi, and S. A. Orszag, Recent advances in lattice Boltzmann computing, in *Annual Reviews of Computational Physics*, Vol. III (D. Stauffer, Ed., World Scientific, Singapore), pp. 195–242 (1995).
13. D. P. Ziegler, Boundary conditions for lattice Boltzmann simulations, *J. Stat. Phys.* **71**, 1171 (1993).
14. I. Ginzbourg and P. M. Alder, Boundary flow condition analysis for the three-dimensional lattice Boltzmann model, *J. Phys. II France* **4**, 191 (1994).
15. X. He, Q. Zou, L.-S. Luo, and M. Dembo, Analytic solutions and analysis on non-slip boundary condition for the lattice Boltzmann BGK model, *J. Stat. Phys.* **87**, 115 (1997).
16. O. Behrend, Solid boundaries in particle suspension simulations via lattice Boltzmann method, *Phys. Rev. E* **52**, 1164 (1995).

17. L.-S. Luo, Analytic solutions of linearized lattice Boltzmann equation for simple flows, *J. Stat. Phys.* **88**, 913 (1997).

18. A. J. C. Ladd, Numerical simulation of particular suspensions via a discretized Boltzmann equation, Part 2, Numerical results, *J. Fluid Mech.* **271**, 311 (1994).

19. D. R. Noble, S. Chen, J. G. Georgiadis, and R. O. Buckius, A consistent hydrodynamic boundary condition for the lattice Boltzmann method, *Phys. Fluid* **7**, 203 (1995).

20. S. Chen, D. Martinez, and R. Mei, On boundary conditions in lattice Boltzmann method, *Phys. Fluids* **8**, 2527 (1996).

21. Q. Zou and X. He, On pressure and velocity boundary conditions for the lattice Boltzmann BGK model, *Phys. Fluids* **9**, 1591 (1997).

22. R. Mei, L.-S. Luo, and W. Shyy, An accurate curved boundary treatment in the lattice Boltzmann method, *J. Comp. Phys.* **155**, 307 (1999).

23. O. Filippova and D. Hänel, Grid refinement for lattice-BGK models, *J. Comp. Phys.* **147**, 219 (1998).

24. F. M. White, *Viscous Fluid Flow* (McGraw-Hill, New York, 1974).

25. J. Salom, *Numerical Simulation of Convection Phenomena Based on Domain Decomposition Techniques and Experimental Validation*, Ph.D. dissertation, Universitat Politecnica de Catalunya, Spain (1999).

26. D. Kandhai, A. Koponen, A. Hoekstra, M. Kataja, J. Timonen, and P. M. A. Sloot, Implementation aspects of 3D lattice-BGK: boundaries, accuracy, and a new fast relaxation method, *J. Comp. Phys.* **150**, 482 (1999).

27. I. Ginzbourg and D. d'Humieres, Local second-order boundary methods for lattice Boltzmann models, *J. Stat. Phys.* **84**, 927 (1996).

28. R. Mei and W. Shyy, On the finite difference-based lattice Boltzmann method in curvilinear coordinates, *J. Comp. Phys.* **143**, 426 (1998).

29. X. He and G. Doolen, Lattice Boltzmann method on curvilinear coordinates systems: Flow around a circular cylinder, *J. Comp. Phys.* **134**, 306 (1997).

30. P. Lallemand and L.-S. Luo, Theory of the lattice Boltzmann method: Dispersion, dissipation, isotropy, Galilean invariance, and stability, *Phys. Rev. E*, to appear (2000).

Force Evaluation in the Lattice Boltzmann Method Involving Curved Geometry

Renwei Mei,[†] Dazhi Yu,[‡] and Wei Shyy[§]
Department of Aerospace Engineering, Mechanics & Engineering Science, University of Florida, Gainesville, Florida 32611-6250

Li-Shi Luo[**]
ICASE, MS 132C, NASA Langley Research Center, 3 West Reid Street, Building 1152, Hampton, Virginia 23681-2199

(Dated: September 25, 2000)

Abstract

The present work investigates two approaches for force evaluation in the lattice Boltzmann equation: the momentum exchange method and the stress integration method on the surface of a body. The boundary condition for the particle distribution functions on curved geometries is handled with second order accuracy based on our recent works [1, 2]. The stress integration method is computationally laborious for two-dimensional flows and in general difficult to implement for three-dimensional flows, while the momentum exchange method is reliable, accurate, and easy to implement for both two-dimensional and three-dimensional flows. Several test cases are selected to evaluate the present methods, including: (i) two-dimensional pressure-driven channel flow; (ii) two-dimensional uniform flow past a column of cylinders; (iii) two-dimensional flow past a cylinder asymmetrically placed in a channel (with vortex shedding); (iv) three-dimensional pressure-driven flow in a circular pipe; and (v) three-dimensional flow past a sphere. The drag evaluated by using the momentum exchange method agrees well with the exact or other published results.

PACS numbers: 47.10.+g, 47.11.+j, 05.20.Dd

[†]Electronic address: rwm@aero.ufl.edu
[‡]Electronic address: ydz@aero.ufl.edu
[§]Electronic address: wss@aero.ufl.edu
[**]Electronic address: luo@icase.edu; http://www.icase.edu/~luo

I. INTRODUCTION

A Background of the lattice Boltzmann equation method

The method of lattice Boltzmann equation (LBE) solves the microscopic kinetic equation for particle distribution function $f(\boldsymbol{x}, \boldsymbol{\xi}, t)$, where $\boldsymbol{\xi}$ is the particle velocity, in phase space $(\boldsymbol{x}, \boldsymbol{\xi})$ and time t, from which the macroscopic quantities (flow mass density ρ and velocity $\boldsymbol{u}$) are obtained through moment integration of $f(\boldsymbol{x}, \boldsymbol{\xi}, t)$. Because the solution procedure is explicit, easy to implement and parallelize, the LBE method has increasingly become an attractive alternative computational method for solving fluid dynamics problems in various systems [3–6]. The most widely used lattice Boltzmann equation [3–6] is a discretized version of the model Boltzmann equation with a single relaxation time approximation due to Bhatnagar, Gross, and Krook (BGK model) [7]

$$\partial_t f + \boldsymbol{\xi} \cdot \boldsymbol{\nabla} f = \frac{1}{\lambda}[f - f^{(0)}], \tag{1}$$

where $f^{(0)}$ is the Maxwell-Boltzmann equilibrium distribution function and λ is the relaxation time. The mass density ρ and momentum density $\rho\boldsymbol{u}$ are the first $(D+1)$ hydrodynamic moments of the distribution function f and $f^{(0)}$ in D-dimensions. It can be shown that the particle velocity space $\boldsymbol{\xi}$ can be discretized and reduced to a very small set of discrete velocities $\{\boldsymbol{\xi}_\alpha | \alpha = 1, 2, \ldots, b\}$, and the hydrodynamic moments of f and $f^{(0)}$ as well as their fluxes can be preserved exactly, because the moment integral can be replaced by quadrature exactly up to a certain order in $\boldsymbol{\xi}$ [8–11]. With velocity space $\boldsymbol{\xi}$ properly discretized, Eq. (1) reduces to a discrete velocity model (DVM) of the Boltzmann equation

$$\partial_t f_\alpha + \boldsymbol{\xi}_\alpha \cdot \boldsymbol{\nabla} f_\alpha = \frac{1}{\lambda}[f_\alpha - f_\alpha^{(0)}], \tag{2}$$

In the above equation, $f_\alpha(\boldsymbol{x}, t) \equiv f(\boldsymbol{x}, \boldsymbol{\xi}_\alpha, t)$ and $f_\alpha^{(0)}(\boldsymbol{x}, t) \equiv f^{(0)}(\boldsymbol{x}, \boldsymbol{\xi}_\alpha, t)$ are the distribution function and the equilibrium distribution function of the α-th discrete velocity $\boldsymbol{\xi}_\alpha$, respectively. Equation (2) is then discretized in space $\boldsymbol{x}$ and time t into

$$f_\alpha(\boldsymbol{x}_i + \boldsymbol{e}_\alpha \delta_t, t + \delta_t) - f_\alpha(\boldsymbol{x}_i, t) = -\frac{1}{\tau}[f_\alpha(\boldsymbol{x}_i, t) - f_\alpha^{(\mathrm{eq})}(\boldsymbol{x}_i, t)], \tag{3}$$

where $\tau = \lambda/\delta_t$ is the dimensionless relaxation time and $\boldsymbol{e}_\alpha$ is a discrete velocity vector. The coherent discretization of space and time is done in such a way that $\delta\boldsymbol{x} = \boldsymbol{e}_\alpha\delta_t$ is always the displacement vector from a lattice site to one of its neighboring sites. The equilibrium distribution function $f_\alpha^{(\mathrm{eq})}(\boldsymbol{x}_i, t)$ in the lattice Boltzmann equation (3) is obtained by expanding the Maxwell-Boltzmann distribution function in Taylor series of $\boldsymbol{u}$ up to second order [8, 9], and can be expressed in general as

$$f_\alpha^{(\mathrm{eq})} = w_\alpha\rho\left[1 + \frac{3}{c^2}(\boldsymbol{e}_\alpha\cdot\boldsymbol{u}) + \frac{9}{2c^4}(\boldsymbol{e}_\alpha\cdot\boldsymbol{u})^2 - \frac{3}{2c^2}\boldsymbol{u}^2\right], \tag{4}$$

where $c \equiv \delta_x/\delta_t$; δ_x is the lattice constant of the underlying lattice space; and coefficient w_α depends on the discrete velocity set $\{\boldsymbol{e}_\alpha\}$ in D spatial dimensions. In what follows, we shall use the lattice units of $\delta_x = 1$ and $\delta_t = 1$. Appendix A provides the details of coefficient w_α and the discrete velocity set $\{\boldsymbol{e}_\alpha\}$ for the two-dimensional nine-velocity model (D2Q9) and the three-dimensional nineteen-velocity model (D3Q19) [12]. Figure 1 shows the discrete velocity sets of the two models. It should be pointed out that there exist other discrete velocity sets $\{\boldsymbol{e}_\alpha\}$ which have the sufficient symmetry for the hydrodynamics [8, 9]. A comparative study of three three-dimensional LBE models including the fifteen-velocity model (D3Q15), the nineteen-velocity model (D3Q19), and the twenty-seven-velocity model (D3Q27), in terms of accuracy and computational efficiency has been conducted by Mei *et al.* [2]. It was found that the nineteen-velocity model (D3Q19) offers a better combination of computational stability and accuracy. The D2Q9 and D3Q19 models will be used in this study for force evaluation in two-dimensional and three-dimensional flows, respectively. Equation (3) is conveniently solved in two steps

$$\text{collision:} \qquad \tilde{f}_\alpha(\boldsymbol{x}_i, t) = f_\alpha(\boldsymbol{x}_i, t) - \frac{1}{\tau}\left[f_\alpha(\boldsymbol{x}_i, t) - f_\alpha^{(\mathrm{eq})}(\boldsymbol{x}_i, t)\right], \tag{5a}$$

$$\text{streaming:} \qquad f_\alpha(\boldsymbol{x}_i + \boldsymbol{e}_\alpha\delta_t, t + \delta_t) = \tilde{f}_\alpha(\boldsymbol{x}_i, t), \tag{5b}$$

which is known as the LBGK scheme [3, 4]. The collision step is completely local, and the streaming step is uniform and requires little computational effort, which makes Eq. (5) ideal for parallel implementation. The simplicity and compact nature of the LBGK scheme, however, necessitate the use of the square lattices of constant spacing ($\delta_x = \delta_y$), and con-

sequently lead to the unity of the local Courant-Friedrichs-Lewy (CFL) number, because $\delta_t = \delta_x$.

B Boundary condition for a curved geometry in the LBE method

Consider a part of an arbitrary curved wall geometry, as shown in Fig. 2, where the filled small circles on the boundary, $\boldsymbol{x}_w$, denote the intersections of the boundary with various lattice- to-lattice links. The fraction of an intersected link in the fluid region, Δ, is defined by

$$\Delta = \frac{\|\boldsymbol{x}_f - \boldsymbol{x}_w\|}{\|\boldsymbol{x}_f - \boldsymbol{x}_b\|}. \tag{6}$$

Obviously the horizontal or vertical distance between $\boldsymbol{x}_b$ and $\boldsymbol{x}_w$ is $\Delta\delta_x$ on the square lattice, and $0 \leq \Delta \leq 1$. In Eq. (5b), the value of $\tilde{f}_\alpha(\boldsymbol{x}_i, t)$ needs to be constructed according to the location of the boundary and the boundary conditions, if the grid point $\boldsymbol{x}_i = \boldsymbol{x}_b$ lies beyond the boundary. In the past, the bounce-back boundary condition has been use to deal with a solid boundary in order to approximate the no-slip boundary condition at the solid boundary [13–21]. However, it is well understood that this bounce-back boundary condition satisfies the no-slip boundary condition with a second-order accuracy (for Couette and Poiseuille flows) at the location one half lattice spacing ($\Delta = 1/2$) outside of a boundary node where the bounce-back collision takes place; and this is only true with simple boundaries of straight line parallel to the lattice grid. For a curved geometry, simply placing the boundary half-way between two nodes will alter the geometry on the grid level and degrade the accuracy of the flow field and the force on the body at finite and higher Reynolds number. To circumvent this difficulty, Mei and Shyy solved Eq. (2) in curvilinear coordinates using a finite difference method to compute f_α [22]. He and Doolen used body-fitted curvilinear coordinates with interpolation throughout the entire mesh, except at the boundaries where the bounce-back boundary condition is used [23]. In the recent works of Filippova and Hänel [24] and Mei *et al.* [1, 2], a second-order accurate boundary condition for curved geometry was developed in conjunction with the use of Cartesian grid in order to retain the advantages of the LBE method. An interpolation scheme is employed only at the boundaries to obtain $\tilde{f}_\alpha(\boldsymbol{x}_i, t)$.

The detailed assessment on the impact of the boundary condition on the accuracy of the flow field have been given in Ref. [1] for some two-dimensional flows and in Ref. [2] for some three-dimensional flows.

C Force evaluation and related works

In spite of numerous improvement for the LBE method during the last several years, one important issue that has not been systematically studied is the accurate determination of the fluid dynamic force involving curved boundaries. Needless to say, accurate evaluation of the force is crucial to the study of fluid dynamics, especially in fluid-structure interaction. Several force evaluation schemes, including momentum exchange [15, 17] and integration of surface stress [23, 25], have been used to evaluate the fluid dynamic force on a curved body in the context of the LBE method.

He and Doolen [23] evaluated the force by integrating the total stress on the surface of the cylinder and the components of the stress tensor were obtained by taking respective velocity gradients. Even though the body-fitted grid was used, an extrapolation was needed to obtain the stress in order to correct the half-grid effect due to the bounce-back boundary condition. Filippova and Hänel [24] developed a second-order accurate boundary condition for curved boundaries. However, the fluid dynamics force on a circular cylinder asymmetrically placed in a two-dimensional channel was obtained by integrating the pressure and deviatoric stresses on the surface of the cylinder by extrapolating from the nearby Cartesian grids to the solid boundary [24, 25]. To gain insight into the method of surface stress integration, it is instructive to examine the variation of the pressure on the surface of a circular cylinder at finite Reynolds number obtained by using the LBE method for flow over a column of cylinders (see Ref. [1], and Sec. III B). Figure 3 shows the pressure coefficient

$$C_P = \frac{p - p_\infty}{\frac{1}{2}\rho U^2}$$

on the surface obtained by using second order extrapolation where p_∞ is the far upstream pressure. Only those boundary points, $\boldsymbol{x}_w$, intersected by the horizontal or vertical velocities, i.e., $\boldsymbol{e}_1$, $\boldsymbol{e}_3$, $\boldsymbol{e}_5$, and $\boldsymbol{e}_7$, are considered in the result given by Fig. 3. If the boundary points

intersected by the links in the diagonal velocities, i.e., $\boldsymbol{e}_2$, $\boldsymbol{e}_4$, $\boldsymbol{e}_6$, and $\boldsymbol{e}_8$, are also considered, the variation of C_P would be more noisy. The components of the deviatoric stress tensor show a similar noisy pattern. It is not clear how the noise in the pressure and stresses affect the accuracy of the fluid dynamic force in the stress integration method. While the programming in the extrapolation and integration is manageable in two-dimensional cases, it is rather laborious in three-dimensional cases.

Instead of the stress integration method, Ladd used the momentum exchange method to compute the fluid force on a sphere in suspension flow [15]. In the flow simulation using the bounce-back boundary condition, the body is effectively replaced by a series of stairs. Each segment on the surface has an area of unity for a cubic lattice. The force on each link [half-way between two lattices at $\boldsymbol{x}_f$ and $\boldsymbol{x}_b = (\boldsymbol{x}_f + \boldsymbol{e}_\alpha \delta_t)$ in which $\boldsymbol{x}_b$ resides in the solid region] results from the momentum exchange (per unit time) between two opposing directions of the neighboring lattices

$$\frac{1}{\delta_t}[\boldsymbol{e}_\alpha f_\alpha(\boldsymbol{x}_f) - \boldsymbol{e}_{\bar{\alpha}} f_{\bar{\alpha}}(\boldsymbol{x}_f + \boldsymbol{e}_\alpha \delta_t)]$$

in which $\boldsymbol{e}_{\bar{\alpha}} \equiv -\boldsymbol{e}_\alpha$. Whereas the momentum exchange method is very easy to implement computationally, its applicability and accuracy for a curved boundary have not been systematically studied. To recapitulate, there are two major problems associated with the method of surface stress integration. First, the components of stress tensor are often noisy on a curved surface due to limited resolution near the body and the use of Cartesian grids. The accuracy of such a method has not been addressed in the literature. Second, the implementation of the extrapolation for Cartesian components of the stress tensor to the boundary surface and the integration of the stresses on the surface of a three-dimensional geometry are very laborious in comparison with the intrinsic simplicity of the lattice Boltzmann simulations for flow field. The problems associated with the method of the momentum exchange are as follows. (a) The scheme was proposed for the case with $\Delta = 1/2$ at every boundary intersection $\boldsymbol{x}_w$. Whether this scheme can be applied to the cases where $\Delta \neq 1/2$, when, for example, the boundary is not straight, needs to be investigated. (b) As in the case of stress integration method, the resolution near a solid body is often limited and the near wall flow

variables can be noisy. If one uses the momentum exchange method to compute the total force, it is not clear what the adequate resolution is to obtain reliable fluid dynamic force on a bluff body at a given (moderate) value of Reynolds number, say, Re $\approx O(10^2)$.

D Scope of the present work

In what follows, two methods for the force evaluation, i.e., the stress integration and the momentum exchange methods, will be described in detail. The shear and normal stresses on the wall in a pressure driven channel flow will be first examined to assess the suitability of the momentum exchange method when $\Delta \neq 1/2$ and analyze the errors incurred. The results on the drag force for flow over a column of circular cylinders using these two methods will be subsequently assessed for the consistency. The drag coefficient at Re = 100 will be compared with the result of Fornberg [26] obtained by using a second-order accurate finite difference scheme with sufficient grid resolution. For flow over a cylinder asymmetrically placed in a channel at Re = 100, the unsteady drag and lift coefficients were computed and compared with the results in the literature. The momentum exchange method is further evaluated for three-dimensional fully developed pipe flow and for a uniform flow over an two-dimensional array of spheres at finite Reynolds number. We found that the simple momentum exchange method for force evaluation gives fairly reliable results for the two-dimensional and three-dimensional flows.

II. METHODS FOR FORCE EVALUATION IN LBE METHOD

A Second-order accurate no-slip boundary condition for curved geometry

The analysis of boundary conditions for a curved boundary in the lattice Boltzmann equation is accomplished by applying Chapman-Enskog expansion for the distribution function at the boundary. The following approximation for post-collision distribution function on the right-hand-side of Eq. (5b) can lead to a second-order accurate no-slip boundary

condition [1, 2, 24]

$$\tilde{f}_{\bar{\alpha}}(\boldsymbol{x}_b,t) = (1-\chi)\tilde{f}_{\alpha}(\boldsymbol{x}_f,t) + \chi f^*_{\alpha}(\boldsymbol{x}_b,t) + 2w_{\alpha}\rho\frac{3}{c^2}\boldsymbol{e}_{\bar{\alpha}}\cdot\boldsymbol{u}_w\,, \tag{7}$$

where

$$\begin{aligned} f^*_{\alpha}(\boldsymbol{x}_b,t) &= w_{\alpha}\rho(\boldsymbol{x}_f,t)\left[1+\frac{3}{c^2}(\boldsymbol{e}_{\alpha}\cdot\boldsymbol{u}_{bf}) + \frac{9}{2c^4}(\boldsymbol{e}_{\alpha}\cdot\boldsymbol{u}_f)^2 - \frac{3}{2c^2}\boldsymbol{u}_f^2\right] \\ &= f^{(\mathrm{eq})}_{\alpha}(\boldsymbol{x}_f,t) + w_{\alpha}\rho(\boldsymbol{x}_f,t)\frac{3}{c^2}\boldsymbol{e}_{\alpha}\cdot(\boldsymbol{u}_{bf}-\boldsymbol{u}_f)\,, \end{aligned} \tag{8}$$

and

$$\boldsymbol{u}_{bf} = \boldsymbol{u}_{ff} = \boldsymbol{u}_f(\boldsymbol{x}_f + \boldsymbol{e}_{\bar{\alpha}}\delta_t, t)\,, \quad \chi = \frac{(2\Delta-1)}{(\tau-2)}\,, \quad 0 \le \Delta < \frac{1}{2}\,, \tag{9a}$$

$$\boldsymbol{u}_{bf} = \frac{1}{2\Delta}(2\Delta-3)\boldsymbol{u}_f + \frac{3}{2\Delta}\boldsymbol{u}_w\,, \quad \chi = \frac{(2\Delta-1)}{(\tau+1/2)}\,, \quad \frac{1}{2} \le \Delta < 1\,. \tag{9b}$$

The above treatment is applicable for both the two-dimensional and three-dimensional lattice Boltzmann models.

By substitution of Eq. (8), Eq. (7) becomes

$$\begin{aligned} \tilde{f}_{\bar{\alpha}}(\boldsymbol{x}_b,t) = \tilde{f}_{\alpha}(\boldsymbol{x}_f,t) &- \chi\left[\tilde{f}_{\alpha}(\boldsymbol{x}_f,t) - f^{(\mathrm{eq})}_{\alpha}(\boldsymbol{x}_f,t)\right] \\ &+ w_{\alpha}\rho(\boldsymbol{x}_f,t)\frac{3}{c^2}\boldsymbol{e}_{\alpha}\cdot(\boldsymbol{u}_{bf}-\boldsymbol{u}_f-2\boldsymbol{u}_w)\,. \end{aligned} \tag{10}$$

Thus, the above treatment of curved boundary can be thought as a modification of the relaxation (the viscous effect) near the wall (via parameter χ), in additional to a forcing term accounting for the momentum exchange effect due to the wall.

B Force evaluation based on stress integration

He and Doolen [23] evaluated the force by integrating the total stresses on the boundary of the cylinder $\partial\Omega$:

$$\boldsymbol{F} = \int_{\partial\Omega} dA\,\hat{\boldsymbol{n}}\cdot\left\{-p\mathsf{I} + \rho\nu[(\boldsymbol{\nabla}:\boldsymbol{u}) + (\boldsymbol{\nabla}:\boldsymbol{u})^{\mathsf{T}}]\right\}\,, \tag{11}$$

where $\hat{\boldsymbol{n}}$ is the unit out normal vector of the boundary $\partial\Omega$. In Ref. [23], a body fitted coordinate system together with grid stretching was used such that a large number of grids

can be placed near the body to yield reliable velocity gradient $\partial_i u_j$. In general, since $\boldsymbol{u}$ is not the primary variable in the LBE simulations and the evaluation of $\boldsymbol{u}$ using $\sum_\alpha \boldsymbol{e}_\alpha f_\alpha$ based on f_α's suffers the loss of accuracy due to the cancellation of two close numbers in f_α's the evaluation of the derivative $\partial_i u_j$ will result in further degradation of the accuracy. Filippova [25] used similar integration scheme to obtain the dynamic force on the body for the force on a circular cylinder [24] except that the deviatoric stresses were evaluated using the non-equilibrium part of the particle distribution function [see Eq. (13) below]. However, since the Cartesian grid was used, the stress vectors on the surface of the body (with arbitrary Δ) have to be computed through an extrapolation procedure based upon the information in the flow field. This leads to further loss of accuracy for finite lattice size δ_x when the shear layer near the wall is not sufficiently resolved.

In Eq. (11), the pressure p can be easily evaluated using the equation of state $p = c_s^2 \rho$. For D2Q9 and D3Q19 models, $c_s^2 = 1/3$ so that $p = \rho/3$. The deviatoric stress for two-dimensional incompressible flow

$$\tau_{ij} = \rho\nu \left(\partial_i u_j + \partial_j u_i\right) \tag{12}$$

can be evaluated using the non-equilibrium part of the distribution function $f_\alpha^{(\mathrm{neq})} = [f_\alpha - f_\alpha^{(\mathrm{eq})}]$

$$\tau_{ij} = \left(1 - \frac{1}{2\tau}\right) \sum_\alpha f_\alpha^{(\mathrm{neq})}(\boldsymbol{x}, t) \left(e_{\alpha,i} e_{\alpha,j} - \frac{1}{D} \boldsymbol{e}_\alpha \cdot \boldsymbol{e}_\alpha \delta_{ij}\right) , \tag{13}$$

where $e_{\alpha,i}$ and $e_{\alpha,j}$ are ith and jth Cartesian component of the discrete velocity $\boldsymbol{e}_\alpha$, respectively. For the flow past a circular cylinder, a separate set of surface points on the cylinder can be introduced in order to carry out the numerical integration given by Eq. (11). The values of the pressure and each of the six components of the symmetric deviatoric stress tensor on the surface points can be obtained using a second-order extrapolation scheme based on the values of p and τ_{ij} at the neighboring fluid lattices. The force exerting on the boundary $\partial\Omega$ is computed as

$$\boldsymbol{F} = \int_{\partial\Omega} dA\, \hat{\boldsymbol{n}} \cdot \left\{-p\mathsf{I} + \rho\nu[(\boldsymbol{\nabla}:\boldsymbol{u}) + (\boldsymbol{\nabla}:\boldsymbol{u})^{\mathsf{T}}]\right\}_{\text{extrapolated}} . \tag{14}$$

It is worth commenting here that for the two-dimensional flow past a cylinder, nearly half of the entire code was taken up by the above force evaluation procedure.

C Method based on the momentum exchange

In order to employ the momentum exchange method efficiently, two scalar arrays, $w(i,j)$ and $w_b(i,j)$ are introduced. A value of 0 is assigned to $w(i,j)$ for the lattice site (i,j) that are occupied by fluid; a value of 1 is assigned to $w(i,j)$ for those lattice nodes inside the solid body. The array $w_b(i,j)$ is set to zero everywhere except for those boundary nodes, $\boldsymbol{x}_b$, where a value of 1 is assigned. For a given nonzero velocity $\boldsymbol{e}_\alpha$, $\boldsymbol{e}_{\bar{\alpha}}$ denotes the velocity in opposite direction, i.e., $\boldsymbol{e}_{\bar{\alpha}} \equiv -\boldsymbol{e}_\alpha$ (see Fig. 2). For a given boundary node $\boldsymbol{x}_b$ inside the solid region with $w_b(i,j) = 1$ and $w(i,j) = 1$, the momentum exchange with all possible neighboring fluid nodes over a time step $\delta_t = 1$ is

$$\sum_{\alpha \neq 0} \boldsymbol{e}_\alpha \left[\tilde{f}_\alpha(\boldsymbol{x}_b, t) + \tilde{f}_{\bar{\alpha}}(\boldsymbol{x}_b + \boldsymbol{e}_\alpha \delta_t, t) \right] \left[1 - w(\boldsymbol{x}_b + \boldsymbol{e}_\alpha \delta_t) \right].$$

Simply summing the contribution over all boundary nodes $\boldsymbol{x}_b$ belonging to the body, the total force (acted by the solid body on the fluid) is obtained as

$$\boldsymbol{F} = \sum_{\text{all } \boldsymbol{x}_b} \sum_{\alpha \neq 0} \boldsymbol{e}_\alpha \left[\tilde{f}_\alpha(\boldsymbol{x}_b, t) + \tilde{f}_{\bar{\alpha}}(\boldsymbol{x}_b + \boldsymbol{e}_\alpha \delta_t, t) \right] \left[1 - w(\boldsymbol{x}_b + \boldsymbol{e}_\alpha \delta_t) \right]. \tag{15}$$

In the momentum exchange method the force $\boldsymbol{F}$ is evaluated after the collision step is carried out and the value of $\tilde{f}_{\bar{\alpha}}$ at boundary given by Eq. (7) has been evaluated. The momentum exchange occurs during the subsequent streaming step when $\tilde{f}_{\bar{\alpha}}(\boldsymbol{x}_b, t + \delta_t)$ and $\tilde{f}_\alpha(\boldsymbol{x}_f, t + \delta_t)$ move to $\boldsymbol{x}_f$ and $\boldsymbol{x}_b$, respectively. As mentioned in the introductory section, the effect of variable Δ is not explicitly included, but it is implicitly taken into account in the determination of $\tilde{f}_{\bar{\alpha}}(\boldsymbol{x}_b, t + \delta_t)$. The applicability of Eq. (15) will be examined and validated.

Clearly, the force is proportional to the number of boundary nodes $\boldsymbol{x}_b$ in the above formula of $\boldsymbol{F}$ and the number of the boundary nodes increase linearly with the size of the body in a two-dimensional flow. However, since the force is normalized by $\rho U^2 r$ in the formula for C_D in two-dimensions [see Eq. (24)], the drag coefficient C_D should be independent of r.

III. RESULTS AND DISCUSSIONS

For straight walls, there is no doubt that Eq. (11) together with the equation of state for pressure and Eq. (13) for τ_{ij} gives accurate result for the force provided that f_α's are accurately computed. To demonstrate the correctness of Eq. (15) based on the momentum exchange for an arbitrary Δ, we first consider the pressure driven channel flow (see Fig. 4) for which exact solutions for the velocity and stresses are known. The second case considered is the two-dimensional flow past a column of circular cylinders at Reynolds number Re = 100 and $H/r = 20$, where H is the distance between the centers of two adjacent cylinders. The values of the drag computed using the two force evaluation methods are then compared with the result of Fornberg [26]. The dependence of the drag on the radius r in the momentum exchange method is examined to assess the reliability of this method. The third case is the two-dimensional flow over a circular cylinder that is asymmetrically placed in a channel at Re = 100 (with vortex shedding). The time dependence of the drag and lift coefficients is compared with results in literature.

We also consider two cases of three-dimensional flow. The first case is the pressure driven flow in a circular pipe for which the exact solutions for both the velocity profile and wall shear stresses are known. The assessment for the momentum exchange method for three-dimensional flows will be made first in this case. Finally, the momentum exchange method will be evaluated by considering the drag on a sphere due to a uniform flow over a sphere in a finite domain. The details for the flow field computation can be found in Ref. [1, 2].

A Two-dimensional pressure-driven channel flow

In the case of the channel flow, the force on the top wall ($y = H$) at a given location x ($i = N_x/2+1$, say) can be evaluated using the momentum exchange method as follows. The wall is located between $j = N_y$ and $N_y - 1$ (Fig. 4). The x and y components of the force

on the fluid at the top wall near the ith node are

$$F_x = [\tilde{f}_6(i,j) + \tilde{f}_2(i-1,j-1)]\, e_{6,x} + [\tilde{f}_8(i,j) + \tilde{f}_4(i+1,j-1)]\, e_{8,x} \tag{16a}$$

$$F_y = [\tilde{f}_6(i,j) + \tilde{f}_2(i-1,j-1)]\, e_{6,y} + [\tilde{f}_8(i,j) + \tilde{f}_4(i+1,j-1)]\, e_{8,y} + [\tilde{f}_7(i,j) + \tilde{f}_3(i,j-1)]\, e_{7,y}\,, \tag{16b}$$

where $e_{\alpha,j}$ denotes the jth Cartesian component of velocity $\boldsymbol{e}_\alpha$. Since $\delta_x = 1$, F_x and F_y are, effectively, the total shear and normal stresses, σ_{xy} and σ_{yy}, which include the pressure and the deviatoric stresses, on the fluid element at $y = H$.

Based on Eq. (13), the deviatoric component of the fluid shear stresses at $j = N_y - 1$ (or $y = N_y - 3 + \Delta$) and $N_y - 2$ (or $y = N_y - 4 + \Delta$) can be exactly evaluated based on the non-equilibrium part of the distribution functions in the flow field if they are correctly given. A linear extrapolation of the deviatoric shear stresses to $y = H = N_y - 3 + 2\Delta$ yields

$$\tau_{xy,w}^{(\mathrm{neq})} = \tau_{xy}(j = N_y - 1) + \Delta[\tau_{xy}(j = N_y - 1) - \tau_{xy}(j = N_y - 2)]\,, \tag{17}$$

where the superscript "(neq)" denotes the value computed from $f_\alpha^{(\mathrm{neq})}$, the subscript w refers to the value at the wall. The deviatoric normal stress, $\tau_{yy,w}^{(\mathrm{neq})}$, can be similarly computed. In a fully developed channel flow, the normal component of the deviatoric stress $\tau_{yy}(y)$ is expected to be zero while the total normal stress $\sigma_{yy}(y)$ is equal to the negative pressure $(-p)$. It needs to be pointed out that this method of evaluating $\tau_{xy,w}^{(\mathrm{neq})}$ given by Eq. (17) for two-dimensional channel flow is equivalent to the method of the surface stress integration based on the extrapolated pressure and the deviatoric stresses on the solid wall except that no numerical integration on the solid surface is needed.

After the velocity profile $u_x(y)$ is obtained from f_α, the shear stress τ_{xy} on the wall can also be calculated using the near wall velocity profile as,

$$\rho\nu \left.\frac{du_x}{dy}\right|_{y=H} = \rho\nu \frac{(2+\Delta)}{(1+\Delta)} \frac{[0 - u_x(j = N_y - 1)]}{\Delta} - \rho\nu \frac{\Delta}{(1+\Delta)} [u_x(j = N_y - 1) - u_x(j = N_y - 2)]\,. \tag{18}$$

In the above, a linear extrapolation is employed to evaluate the velocity derivative $\frac{du_x}{dy}|_{y=H}$

at the wall. Finally, the exact solution for the fluid shear stress on the wall ($y = H$) is

$$\tau_{xy,w}^{\text{exact}} = \frac{1}{2}\frac{dp}{dx}H\,, \qquad H = N_y - 3 + 2\Delta \tag{19}$$

based on the parabolic velocity profile or simple control volume analysis. This exact result can be used to assess the accuracy of the aforementioned methods for the force evaluation.

In the LBE simulations, the pressure gradient is enforced through the addition of an equivalent body force after the collision step [2, 23]. While the velocity field given by the LBE solution can be unique, the pressure field [thus the density field $\rho(x, y)$] can only be unique up to an arbitrary constant. In view of Eq. (18), it is difficult to compare the stresses for different cases if $\rho(i, j)$ converges to different values in each case. To circumvent this difficulty, the density field in the channel flow simulation is normalized by $\rho(i = 2, j = N_y/2)$ at every time step. This normalization procedure results in $\rho(x, y) = 1$ throughout the entire computational domain. It is also applied to the three-dimensional flow in a circular pipe.

Table I compares the numerical values of the shear stress for a typical case ($N_y = 35$, $dp/dx = -10^{-6}$ in the lattice units, and $\tau = 0.6$) based on: $\tau_{xy,w}^{\text{exact}}$ given by Eq. (19), F_x given by Eq. (16a), $\tau_{xy,w}^{(\text{neq})}$ given by Eq. (17), and $\rho\nu\frac{du_x}{dy}|_{y=H}$ given by Eq. (18). Also listed is the comparison between F_y given by Eq. (16b) and $-p$. All computations are carried out with double precision accuracy.

It is noted that $\tau_{xy,w}^{(\text{neq})}$ is identical to $\tau_{xy,w}^{\text{exact}}$ for all values of Δ. Closer examination of the shear stress profile using Eq. (13) across the channel reveals that $\tau_{xy,w}^{(\text{neq})}(y)$ is also equal to the exact shear stress profile $\tau_{xy}^{\text{exact}}(y)$, which is linear, despite the errors in the velocity profile $u_x(y)$ for all values of Δ. A linear extrapolation, Eq. (17), for a linear profile therefore gives the exact wall shear stress. Thus, the exactness of $\tau_{xy,w}^{(\text{neq})}$ in the LBE simulation of channel flow indicates the reliability of the LBE solution for the stress field $\tau_{ij}^{(\text{neq})}(x, y)$ by using Eq. (13). However, as Fig. 3 indicates, the accuracy of the integrating $\tau_{ij}^{(\text{neq})}(x, y)$ to obtain the fluid dynamic force in nontrivial geometries is not clear; this will be further investigated in the following sections.

For $0 < \Delta < 1$, the normal force F_y given by Eq. (16b) based on the momentum exchange method agrees exactly with the pressure on the wall. This is a rather special quantity

since deviatoric component of the force is identically zero. Nevertheless, the method of the momentum exchange does give a reliable value for the normal stress.

For the shear (tangential) force, it is observed from Table I that for fixed dp/dx, F_x does not change as Δ increases from 0.01 to 0.99. On the other hand, the exact result $\tau_{xy,w}^{\text{exact}} = \frac{1}{2}\frac{dp}{dx}(N_y - 3 + 2\Delta)$, increases linearly with Δ. Further computations were carried out over a range of N_y (= 35, 67, 99, and 131) and τ (= 0.505, 0.51, 0.52, 0.6, 0.7, 0.8, 0.9, 1.0, 1.2, 1.4, and 1.6). The results indicate that the momentum exchange method gives the shear stress on the top wall as

$$F_x = \frac{1}{2}\frac{dp}{dx}\left(N_y - 3 + \frac{2}{3}\right) . \tag{20}$$

That is, F_x is independent of τ and Δ. The error in F_x is zero when $\Delta = 1/3$. The absolute error attains the maximum when $\Delta = 1$ which gives the relative error of $\frac{4}{3H}$ for F_x. Although the frequently used momentum exchange method is a natural choice for the force evaluation in conjunction with the bounce-back boundary condition for $\Delta = 1/2$, one must be aware of that this method is not exact and the error in the force evaluation using the momentum exchange method depends on Δ and the resolution.

The error in F_x is due to the fact that the derivatives of the velocity field are not considered in the boundary conditions. This can be understood by analyzing Eq. (16a). At the steady state, and with the approximation that

$$\tilde{f}_\alpha \approx f_\alpha^{(\text{eq})} + f_\alpha^{(1)} = f_\alpha^{(\text{eq})} - \frac{1}{\tau} w_\alpha \rho \frac{3}{c^2}(\boldsymbol{e}_\alpha \cdot \boldsymbol{\nabla})(\boldsymbol{e}_\alpha \cdot \boldsymbol{u}) , \tag{21}$$

Equation (16a) at the top wall becomes

$$F_x \approx 2 w_2 \rho \frac{3}{c^2} \boldsymbol{e}_2 \cdot (\boldsymbol{u}_{bf} + \boldsymbol{u}_f - 2\boldsymbol{u}_w) , \tag{22}$$

where the substitution of Eq. (10) for $\tilde{f}_6$ and $\tilde{f}_8$ has been made. The only term in the above equation which has Δ dependence is $\boldsymbol{u}_{bf}$. When $0 \leq \Delta$ 1/2, F_x is independent of Δ, and when $1/2 \leq \Delta < 1$, F_x weakly depends on Δ because $\boldsymbol{u}_w = 0$ in this case [see Eqs. (9)]. In the case where F_x is obtained by summing over a set of symmetric lattice points, cancellations in the summation may further weaken the dependence of F_x on Δ.

Table I also shows that for the shear stress based on taking the derivative of the velocity, the loss of accuracy is quite significant for small values of Δ (≤ 0.05) for $\tau = 0.6$. For other values of Δ (≥ 0.3), the accuracy is comparable with that of F_x. However, as shown in Fig. 5(a), the accuracy of $\rho\nu\frac{du_x}{dy}|_{y=H}$ based on the near-wall velocity derivative deteriorates as the relaxation time τ increases (from 0.51 to 1.6). To see the cause of the increasing error in $\rho\nu\frac{du_x}{dy}|_{y=H}$, Fig. 5(b) shows dimensionless wall velocity, u_w/u_c, obtained by a three-point second-order Lagrangian extrapolation of the near wall velocity $u_x(y)$ as a function of τ. The increasing slip velocity u_w on the wall with the increasing relaxation time τ was also observed in Ref. [16]. It is the result of increasing particle mean free path that causes the deviation of the kinetic solution from the hydrodynamic solution. It is clear that the poor performance of $\rho\nu\frac{du_x}{dy}|_{y=H}$ is associated with the increasing error in the near wall velocity profile as τ increases. Since the stress tensor τ_{ij} can be calculated directly from f_α [see Eq. (13)] without the need for directly computing velocity derivatives, the force evaluation method based on the evaluation of the velocity gradient in the form of Eq. (12) is not recommended.

B Steady uniform flow over a column of cylinders

For a uniform flow over a column of circular cylinders of radius r and center-to-center distance H (see the left part of Fig. 9 for illustration), symmetry conditions for f_α's are imposed at $y = \pm H/2$. Most of the details of flow field simulation can be found in Ref. [1]. The Reynolds number is defined by the diameter of the cylinder d as $\mathrm{Re} = Ud/\nu$, where U is the uniform velocity in the inlet. It must be noted that for a consistent determination of the force, the upstream boundary must be placed far upstream. A shorter distance between the cylinder and the boundary will result in higher drag. In this study, it is placed at about 20 radii to the left of the center of the cylinder. Reducing the distance between boundary and the cylinder to 12.5 radii while keeping the rest of the computational parameters fixed would increase the drag coefficient by about 1.8% at $\mathrm{Re} = 100$. The downstream boundary is located about 25 – 30 radii behind the cylinder to allow sufficient wake development. The

simulation is terminated when the following criterion based on the relative L_2-norm error in the fluid region Ω is satisfied,

$$E_2 = \sqrt{\frac{\sum_{\boldsymbol{x}_i \in \Omega} \|\boldsymbol{u}(\boldsymbol{x}_i, t+1) - \boldsymbol{u}(\boldsymbol{x}_i, t)\|^2}{\sum_{\boldsymbol{x}_i \in \Omega} \|\boldsymbol{u}(\boldsymbol{x}_i, t+1)\|^2}} \leq \epsilon \,. \tag{23}$$

In this case, $\epsilon = 10^{-6}$ was chosen for both Re = 10 and 100.

Following Fornberg [26], the drag coefficient over a circular cylinder of radius r is defined as

$$C_D = \frac{|F_x|}{\rho U^2 r} \,. \tag{24}$$

Figure 6(a) compares C_D obtained from: momentum exchange method, surface stress integration, and finite difference result of Fornberg [26] using a vorticity-stream function formulation at Re = 100, $H/r = 20$, and radius r ranging from 2.8 to 13.2. For $r > 8$, both methods of momentum exchange and the stress integration give satisfactory results for C_D in comparison with the value of 1.248 given in Ref. [26]. This adds credence to the validity of Eq. (15) for evaluating the total force on a body. The values of C_D from the momentum exchange method have a little less variation than that from the stress integration. Accepting an error of less than 5%, the reliable data for C_D can be obtained, using the momentum exchange method, for $r > 5$. That is, 10 lattices cross the diameter of the cylinder are necessary to obtain reliable values of the force. This is consistent with the finding by Ladd [15]. In the range of $5 < r < 7$, the stress integration method gives more scattered result than the method of momentum exchange. For smaller radius, i.e., coarser lattice resolution, while both methods give poor results (due to insufficient resolution), the stress integration yields much larger errors.

Figure 6(b) compares C_D obtained from the methods of momentum exchange and the stress integration for Re = 10. The momentum exchange method seems to gives a converged result at larger r (> 8). Based on the data for $r > 8$, an average values of $C_D \approx 3.356$ is obtained. In contrast, the stress integration method has a larger scattering than the large r result from the momentum exchange method even for $r > 8$. Averaging over the results

for $r > 8$, the stress integration gives $C_D \approx 3.319$. The difference between converged results of two methods is about 1%. For r less than or around 5, the scattering in C_D from the stress integration method is much larger than that in the momentum exchange method. The conclusions from the comparisons in Fig. 6 are as follows: (i) both methods for force evaluation can give accurate results; (ii) the momentum exchange method gives more consistent drag; and (iii) in the range of $10 < \mathrm{Re} < 100$, a resolution of 10 lattices across the diameter of the cylinder are needed in order to obtain consistent and reliable drag values. In other words, the lattice (grid) Reynolds number Re^* should be less than 10 in the calculations.

In the above results presented in Figs. 6(a) and 6(b), the center of the cylinder is placed on a lattice grid thus the computational mesh is symmetric with respect to the geometry of the cylinder. To test the effect of the mesh symmetry on the accuracy of the force evaluation, the calculation of the flow at $\mathrm{Re} = 10$ is repeated with different values of the cylinder center offset Δ_x in x direction, or Δ_y in y direction. The radius of the cylinder is deliberately chosen to be only 6.4 lattice grids. In order to preserve the mirror symmetry of the flow in y-direction, we use different boundary conditions for upper and lower boundaries (at $y = \pm H$). For $\Delta_x = 0$ while varying Δ_y, we use the periodic boundary conditions at $y = \pm H$. For $\Delta_y = 0$ while varying Δ_x, we use the symmetric boundary conditions. The results of the drag coefficient C_D are presented in Table II. The variation of C_D due to the change of the center of cylinder offset from a grid point is less than 1%. We notice that the variation in C_D due to Δ_y is larger than that due to Δ_x. This is precisely because of the asymmetry of the mesh due to $\Delta_y \neq 0$, while the offset in x-direction maintains the flow symmetry in y-direction. This asymmetry due to $\Delta_y \neq 0$ results in the change of the lift coefficient from $O(10^{-12})$ to $O(10^{-3})$. It is our observation that the accuracy of the force evaluation schemes used here is dictated by that of the boundary conditions at the solid walls. The error due to the symmetry of the computational mesh with respect to the geometry of an object is well bounded. This is also observed in other independent studies [27, 28].

It is worth noting that the wall shear stress in the channel flow obtained by using the

method of momentum exchange has a relative error proportional to the resolution across the channel. For a resolution of 10 – 20 lattices across the diameter considered here, the relative error in the drag appears, however, smaller than in the channel flow case. At Re = 100, with $r > 10$, the average value of the drag obtained by using the method of momentum method has a 1.7% relative error comparing with Fornberg's data [26]. If the boundary layer thickness is estimated roughly to be $3 \times 2r/\sqrt{\mathrm{Re}} \approx 6$, there are only about 6 lattices across the boundary layer over which the velocity profile changes substantially. Based on the insight from the channel flow result, it is possible that the deviatoric shear stresses on the surface of the cylinder that are effectively incorporated in the method of momentum exchange suffer comparable level of error as in the channel flow. The effective error cancellation over the entire surface of the body may have contributed to the good convergence behavior in the drag shown in Figs. 6(a) and 6(b).

C Flow over an asymmetrically placed circular cylinder in channel with vortex shedding

Schäfer and Turek [29] reported a set of benchmark results for a laminar flow over a circular cylinder of radius r that is asymmetrically placed inside a channel. In the present study, $r = 12.8$ is used and the center of the cylinder coincides with a grid point. The distance from the center of the cylinder to the upper wall and lower wall is $h_+ = 4.2r$ and $h_- = 4.0r$, respectively. This results in $\Delta_+ = 0.76$ for the upper wall and $\Delta_- = 0.2$ for the lower wall, respectively. The channel inlet has a parabolic profile and it is placed at 4 radii upstream of the cylinder center according to the specification of the benchmark test [29]. This results in $\Delta = 0.2$ for the inlet boundary. A zeroth-order extrapolation for f_α is used at the exit boundary which is located 40 radii downstream of the cylinder center. Thus there are a total of 564×105 square lattices in the flow field. For $\mathrm{Re} = 2r\bar{U}/\nu = 100$ based on the average inlet velocity $\bar{U}$, the use of relaxation time $\tau = 0.55$ requires $\bar{U} = 0.095$.

At this Reynolds number, the flow becomes unsteady and periodic vortex shedding is

observed. Figures 7(a) and 7(b) compare the lift coefficient

$$C_L = \frac{F_y}{\rho \bar{U}^2 r},$$

and the drag coefficient C_D [see Eq. (24)] with the benchmark results in Ref. [29]. We first note that the present numerical value of Strouhal number $\mathrm{St} = 2r/\bar{U}T$ is 0.300, where T is the period of the lift curve. This agrees very well with the range of C_L values (0.2995 – 0.305) given in Ref. [29]. We note that the difference in $C_L(t)$ between the momentum exchange method and the surface stress integration method is indiscernible graphically. For the drag coefficient $C_D(t)$, it is interesting to note that although there is about 0.25% difference between the results given by momentum exchange method and the surface stress integration method, both methods of force evaluation give two peaks in the $C_D(t)$ curves. Physically, these two peaks in $C_D(t)$ curve correspond to the existence of a weaker vortex and a stronger vortex alternately shed behind the cylinder. The difference in the strength of the vortices results from the difference: $h_+/r = 4.2$ and $h_-/r = 4.0$ in the passages between the cylinder and the channel walls. There is no report on the occurrence of these two peaks in Ref. [29]. Instead, a range of the maximum C_D (from 3.22 to 3.24) by different researchers was given. The present value of the higher peak is well within the range. A further refined computation of the present problem using a multi-block procedure [30] with $r = 40$ in the fine grid region yield nearly the same results for $C_D(t)$ and $C_L(t)$.

D Pressure driven flow in a circular pipe

The steady state flow field was obtained by using D3Q19 model with $\tau = 0.52$ [2]. Eq. (15) is used to evaluate the force on the boundary points along the circumference of the pipe over a distance of one lattice in the axial direction. The resulting axial force, F_x, is, equivalently, the force given by $\tau_w(2\pi r \delta_x)$ where τ_w is the wall shear stress and r is the pipe radius. For a fully developed flow inside a circular pipe, the exact fluid shear stress at the pipe wall is given by

$$\tau_w^{\text{exact}}(2\pi r) = \pi r^2 \frac{dp}{dx}. \tag{25}$$

We examine the normalized axial force,

$$\eta = \frac{F_x}{\pi r^2 \frac{dp}{dx}} . \tag{26}$$

Figure 8 shows the normalized coefficient η over a range of r: 3.5 – 23.5. Except for $r \leq 5$, η is rather close to 1. It was noticed in Ref. [2] that the accuracy of LBE solution for the pipe flow is not as good as that for the two-dimensional channel flow due to the distribution of values of Δ around the pipe. The accuracy of the drag is dictated by the accuracy of the flow field if the force evaluation method is exact. For the pipe flow, the error in F_x results from the inaccuracy in the flow field and the errors in the force evaluation scheme based on momentum exchange (as seen in the previous section for the two-dimensional channel flow case). For $r > 5$, the largest error in F_x is about 3.5% and it occurs at $r = 15.5$. Again, there is no systematic error in F_x. Given the complexity of the boundary in this three-dimensional flow, the results shown in Fig. 8 are satisfactory in the sense that it adds further credence to the momentum exchange method for force evaluation.

E Steady uniform flow over a sphere

To limit the computational effort, a finite domain of $-H/2 \leq y \leq H/2$ and $-H/2 \leq z \leq H/2$, with $H/r = 10$ is used to compute the flow past a sphere of radius r (see Fig. 9). Two cases are considered: (a) the flow past a single sphere, and (b) the flow over an two-dimensional array of spheres (all located at $x = 0$) with the center of the spheres forming square lattices. In the former case, the boundary conditions at $j_y = 1$ ($y = H/2$ corresponds to $j_y = 2$) for f_α's are given by the following linear extrapolation

$$f_\alpha(j_x, 1, j_z) = 2\, f_\alpha(j_x, 2, j_z) - f_\alpha(j_x, 3, j_z) . \tag{27}$$

The velocity at $j_y = 2$ is set as

$$\boldsymbol{u}(j_x, 2, j_z) = \boldsymbol{u}(j_x, 3, j_z) . \tag{28}$$

Similar treatment is applied at $y = H/2$ and $z = \pm H/2$. In the latter case, symmetry conditions are posed on f_α's at $j_y = 1$ by using the values of f_α's at $j_y = 3$ (see Ref. [1] for

the two-dimensional case). At the inlet, a uniform velocity profile is imposed at $j_x = 1.5$ (half way between the first and second lattices). The upstream boundary is located at 7.5 radii to the left of the sphere center in all simulations.

For flow over a sphere, the drag coefficient is often expressed as

$$C_D = -\frac{F_x}{\frac{1}{2}\rho U^2 \pi r^2} = \frac{24}{\mathrm{Re}}\phi, \quad \phi = -\frac{F_x}{6\pi r U \rho \nu}, \tag{29}$$

where ϕ accounts for the non-Stokesian effect of the drag. For two types of the boundary conditions at ($y = \pm H/2$ and $z = \pm H/2$), ϕ_s denotes the non-Stokesian correction for the case where the symmetry conditions are imposed at ($y = \pm H/2$ and $z = \pm H/2$) and ϕ_∞ denotes the results for the case where the extrapolation for f_α is used at ($y = \pm H/2$ and $z = \pm H/2$) in order to simulate the unbounded flow.

Figure 10(a) shows the non-Stokesian coefficient ϕ_∞ for $r = 3.0$, 3.2, 3.4, 3.6, 3.8, 4.0, 5.1, 5.2, 5.4, 5.6 and 5.8, for $H/r = 10$ at $\mathrm{Re} = 10$. The relaxation time is $\tau = 0.7$. With this range of r, the number of the boundary nodes on the surface of the sphere increases roughly by a factor of $(5.8/3)^2 \approx 3.74$; the actual counts of the boundary nodes $\boldsymbol{x}_b$ gives a ratio $2370/546 = 4.35$. The largest difference is 1.9% between $r = 3.0$ and $r = 3.2$ which have the least resolution in the cases investigated. For a uniform flow over an unbounded sphere, an independent computation using finite difference method based on the vorticity-stream function formulation with high resolution gives a drag coefficient $\phi \approx 1.7986$ at $\mathrm{Re} = 10$. The largest difference between this result and the LBE results is 1.36% at $r = 3.2$. If the LBE data for the drag is averaged over the range of r, one obtains $\phi \approx 1.8086$ which differs from 1.7986 by 0.54%. Hence, the LBE solutions based on $3.0 \leq r \leq 5.8$ give quite consistent drag force. Figure 10(b) shows the non-Stokesian correction factor ϕ_s for a uniform flow over a planar array of spheres for $3.0 \leq r \leq 5.8$ and $H/r = 10$, at $\mathrm{Re} = 10$. It is important to note that with the improvement of the surface resolution by a factor of 4.35, there is little systematic variation in $\phi_s(r)$. The largest deviation from the average value, $\bar{\phi}_s \approx 1.963$, is 1.1% at $r = 5.0$. It is clear that the LBE solution gives reliable fluid dynamic force on a sphere at $r \approx 3.5$ for a moderate value of Re. The set of data for ϕ_s is inherently more consistent than that for ϕ_∞ since the symmetry boundary condition can be exactly specified

at $y = \pm H/2$ and $z = \pm H/2$, while the extrapolation conditions given by Eqs. (27) and (28) do not guarantee the free stream condition at $y = \pm H/2$ and $z = \pm H/2$. Yet, both ϕ_∞ and ϕ_s exhibit remarkable self-consistency from coarse to not-so-coarse resolutions.

IV. CONCLUSIONS

Two methods for evaluating the fluid force in conjunction with the method of lattice Boltzmann equation for solving fluid flows involving curved geometry have been examined. The momentum exchange method is very simple to implement. It is shown in the channel flow simulation that momentum exchange method is not an exact method. The error in the wall shear stress is inversely proportional to the resolution. In two- and three-dimensional flows over a bluff body, it can give accurate drag value when there are at least 10 lattices across the body at Re $\sim$ 100. The method of integrating the stresses on the surface of the body gives similar result when there is sufficient resolution but a much larger uncertainty exists when the resolution is limited in comparison with the method of momentum exchange. In addition, this method requires considerably more efforts in implementing the extrapolation and integration on the body surface in comparison with the method of momentum exchange. The method of momentum exchange is thus recommended for force evaluation on curved bodies.

This work is supported by NASA Langley Research Center. R. Mei also acknowledges partial support of the Engineering Research Center (ERC) for Particle Science and Technology at the University of Florida, the National Science Foundation (EEC-9402989), and Industrial partners of the ERC.

APPENDIX A: LBE MODELS IN TWO AND THREE DIMENSIONS

The nine-velocity (or 9-bit) LBE model on a two-dimensional square lattice, denoted as the D2Q9 model, has been widely used for simulations of two-dimensional flows. For three-dimensional flows, there are several cubic lattice models, such as the fifteen-velocity (D3Q15), nineteen-velocity (D3Q19), and twenty-seven-velocity (D3Q27) models, which have been

used in the literature [12]. All these models have a rest particle (with zero velocity) in the discretized velocity set $\{\boldsymbol{e}_\alpha|\alpha = 0,\ 1,\ \ldots,\ ,\ (b-1)\}$. For athermal fluids, the equilibrium distributions for the D2Q9, D3Q15, D3Q19, and D3Q27 models are all of the following form [8, 9]

$$f_\alpha^{(\mathrm{eq})} = w_\alpha \rho \left[1 + \frac{3}{c^2}(\boldsymbol{e}_\alpha \cdot \boldsymbol{u}) + \frac{9}{2c^4}(\boldsymbol{e}_\alpha \cdot \boldsymbol{u})^2 - \frac{3}{2c^2}\boldsymbol{u}^2\right], \tag{A1}$$

where w_α is a weighting factor and $\boldsymbol{e}_\alpha$ is a discrete velocity, $c \equiv \delta_x/\delta_t$ is the unit speed, and δ_x and δ_t are the lattice constant and the time step, respectively. The discrete velocities for the D2Q9 models are

$$\boldsymbol{e}_\alpha = \begin{cases} (0,\ 0), & \alpha = 0 \\ (\pm 1,\ 0)\,c,\ (0,\ \pm 1)\,c, & \alpha = 1,\ 3,\ 5,\ 7 \\ (\pm 1,\ \pm 1)\,c, & \alpha = 2,\ 4,\ 6,\ 8, \end{cases} \tag{A2}$$

and the values of the weighting factor w_α are

$$w_\alpha = \begin{cases} \frac{4}{9}, & \alpha = 0 \\ \frac{1}{9}, & \alpha = 1,\ 3,\ 5,\ 7 \\ \frac{1}{36}, & \alpha = 2,\ 4,\ 6,\ 8. \end{cases} \tag{A3}$$

For the D3Q19 model, the discrete velocities are

$$\boldsymbol{e}_\alpha = \begin{cases} (0,\ 0), & \alpha = 0 \\ (\pm 1,\ 0,\ 0)\,c,\ (0,\ \pm 1,\ 0)\,c,\ (0,\ 0,\ \pm 1)\,c, & \alpha = 1\text{–}6 \\ (\pm 1,\ \pm 1,\ 0)\,c,\ (0,\ \pm 1,\ \pm 1)\,c,\ (\pm 1,\ 0,\ \pm 1)\,c, & \alpha = 7\text{–}18\,, \end{cases} \tag{A4}$$

and the weighting factor w_α is given by [9]

$$w_\alpha = \begin{cases} \frac{1}{3}, & \alpha = 0 \\ \frac{1}{18}, & \alpha = 1\text{–}6 \\ \frac{1}{36}, & \alpha = 7\text{–}18\,. \end{cases} \tag{A5}$$

The discrete velocity sets $\{\boldsymbol{e}_\alpha\}$ for the D2Q9 and D3Q19 models are shown in Fig. 1.

The density and velocity can be computed from f_α:

$$\rho = \sum_\alpha f_\alpha = \sum_\alpha f_\alpha^{(\mathrm{eq})}, \tag{A6a}$$

$$\rho \boldsymbol{u} = \sum_\alpha \boldsymbol{e}_\alpha f_\alpha = \sum_\alpha \boldsymbol{e}_\alpha f_\alpha^{(\mathrm{eq})}. \tag{A6b}$$

The speed of sound of the above LBE models is

$$c_s = \frac{1}{\sqrt{3}} c$$

and the equation of state is that of an ideal gas such that

$$p = c_s^2 \rho \,. \tag{A7}$$

The viscosity of the fluid is

$$\nu = c_s^2 \lambda$$

for the discrete velocity model of Eq. (2). It should be noted that the equilibrium distribution function $f_\alpha^{(\mathrm{eq})}$ is in fact a Taylor series expansion of the Maxwellian $f^{(0)}$ [8, 9]. This approximation of $f_\alpha^{(\mathrm{eq})}$ in algebraic form by making the LBE method valid only in the incompressible flow limit $u/c \to 0$.

Equation (2) is often discretized in space $\boldsymbol{x}$ and time t into the lattice Boltzmann equation

$$f_\alpha(\boldsymbol{x}_i + \boldsymbol{e}_\alpha \delta_t, t + \delta_t) - f_\alpha(\boldsymbol{x}_i, t) = -\frac{1}{\tau}[f_\alpha(\boldsymbol{x}_i, t) - f_\alpha^{(\mathrm{eq})}(\boldsymbol{x}_i, t)] \,, \tag{A8}$$

where $\tau = \lambda/\delta_t$. For this LBGK model [3, 4], the viscosity in the Navier-Stokes equation derived from the above lattice Boltzmann equation is

$$\nu = \left(\tau - \frac{1}{2}\right) c_s^2 \, \delta_t \,. \tag{A9}$$

The $-1/2$ correction in the above formula for ν comes from the second order derivatives of f_α when $f_\alpha(\boldsymbol{x}_i + \boldsymbol{e}_\alpha \delta_t, t + \delta_t)$ in Eq. (A8) is expanded in a Taylor series in $\boldsymbol{u}$. This correction in ν makes the lattice Boltzmann method formally a second order method for solving incompressible flows [9]. Obviously, the physical and computational stabilities require that $\tau > 1/2$.

REFERENCES

[1] R. Mei, L.-S. Luo, and W. Shyy, J. Comput. Phys. **155**, 307 (1999).

[2] R. Mei, W. Shyy, D. Yu, and L.-S. Luo, J. Comput. Phys. **161**, 680 (2000).

[3] H. Chen, S. Chen, and W.H. Matthaeus, Phys. Rev. A **45**, R5339 (1992).

[4] Y.H. Qian, D. d'Humires, P. Lallemand, Europhys. Lett. **17**, 479 (1992).

[5] R. Benzi, S. Succi, and M. Vergassola, Phys. Rep. **222**, 145 (1992).

[6] S. Chen and G.D. Doolen, Ann. Rev. Fluid Mech. **30**, 329 (1998).

[7] P.L. Bhatnagar, E.P. Gross, and M. Krook, Phys. Rev. **94**, 511 (1954).

[8] X. He and L.-S. Luo, Phys. Rev. E **55**, R6333 (1997).

[9] X. He and L.-S. Luo, Phys. Rev. E **56**, 6811 (1997).

[10] T. Abe, J. Comput. Phys. **131**, 241 (1997).

[11] X. Shan and X. He, Phys. Rev. Lett. **80**, 65 (1998).

[12] Y.H. Qian, S. Succi, S.A. Orszag, in *Annual Reviews of Computational Physics*, Vol. III, edited by D. Stauffer, (World Scientific, Singapore, 1995).

[13] D.P. Ziegler, J. Stat. Phys. **71**, 1171 (1993).

[14] I. Ginzbourg and P.M. Alder, J. Phys. II France **4**, 191 (1994).

[15] A.J.C. Ladd, J. Fluid Mech. **271**, 311 (1994).

[16] D.R. Noble, S. Chen, J.G. Georgiadis, and R.O. Buckius, Phys. Fluid **7**, 203 (1995).

[17] O. Behrend, Phys. Rev. E. **52**, 1164 (1995).

[18] S. Chen, D. Martínez, and R. Mei, Phys. Fluids **8**, 2527 (1996).

[19] X. He, Q. Zou, L.-S. Luo, and M. Dembo, J. Stat. Phys. **87**, 115 (1997).

[20] L.-S. Luo, J. Stat. Phys. **88**, 913 (1997).

[21] Q. Zou and X. He, Phys. Fluids **9**, 1591 (1997).

[22] R. Mei and W. Shyy, J. Comput. Phys. **143**, 426 (1998).

[23] X. He and G. Doolen, J. Comput. Phys. **134**, 306 (1997).

[24] O. Filippova and D. Hänel, J. Comput. Phys. **147**, 219 (1998).

[25] O. Filippova (private communication).

[26] B. Fornberg, J. Fluid Mech. **225**, 655 (1991).

[27] M. Bouzidi, Firdaouss, and P. Lallemand, to appear in Phys. Fluids (2001).

[28] D. d'Humières, M. Bouzidi, and P. Lallemand, to appear in Phys. Rev. E **63**, 066702 (2001).

[29] M. Schäfer and S. Turek, in *Notes in Numerical Fluid Mechanics*, Vol. 52, (Vieweg

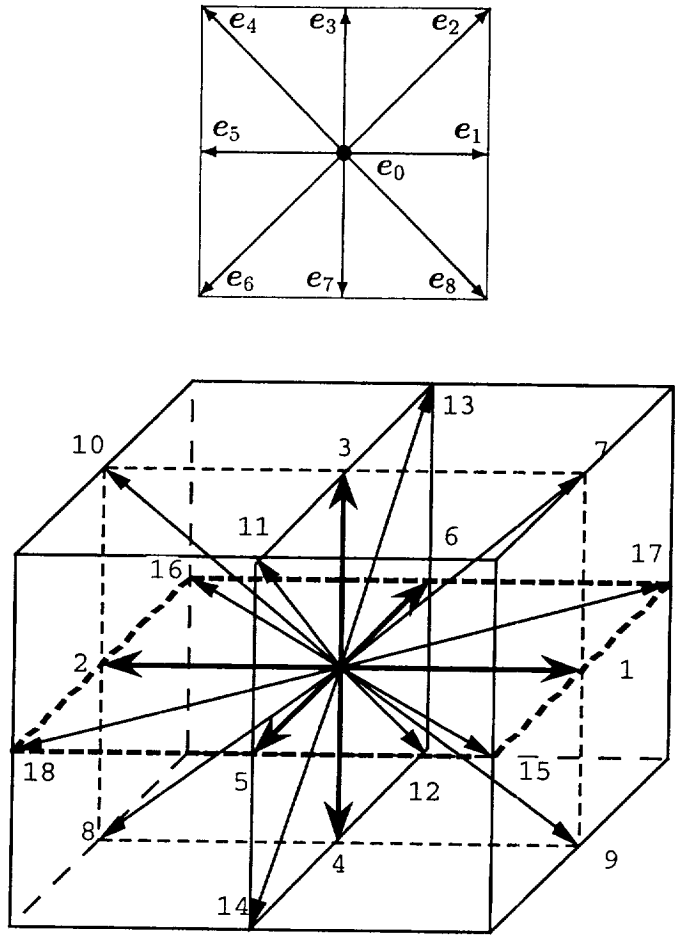

FIG. 1: Discrete velocity set $\{e_\alpha\}$. (top) Two-dimensional nine-velocity (D2Q9) model. (bottom) Three-dimensional nineteen-velocity (D3Q19) model.

Verlag, Braunschweig, 1999).

[30] D. Yu, R. Mei, and W. Shyy, submitted to J. Comput. Phys. (2000).

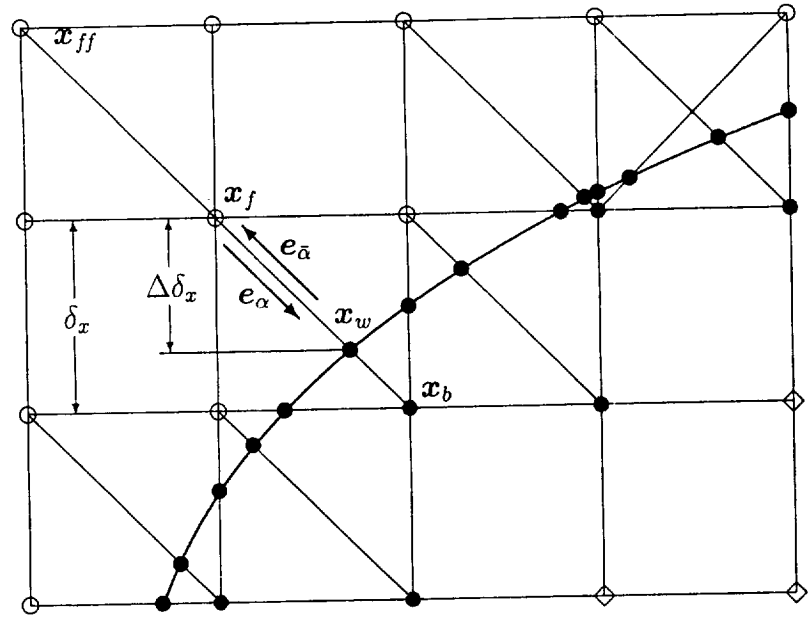

FIG. 2: Layout of the regularly spaced lattices and curved wall boundary. The circles (○), discs (●), shaded discs (●), and diamonds (◇) denote fluid nodes, boundary locations ($\boldsymbol{x}_w$), solid nodes which are also boundary nodes ($\boldsymbol{x}_b$) inside solid, and solid nodes, respectively.

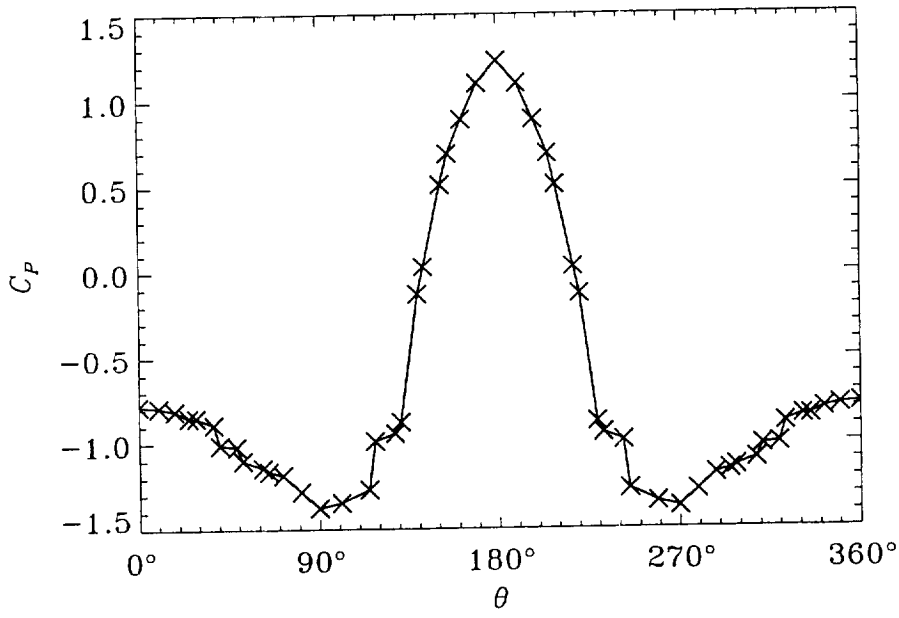

FIG. 3: Distribution of the pressure coefficient C_P on the surface of a 2D circular cylinder of radius $r = 6.6$, and center-to-center distance $H/r = 10$. The stanation point is located at $\theta = 180°$. The result is obtained with $\tau = 0.6$ and $\mathrm{Re} = 40$.

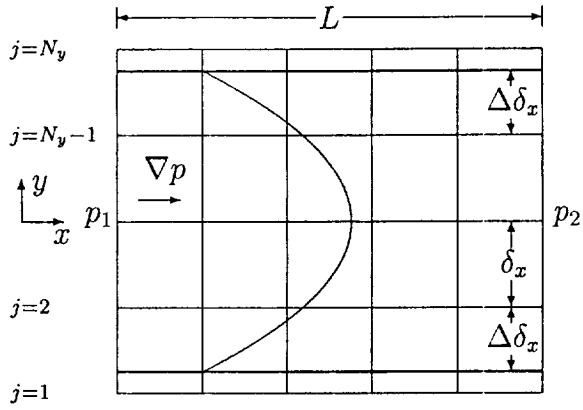

FIG. 4: The channel flow configuration in the LBE simulations with an arbitrary Δ.

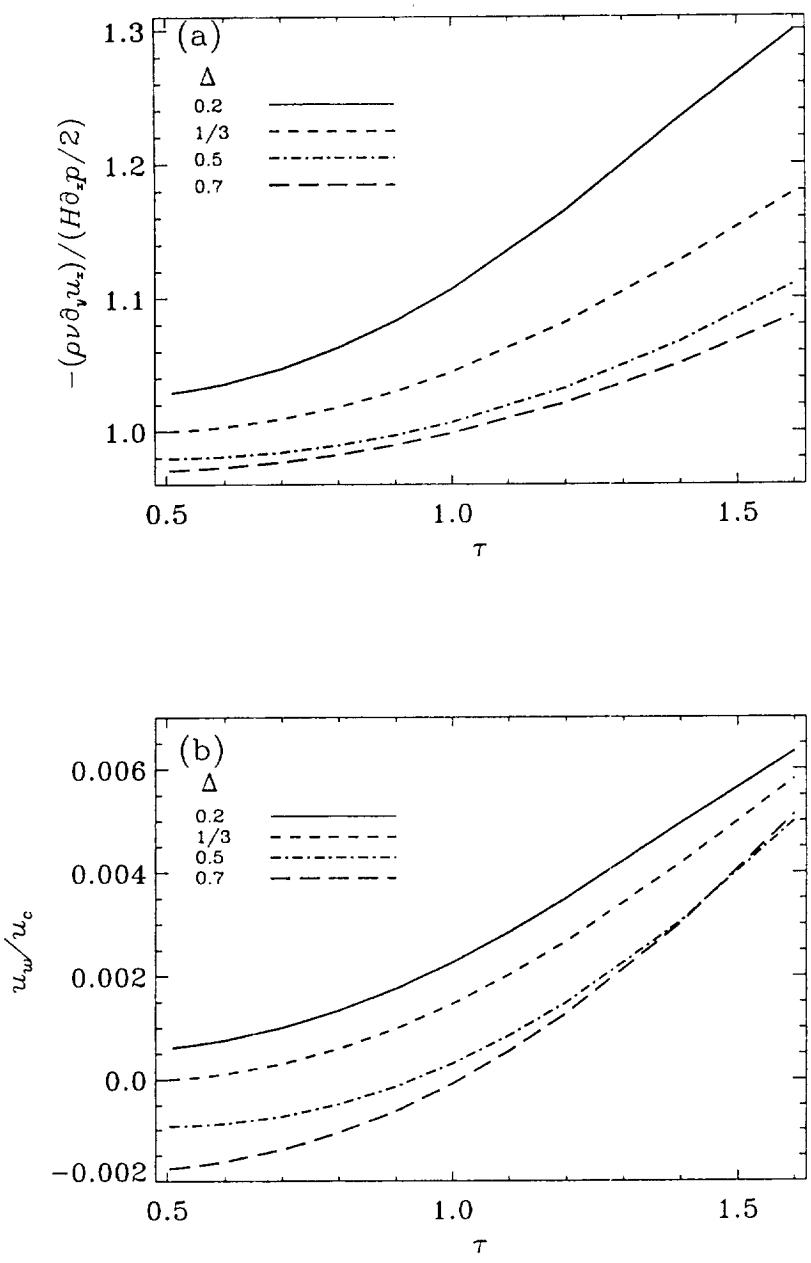

FIG. 5: The LBE simulations of the channel flow, with $\Delta = 0.2$, 1/3, 0.5, and 0.7. The pressure drop is $\partial_x p = -1.0 \times 10^{-6}$ in lattice units. (a) Ratio between the wall force, $\rho\nu\partial_y u_x|_{y=H}$, evaluated by using Eq. (18), and the exact value $-\tau_{xy,w}^{\text{exact}} = -H\partial_x p/2$, given by Eq. (19) as a function of τ. (b) Normalized wall slip velocity u_w/u_c as a function of τ.

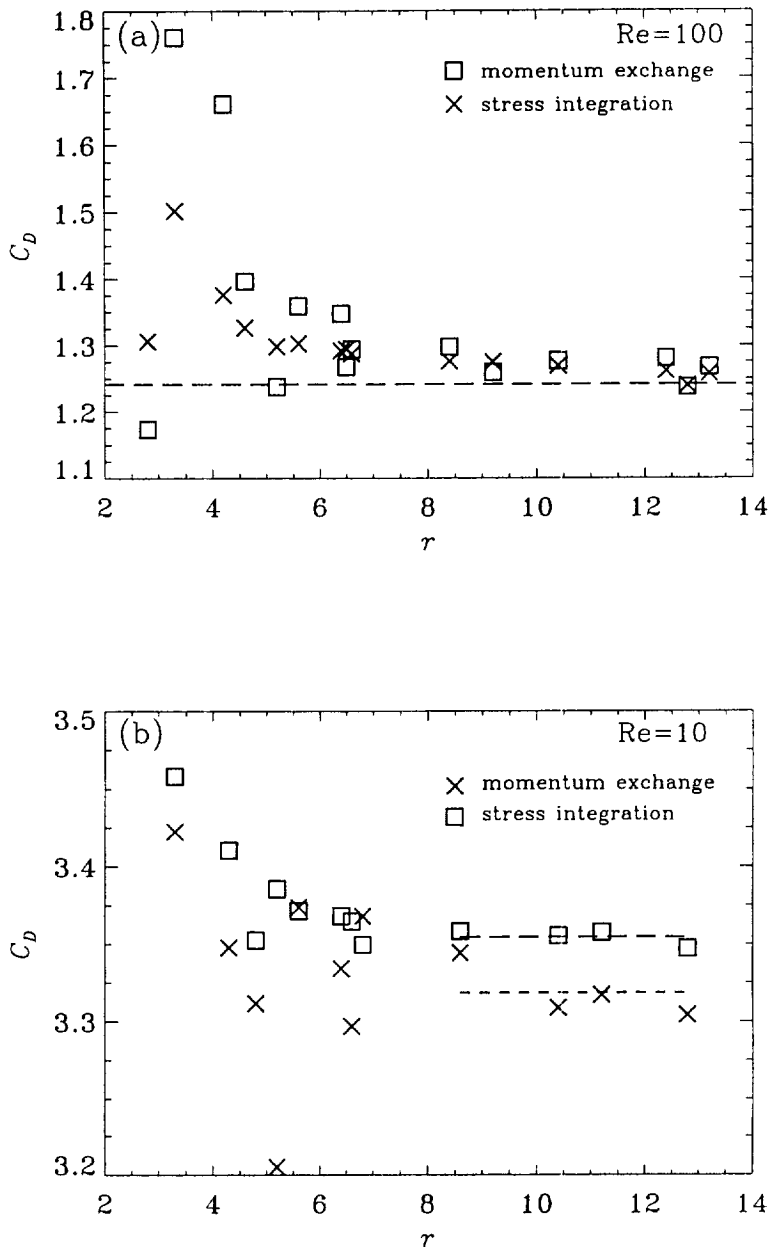

FIG. 6: The drag coefficient for a uniform flow past a column of cylinders over a range of radius r. (a) Re = 100. The dashed line indicate the C_D value of Ref. [26] ($C_D = 1.242$); and (b) Re = 10. The dashed lines indicate the values of C_D averaged over 4 largest radii.

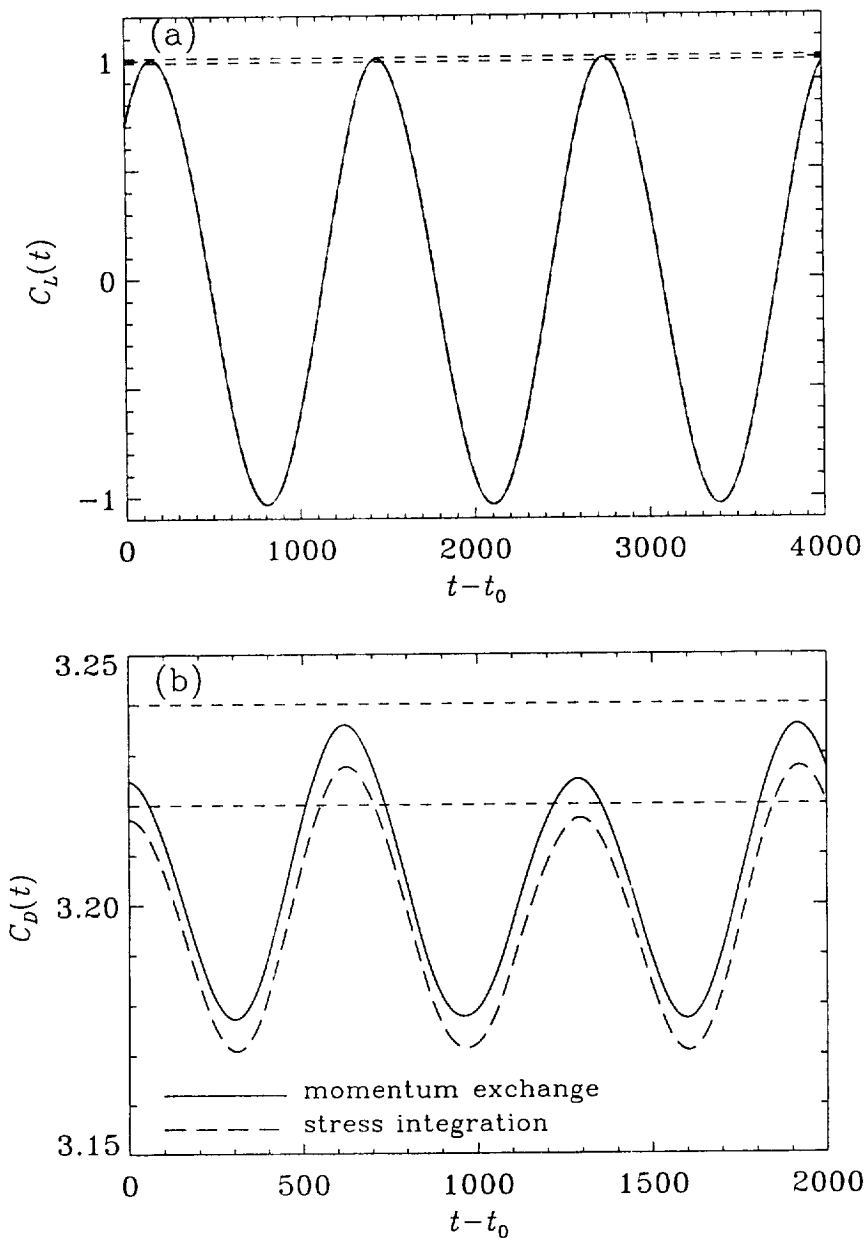

FIG. 7: The 2D flow past a cylinder asymmetrically placed in a channel. The variations of lift and drag coefficients as function of time t (after an initial run time of t_0) are compared with the benchmark results in Ref. [29]. The dashed horizontal lines indicate the upper and lower bounds in Ref. [29]. The solid and dashed curves are the results obtained by using momentum exchange and stress integration, respectively. (a) The lift coefficient $C_L(t)$. Note that the results obtained by using the two methods are indistinguishable on the graph. (b) The drag coefficient $C_D(t)$.

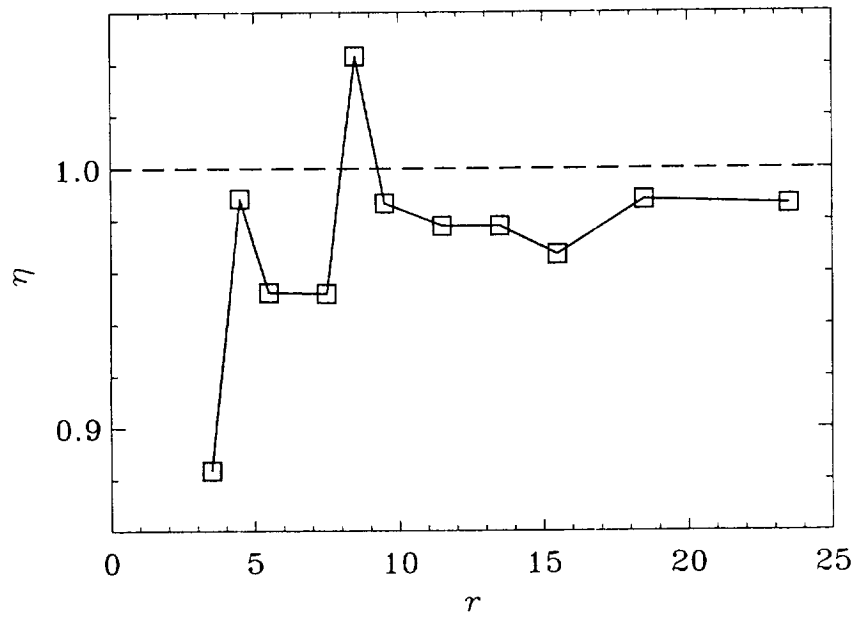

FIG. 8: The ratio η between the tangential force F_x on the pipe and its exact value $(\pi r^2\, dp/dx)$ over a range of pipe radius r.

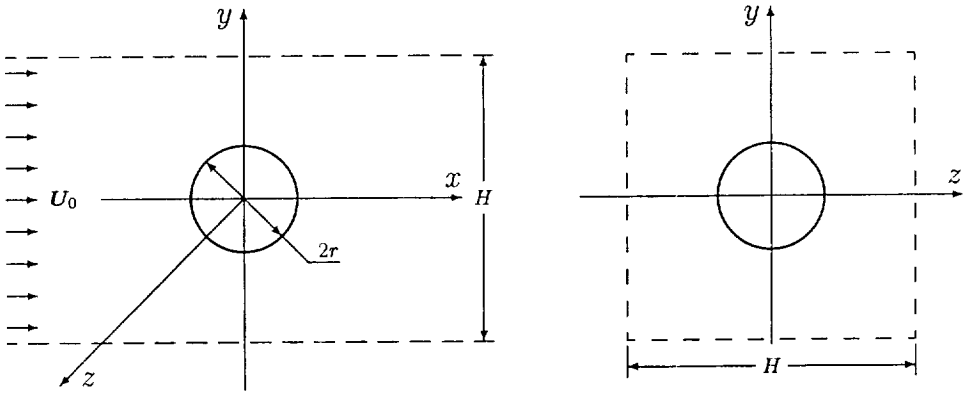

FIG. 9: Computational domain for the uniform flow past a sphere of radius r. The dashed lines indicate boundaries of computational domain. (left) Unbounded domain in xy plane, and (right) bounded domain in yz plane.

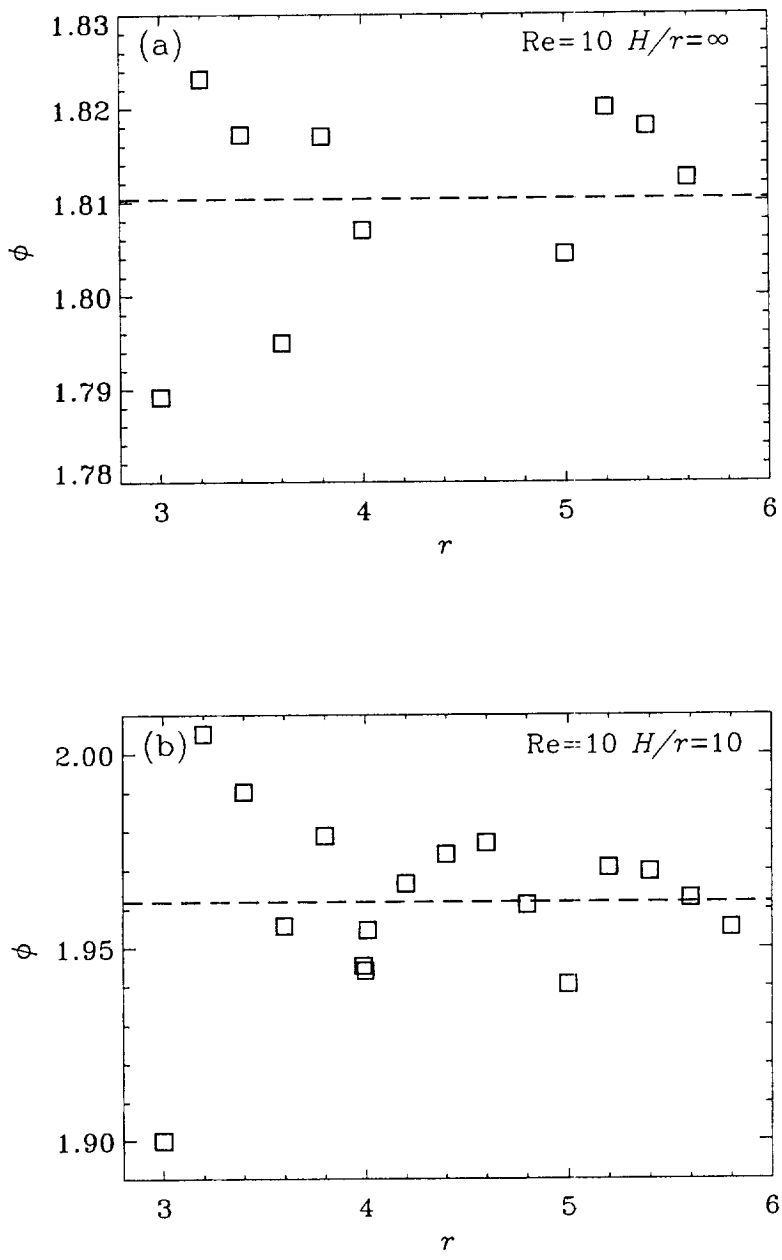

FIG. 10: Flow past sphere. Variation of the non-Stokesian correction factor $\phi = -F_x/6\pi r U \rho\nu$ as a function of sphere radius r at Re $= 10$. The dashed lines are values of $\phi(r)$ averaged over r. (a) The flow past a single sphere in an unbounded field ($H/r = \infty$). (b) The flow past a planer array of spheres ($H/r = 10$).

Δ	$-\tau_{xy,w}^{\text{exact}} \times 10^5$	$-F_x \times 10^5$	$-\tau_{xy,w}^{\text{neq}} \times 10^5$	$-\rho\nu\frac{du_x}{dy}\|_{y=H} \times 10^5$	$-F_y$	p
0.01	1.601	1.6333	1.6010	3.5294	0.3333	0.3333
0.02	1.602	1.6333	1.6020	2.5555	0.3333	0.3333
0.03	1.603	1.6333	1.6030	2.2309	0.3333	0.3333
0.04	1.604	1.6333	1.6040	2.0685	0.3333	0.3333
0.05	1.605	1.6333	1.6050	1.9710	0.3333	0.3333
0.1	1.610	1.6333	1.6100	1.7760	0.3333	0.3333
0.2	1.620	1.6333	1.6200	1.6781	0.3333	0.3333
0.25	1.625	1.6333	1.6250	1.6583	0.3333	0.3333
0.3	1.630	1.6333	1.6300	1.6451	0.3333	0.3333
0.3333	1.633	1.6333	1.6330	1.6385	0.3333	0.3333
0.35	1.635	1.6333	1.6350	1.6357	0.3333	0.3333
0.4	1.640	1.6333	1.6400	1.6285	0.3333	0.3333
0.5	1.650	1.6333	1.6500	1.6184	0.3333	0.3333
0.6	1.660	1.6333	1.6600	1.6214	0.3333	0.3333
0.7	1.670	1.6333	1.6700	1.6244	0.3333	0.3333
0.8	1.680	1.6333	1.6800	1.6274	0.3333	0.3333
0.9	1.690	1.6333	1.6900	1.6305	0.3333	0.3333
0.95	1.695	1.6333	1.6950	1.6321	0.3333	0.3333
0.99	1.699	1.6333	1.6990	1.6335	0.3333	0.3333

TABLE I: Comparison of fluid stresses at $y = H$ in a two-dimensional pressure driven channel flow with $dp/dx = -1.0 \times 10^{-6}$ in the lattice units, $N_y = 35$ and $\tau = 0.6$ as a function of Δ. Column 2, $-\tau_{xy,w}^{\text{exact}}$ given by Eq. (19); Column 3, $-F_x$ given by Eq. (16a); Column 4, $-\tau_{xy,w}^{\text{neq}}$ given by Eq. (17); Column 5, $-\rho\nu\frac{du_x}{dy}|_{y=H}$ Eq. (18); Column 6, $-F_y$ given by Eq. (16b); Column 7, pressure p obtained in the simulation.

$\Delta_x = 0$, periodic BC at $y = \pm H$					
Δ_y	0	0.2	0.4	0.6	0.8
C_D	3.3780	3.3755	3.3576	3.3636	3.3755
$\Delta_y = 0$, symmetric BC in $y = \pm H$					
Δ_x	0	0.2	0.4	0.6	0.8
C_D	3.3745	3.3844	3.3847	3.3838	3.3860

TABLE II: The effect of the symmetry of computational mesh on the force evaluation for the steady uniform flow over a column of cylinders. The Reynolds number Re = 10 ($\tau = 0.7$), and the radius of the cylinder $r = 6.4\delta_x$. The variation of C_D due to the change of the center of cylinder offset from a grid point is less than 1%.

A MULTI-BLOCK LATTICE BOLTZMANN METHOD FOR FLUID FLOWS

Dazhi Yu**, Renwei Mei*, and Wei Shyy†

Department of Aerospace engineering, Mechanics and Engineering Science
University of Florida, Gainesville, FL 32611-6250 USA

ABSTRACT

Compared to Navier-Stokes equation-based approach, the method of lattice Boltzmann Equation (LBE) offers an alternate treatment for fluid dynamics. However the LBE method often employs certain regular lattices to maintain a compact and efficient computational procedure. This limitation makes it difficult to perform flow simulations when there is a need for high resolution near the body and/or there is a far-field boundary. To resolve these difficulties, a multi-block method is developed. In this method, the flow field is divided into blocks. In each block, the grid is uniform and the grid size is chosen according to the desired resolution. In this paper, an accurate interface treatment between neighboring blocks is derived to ensure the continuity of mass, momentum, and stresses across the interface. Several test cases are employed to demonstrate that the present multi-block method can greatly improve the accuracy and computational efficiency.

1. BACKGROUND OF THE LATTICE BOLTZMANN METHOD

Recently, there has been much progress in developing and employing the method of the lattice Boltzmann equation (LBE) [1-3] as an alternative, non-traditional computational technique for solving complex fluid dynamic systems [4-5]. In an NS equation-based macroscopic method for computational fluid dynamics (CFD), the macroscopic variables of interest, such as velocity $\boldsymbol{u}$ and pressure p, are obtained by solving the Navier-Stokes (NS) equations [6-8]. In the LBE approach, one solves the kinetic equation for the particle mass distribution function $f(x,\xi,t)$ and the macroscopic quantities (such as mass density ρ and momentum density $\rho\boldsymbol{u}$) can then be obtained by evaluating the hydrodynamic moments of the distribution function f.

A popular kinetic model is the Boltzmann equation with the single relaxation time approximation [9]:

$$\frac{\partial f}{\partial t} + \boldsymbol{\xi}\cdot\nabla f = -\frac{1}{\lambda}(f - f^{(0)}) \tag{1}$$

where ξ is the particle velocity, $f^{(0)}$ is the equilibrium distribution function (the Maxwell-Boltzmann distribution function), and λ is the relaxation time. The mass density ρ and momentum density $\rho\boldsymbol{u}$ are the hydrodynamic moments of the distribution function f.

To solve for f numerically, Eq. (1) is first discretized in the velocity space ξ using a finite set of velocities $\{\xi_\alpha\}$ without affecting the conservation laws [5, 9-11],

$$\frac{\partial f_\alpha}{\partial t} + \boldsymbol{\xi}_\alpha\cdot\nabla f_\alpha = -\frac{1}{\lambda}(f_\alpha - f_\alpha^{(eq)}) \tag{2}$$

In the above, $f_\alpha(\boldsymbol{x}, t) \equiv f(\boldsymbol{x}, \xi_\alpha, t)$ is the distribution function associated with the direction ξ_α and $f_\alpha^{(eq)}$ is equilibrium distribution function of the α-th discrete velocity. The 9-bit (or 9-velocity) square lattice model, which is also called Q9D2 model (Fig. 1) has been widely used for simulating 2-D flows. For Q9D2 model, we use $\boldsymbol{e}_\alpha$ to denote the discrete velocity set and we have

$$\begin{aligned} &\boldsymbol{e}_0 = 0, \\ &\boldsymbol{e}_\alpha = (\cos((\alpha-1)\pi/4), \sin((\alpha-1)\pi/4)) \\ &\qquad\qquad \text{for } \alpha=1, 3, 5, 7, \\ &\boldsymbol{e}_\alpha = \sqrt{2}(\cos((\alpha-1)\pi/4), \sin((\alpha-1)\pi/4)) \\ &\qquad\qquad \text{for } \alpha=2, 4, 6, 8 \end{aligned} \tag{3}$$

where $c = \delta x/\delta t$, δx and δt are the lattice constant and the time step size, respectively. The equilibrium distributions for Q9D2 model (as well as for some of the 3-D lattice models) are in the form of

$$f_\alpha^{(eq)} = \rho w_\alpha\left[1 + \frac{3}{c^2}(\mathbf{e}_\alpha\cdot\boldsymbol{u})^2 + \frac{9}{2c^4}(\mathbf{e}_\alpha\cdot\boldsymbol{u})^2 - \frac{3}{2c^2}(\boldsymbol{u}\cdot\boldsymbol{u})^2\right] \tag{4}$$

where w_α is the weighting factor given by

$$w_\alpha = \begin{cases} 4/9, & \alpha = 0 \\ 1/9, & \alpha = 1,3,5,7 \\ 1/36, & \alpha = 2,4,6,8. \end{cases} \tag{5}$$

With the discretized velocity space, the density and momentum flux can be evaluated as

$$\rho = \sum_{k=0}^{8} f_\alpha = \sum_{k=0}^{8} f_\alpha^{(eq)} \tag{6a}$$

and

** Graduate student * Associate professor. † Professor and Chair, Associate Fellow AIAA.

$$\rho \boldsymbol{u} = \sum_{k=1}^{8} \boldsymbol{e}_\alpha f_\alpha = \sum_{k=1}^{8} \boldsymbol{e}_\alpha f_\alpha^{(eq)} \qquad (6b)$$

The speed of sound of this model is $c_s = c/\sqrt{3}$ and the equation of state is that of an ideal gas,

$$p = \rho c_s^2 \qquad (7)$$

Equation (2) can be further discretized in space and time. The completely discretized form of Eq. (1), with the time step δt and space step $\boldsymbol{e}_\alpha \delta t$, is:

$$f_\alpha(\boldsymbol{x}_i + \boldsymbol{e}_\alpha \delta t, t + \delta t) - f_\alpha(\boldsymbol{x}_i, t) = -\frac{1}{\tau}[f_\alpha(\boldsymbol{x}_i, t) - f_\alpha^{(eq)}(\boldsymbol{x}_i, t)] \qquad (8)$$

where $\tau = \lambda/\delta t$, and $\boldsymbol{x}_i$ is a point in the discretized physical space. The above equation is the lattice Boltzmann equation [1-3] with Bhatnagar-Gross-Krook (BGK) approximation [9]. The viscosity in the NS equation derived from Eq. (8) is

$$\nu = (2\tau - 1) c_s \delta t \qquad (9)$$

This choice for the viscosity makes formally the LBGK scheme a second order method for solving incompressible flows [10,11]. The positivity of the viscosity requires that $\tau > 1/2$. Equation (8) can be solved as:

collision step:

$$\tilde{f}_\alpha(\boldsymbol{x}_i, t) = f_\alpha(\boldsymbol{x}_i, t) - \frac{1}{\tau}[f_\alpha(\boldsymbol{x}_i, t) - f_\alpha^{(eq)}(\boldsymbol{x}_i, t)] \qquad (10a)$$

streaming step:

$$f_\alpha(\boldsymbol{x}_i + \boldsymbol{e}_\alpha \delta t, t + \delta t) = \tilde{f}_\alpha(\boldsymbol{x}_i, t) \qquad (10b)$$

where ~ denotes the post-collision state of the distribution function. It is noted that the collision step is completely local and the streaming step takes very little computational effort. Equation (10) is explicit, easy to implement, and straightforward to parallelize.

Those inherent advantages of the LBE method require the use of regular lattice (such as a square lattice or hexagonal lattice) and that the lattice spacing be equally distributed. This is in direct contrast to the many finite difference/volume/element methods in which body fitted coordinates can be used and the grid stretching can be easily applied. However, it should be noted that there has also been growing interest in the macroscopic method to employ the Cartesian grid for complex flow problems [12,13]. A challenge of such Cartesian grid approaches is to offer high resolution near the body and to place the outer boundary far away from the body. In order to use the regularly spaced lattice while developing the capability to place the outer boundary far away, it is desirable to divide the computational domain into a number of blocks within which a fixed, constant lattice spacing can be used and Eq. (10) is implemented in each block as in the standard LBE method. Again, such an approach has been actively employed in the macroscopic methods with both Cartesian and curvilinear coordinates.

This paper describes a multi-block strategy for the LBE method. In each block, constant value of $\delta x = \delta y = \delta t$ is used. The information exchange on the interface between the neighboring blocks of different lattice spacing δx for the primary variables f_α's is implemented to ensure the mass conservation and the continuity of stresses between blocks. A lid-driven cavity flow is computed using a single block with uniform grid and the present multi-block method. The results are compared with published benchmark results . A channel flow with a parabolic velocity profile at the inlet over an asymmetrically placed cylinder at Re=100 (based on the average incoming velocity) is computed next using the multi-block method. Finally, flow over NACA0012 airfoil at Re=500-5000 is computed. The present study shows that the multi-block strategy can greatly improve the computational efficiency of the LBE method.

2. BASICS OF THE MULTI-BLOCK STRATEGY IN THE LBE METHOD

To illustrate the basic idea, a two-block system (a coarse and a fine, as shown in Fig. 2) is considered in the derivation for the interfacial information exchange. The ratio of the lattice space between the two-grid system is

$$m = \delta x_c / \delta x_f \qquad (11)$$

For a given lattice size δx, the viscosity of the fluid is

$$\nu = (2\tau - 1)\delta_x c / 6 \qquad (12)$$

In order to keep viscosity ν, and thus Re, the same in the entire flow field involing different lattice sizes, the relation of relaxation times, τ_f on the fine grid and τ_c on the coarse gird, must obey the following relation:

$$\tau_f = \frac{1}{2} + m(\tau_c - \frac{1}{2}) \qquad (13)$$

for $c=1$. To keep the variables and their derivatives continuous on interface between two systems of different grids, consistent, accurate relationship between the two grid systems must be developed.

The Chapman-Enskog expansion gives,

$$f_\alpha(\boldsymbol{x}, t) = f_\alpha^{(eq)}(\boldsymbol{x}, t) + f_\alpha^{(1)}(\boldsymbol{x}, t) + \ldots \qquad (14)$$

$$f_\alpha^{(1)}(\boldsymbol{x}, t) = -\lambda[\frac{\partial f_\alpha^{eq}}{\partial t} + \xi_\alpha \cdot \nabla f_\alpha^{eq}] = -\lambda \frac{D f_\alpha^{(eq)}}{Dt} = -\tau \delta t \frac{D f_\alpha^{(eq)}}{Dt} \qquad (15)$$

It is noted that

$$f_\alpha^{(1)} = f_\alpha - f_\alpha^{(eq)} = f_\alpha^{(non-eq)} \qquad (16)$$

is the non-equilibrium part of the distribution function based on which the deviatoric stresses are evaluated.

The collision step (Eq. (10a)) gives

$$\tilde{f}_\alpha(x_i,t) = (1-\frac{1}{\tau})f_\alpha(x_i,t) + \frac{1}{\tau}f_\alpha^{(eq)}(x_i,t) \quad (17)$$

Sustituting (9) into (17) leads to

$$\tilde{f}_\alpha(x_i,t) = (1-\frac{1}{\tau})f_\alpha^{(eq)}(x_i,t) + f_\alpha^{(1)}(x_i,t) + ...] + \frac{1}{\tau}f_\alpha^{(eq)}(x_i,t)$$

$$= f_\alpha^{(eq)}(x_i,t) + \frac{\tau-1}{\tau}f_\alpha^{(1)}(x_i,t) + ... \quad (18)$$

Denoting the coarse-grid results with superscript c and fine-grid result with superscript f, the post-collision step gives

$$\tilde{f}_\alpha^c = f_\alpha^{(eq,c)} + \frac{\tau_c-1}{\tau_c}f_\alpha^{(1,c)} + ... \quad (19)$$

Similarly,

$$\tilde{f}_\alpha^f = f_\alpha^{(eq,f)} + \frac{\tau_f-1}{\tau_f}f_\alpha^{(1,f)} + ... \quad (20)$$

Since the velocity and density must be continuous on the interface between the two grids and $f_\alpha^{(eq)}$ from equation (4), it is seen that

$$f_\alpha^{(eq,c)} = f_\alpha^{(eq,f)} \quad (21)$$

To maintain the continuity in the deviatoric stresses, in the 2-D case,

$$\tau_{ij} = (1-\frac{1}{2\tau})\sum_{\alpha=1}^{8}[f_\alpha - f_\alpha^{(eq)}](e_{\alpha i}e_{\alpha j} - \frac{1}{2}e_\alpha \cdot e_\alpha \delta_{ij})$$

$$= (1-\frac{1}{2\tau})\sum_{\alpha=1}^{8} f_\alpha^{(non\text{-}eq)}(e_{\alpha i}e_{\alpha j} - \frac{1}{2}e_\alpha \cdot e_\alpha \delta_{ij}) \quad (22)$$

it is obvious that one requires

$$(1-\frac{1}{2\tau_c})\, f_\alpha^{(non\text{-}eq,c)} = (1-\frac{1}{2\tau_f})\, f_\alpha^{(non\text{-}eq,f)} \quad (23)$$

or

$$(1-\frac{1}{2\tau_c})\, f_\alpha^{(1,c)} = (1-\frac{1}{2\tau_f})\, f_\alpha^{(1,f)}$$

or

$$f_\alpha^{(1,c)} = m\frac{\tau_c}{\tau_f}\, f_\alpha^{(1,f)} \quad (24)$$

Substituting (24) into (19) one obtains

$$\tilde{f}_\alpha^c = f_\alpha^{(eq,c)} + m\frac{\tau_c-1}{\tau_f}f_\alpha^{(1,f)} + ... \quad (25)$$

Using Eqs. (20, 21), the above becomes

$$\tilde{f}_\alpha^c = f_\alpha^{(eq,f)} + m\frac{\tau_c-1}{\tau_f}\frac{\tau_f}{\tau_f-1}[\tilde{f}_\alpha^f - f_\alpha^{(eq,f)}]$$

$$= f_\alpha^{(eq,f)} + m\frac{\tau_c-1}{\tau_f-1}[\tilde{f}_\alpha^f - f_\alpha^{(eq,f)}] \quad (26)$$

In transferring the data from the coarse grids to the fine grids, one similarly obtains

$$\tilde{f}_\alpha^f = f_\alpha^{(eq,c)} + \frac{\tau_f-1}{m(\tau_c-1)}[\tilde{f}_\alpha^c - f_\alpha^{(eq,c)}] \quad (27)$$

On the interface between two blocks, there are m values of $\tilde{f}_\alpha^f$ needed for each $f_\alpha^{(eq,c)}$ and $\tilde{f}_\alpha^c$. Thus, spatial and temporal interpolation procedures for the values of $f_\alpha^{(eq,c)}$ and $\tilde{f}_\alpha^c$ on the fine-grid lattice is used to complete the evaluation of $\tilde{f}_\alpha^f$. There are two kinds of interpolation are used along the interface: interpolation in space and interpolation in time. To eliminate the possibility of asymmetry caused by interpolations, a symmetric, 4-point spline fitting is used for spatial interpolation. We found that it is very important to maintain the symmetry in the interpolation along the interface. For example if a 3-point Lagrangian interpolation is used for spatial interpolation, the asymmetry caused by the interpolation can generate a lift coefficient of 0.01 for steady flow over cylinder at Re=20. And if flow is inherently unsteady, this asymmetry could exaggerate the extent of the unsteadiness over long time. For temporal interpolation, a 3-point Lagrangian interpolation is used.

3. RESULTS AND DISCUSSIONS

In all three cases considered here, the boundary condition for f_α in the solid region near a wall is obtained using the formulations given in Ref. [14] for a curved geometry.

3.1 Lid-driven cavity flow

The lid-drive cavity flow has been extensively used as a benchmark solution to test the accuracy of a numerical method in spite of the fact that two singular points at the upper corner require high resolution to obtain smooth stresses near the corner points. To assess the LBE results, the bench mark solution of Ref. [15] are used for comparison.

The computations are carried out using a single-block with uniform lattice (129x129) with the walls placed halfway between lattices and a multi-block whose layout is shown in Fig. 3. Near the two upper corner points, the grid resolution is increased by factor 4. The relaxation time is τ_c= 0.56 for coarse-grid block and τ_f =0.74 for the fine-grid block. The upper wall velocity is U=0.0155945. The initial condition for the density is unity and that for velocity is zero. The streamlines shown in Fig. 4 are obtained from the single block solution and the pattern is not discernable from those of the multi-block solution. The positions of the centers of the primary vortices are (0.6154, 0.7391) and (0.6172, 0.7390) for uniform grid and multi-block

respectively, comparing with the value (0.6172, 0.7344) from reference [15]. The u- and v-components of the velocity along the vertical line and horizontal line through geometry center are shown in Fig 5a and 5b, respectively, along with the bench mark result. It is seen that while the single block method with 129x129 lattices can capture most of physical variables accurately, the multi-block method gives more accurate velocity profiles. Fig. 5 shows the pressure contour from the single-block computation. Because of the singularity at the upper corners, the density contour has a very large region of spatial oscillations due to the insufficient resolution near the singularity. Fig. 7 shows the pressure contours obtained from the multi-block solution. Significant improvement in the smoothness of the solution for the pressure field over that of the single block solution is observed. If the finest grid size is used in the entire region, it will require a significantly longer CPU time and much larger computer memory.

In an NS solver for incompressible flows, because the decoupling of thermodynamic pressure and velocity field, it is crucial to maintain the mass conservation of the entire flow domain. This issue becomes more critical when the multi-block method is used [8, 16]. Also for incompressible flows, the pressure is arbitrary up to a constant. Hence coupling the pressure term while maintaining the mass flux conservation is very important. Generally speaking, it is difficult to maintain simultaneously the continuity of mass, momentum, and stresses across the interface between neighboring blocks because interpolations are applied separately along the interface to evaluate mass flux, momentum flux, and pressure. Hence it is often difficult to use large grid size ratio (m) between two neighboring blocks. In multi-block LBE method, the continuities of mass and stresses are ensured through the use of Equations (26-27). The most important point is that interpolations are only applied to f_i's along the interface and this automatically ensures the consistency in the transfer of various flux terms across the interface.

To validate the above arguments, pressure, shear stress, mass flux and momentum flux near the block interfaces are examined next. Fig. 8 shows the local, enlarged view of the pressure contour around an interface corner point indicated by the circle in Fig. 7. Clearly, the pressure is rather smooth across the interface with the coarse-to-fine grid size ratio of m=4. Figs. 9-11 show the contours of shear stress, mass flux, and momentum flux ρu_x^2. It is seen that these physical quantities are all smooth across the interface.

To demonstrate this issue more clearly, macroscopic physical quantities on one part of the interface (i.e. line A-B in Fig. 3) are plotted in Figs. 12-17. After streaming step there is no physical value on the interface for the fine grid. Here we use second order extrapolation to get fine grid value on interface. Figs. 12-15 show that mass and momentum flux match very well between fine- and coarse-grid. Fig. 16 shows the shear stress. In most part of the interface two sets of values agree very well with each other. The discrepancy appears near the upper wall. It is noted that for in the fine-grid blocks, the top moving wall is located half-way between two horizontal, fine-grid lattices with a distance of $\Delta_f \delta x_f = 0.5 \delta x_f$. In the coarse-grid block, the distance between the wall to the nearest lattice in the fluid region is $\Delta_c \delta x_c = 0.5 \delta x_f = 0.5 \delta x_c / 4 = 0.125\ \delta x_c$ for m=4. This mismatch ($\Delta_f \neq \Delta_c$) will result in different errors in the boundary condition for f_i's. This subsequently affects the accuracy of the shear stress near the corner of block and wall. The same problem also appears in Fig. 17 for pressure.

3.2 Channel flow over an asymmetrical placed cylinder at Re=100

Schäfer & Turek [17] reported some benchmark results for a laminar flow over a circular cylinder placed asymmetrically inside a channel. The cylinder has a radius of 0.1m and is asymmetrically placed in the channel. The center to the upper wall distance is h_+/r=0.21m and the center to the lower wall distance is h_-/r=0.20m. In the LBE computation, r=5 lattice is used in the coarse grid system and the coarse-to-fine lattice spacing ratio is m=4. The coarse-grid block has a total of 220×42 lattices. The relaxation times are τ_c = 0.52 for and τ_f =0.58. The channel inlet has a parabolic velocity and is located about 4 radii upstream of the cylinder center. A zeroth-order extrapolation for f_α is used. The Reynolds number based on the average inlet velocity and the diameter of the cylinder is Re=100.

At this Reynolds number, the flow becomes unsteady and periodic vortex shedding is observed. The numerical value of Strouhal number is 0.300 and it agrees very well with the value (0.2995-0.305) in reference [17]. An instantaneous streamline plot is shown in Fig. 18 after the dynamically periodic solution is established. The drag and lift are shown in Fig. 19. The unsteady characteristics of the flow agree well with the reported results in [17] and comparable with a similar computation using lattice Boltzmann method [18].

3.3 Steady flow over NACA0012 airfoil

The NACA 0012 airfoil (Fig. 20) is a popular wing model, which has been used extensively. Flow fields at Re=500, 1000, 2000, and 5000 are presently computed with the multi-block LBE scheme. Fig. 21 shows the entire computational domain and the schematic of the multi-block arrangement. There are 150 lattices (grids) along the chord in the finest block. At the inlet, upper,

and lower boundaries, the equilibrium boundary condition is used. At the downstream boundary a zeroth order extrapolation for f_i's is used.

Fig. 22 shows the density contour, streamlines and velocity vector of the converged solution at Re=2000 and zero angle of attack. To investigate the effect of grid resolution, two sets of grid systems are used for the flow field at Re=500: a fine grid system and a coarse grid system (with resolution reduced by a factor of 2 in every block from the fine grid system). Fig. 23 shows the velocity profiles at $(x-x_{LE})/L=0.06$ where L is the chord length and x_{LE} is the location of the leading edge. The two sets of velocity profiles agree well with each other, although the fine grid solution appears to have smoother u-component velocity profile, as expected.

Fig. 24 compares the drag coefficient C_d between the present LBE simulation and those calculated from Xfoil [19]. It can be seen that two sets of results agree with each other very well for the entire range of Reynolds numbers investigated in this study.

It is also noted that at Re=500, the present value of C_d=0.1761 compare very well with the results reported in Ref. [20]: C_d=0.1762 obtained using a Navier-Stokes equation-based finite difference method and C_d=0.1717 using Powerflow code developed by EXA Corporation, which is based on the lattice Boltzmann equation method. In addition, the present simulation for the symmetrical flow at Re=500 gives a lift coefficient of $|C_L| < 6 \times 10^{-14}$. Ref. [20] reported $C_L = 1.15\times10^{-7}$ using an NS equation-solver and $C_L = 2.27\times10^{-4}$ using EXA's Powerflow code. This suggests that the present multi-block code preserve the symmetry very well.

Finally, it is worth pointing out that there is a tremendous saving in the computational cost using the multi-block method in LBE simulations. There are three different sizes of grids used for the NACA0012 airfoil simulation. There are 513×65=33345 fine grids, 23300 intermediate grids with m=4, and 37407 coarse grids (with m=8 in reference to the finest grids). This gives a total of about 9.4×10^4 grids in the entire domain. If the fine grid system is used in the entire domain, the number of the grids would be $N_x \times N_y$= 2849×577~ 1.64×10^5 which is 18 times more than in the multi-block case. This represents a saving of 18 times in the memory. Furthermore, since $\delta t=\delta x=\delta y$ in the LBE simulation, one time step marching in the coarsest grid system (m=8) requires 2 sweeps in the intermediate grid blocks and 8 sweeps in the finest grid blocks. The ratio of the computational efforts required to carry out a single-block simulations to that for a multi-block simulation for a given period of physical time would be $1.64\times10^5\times8/(33345\times8+23300\times2+37407) \sim 38$. Clearly, more saving can be achieved if more blocks of different sizes are used.

4. CONCLUDING REMARKS

A multi-block strategy is developed for the lattice Boltzmann method. The interface condition is derived to ensure the mass conservation and stress continuity between neighboring blocks. Favorable computational results are obtained in three test cases. There is a significant potential for the multi-block strategy in the LBE method in the aerodynamics application since the boundary conditions at infinity and on the wall can both be reconciled.

5. ACKNOWLEDGMENTS

The work reported in this paper has been partially supported by NASA Langley Research Center, with David Rudy as the project monitor. The authors thank Dr. Li-Shi Luo for many helpful discussions.

6. REFERENCES

[1] G. McNamara & G. Zanetti, Use of the Boltzmann equation to simulate lattice-gas automata, *Phys. Rev. Lett.* **61**, 2332 (1988).

[2] F. Higuera, S. Succi, & R. Benzi, Lattice gas dynamics with enhanced collisions, *Europhys. Lett.* **9**, 345 (1989).

[3] H. Chen, S. Chen, & W. H. Matthaeus, Recovery of the Navier-Stokes equations using a lattice-gas Boltzmann method, *Phys. Rev. A.* **45**, R5339-R5342 (1992).

[4] R. Benzi, S. Succi, & M. Vergassola, The lattice Boltzmann equation: Theory and applications, *Phys. Rep.* **222**, 145-197 (1992).

[5] S. Chen & G. D. Doolen, Lattice Boltzmann method for fluid flows, *Ann. Rev. Fluid Mech.* **30**, 329-364 (1998).

[6] R. Peyret & T. D. Taylor, *Computational Technique for Fluid Dynamics*, Vol. II, (Springer-Verlag, New York, 1983).

[7] C. A. J. Fletcher, *Computational Techniques for Fluid Dynamics*, Vols. I & II, (Springer-Verlag, New York, 1988).

[8] W. Shyy, *Computational Modeling for Fluid Flow and Interfacial Transport*, Corrected printing, (Elsevier, Amsterdam, 1997).

[9] P. L. Bhatnagar, E. P. Gross, & M. Krook, A model for collision processes in gases. I. Small amplitude processes in charged and neutral one-component system, *Phys. Rev. A*, **94**, 511-525 (1954).

[10] X. He & L.-S. Luo, A priori derivation of the lattice Boltzmann equation, *Phys. Rev. E* **55**, R6333-R6336 (1997).

[11] X. He & L.-S. Luo, Theory of the lattice Boltzmann equation: From Boltzmann equation to lattice Boltzmann equation, *Phys. Rev. E* **56**, 6811 (1997).

[12] W. Shyy, H. S. Udaykumar, M. M. Rao, & R. W. Smith, *Computational Fluid Dynamics With Moving Boundaries*, Taylor & Francis, (1996).

[13] T. Ye, R. Mittal, H. S. Udaykumar, & W. Shyy, An accurate Cartesian grid method for viscous incompressible flows with complex immersed boundaries, *J. Comp. Pyhs.* **156,** 209-240(1999).

[14] R. Mei, L. Luo & W. Shyy, An accurate curved boundary treatment in the lattice Boltzmann method," *J. Computational Physics*, **155**, 307-330, (1999).

[15] U. Ghia, K. N. Ghia, & C. T. Shin, High-Re solution for incompressible flow using the Navier-Stokes equations and a mutigrid method, *J. Comput. Phys.* 48 (1982), 387-411.

[16] W. Shyy, S.S. Thakur, H. Ouyang, J. Liu, & E. Blosch, *Computational Techniques for Complex Transport Phenomena*, Cambridge University Press, New York, (1999).

[17] M. Schäfer & S. Turek, Benchmark computations of laminar flow over a cylinder, in *Notes in Numerical Fluid Mechanics*, (Vieweg Verlag, Braunschweig), **52,** 547 (1996).

[18] O. Filippova & D. Hänel, Grid refinement for lattice-BGK models, *J. Comp. Phys.* **147**, 219-228 (1998).

[19] M. Drela & M. B. Giles, Viscous-inviscid Analysis of Transonic and Low Reynolds Number Airfoils. *AIAA J.* Vol. 25, 1347-1355 (1987).

[20] D. P. Lockard, L.-S. Luo, & B.A. Singer, Evaluation of Powerflow for aerodynamic applications, preprint (2000).

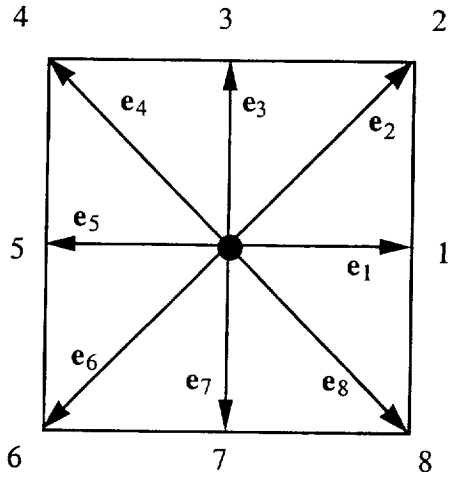

Fig. 1 A 2-D, 9-velocity lattice.

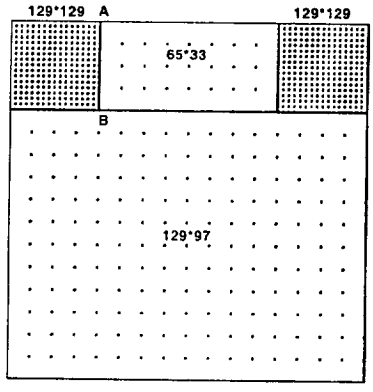

Fig. 3 Block layout for a 2-D cavity. Lattice spacing is reduced by a factor of 8 for graphical clarity.

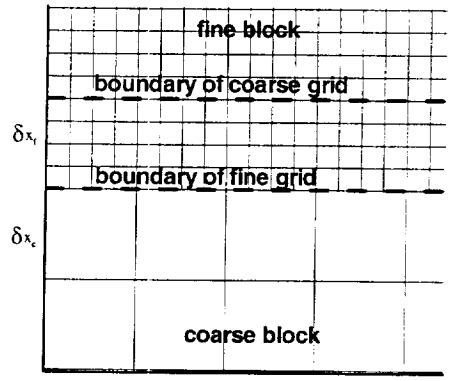

Fig. 2 Interface characteristics between two blocks of different lattice spacing.

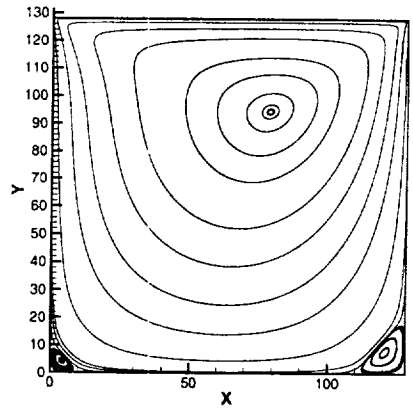

Fig 4 Streamlines in the cavity flow at Re=100.

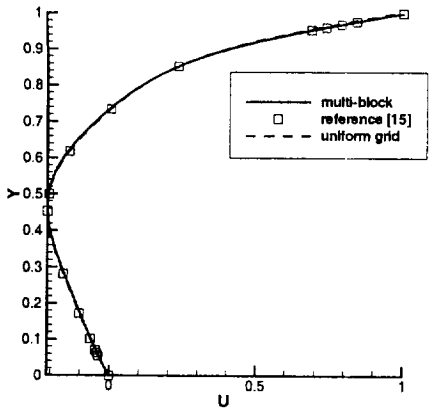

Fig 5a Comparison of u-velocity along the vertical line through geometric center.

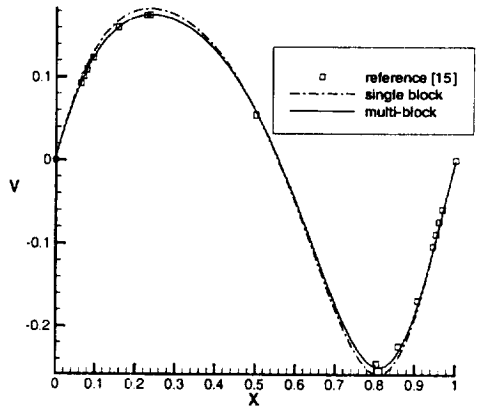

Fig 5b Comparison of v-velocity along the horizontal line through geometric center.

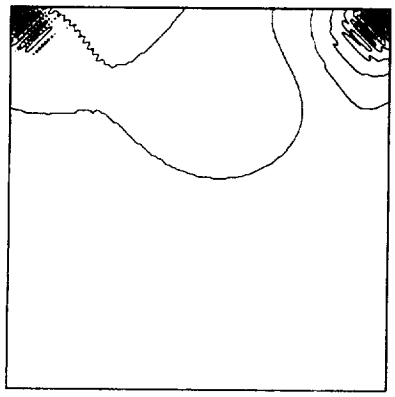

Fig 6 Pressure contours in the cavity flow from the single-block LBE simulation.

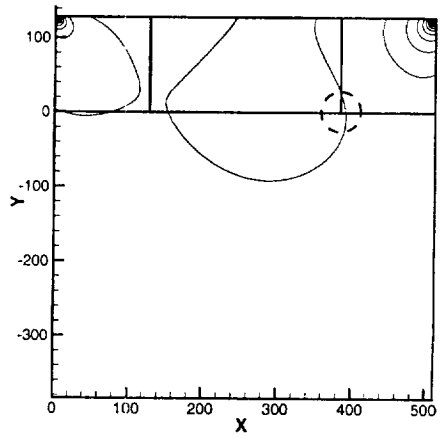

Fig.7 Pressure contours in the cavity from multi-block LBE solution. (For the circled region, see Fig. 8)

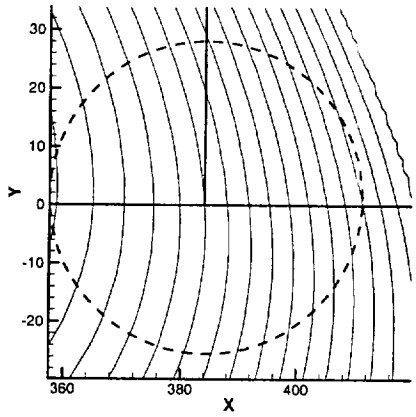

Fig. 8 Enlarged view of pressure contour in the circled region in Fig. 7 near the intersection of three blocks. The figure demonstrates that the block interface and corner are well handled.

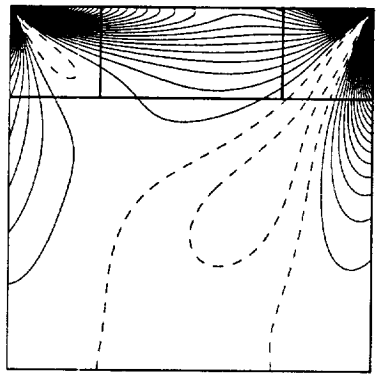

Fig. 9 Shear stress contour. Solid and dash lines represent positive and negtive values, respectrively.

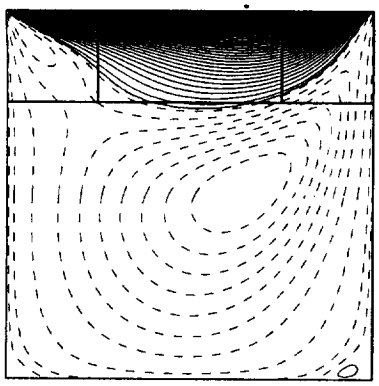

Fig. 10 Contour of x-component mass flux ρu_x. Solid and dash lines represent positive and negtive values, respectrively..

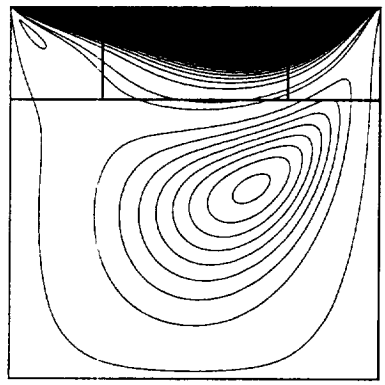

Fig. 11 Contour of momentum flux in the x-direction $\rho \cdot u_x^2$.

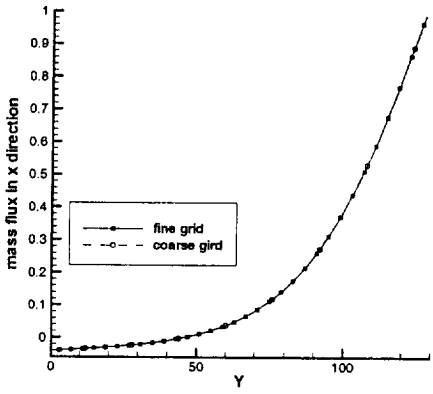

Fig.12 The x-component of the mass flux $\rho u_x /(\rho_0 U)$ on the interface AB. In Figs 12-15, ρ_0=1 and U=0.0155945.

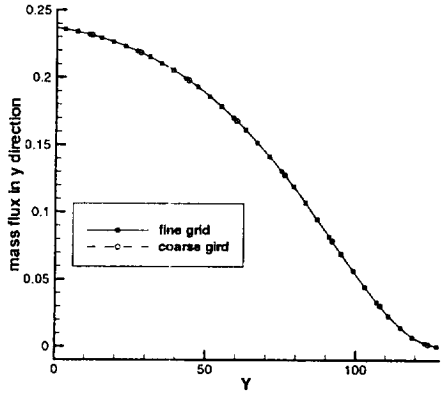

Fig. 13 The x-component of the mass flux $\rho u_y /(\rho_0 U)$ on the interface AB.

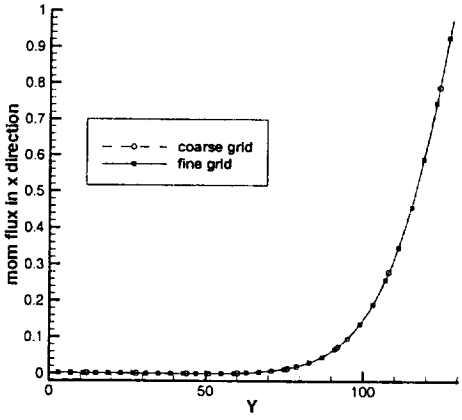

Fig. 14 The x-component of the momentum flux , $\rho u_x^2 / \rho_0 U^2$, on the interface AB.

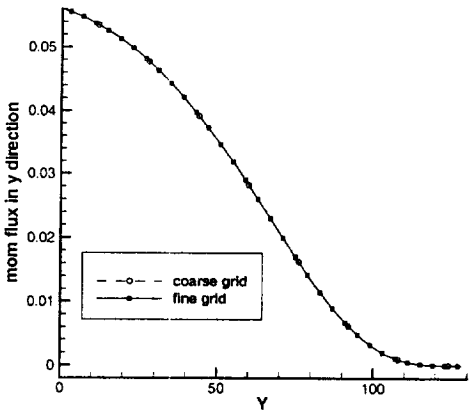

Fig.15 The y-component of the momentum flux, $\rho u_x u_y / \rho_0 U^2$, on the interface AB.

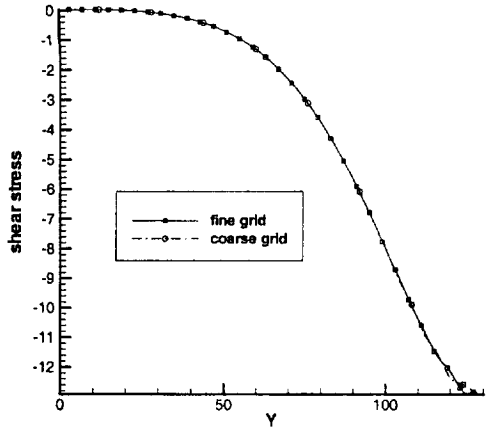

Fig. 16 Shear stress τ_{xy} $/(\mu U / H)$ on the interface AB.

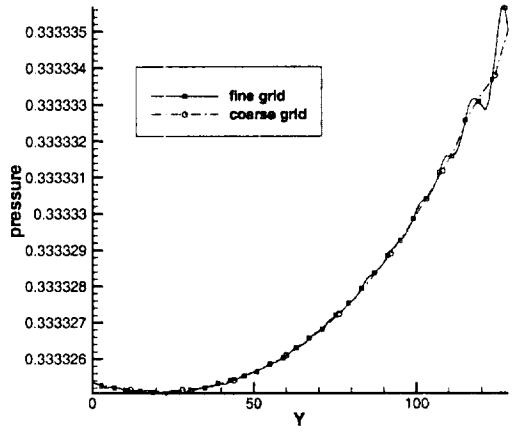

Fig. 17 Pressure on the interface AB.

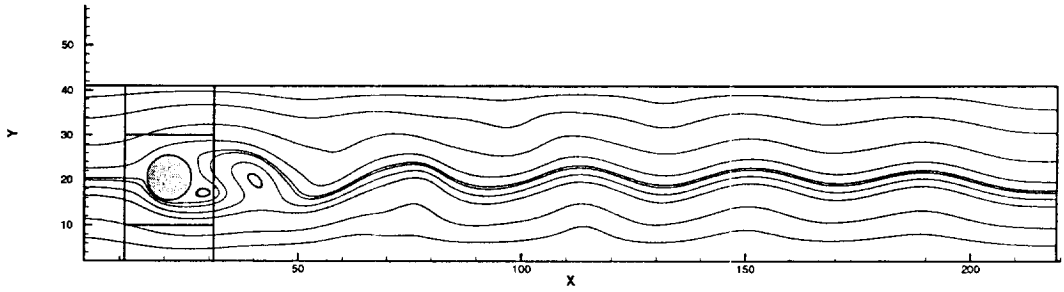

Fig. 18 Instantaneous streamlines for channel flow over an asymetrically placed cylinder at Re=100.

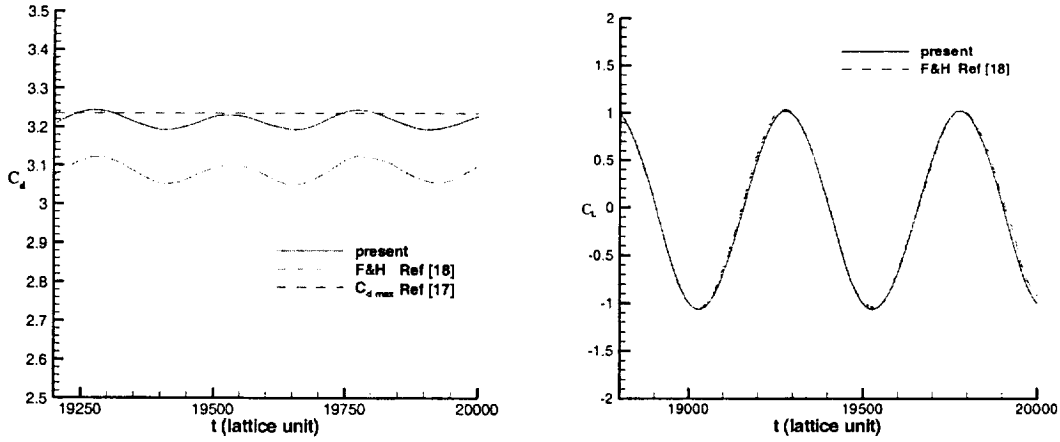

Fig. 19 Unsteady drag and lift coefficients on the cylinder

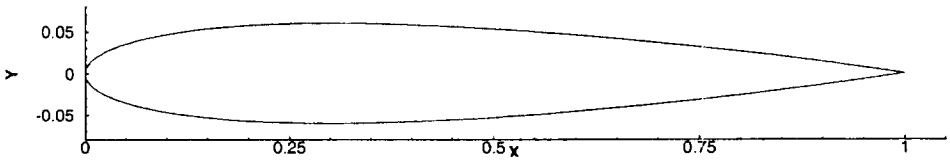

Fig. 20 NACA 0012 airfoil.

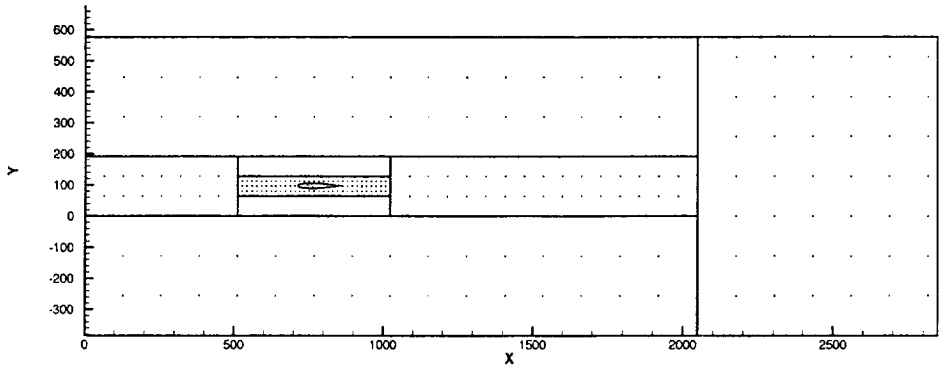

Fig. 21 Block and lattice layout for flow over NACA 0012. The lattice spacing is reduced by a factor 16 for graphical clarity.

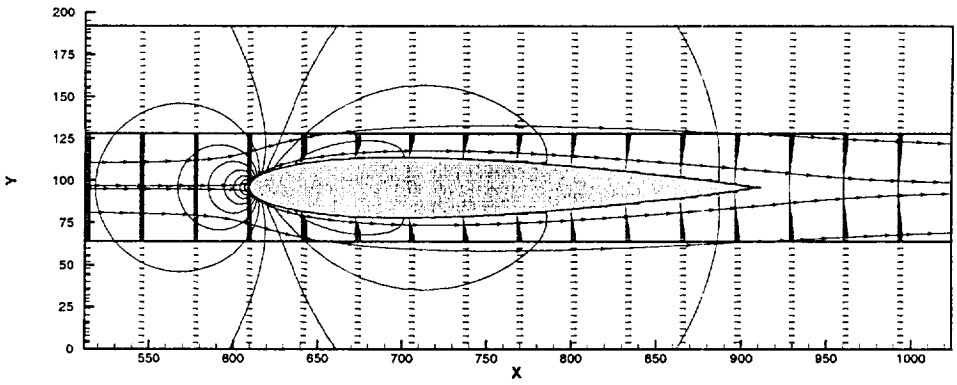

Fig. 22 Streamlines, pressure contour, velocity vector for flows over NACA 0012 airfoil at Re=2000.

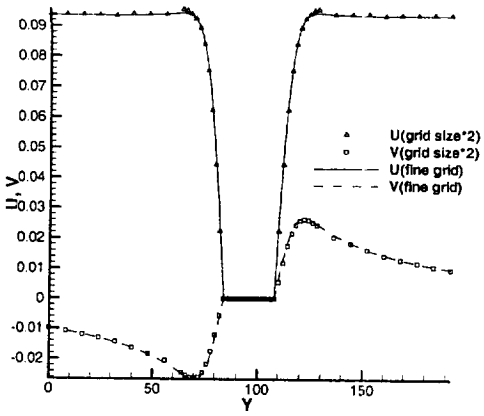

Fig. 23 Grid-independence test of the velocity profiles near the leading edge at $(x-x_{LE})/L=0.06$ for flow over NACA0012 airfoil at Re=500.

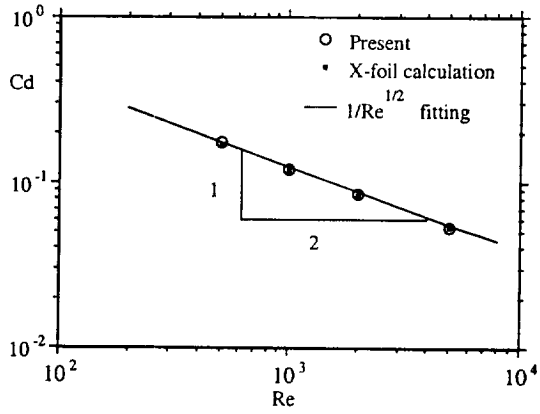

Fig. 24 Comparison of C_d between the present simulation and Xfoil calculation as a function of *Re* for flow over NACA0012 airfoil. The straight line is the slope according to the laminar boundary layer theory.

AIAA 2000-2614
A Multi-block Lattice Boltzmann Method for Fluid Flows

Dazhi Yu, Renwei Mei and Wei Shyy

University of Florida
Gainesville, FL, USA

Fluids 2000
19-22 June 2000 / Denver, CO

Theory of the lattice Boltzmann method: Dispersion, dissipation, isotropy, Galilean invariance, and stability

Pierre Lallemand[1,*] and Li-Shi Luo[2,†]
[1]*Laboratoire ASCI, Université Paris–Sud (Paris XI Orsay), Bâtiment 506, 91405 Orsay Cedex, France*
[2]*ICASE, MS 132C, NASA Langley Research Center, 3 West Reid Street, Building 1152, Hampton, Virginia 23681-2199*
(Received 1 November 1999)

The generalized hydrodynamics (the wave vector dependence of the transport coefficients) of a generalized lattice Boltzmann equation (LBE) is studied in detail. The generalized lattice Boltzmann equation is constructed in moment space rather than in discrete velocity space. The generalized hydrodynamics of the model is obtained by solving the dispersion equation of the linearized LBE either analytically by using perturbation technique or numerically. The proposed LBE model has a maximum number of adjustable parameters for the given set of discrete velocities. Generalized hydrodynamics characterizes dispersion, dissipation (hyperviscosities), anisotropy, and lack of Galilean invariance of the model, and can be applied to select the values of the adjustable parameters that optimize the properties of the model. The proposed generalized hydrodynamic analysis also provides some insights into stability and proper initial conditions for LBE simulations. The stability properties of some two-dimensional LBE models are analyzed and compared with each other in the parameter space of the mean streaming velocity and the viscous relaxation time. The procedure described in this work can be applied to analyze other LBE models. As examples, LBE models with various interpolation schemes are analyzed. Numerical results on shear flow with an initially discontinuous velocity profile (shock) with or without a constant streaming velocity are shown to demonstrate the dispersion effects in the LBE model; the results compare favorably with our theoretical analysis. We also show that whereas linear analysis of the LBE evolution operator is equivalent to Chapman-Enskog analysis in the long-wavelength limit (wave vector $\mathbf{k}=\mathbf{0}$), it can also provide results for large values of $\mathbf{k}$. Such results are important for the stability and other hydrodynamic properties of the LBE method and cannot be obtained through Chapman-Enskog analysis.

PACS number(s): 47.10.+g, 47.11.+j, 05.20.Dd

I. INTRODUCTION

The method of lattice Boltzmann equation (LBE) is an innovative numerical method based on kinetic theory to simulate various hydrodynamic systems [1–3]. Although the LBE method was developed only a decade ago, it has attracted significant attention recently [4,5], especially in the area of complex fluids including multiphase fluids [6–11], suspensions in fluid [12], and viscoelastic fluids [13,14]. The lattice Boltzmann equation was introduced to overcome some serious deficiencies of its historic predecessor: the lattice gas automata (LGA) [15–17]. The lattice Boltzmann equation circumvents two major shortcomings of the lattice gas automata: intrinsic noise and limited values of transport coefficients, both due to the Boolean nature of the LGA method. However, despite the notable success of the LBE method in simulating laminar [18–21] and turbulent [22] flows, understanding of some important theoretical aspects of the LBE method, such as the stability of the LBE method, is still lacking. It was only very recently that the formal connections between the lattice Boltzmann equation and the continuous Boltzmann equation [23–25] and other kinetic schemes [26] were established.

In this work we intend to study two important aspects of the LBE method which have not been systematically studied yet: (a) the dispersion effects due to the presence of a lattice space and (b) conditions for stability. We first construct a LBE model in moment space based upon the generalized lattice Boltzmann equation due to d'Humières [27]. The proposed model has a maximum number of adjustable parameters allowed by the freedom provided by a given discrete velocity set. These adjustable parameters are used to optimize the properties of the model through a systematic analysis of the generalized hydrodynamics of the model. Generalized hydrodynamics characterizes dispersion, dissipation (hyperviscosities), anisotropy, lack of Galilean invariance, and instability of the LBE models in general. The proposed generalized hydrodynamic analysis enables us to improve the properties of the models in general. The analysis also provides us better insights into the conditions under which the LBE method is applicable and comparable to conventional computational fluid dynamics techniques.

Furthermore, from a theoretical perspective, we would like to argue that our approach can circumvent the Chapman-Enskog analysis to obtain the macroscopic equations from the LBE models [27,13,14]. The essence of our argument is that the validity of the Chapman-Enskog analysis is entirely based upon the fact that there are two disparate spatial scales in real fluids: the kinetic (mean-free-path) and the hydrodynamic scales the ratio of which is the Knudsen number. When the LBE method is used to simulate hydrodynamic motion over a few lattice spacings, there is no such separa-

*Electronic address: lalleman@asci.fr
†Author to whom correspondence should be addressed. Electronic address: luo@icase.edu

tion of the two scales. Therefore, the applicability of Chapman-Enskog analysis to the LBE models might become dubious. Under the circumstances, analyzing the generalized hydrodynamics of the model becomes not only appropriate but also necessary.

It should also be pointed out that there exists previous work on the generalized hydrodynamics of the LGA models [28–32] and the LBE models [33]. However, the previous work only provides analysis on nonhydrodynamic behavior of the models at finite wavelength, without addressing important issues such as the instability of the LBE method or providing insights into constructing better models. In the present work, by using a model with as many adjustable parameters as possible, we analyze the generalized hydrodynamics of the model so that we can identify the causes of certain nonhydrodynamic behavior, such as anisotropy, and lack of Galilean invariance, and instability. Therefore, the analysis shows how to improve the model in a systematic and coherent fashion.

This paper is organized as follows. Section II gives a brief introduction to the two-dimensional (20) nine-velocity LBE model in discrete velocity space. Section III discusses the generalized LBE model in moment space. Section IV derives the linearized lattice Boltzmann equation from the generalized LBE model. Section V analyzes the hydrodynamic modes of the linearized evolution operator of the generalized LBE model, and the generalized hydrodynamics of the model. The dispersion, dissipation, isotropy, and Galilean invariance of the model are discussed. The eigenvalue problem of the linearized evolution operator is solved analytically and numerically. Section VI analyzes the stability of the LBE model with Bhatnagar-Gross-Krook (BGK) approximation, and compares with the stability of the LBE model presented in this paper. Section VII discusses the correct initial conditions in the LBE simulations, and presents numerical tests of shear flows with discontinuities in the initial velocity profile. Section VIII provides a summary and concludes the paper. Two appendices provide additional analysis for variations of the LBE models. Appendix A analyzes a model with coupling between density ρ and velocity $\mathbf{u}$, and Appendix B analyzes the LBE models with various interpolation schemes.

II. 2D NINE-VELOCITY LBE MODEL

The guiding principle of the LBE models is to construct a dynamical system on a simple lattice of high symmetry (mostly square in 2D and cubic in 3D) involving a number of quantities that can be interpreted as the single-particle distribution functions of fictitious particles on the links of the lattice. These quantities then evolve in a discrete time according to certain rules that are chosen to attain some desirable macroscopic behavior that emerges at scales large relative to the lattice spacing. One possible "desirable behavior" is that of a compressible thermal or athermal viscous fluid. (To simplify the analysis, in this work we shall restrict our analysis to the athermal case.) We shall demonstrate that the LBE models can satisfactorily mimic the fluid behavior to an extent that the models are indeed useful in simulating flows according to the similarity principle of fluid mechanics. For the sake of simplicity, we confine our discussions here to two-dimensional space. The extension to three-dimensional space is straightforward, albeit tedious.

A particular two-dimensional LBE model considered in this work is the nine-velocity model. In this model, space is discretized into a square lattice, and there are nine discrete velocities given by

$$\mathbf{e}_\alpha=\begin{cases}(0,0), & \alpha=0,\\ (\cos[(\alpha-1)\pi/2],\sin[(\alpha-1)\pi/2])c, & \alpha=1-4,\\ (\cos[(2\alpha-9)\pi/4],\sin[(2\alpha-9)\pi/4])\sqrt{2}c, & \alpha=5-8,\end{cases} \tag{1}$$

where $c=\delta_x/\delta_t$ is the unit of velocity and δ_x and δ_t are the lattice constant of the lattice space and the unit of time (time step), respectively. From here on we shall use the units of $\delta_x=1$ and $\delta_t=1$ such that all the relevant quantities are dimensionless. The above discrete velocities correspond to the particle motion from a lattice node $\mathbf{r}_j$ to either itself, one of the four nearest neighbors ($\alpha=1-4$), or one of the four next-nearest neighbors ($\alpha=5-8$). This model can easily be extended to include more discrete velocities and in space of higher dimensions, thereby including further distant neighbors to which the particles move in one time step. Nevertheless, "hopping" to a neighbor on the lattice induces inherent limitations in the discretization of velocity space.

For the particular model discussed here, nine real numbers describe the medium at each node $\mathbf{r}_j$ of a square lattice:

$$\{f_\alpha(\mathbf{r}_j)|\alpha=0,1,\ldots,8\}.$$

The number f_α can be considered as the distribution function of velocity $\mathbf{e}_\alpha$ at location $\mathbf{r}_j$ (and at a particular time t). The set $\{f_\alpha\}$ can be represented by a vector in $\mathbf{R}^9$ that defines the state of the medium at each lattice node:

$$|f(\mathbf{r}_j)\rangle\equiv(f_0,f_1,\ldots,f_8)^T. \tag{2}$$

Once the vector $|f(\mathbf{r}_j)\rangle$ is given at a point $\mathbf{r}_j$ in space, the state of the medium at this point is fully specified.

The evolution of the medium occurs at discrete times $t=n\delta_t$ (with $\delta_t=1$). The evolution consists of two steps: (1) motion to the relevant neighbors (modeling of advection) (2) redistribution of the $\{f_\alpha\}$ at each node (modeling of collisions). These steps are described by the equation

$$f_\alpha(\mathbf{r}_j+\mathbf{e}_\alpha,t+1)=f_\alpha(\mathbf{r}_j,t)+\Omega_\alpha(f). \tag{3}$$

The above equation is the so-called lattice Boltzmann equation (LBE). The lattice Boltzmann equation can be rewritten in a concise vector form:

$$|f(\mathbf{r}_j+\mathbf{e}_\alpha,t+1)\rangle=|f(\mathbf{r}_j t)\rangle+|\Delta f\rangle, \tag{4}$$

where the following notations are adopted:

$$|f(\mathbf{r}_j+\mathbf{e}_\alpha,t+1)\rangle\equiv[f_0(\mathbf{r}_j+\mathbf{e}_0,t+1),f_1(\mathbf{r}_j+\mathbf{e}_1,t+1),\ldots,f_8(\mathbf{r}_j+\mathbf{e}_8,t+1)]^{\mathrm{T}}, \tag{5a}$$

$$|\Delta f\rangle\equiv[\Omega_0(f),\Omega_1(f),\ldots,\Omega_8(f)]^{\mathrm{T}}, \tag{5b}$$

so that $|f(\mathbf{r}_j+\mathbf{e}_\alpha,t+1)\rangle$ is the vector of a state after advection, and $|\Delta f\rangle$ is the vector of the changes in $|f\rangle$ due to collision Ω.

The advection is straightforward in the LBE models. The collisions represented by the operator Ω may be rather complicated. However, Ω must satisfy conservation laws and be compatible with the symmetry of the model (the underlying lattice space). This might simplify Ω considerably. One simple collision model is the BGK model [34,2,3]:

$$\Omega_\alpha=-\frac{1}{\tau}[f_\alpha-f_\alpha^{(\mathrm{eq})}], \tag{6}$$

where τ is the relaxation time in units of time step δ_t (which is set to be 1 here), and $f_\alpha^{(\mathrm{eq})}$ is the equilibrium distribution function that satisfies the following conservation conditions for an athermal medium:

$$\rho=\sum_\alpha f_\alpha^{(\mathrm{eq})}=\sum_\alpha f_\alpha, \tag{7a}$$

$$\rho\mathbf{u}=\sum_\alpha \mathbf{e}_\alpha f_\alpha^{(\mathrm{eq})}=\sum_\alpha \mathbf{e}_\alpha f_\alpha, \tag{7b}$$

where ρ and $\mathbf{u}$ are the (mass) density and the velocity of the medium at each lattice node, respectively. For the so-called nine-velocity BGK model, the equilibrium is usually taken as

$$f_\alpha^{(\mathrm{eq})}=w_\alpha\rho\left[1+3(\mathbf{e}_\alpha\cdot\mathbf{u})+\frac{9}{2}(\mathbf{e}_\alpha\cdot\mathbf{u})^2-\frac{3}{2}\mathbf{u}^2\right], \tag{8}$$

where $w_0=4/9$, $w_{1,2,3,4}=1/9$, and $w_{5,6,7,8}=1/36$.

Some shortcomings of the BGK model are apparent. For instance, because the model relies on a single relaxation parameter τ, the Prandtl number must be unity when the model is applied to thermal fluids, among other things. One way to overcome these shortcomings of the BGK LBE model [2,3] is to use a generalized LBE model which nevertheless retains the simplicity and computational efficiency of the BGK LBE model.

III. MOMENT REPRESENTATION AND GENERALIZED 2D LBE

Given a set of b discrete velocities, $\{\mathbf{e}_\alpha|\alpha=0,1,\ldots,(b-1)\}$ with corresponding distribution functions, $\{f_\alpha|\alpha=0,1,\ldots,(b-1)\}$, one can construct a b-dimensional vector space R^b based upon the discrete velocity set, and this is usually the space mostly used in the preceding discussion of the LBE models. One can also construct a space based upon the (velocity) moments of $\{f_\alpha\}$. Obviously, there are b independent moments for the discrete velocity set. The reason in favor of using the moment representation is somewhat obvious. It is well understood in the context of kinetic theory that various physical processes in fluids, such as viscous transport, can be approximately described by coupling or interaction among "modes" (of the collision operator), and these modes are directly related to the moments (e.g., the hydrodynamic modes are linear combinations of mass, and momenta moments). Thus the moment representation provides a convenient and effective means by which to incorporate the physics into the LBE models. Because the physical significance of the moments is obvious (hydrodynamic quantities and their fluxes, etc.), the relaxation parameters of the moments are directly related to the various transport coefficients. This mechanism allows us to control each mode independently. This also overcomes some obvious deficiencies of the usual BGK LBE model, such as a fixed Prandtl number, which is due to a single relaxation parameter of the model.

For the nine-velocity LBE model, we choose the following moments to represent the model:

$$|\rho\rangle=(1,1,1,1,1,1,1,1,1)^{\mathrm{T}}, \tag{9a}$$

$$|e\rangle=(-4,-1,-1,-1,-1,2,2,2,2)^{\mathrm{T}}, \tag{9b}$$

$$|\varepsilon\rangle=(4,2,2,2,2,1,1,1,1)^{\mathrm{T}}, \tag{9c}$$

$$|j_x\rangle=(0,1,0,-1,0,1,-1,-1,1)^{\mathrm{T}}, \tag{9d}$$

$$|q_x\rangle=(0,-2,0,2,0,1,-1,-1,1)^{\mathrm{T}}, \tag{9e}$$

$$|j_y\rangle=(0,0,1,0,-1,1,1,-1,-1)^{\mathrm{T}}, \tag{9f}$$

$$|q_y\rangle=(0,0,-2,0,2,1,1,-1,-1)^{\mathrm{T}}, \tag{9g}$$

$$|p_{xx}\rangle=(0,1,-1,1,-1,0,0,0,0)^{\mathrm{T}}, \tag{9h}$$

$$|p_{xy}\rangle=(0,0,0,0,0,1,-1,1,-1)^{\mathrm{T}}. \tag{9i}$$

The above vectors are represented in the space $\mathrm{V}=\mathrm{R}^9$ spanned by the discrete velocities $\{\mathbf{e}_\alpha\}$, and they are mutually orthogonal to each other. These vectors are not normalized; this makes the algebraic expressions involving these vectors which follow simpler. Note that the above vectors have an explicit physical significance related to the moments of $\{f_\alpha\}$ in discrete velocity space: $|\rho\rangle$ is the density mode; $|e\rangle$ is the energy mode; $|\varepsilon\rangle$ is related to energy square; $|j_x\rangle$ and $|j_y\rangle$ correspond to the x and y components of momentum (mass flux); $|q_x\rangle$ and $|q_y\rangle$ correspond to the x and y components of energy flux; and $|p_{xx}\rangle$ and $|p_{xy}\rangle$ correspond to the diagonal and off-diagonal component of the stress tensor. The components of these vectors in discrete velocity space $\mathrm{V}=\mathrm{R}^9$ are constructed as follows:

$$|\rho\rangle_\alpha=|\mathbf{e}_\alpha|^0=1, \tag{10a}$$

$$|e\rangle_\alpha = -4|\mathbf{e}_\alpha|^0 + 3(e_{\alpha,x}^2 + e_{\alpha,y}^2), \tag{10b}$$

$$|\varepsilon\rangle_\alpha = 4|\mathbf{e}_\alpha|^0 - \frac{21}{2}(e_{\alpha,x}^2 + e_{\alpha,y}^2) + \frac{9}{2}(e_{\alpha,x}^2 + e_{\alpha,y}^2)^2, \tag{10c}$$

$$|j_x\rangle_\alpha = e_{\alpha,x}, \tag{10d}$$

$$|q_x\rangle_\alpha = [-5|\mathbf{e}_\alpha|^0 + 3(e_{\alpha,x}^2 + e_{\alpha,y}^2)]e_{\alpha,x}, \tag{10e}$$

$$|j_y\rangle_\alpha = e_{\alpha,y}, \tag{10f}$$

$$|q_y\rangle_\alpha = [-5|\mathbf{e}_\alpha|^0 + 3(e_{\alpha,x}^2 + e_{\alpha,y}^2)]e_{\alpha,y}, \tag{10g}$$

$$|p_{xx}\rangle_\alpha = e_{\alpha,x}^2 - e_{\alpha,y}^2, \tag{10h}$$

$$|p_{xy}\rangle_\alpha = e_{\alpha,x}e_{\alpha,y}. \tag{10i}$$

Thus,

$$\rho = \langle\rho|f\rangle = \langle f|\rho\rangle, \tag{11a}$$

$$e = \langle e|f\rangle = \langle f|e\rangle, \tag{11b}$$

$$\varepsilon = \langle\varepsilon|f\rangle = \langle f|\varepsilon\rangle, \tag{11c}$$

$$j_x = \langle j_x|f\rangle = \langle f|j_x\rangle, \tag{11d}$$

$$q_x = \langle q_x|f\rangle = \langle f|q_x\rangle, \tag{11e}$$

$$j_y = \langle j_y|f\rangle = \langle f|j_y\rangle, \tag{11f}$$

$$q_y = \langle q_y|f\rangle = \langle f|q_y\rangle, \tag{11g}$$

$$p_{xx} = \langle p_{xx}|f\rangle = \langle f|p_{xx}\rangle, \tag{11h}$$

$$p_{xy} = \langle p_{xy}|f\rangle = \langle f|p_{xy}\rangle. \tag{11i}$$

Similar to $\{f_\alpha\}$, the above set of moments can also be concisely represented by a vector:

$$|\varrho\rangle \equiv (\rho, e, \varepsilon, j_x, q_x, j_y, q_y, p_{xx}, p_{xy})^T. \tag{12}$$

There obviously exists a transformation matrix M between $|\varrho\rangle$ and $|f\rangle$ such that

$$|\varrho\rangle = \mathsf{M}|f\rangle, \tag{13a}$$

$$|f\rangle = \mathsf{M}^{-1}|\varrho\rangle. \tag{13b}$$

In other words, the matrix M transforms a vector in the vector space V spanned by the discrete velocities into a vector in the vector space $\mathbf{M} = \mathbf{R}^b$ spanned by the moments of $\{f_\alpha\}$. The transformation matrix M is explicitly given by

$$\mathsf{M} \equiv \begin{pmatrix} \langle\rho| \\ \langle e| \\ \langle\varepsilon| \\ \langle j_x| \\ \langle q_x| \\ \langle j_y| \\ \langle q_y| \\ \langle p_{xx}| \\ \langle p_{xy}| \end{pmatrix} \equiv \begin{pmatrix} 1 & 1 & 1 & 1 & 1 & 1 & 1 & 1 & 1 \\ -4 & -1 & -1 & -1 & -1 & 2 & 2 & 2 & 2 \\ 4 & -2 & -2 & -2 & -2 & 1 & 1 & 1 & 1 \\ 0 & 1 & 0 & -1 & 0 & 1 & -1 & -1 & 1 \\ 0 & -2 & 0 & 2 & 0 & 1 & -1 & -1 & 1 \\ 0 & 0 & 1 & 0 & -1 & 1 & 1 & -1 & -1 \\ 0 & 0 & -2 & 0 & 2 & 1 & 1 & -1 & -1 \\ 0 & 1 & -1 & 1 & -1 & 0 & 0 & 0 & 0 \\ 0 & 0 & 0 & 0 & 0 & 1 & -1 & 1 & -1 \end{pmatrix} \equiv (|\rho\rangle, |e\rangle, |\varepsilon\rangle, |j_x\rangle, |q_x\rangle, |j_y\rangle, |q_y\rangle, |p_{xx}\rangle, |p_{xy}\rangle)^T. \tag{14}$$

The rows of the transformation matrix M are organized in the order of the corresponding tensor, rather than in the order of the corresponding moment. The first three rows of M correspond to ρ, e, and ε, which are scalars or zeroth-order tensors, and they are zeroth-order, second-order, and fourth-order moments of $\{f_\alpha\}$, respectively. The next four rows correspond to j_x, q_x, j_y, and q_y, which are vectors or first-order tensors, and j_x and j_y are the first-order moments, whereas q_x and q_y are the third-order ones. The last two rows represent the stress tensor, which are second-order moments and second-order tensors. Again, this can easily be generalized to models using a larger discrete velocity set, and thus higher-order moments, and in three-dimensional space. The main difficulty when using the LBE method to simulate a real isotropic fluid is how to systematically eliminate as much as possible the effects due to the symmetry of the underlying lattice. We shall proceed to analyze some simple (but nontrivial) hydrodynamic situations, and to make the flows as independent of the lattice symmetry as possible.

Because the medium simulated by the model is athermal, the only conserved quantities in the system are density ρ and linear momentum $\mathbf{j} = (j_x, j_y)$. Collisions do not change the conserved quantities. Therefore, in the moment space M, collisions have no effect on these three quantities. We should stress that the conservation of energy is not considered here because the model is constructed to simulate an athermal medium. Moreover, we find that the nine-velocity model is inadequate to simulate a thermal medium because it cannot have an isotropic Fourier law for the diffusion of heat. Although the conserved moments are not affected by collisions, the nonconserved moments are affected by collisions, which in turn cause changes in the gradients or fluxes of the conserved moments, which are higher-order moments. In what follows, the modeling of the changes of the nonconserved moments is described.

Inspired by the kinetic theory for Maxwell molecules [35], we assume that the nonconserved moments relax linearly towards their equilibrium values that are functions of

the conserved quantities. The relaxation equations for the nonconserved moments are prescribed as follows:

$$e^* = e - s_2[e - e^{(\mathrm{eq})}], \tag{15a}$$

$$\varepsilon^* = \varepsilon - s_3[\varepsilon - \varepsilon^{(\mathrm{eq})}], \tag{15b}$$

$$q_x^* = q_x - s_5[q_x - q_x^{(\mathrm{eq})}], \tag{15c}$$

$$q_y^* = q_y - s_7[q_y - q_y^{(\mathrm{eq})}], \tag{15d}$$

$$p_{xx}^* = p_{xx} - s_8[p_{xx} - p_{xx}^{(\mathrm{eq})}], \tag{15e}$$

$$p_{xy}^* = p_{xy} - s_9[p_{xy} - p_{xy}^{(\mathrm{eq})}], \tag{15f}$$

where the quantities with and without superscript * are post-collision and pre-collision values, respectively. The equilibrium values of the nonconserved moments in the above equations can be chosen at will provided that the symmetry of the problem is respected. We choose

$$e^{(\mathrm{eq})} = \frac{1}{\langle e|e\rangle}[\alpha_2\langle\rho|\rho\rangle\rho + \gamma_2(\langle j_x|j_x\rangle j_x^2 + \langle j_y|j_y\rangle j_y^2)]$$

$$= \frac{1}{4}\alpha_2\rho + \frac{1}{6}\gamma_2(j_x^2 + j_y^2), \tag{16a}$$

$$\varepsilon^{(\mathrm{eq})} = \frac{1}{\langle\varepsilon|\varepsilon\rangle}[\alpha_3\langle\rho|\rho\rangle\rho + \gamma_4(\langle j_x|j_x\rangle j_x^2 + \langle j_y|j_y\rangle j_y^2)]$$

$$= \frac{1}{4}\alpha_3\rho + \frac{1}{6}\gamma_4(j_x^2 + j_y^2), \tag{16b}$$

$$q_x^{(\mathrm{eq})} = \frac{\langle j_x|j_x\rangle}{\langle q_x|q_x\rangle}c_1 j_x = \frac{1}{2}c_1 j_x, \tag{16c}$$

$$q_y^{(\mathrm{eq})} = \frac{\langle j_y|j_y\rangle}{\langle q_y|q_y\rangle}c_1 j_y = \frac{1}{2}c_1 j_y, \tag{16d}$$

$$p_{xx}^{(\mathrm{eq})} = \gamma_1\frac{1}{\langle p_{xx}|p_{xx}\rangle}(\langle j_x|j_x\rangle j_x^2 - \langle j_y|j_y\rangle j_y^2) = \frac{1}{2}\gamma_1(j_x^2 - j_y^2), \tag{16e}$$

$$p_{xy}^{(\mathrm{eq})} = \gamma_3\frac{\sqrt{\langle j_x|j_x\rangle\langle j_y|j_y\rangle}}{\langle p_{xx}|p_{xx}\rangle}(j_x j_y) = \frac{1}{2}\gamma_3(j_x j_y). \tag{16f}$$

The values of the coefficients in the above equilibria (c_1, $\alpha_{2,3}$, and $\gamma_{1,2,3,4}$) will be determined in the next section and summarized in Sec. V E. The choices of the above equilibria are made based upon inspection of the corresponding moments given by Eqs. (10), or the physical significance of these moments. Note that in principle q_x and q_y can include terms involving third-order terms in terms of moment, such as j_x^3 and $j_x p_{xx}$ [14], and ε can include fourth-order terms. Nevertheless, for the nine-velocity model, these terms of higher order are not considered because either they do not affect the hydrodynamics of the model significantly, or they lead to some highly anisotropic behavior which is undesirable in the LBE modeling of hydrodynamics.

Clearly, LBE modeling of fluids is rather different from real molecular dynamics. Therefore, it is not necessary to try to solve the mathematically difficult problem to create an interparticle collision mechanism for the fictitious particles in the LBE models that would give the same eigenmodes of the collision operator in the continuous Boltzmann equation. However, what can be accomplished is that by carefully crafting a simple model with certain degrees of freedom, we can optimize large-scale properties of the model in the sense that generalized hydrodynamic effects (deviations from hydrodynamics) are minimized.

The values of the unknown parameters, c_1, $\alpha_{2,3}$, and $\gamma_{1,2,3,4}$, shall be determined by a study of the modes of the linearized collision operator with a periodic lattice of size $N_x \times N_y$.

It should be noted that in Eq. (16) the density ρ does not appear in the terms quadratic in $\mathbf{j}$. This implies that the density fluctuation is decoupled from the momentum equation, similar to an incompressible LBE model with a modified equilibrium distribution function [36]:

$$f_\alpha^{(\mathrm{eq})} = w_\alpha\left\{\rho + \rho_0\left[3(\mathbf{e}_\alpha\cdot\mathbf{u}) + \frac{9}{2}(\mathbf{e}_\alpha\cdot\mathbf{u})^2 - \frac{3}{2}\mathbf{u}^2\right]\right\}, \tag{17}$$

where the mean density ρ_0 is usually set to be 1. The model corresponding to the equilibrium distribution function of Eq. (8) shall be analyzed in Appendix A.

IV. LINEARIZED LBE

We consider the particular situation where the state of the medium is a flow specified by uniform and steady density ρ (usually $\rho = 1$, so the uniform density may not appear in subsequent expressions) and velocity in Cartesian coordinates $\mathbf{V} = (V_x, V_y)$, with a small fluctuation superimposed:

$$|f\rangle = |f^{(0)}\rangle + |\delta f\rangle, \tag{18}$$

where $|f^{(0)}\rangle$ represents the uniform equilibrium state specified by uniform and steady density ρ and velocity $\mathbf{V} = (V_x, V_y)$, and $|\delta f\rangle$ is the fluctuation. The linearized Boltzmann equation is

$$|\delta f(\mathbf{r}_j + \mathbf{e}_\alpha, t+1)\rangle = |\delta f(\mathbf{r}_j, t)\rangle + \Omega^{(0)}|\delta f(\mathbf{r}_j, t)\rangle \tag{19}$$

where $\Omega^{(0)}$ is the linearized collision operator:

$$\Omega_{\beta\alpha}^{(0)} = \left.\frac{\partial\Omega_\alpha}{\partial f_\beta}\right|_{|f\rangle = |f^{(0)}\rangle} \equiv \Omega_{\alpha,\beta}(\{f_\alpha^{(0)}\}). \tag{20}$$

In the moment space $\mathbf{M}$, the linearized collision operator can be easily obtained by using Eqs. (15) and (16):

$$\mathsf{C}_{\beta\alpha} = \frac{\langle\varrho_\beta|\varrho_\beta\rangle}{\langle\varrho_\alpha|\varrho_\alpha\rangle}\left.\frac{\partial\Delta\varrho_\alpha}{\partial\varrho_\beta}\right|_{|\varrho\rangle = |\varrho^{(0)}\rangle}, \tag{21}$$

where ϱ_α and $|\varrho_\alpha\rangle$, $\alpha = 0,1,\ldots,(b-1)$ are the moments defined by Eqs. (11) and the corresponding vectors in $\mathbf{V} = \mathbb{R}^9$ defined by Eqs. (9); $\Delta\varrho_\alpha$ is the change of the moment due to collision given by Eqs. (15); $|\varrho\rangle = |\varrho^{(0)}\rangle$ is the vector of all moments at the uniform equilibrium state [see Eq. (12) for the definition of $|\varrho\rangle$]. Obviously the linearized collision

operator C depends on the uniform state specified by density ρ and velocity $\mathbf{V}=(V_x,V_y)$, upon which the perturbation $|\delta f\rangle$ is superimposed. Specifically, for the nine-velocity model,

$$\mathsf{C}=\begin{pmatrix} 0 & 0 & 0 & 0 & 0 & 0 & 0 & 0 & 0 \\ s_2\alpha_2/4 & -s_2 & 0 & s_2\gamma_2V_x/3 & 0 & s_2\gamma_2V_y/3 & 0 & 0 & 0 \\ s_3\alpha_3/4 & 0 & -s_3 & s_3\gamma_4V_x/3 & 0 & s_3\gamma_4V_y/3 & 0 & 0 & 0 \\ 0 & 0 & 0 & 0 & 0 & 0 & 0 & 0 & 0 \\ 0 & 0 & 0 & s_5c_1/2 & -s_5 & 0 & 0 & 0 & 0 \\ 0 & 0 & 0 & 0 & 0 & 0 & 0 & 0 & 0 \\ 0 & 0 & 0 & 0 & 0 & s_7c_1/2 & -s_7 & 0 & 0 \\ 0 & 0 & 0 & 3s_8\gamma_1V_x & 0 & -3s_8\gamma_1V_y & 0 & -s_8 & 0 \\ 0 & 0 & 0 & 3s_9\gamma_3V_y/2 & 0 & 3s_9\gamma_3V_x/2 & 0 & 0 & -s_9 \end{pmatrix}. \tag{22}$$

The perturbation in the moments corresponding to $|\delta f\rangle$ is $|\delta\varrho\rangle$, and $|\delta\varrho\rangle=\mathsf{M}|\delta f\rangle$. The change of the perturbation due to collisions is linearly approximated by $|\Delta\varrho\rangle=\mathsf{C}|\delta\varrho\rangle$ in the moment space $\mathbf{M}$ spanned by $\{|\varrho_\alpha\rangle|\alpha=0,1,\ldots,(b-1)\}$. This change of state in discrete velocity space $\mathbf{V}$ is $|\Delta f\rangle=\mathsf{M}^{-1}\mathsf{C}|\delta\varrho\rangle$. Therefore, Eq. (19) becomes

$$|\delta f(\mathbf{r}_j+\mathbf{e}_\alpha,t+1)\rangle=|\delta f(\mathbf{r}_j,t)\rangle+\mathsf{M}^{-1}\mathsf{C}\mathsf{M}|\delta f(\mathbf{r}_j,t)\rangle. \tag{23}$$

In Fourier space, the above equation becomes

$$\mathsf{A}|\delta f(\mathbf{k},t+1)\rangle=[\mathsf{I}+\mathsf{M}^{-1}\mathsf{C}\mathsf{M}]|\delta f(\mathbf{k},t)\rangle, \tag{24}$$

where A is the advection operator represented by the following diagonal matrix in discrete velocity space $\mathbf{V}=\mathbf{R}^9$:

$$\mathsf{A}_{\alpha\beta}=\exp(i\mathbf{e}_\alpha\cdot\mathbf{k})\delta_{\alpha\beta}, \tag{25}$$

where $\delta_{\alpha\beta}$ is the Kronecker delta. It should be noted that for a mode of wave number $\mathbf{k}=(k_x,k_y)$ in Cartesian coordinates, the advection operator A in the above equation can be written as follows:

$$\mathsf{A}=\mathrm{diag}(1,p,q,1/p,1/q,pq,q/p,1/pq,p/q), \tag{26}$$

where

$$p=e^{ik_x},\quad q=e^{ik_y}. \tag{27}$$

The advection can be decomposed into two parts, along two orthogonal directions, such as x axis and y axis in Cartesian coordinates:

$$\mathsf{A}(k_x)\equiv\mathsf{A}(k_x,k_y=0)=\mathrm{diag}(1,p,1,1/p,1,p,1/p,1/p,p),$$

$$\mathsf{A}(k_y)\equiv\mathsf{A}(k_x=0,k_y)=\mathrm{diag}(1,1,q,1,1/q,q,q,1/q,1/q),$$

and $\mathsf{A}(k_x)$ and $\mathsf{A}(k_y)$ commute with each other:

$$\mathsf{A}=\mathsf{A}(k_x)\mathsf{A}(k_y)=\mathsf{A}(k_y)\mathsf{A}(k_x),$$

i.e., the advection operation can be applied along the x direction first, and then along the y direction, or *vice versa*. The linearized evolution equation (24) can be further written in a concise form:

$$|\delta f(\mathbf{k},t+1)\rangle=\mathsf{L}|\delta f(\mathbf{k},t)\rangle, \tag{28}$$

where

$$\mathsf{L}\equiv\mathsf{A}^{-1}[\mathsf{I}+\mathsf{M}^{-1}\mathsf{C}\mathsf{M}], \tag{29}$$

is the linearized evolution operator.

V. MODES OF LINEARIZED LBE

A. Hydrodynamic modes and transport coefficients

The evolution equation (23) is a difference equation that has a general solution:

$$|G(\mathbf{r}_j,t=l)\rangle=K_x^mK_y^nz^l|G_0\rangle, \tag{30}$$

where m and n are indices for space ($\mathbf{r}_j=m\hat{\mathbf{x}}+n\hat{\mathbf{y}}$), and $\hat{\mathbf{x}}$ and $\hat{\mathbf{y}}$ are units vectors along the x axis and y axis, respectively; $|G_0\rangle$ is the initial state. We can consider the particular case of a periodic system such that the spatial dependence of the above general solution can be chosen as

$$|\delta f\rangle=\exp(-i\mathbf{k}\cdot\mathbf{r}_j+zt)|G(\mathbf{r}_j,t)\rangle. \tag{31}$$

By substituting Eqs. (30) and (31) into the linearized LBE (28), we obtain the following equation:

$$z|G_0\rangle=\mathsf{L}|G_0\rangle, \tag{32}$$

The above equation leads to the dispersion relation between z and $\mathbf{k}$:

$$\det[\mathsf{L}-z\mathsf{I}]=0, \tag{33}$$

which determines the transport behaviors of various modes depending on the wave vector $\mathbf{k}$. The solution of the above eigenvalue problem of the linearized evolution operator L provides not only the dispersion relation, but also the solution of the initial value problem of Eq. (28):

$$|\delta f(\mathbf{k},t)\rangle=\mathsf{L}^t|\delta f(\mathbf{k},0)\rangle=\sum_{\alpha=1}^{b}z_\alpha^t|z_\alpha\rangle\langle z_\alpha|\delta f(\mathbf{k},0)\rangle,$$

where $|z_\alpha\rangle$ is the eigenvector of L with eigenvalues z_α in discrete velocity space V.

The eigenvalue problem of Eq. (33) cannot be solved analytically in general, except for some very special cases. Nevertheless, it can be easily solved numerically using various packages for linear algebra, such as LAPACK. For small $\mathbf{k}$, it can be solved by a series expansions in $\mathbf{k}$. The only part of L that has $\mathbf{k}$ dependence is the advection operator A. Therefore, we can expand A^{-1} in L:

$$\mathsf{K}\equiv\mathsf{A}^{-1}=\mathsf{K}^{(0)}+\mathsf{K}^{(1)}(\mathbf{k})+\mathsf{K}^{(2)}(\mathbf{k}^2)+\cdots+\mathsf{K}^{(n)}(\mathbf{k}^n)+\cdots, \tag{34}$$

where $\mathsf{K}^{(n)}$ depends on $\mathbf{k}^n$:

$$\mathsf{K}^{(n)}_{\alpha\beta}=\frac{1}{n!}(-i\boldsymbol{k}\cdot\boldsymbol{e}_\alpha)^n\delta_{\alpha\beta}. \tag{35}$$

When $\mathbf{k}=\mathbf{0}$, the eigenvalue problem of the $(b\times b)$ matrix $\mathsf{L}^{(0)}=(\mathsf{I}+\mathsf{M}^{-1}\mathsf{C}\mathsf{M})$ can be solved analytically. There exists an eigenvalue of 1 with threefold degeneracy, which corresponds to three hydrodynamic (conserved) modes in the system: one transverse (shear) and two longitudinal (sound) modes. It is interesting to note that when $\mathbf{k}=(\pi,0)$ or $\mathbf{k}=(0,\pi)$, L also has an eigenvalue of -1, which corresponds to the checkerboard mode, i.e., it is a conserved mode of L^2. Being a neutral mode as far as stability is concerned, it will be necessary to study how it is affected by a mean velocity $\mathbf{V}$. Thus we shall have to analyze the model for k ranging from 0 to π, which the standard Chapman-Enskog analysis cannot do.

The hydrodynamic modes at $\mathbf{k}=\mathbf{0}$ are

$$|\varrho_T\rangle=\cos\theta|j_x\rangle-\sin\theta|j_y\rangle\equiv|j_T\rangle, \tag{36a}$$

$$|\varrho_\pm\rangle=|\rho\rangle\pm(\cos\theta|j_x\rangle+\sin\theta|j_y\rangle)\equiv|\rho\rangle\pm|j_L\rangle, \tag{36b}$$

where θ is the polar angle of wave vector $\mathbf{k}$. For finite $\mathbf{k}$, the behavior of these hydrodynamic modes depends upon $\mathbf{k}$. In two-dimensional space, these linearized hydrodynamic modes behave as follows [37]:

$$\begin{aligned}|\varrho_T(t)\rangle&=z_T^t|\varrho_T(0)\rangle\\&=\exp[-ik(gV\cos\phi)t]\\&\quad\times\exp(-\nu k^2t)|\varrho_T(0)\rangle,\end{aligned} \tag{37a}$$

$$\begin{aligned}|\varrho_\pm(t)\rangle&=z_\pm^t|\varrho_\pm(0)\rangle\\&=\exp[\pm ik(c_s\pm gV\cos\phi)t]\\&\quad\times\exp[-(\nu/2+\zeta)k^2t]|\varrho_\pm(0)\rangle,\end{aligned} \tag{37b}$$

where ν and ζ are the shear and bulk viscosity, respectively; the coefficient g indicates whether the system is Galilean invariant (that $g=1$ implies Galilean invariance); c_s is the sound speed; V is the magnitude of the uniform streaming velocity of the system $\mathbf{V}=(V_x,V_y)$; and ϕ is angle between the streaming velocity $\mathbf{V}$ and the wave vector $\mathbf{k}$. The Galilean-coefficient $g(\mathbf{k})$ is similar to the g factor in the Frish-Hasslacher-Pomeau lattice gas automata [15–17], which also determines the Galilean invariance of the system.

The transport coefficients and the Galilean-coefficient are related to the eigenvalues of L as the following:

$$\nu(\mathbf{k})=-\frac{1}{k^2}\mathrm{Re}[\ln z_T(\mathbf{k})], \tag{38a}$$

$$g(k)V\cos\phi=-\frac{1}{k}\mathrm{Im}[\ln z_T(\mathbf{k})], \tag{38b}$$

$$\frac{1}{2}\nu(\mathbf{k})+\zeta(\mathbf{k})=-\frac{1}{k^2}\mathrm{Re}[\ln z_\pm(\mathbf{k})], \tag{38c}$$

$$c_s(\mathbf{k})\pm g(\mathbf{k})V\cos\phi=\mp\frac{1}{k}\mathrm{Im}[\ln z_\pm(\mathbf{k})], \tag{38d}$$

where $z_T(\mathbf{k})$ and $z_\pm(\mathbf{k})$ are the eigenvalues corresponding to the hydrodynamic modes of the linearized evolution operator L. Since the transport coefficients can be obtained through a perturbation analysis, we shall use the following series expansion in $\mathbf{k}$:

$$\nu(\mathbf{k})=\nu_0-\nu_1k^2+\ldots+(-1)^n\nu_nk^{2n}+\cdots, \tag{39a}$$

$$\zeta(\mathbf{k})=\zeta_0-\zeta_1k^2+\ldots+(-1)^n\zeta_nk^{2n}+\cdots, \tag{39b}$$

$$c_s(\mathbf{k})=C_0-C_1k^2+\ldots+(-1)^nC_nk^{2n}+\cdots, \tag{39c}$$

$$g(\mathbf{k})=g_0-g_1k^2+\ldots+(-1)^ng_nk^{2n}+\cdots. \tag{39d}$$

It should be noted that, in the usual Chapman-Enskog analysis of LBE models, one only obtains the values of the transport coefficients at $\mathbf{k}=\mathbf{0}$. As we shall demonstrate later, higher-order corrections to the transport coefficients (i.e., hyperviscosities) are important to the LBE hydrodynamics, especially for spatial scales of a few lattice spacings.

One possible method by which to solve the dispersion relation $\det[\mathsf{L}-z\mathsf{I}]=0$ is to apply the Gaussian elimination technique using $1/s_\alpha$ as small parameters for the nonconserved modes (the kinetic modes). Starting from a 9×9 ($b\times b$ in general) determinant, we obtain a 3×3 determinant for the three conserved modes. The elements of this new determinant are computed as a series of $1/s_\alpha$ and $\mathbf{k}$ with the necessary numbers of terms to achieve a given accuracy when computing the roots of the dispersion equation.

It should be mentioned that the value of the present technique is that it provides a very simple means by which to analyze models with various streaming and collision rules with as many adjustable parameters as possible to be determined later when trying to satisfy either the stability criteria or physical requirements to model various hydrodynamic systems. Free parameters are the equilibrium coefficients in Eqs. (16): c_1, α_i, and γ_i; and relaxation rates s_α.

B. Case with no streaming velocity ($V=0$)

We first consider the case in which the streaming velocity $\mathbf{V}=\mathbf{0}$. To the first order in $\mathbf{k}$, we obtain two solutions of $\mathrm{Im}(\ln z_\pm)=\mp ikc_s$ with

$$c_s^2=\frac{1}{3}\left(2+\frac{\alpha_2}{8}\right). \tag{40}$$

These are the sound modes supported by the medium. At the next order, we obtain modes with $\mathrm{Re}(\ln z_T)=-\nu_0 k^2$. To enforce isotropy we need to have

$$\frac{1}{s_9}-\frac{1}{2}=2\left(\frac{1}{s_8}-\frac{1}{2}\right)\frac{(c_1+4)}{(2-c_1)}, \tag{41}$$

such that the θ dependence in ν_0 vanishes,

$$\nu_0=\frac{(2-c_1)}{12}\left(\frac{1}{s_8}-\frac{1}{2}\right), \tag{42}$$

which can be interpreted as the shear viscosity of the medium in the limit $\mathbf{k}=\mathbf{0}$ (measured in basic units of space and time). For the sound modes, we also find an attenuation rate $\mathrm{Re}(\ln z_\pm)=-(\nu_0/2+\zeta_0)k^2$ where $(\nu_0/2+\zeta_0)$ is the longitudinal kinematic viscosity in a two-dimensional system. The bulk viscosity of the model at long-wave-length limit $\mathbf{k}=\mathbf{0}$ is

$$\zeta_0=\frac{(c_1+10-12c_s^2)}{24}\left(\frac{1}{s_2}-\frac{1}{2}\right). \tag{43}$$

The positivity of the transport coefficients leads to the bounds on the adjustable parameters:

$$-16<\alpha_2, \tag{44a}$$

$$-4<c_1<2, \tag{44b}$$

and the bounds on the following relaxation parameters:

$$0<s_2<2, \tag{45a}$$

$$0<s_8<2. \tag{45b}$$

The bounds for α_2 and c_1 will be further narrowed in the following analysis. Based upon the above results of ν_0, ζ_0, and c_s, it is clear that the model is isotropic at rest (i.e., the streaming velocity $\mathbf{V}=\mathbf{0}$) and in the limit of $\mathbf{k}=\mathbf{0}$. The Galilean-coefficient g cannot be determined when the streaming velocity $V=0$. Therefore, the case of a finite streaming velocity $\mathbf{V}$ is considered next.

C. Case with a constant streaming velocity V

As indicated by Eqs. (38), to the first order in $\mathbf{k}$, the three hydrodynamic roots of the dispersion equation (z_T and $z_\pm$) give the phase $gV\cos\phi$ and the sound speed c_s. In order to cause the root of the transverse mode (z_T) to have a correct phase corresponding to the streaming velocity $\mathbf{V}$, as expected for a model satisfying Galilean invariance, i.e., $g_0=1$, we must set

$$\gamma_1=\gamma_3=\frac{2}{3}. \tag{46}$$

If we further set

$$\gamma_2=18, \tag{47}$$

then we obtain the roots of the sound modes ($z_\pm$) which lead to the sound speed

$$C_s=V\cos\phi\pm\sqrt{c_s^2+V^2\cos^2\phi}, \tag{48}$$

where $V\cos\phi\equiv\mathbf{V}\cdot\hat{\mathbf{k}}$, and $\hat{\mathbf{k}}$ is the unit vector parallel to $\mathbf{k}$. This clearly shows that the system obeys Galilean invariance only up to first order in $\mathbf{V}$. One way to correct this defect is to allow for compressibility effects in the equilibrium properties, as shown in Appendix A. The dispersion of sound can be computed either analytically, by carrying out the perturbation expansion in $\mathbf{k}$, or numerically, by solving the eigenvalue problem for any value of $\mathbf{k}$. The dispersion of sound is important when studying the nonlinear acoustic properties of the medium.

Second, the attenuation of the transverse wave depends not only on $\mathbf{V}$ but also on the direction of the wave vector $\mathbf{k}$. In order to eliminate the anisotropy in the $\mathbf{V}$ dependence of the shear wave attenuation, we must choose

$$c_1=-2. \tag{49}$$

With the above choice of c_1, the shear viscosity in the limit of $\mathbf{k}=\mathbf{0}$ is given by

$$\begin{aligned}\nu_0=&[s_2(2-s_8)[c_s^2+(1-3c_s^2)V^2\cos^2\phi]+3[2(s_8-s_2)\\&+s_8(s_2-2)\cos^2\phi]V^4\cos^2\phi]/[6s_2s_8\\&\times(V^2\cos^2\phi+c_s^2)].\end{aligned} \tag{50}$$

Similarly, from the attenuation of acoustic waves, one obtains the bulk viscosity (in the limit of $\mathbf{k}=\mathbf{0}$) that has a complicated dependence on the streaming velocity $\mathbf{V}$:

$$\begin{aligned}\zeta_0=&(V\cos\phi\sqrt{V^2\cos^2\phi+c_s^2}\{12V^2[(s_2-s_8)\\&+s_2(s_8-2)\cos^2\phi]+(2s_2-3s_2s_8+4s_8)(1-3c_s^2)\}\\&+3V^4\cos^2\phi[\cos^2\phi(2s_8+3s_2s_8-8s_2)+6(s_2-s_8)]\\&+2V^2\cos^2\phi[6(s_2s_8-s_2-s_8)c_s^2+s_8(2-s_2)]\\&+c_s^2[6V^2(s_2-s_8)+s_8(2-s_2)\\&\times(2-3c_s^2)])/\{12s_2s_8(V^2\cos^2\phi+c_s^2)\}.\end{aligned} \tag{51}$$

It is obvious that the streaming velocity $\mathbf{V}$ has a second order effect on ν_0, and a first-order effect on ζ_0. A careful inspection of the above result of ζ_0 indicates that the first-order effect of $\mathbf{V}$ on ζ_0 can be eliminated by setting $c_s^2=1/3$ (or, equivalently, $\alpha_2=-8$). Furthermore, the second-order effect of $\mathbf{V}$ on the sound speed and the longitudinal attenuation can also be eliminated by using a slightly more complicated model with thirteen velocities, as noted by a previous work [38].

In summary, although all the transport coefficients are isotropic in the limit $\mathbf{k}=\mathbf{0}$, some undesirable features of the LBE models can be clearly observed at the second order in $\mathbf{k}$ when the streaming velocity $\mathbf{V}$ has a finite magnitude. First, the acoustic wave propagation is not Galilean invariant. Second, both the shear and the bulk viscosities depend on $\mathbf{V}$. Nevertheless, these effects are of second order in $\mathbf{V}$, and can be improved to higher order in both $\mathbf{k}$ and $\mathbf{V}$ by incorporat-

ing compressibility into the equilibrium properties of the moments (see Appendix A) or using models with a larger velocity set.

D. Third-order result

The analysis in the preceding subsections shows that isotropy for the hydrodynamic modes of the dispersion equation can be attained to the first and second orders in $\mathbf{k}$ by carefully adjusting the parameters in the model. In the situation with a uniform streaming velocity $\mathbf{V}$ parallel to $\mathbf{k}$, we find that the third-order term in $\mathbf{k}$ for the shear mode is anisotropic, i.e.,

$$g_1=-\left(\frac{2}{3s_8^2}-\frac{2}{3s_8}+\frac{1}{9}\right)+\left(\frac{1}{3}-\frac{2}{s_8}+\frac{2}{s_8^2}\right)V^2\cos^2\phi + \left[\frac{1}{3}-\frac{1}{s_8}+\frac{1}{s_5}\left(\frac{2}{s_8}-1\right)\right]\left(\cos^4\theta-\cos^2\theta+\frac{1}{3}\right). \tag{52}$$

The anisotropic term in g_1 (depending on $\cos\theta$) can be eliminated if we choose

$$s_5=3\frac{(2-s_8)}{(3-s_8)}. \tag{53}$$

As indicated by Eq. (42), parameter s_8 is usually chosen close to 2 from below in order to obtain a small shear viscosity (and, consequently, a large Reynolds number). Therefore, the preceding expression yields a small value for s_5. This would lead to an undesirable consequence: Mode $|q_x\rangle$ relaxed with the relaxation parameter s_5 would become a quasiconserved mode leading to some sort of viscoelastic effect [14]. Therefore, we usually choose to have large s_5 such that the advection coefficient of transverse waves has an angular dependence for nonzero $\mathbf{k}$ in third order in $\mathbf{k}$. That is, the physical conservation laws are preserved at the expense of the isotropy of the dispersion in third order (and all higher orders) in $\mathbf{k}$.

It should be noted that the value of g has effects on the Reynolds number because the time t needs to be rescaled as gt.

E. Optimization of the model and connection to the BGK LBE model

Among seven adjustable parameters (c_1, α_i, and γ_i) in the equilibrium values of the moments in the model [see Eqs. (16)], so far only five of these parameters have been fixed by enforcing the model to satisfy certain basic physics as shown in the preceding analysis: $c_1=-2$, $\alpha_2=-8$, $\gamma_1=\gamma_3=2/3$, and $\gamma_2=18$. These parameter values are the optimal choice in the sense that they yield the desirable properties (isotropy, Galilean invariance, etc.) to the highest order possible in wave vector $\mathbf{k}$. It should be stressed that the constraints imposed by isotropy and Galilean invariance are beyond the conservation constraints — models with only conservation constraints would not necessarily be isotropic and Galilean invariant in general, as observed in some newly proposed LBE models for nonideal gases [39,40,9]. Two other parameters, α_3 and γ_4, remain adjustable. In addition, there are six relaxation parameters s_i in the model as opposed to one in the LBE BGK model. Two of them, s_2 and s_8, determine the bulk and the shear viscosities, respectively. Also, because $c_1=-2$, $s_9=s_8$ [see Eq. (41)]. The remaining three relaxation parameters, s_3, s_5, and s_7, can be adjusted without having any effect on the transport coefficients in the order of $\mathbf{k}^2$. However, they do have effects in higher-order terms. Therefore, one can keep values of these three relaxation parameters only slightly larger than 1 (no severe overrelaxation effects are produced by these modes) such that the corresponding kinetic modes are well separated from those modes more directly affecting hydrodynamic transport.

It is interesting to note that the present model degenerates to the BGK LBE model [2,3] if we use a single relaxation parameter for all the modes, i.e., $s_\alpha=1/\tau$, and choose

$$\alpha_3=4, \tag{54a}$$

$$\gamma_4=-18. \tag{54b}$$

Therefore, in the BGK LBE model, all the modes relax with exactly the same relaxation parameter so there is no separation in time scales among the kinetic modes. This may severely affect the dynamics and the stability of the system, due to the coupling among these modes.

VI. LOCAL STABILITY ANALYSIS

The stability of the LBE method has not been well understood, although there exists some preliminary work [41,42]. However, previous work does not provide much theoretical insight into either the causes or the remedies for the instability of the LBE method. In the following analysis, a systematic procedure that identifies some causes of instability is discussed and illustrated by some examples.

Our stability analysis relies on the eigenvalue problem for the linearized evolution operator L, the dispersion equation. For large values of $\mathbf{k}$, one could in principle analyze the dispersion equation to higher order by perturbation expansion. In practice, it is more efficient to compute the roots of the dispersion equation numerically. We shall try to identify the conditions under which one of the modes becomes unstable: instability occurs when $\mathrm{Re}(\ln z_\alpha)<0$.

We have noticed some interesting qualitative properties of the dispersion for the nine-velocity model when wave vector $\mathbf{k}$ is parallel to certain special directions with respect to the lattice line. These properties are listed in Table I. These qualitative behaviors of the dispersion equation already demonstrate the strong anisotropy of the dispersion relations dictated by the lattice symmetry.

To exhibit the complex behavior of the dispersion equation, we compute the roots of the dispersion equation with a given set of parameters. Figures 1(a) and 1(b) show the real and imaginary parts of the logarithm of the eigenvalues as functions of $\mathbf{k}$, respectively. Figure 1 clearly exhibits the coalescence and branching of the roots. This suggests a complicated interplay between the modes of collision operator affecting the stability of the model. The asymmetric feature of these curves is due to the presence of a constant streaming.

The growth rate of a mode $|z_\alpha\rangle$, $\mathrm{Re}(\ln z_\alpha)$, depends on all

TABLE I. Special properties of the dispersion relation when wave vector **k** is of some special values.

k	Dispersion equation	Conditions
(0,0)	$[z-1]^3=0$ $[z-(1-s_2)]=0$ $[z-(1-s_3)]=0$ $[z-(1-s_5)]^2=0$ $[z-(1-s_8)]^2=0$	$s_7=s_5$
$(\pm 1,0)\pi$ or $(0,\pm 1)\pi$	$[z+1]=0$ $[z+(1-s_5)]=0$ or $[z+(1-s_7)]=0$ $[z+(1-s_8)]=0$ or $[z+(1-s_9)]=0$ $[z^2-\frac{1}{3}s_5z+s_5-1]=0$ $[z^4+\frac{1}{3}(s_3-2s_2)z^3$ $+\frac{1}{9}\{s_2(s_8-4s_3)-6s_3s_8+9(s_2+s_3+s_8-2)\}z^2$ $+\frac{1}{3}(s_8-1)(s_2(s_3-2)+s_3)z$ $+(1-s_2)(1-s_3)(1-s_8)]=0$	
$(\pm 1,\pm 1)\pi$	$[z-(1-s_8)]^2=0$ $[z^2-\frac{1}{3}s_5z+s_5-1]^2=0$ $[z^3+\frac{1}{9}(11s_2-3s_3-9)z^2$ $+\frac{1}{9}\{3(4s_3-3)-s_2(s_3+2)\}z$ $+(1-s_2)(1-s_3)]=0$	

the adjustable parameters: the relaxation parameters, the streaming velocity **V**, and the wave vector **k**. To illustrate this dependence, we consider the BGK LBE model with $1/\tau=1.99$. Figure 2 shows the growth rate for the most unstable mode as a function of streaming velocity **V** and wave vector **k**. For each **V**, we let **k** be parallel to **V**, with a polar angle θ with respect to the x axis. Then we search for the most unstable mode in the interval $0\leq k\leq\pi$. For the nine-velocity BGK LBE model, the unstable mode starts to appear above $V\approx 0.07$. Figure 2 shows the strong anisotropy of the unstable mode: the growth rate significantly depends on the direction of **k**, and the critical value of **k** at which the unstable mode starts to appear is also strongly anisotropic. We also compute the growth rate for the most unstable mode with **V** perpendicular to **k**, and find that the stability of the model is generally qualitatively the same as when **V** is parallel to **k**, but is slightly more stable. Generally, we find that the transverse mode is more stable than longitudinal modes. In many instances we have observed that sound waves propagating in the direction of the mean flow velocity **V** can be quite unstable. This instability may be reduced by making the first-order **V**-dependent term in the attenuation of the sound waves [ζ_0 in Eq. (51)] equal to 0 by choosing $c_s^2=1/3$, as indicated in the preceding section. It should be noted that when the growth rate is infinitesimal, it takes an extremely long time for the instability to develop in simulations. Because the unstable modes we have observed have a large wave vector k (small spatial scale), as a practical means of reducing the effect of instabilities in LBE simulations, some kind of spatial or temporal filtering technique may be used in the LBE schemes to reduce small-scale fluctuations and thus to limit the development of instabilities.

It should be pointed out that we do not discuss here the influence of boundary conditions that may completely change the stability behavior of the model through either

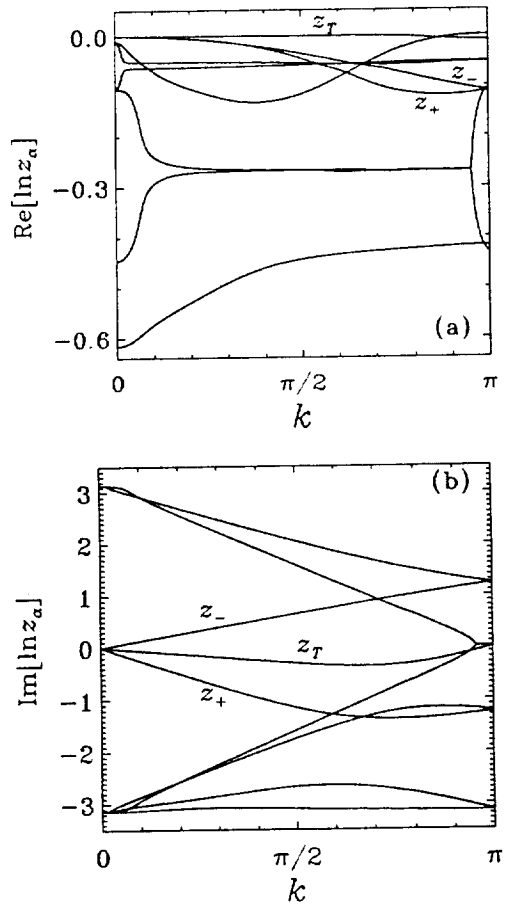

FIG. 1. Logarithmic eigenvalues of the nine-velocity model. The values of the parameters are $\alpha_2=-8$, $\alpha_3=4$, $c_1=-2$, $\gamma_1=\gamma_3=2/3$, $\gamma_2=18$, and $\gamma_4=-18$. The relaxation parameters are $s_2=1.64$, $s_3=1.54$, $s_5=s_7=1.9$, and $s_8=s_9=1.99$. The streaming velocity **V** is parallel to **k** with $V=0.2$, and **k** is along the x axis. (a) $\mathrm{Re}(\ln z_\alpha)$ and (b) $\mathrm{Im}(\ln z_\alpha)$.

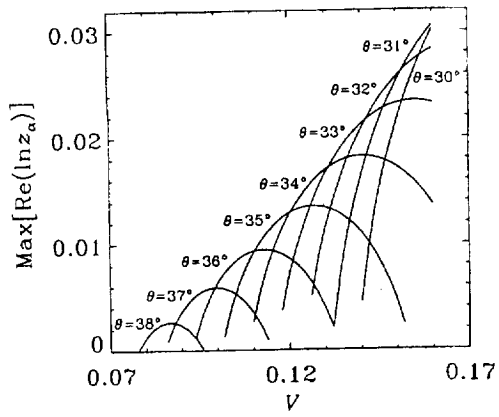

FIG. 2. Growth rate of the most unstable mode for the BGK LBE model $-\ln z_\alpha$ vs the streaming velocity magnitude V. The relaxation parameter $s_8=1/\tau=1.99$. The wave vector $\mathbf{k}$ is set parallel to the streaming velocity $\mathbf{V}$. For each value of $\mathbf{V}$ with a polar angle θ with respect to the x axis, the growth rate is computed in the interval $0<k\leq\pi$ in $\mathbf{k}$ space. Each curve corresponds to the growth rate of the most unstable mode with a given $\mathbf{V}$, and $\mathbf{k}$ parallel to $\mathbf{V}$ with the polar angle θ with respect to the x axis.

large-scale genuine hydrodynamic behavior or local excitation of Knudsen modes.

As previously indicated, the adjustable parameters in our model can be used to alter the properties of the model. The stability of the BGK LBE model and our model is compared in Fig. 3. In this case we choose the adjustable parameters in our model to be the same as the BGK LBE model, but maintain the freedom of different modes to relax with different relaxation parameters s_α. Figure 2 shows that for each given value of $\mathbf{V}$, there exists a maximum value of $s_8=1/\tau$ (which determines the shear viscosity) below which there is no unstable mode. The values of other relaxation parameters used in our model are $s_2=1.63$, $s_3=1.14$, $s_5=s_7=1.92$, and $s_9=s_8=1/\tau$. Figure 3 clearly shows that our model is more stable than the BGK LBE model in the interval $1.9\leq s_8=1/\tau\leq 1.99$. Therefore, we can conclude that by carefully separating the kinetic modes with different relaxation rates, we can indeed improve the stability of the LBE model significantly.

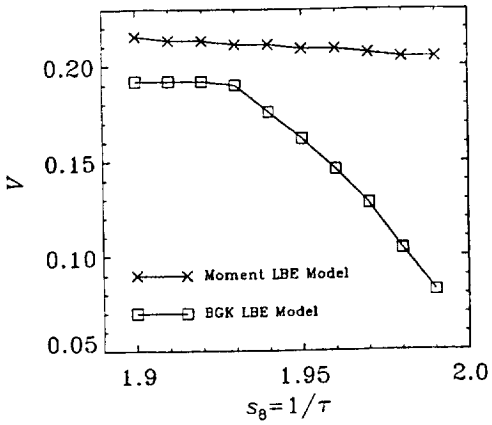

FIG. 3. Stability of the generalized LBE model vs the BGK LBE model in the parameter space of V and $s_8=1/\tau$. The lines with symbols □ and × are results for the BGK LBE model and the model proposed in this work, respectively. The region under each curve is the stable region in the parameter space of V and $s_8=1/\tau$. Note that the stability of the BGK LBE model starts to deteriorate after $s_8\geq 1.92$, whereas the stability of the proposed generalized LBE model remains virtually intact.

VII. NUMERICAL SIMULATIONS OF SHEAR FLOW DECAY

To illustrate the dispersion effects on the shear viscosity in hydrodynamic simulations using the LBE method, we conduct a series of numerical simulations of the shear flow decay with different initial velocity profiles. The numerical implementation of the model is discussed next.

A. Numerical implementation and initial conditions

The evolution of the model still consists of two steps: advection and collision. The advection is executed in discrete velocity space, namely, to $|f(\mathbf{x},t)\rangle$, but not to the moments $|\varrho(\mathbf{x},t)\rangle$. However, the collision is executed in moment space. Therefore, the evolution involves transformation between discrete velocity space $\mathbf{V}$ and moment space $\mathbf{M}$, similar to Fourier transform in the spectral or Galerkin methods. The evolution equation of the model is

$$|f(\mathbf{x}+\mathbf{e}_\alpha\delta_t,t+\delta_t)\rangle=|f(\mathbf{x},t)\rangle+\mathsf{M}^{-1}\mathsf{S}[|\varrho(\mathbf{x},t)\rangle-|\varrho^{(\mathrm{eq})}\rangle], \tag{55}$$

where S is the diagonal relaxation matrix:

$$\mathsf{S}\equiv\mathrm{diag}(0,-s_2,-s_3,0,-s_5,0,-s_7,-s_8,-s_9). \tag{56}$$

In simulations using the LBE method, the initial conditions provided are usually specified by velocity and pressure (density) fields. Often the initial condition of f_α is set to its equilibrium value corresponding to the given flow fields, with a constant density if the initial pressure field is not specified. The initial conditions of f_α can include the first-order effect $f_\alpha^{(1)}$. The first-order effect in moment space is obtained through Eq. (55):

$$|\varrho^{(1)}\rangle=\mathsf{S}^{-1}\mathsf{M}\mathsf{D}|f^{(\mathrm{eq})}\rangle, \tag{57}$$

where D is a diagonal differential operator:

$$\mathsf{D}_{\alpha\beta}=\delta_{\alpha\beta}\mathbf{e}_\alpha\cdot\nabla. \tag{58}$$

Equation (57) is similar to Chapman-Enskog analysis of $f_\alpha^{(1)}$.

For the shear flow, only the initial velocity profile is given. The density mode is set to be uniform initially. The remaining modes are initialized as the following:

$$\rho=1, \tag{59a}$$

$$e=-2+3(u_x^2+u_y^2), \tag{59b}$$

$$\varepsilon=1-3(u_x^2+u_y^2), \tag{59c}$$

$$q_x=-u_x, \tag{59d}$$

$$q_y=-u_y, \tag{59e}$$

$$p_{xx}=(u_x^2-u_y^2)-\frac{2}{3s_8}(\partial_x u_x-\partial_y u_y), \tag{59f}$$

$$p_{xy}=u_x u_y-\frac{1}{3s_8}(\partial_y u_x+\partial_x u_y). \tag{59g}$$

The terms in p_{xx} and p_{xy} involving derivatives of the velocity field take into account viscous effects in the initial conditions. These terms are obtained through Eq. (57). The first-order terms in turn induce second-order contributions (with respect to space derivatives) which are not included here. This leads to weak transients of short duration if there is separation of time scales $(2-s_8)\ll(2-s_5)$.

Our first test is the decay of a sinusoidal wave in a periodic system for various values of $\mathbf{k}$. The numerical and theoretical results agree with each other extremely well and confirm the $\mathbf{k}$ dependence of g and ν. The agreement indicates that our local analysis is indeed sufficiently accurate in this case.

The next case considered is more interesting and revealing because the initial velocity contains shocks. Consider a periodic domain of size $N_x\times N_y=84\times 4$. At time $t=0$, we take a shear wave $u_y(x,0)$ of rectangular shape (discontinuities in u_y at $x=N_x/4$ and $x=3N_x/4$):

$$u_y(x,0)=U_0, \quad 1<x\leq N_x/4,$$

$$3N_x/4<x\leq N_x,$$

$$u_y(x,0)=-U_0, \quad N_x/4<x\leq 3N_x/4.$$

The initial condition $u_x(x,0)$ is set to a constant everywhere. We consider two separate cases with and without a constant streaming velocity $\mathbf{V}$.

B. Steady case (V=0)

For the case of zero streaming velocity, the initial condition for u_x is zero in the system. The solution of the Navier-Stokes equation for this simple problem is

$$u_y(x,t)=\sum_n a_n \exp(-\nu_n k_n^2 t)\cos(k_n x), \tag{60}$$

where a_n is the Fourier coefficient of the initial velocity profile $u_y(x,0)$, $\nu_n\equiv\nu(k_n)$, and $k_n=2\pi(2n-1)/N_x$. The magnitude of the $u_y(x,0)$, $U_0=0.0001$ in the simulations.

Figures 4(a) and 4(b) show the decay of the rectangular shear wave simulated by the normal LBE scheme and the LBE scheme with second-order central interpolation (with $r=0.5$, where r is the ratio between advection length δ_x and grid size Δ_x), respectively. (The detailed analysis of LBE schemes with various interpolations is provided in Appendix B.) The lines are theoretical results of Eq. (60) with $\nu(k_n)$ obtained numerically. The times at which the profile of $u_y(x,t)$ (normalized by U_0) shown in Fig. 4 are $t=100, 200, \ldots, 500$. The numerical and theoretical results agree closely with each other. The close agreement shows the accuracy of the theory. In Fig. 4(b), the overshoots at early times due to the discontinuous initial condition are well captured by the analysis. This overshoot is entirely due to the strong $\mathbf{k}$ dependence of $\nu(\mathbf{k})$ caused by the interpolation. This phenomena is not necessarily connected to the Burnett effect, as claimed by a previous work [46]. This artifact is also commonly observed in other CFD methods involving interpolations.

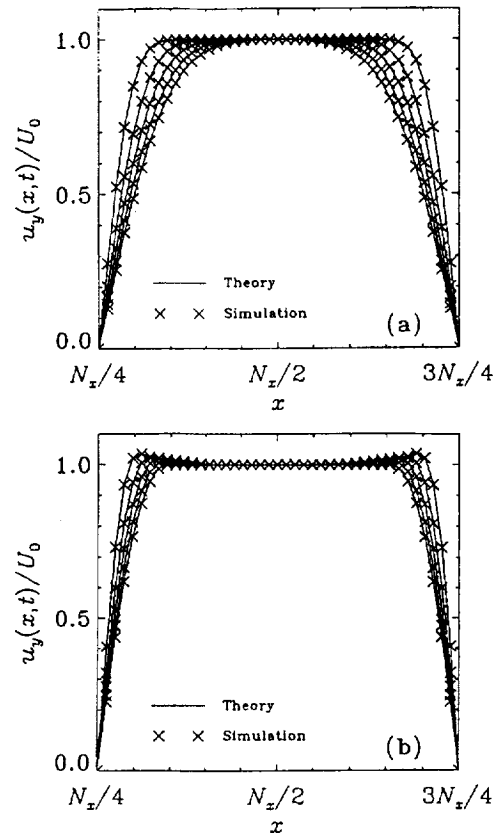

FIG. 4. Decay of discontinuous shear wave velocity profile $u_y(x,t)$. The lines and symbols (×) are theoretical [Eq. (60)] and numerical results, respectively. Only the positive half of each velocity profile is shown. LBE model (a) with no interpolation, (b) with the central interpolation and $r=0.5$.

Figure 5 shows the decay of $u_y(x,t)$ at one location of

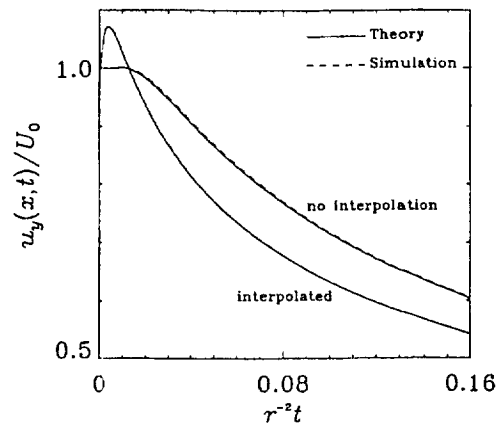

FIG. 5. Decay of discontinuous shear wave velocity $u_y(x,t)$ at a location close to the discontinuity $x=3N_x/4$. The solid lines and dashed lines are theoretical and numerical results, respectively. The LBE scheme with no interpolation does not have an overshooting, whereas the LBE scheme with central interpolation and $r=0.5$ has. The time is rescaled as $r^{-2}t$.

discontinuity, $x=3N_x/4=63$. We tested the normal LBE scheme without interpolation and the LBE scheme with second-order central interpolation with $r=0.5$, and compared the numerical results with theoretical ones. Again, the numerical and theoretical results agree very well with each other for both cases (with and without interpolation). Note that the time is rescaled as $r^{-2}t$ in the figure. It should be pointed out that the LBE solutions of the flow differ from the analytic solution of the Navier-Stokes equation in both short-time and long-time behavior. Interpolation causes overshoot in the velocity at the initial stage. Even without interpolation, the LBE solution does not decay (exponentially) right away. This is due to the variation of the viscosity with $\mathbf{k}$ and this could be interpreted as the influence of the kinetic modes. (If we had a vanishingly small Knudsen number, then the $\mathbf{k}$ dependence would be negligible; however, all relaxation rates must be smaller than 2 so that higher modes can play a role.) This transient behavior is due to the higher-order effect (of velocity gradient), as discussed previously.

C. Streaming case (V=constant)

We also consider the case with a constant streaming in the initial velocity, i.e., $u_x(x,0)=V_x=0.08$. This allows us to check the effects of the non-Galilean invariance in the system. With a constant streaming velocity, the solution of the Navier-Stokes equation is

$$u_y(x,t)=\sum_n a_n \exp(-\nu_n k_n^2 t)\cos[k_n(x-g_n V_x t)], \quad (61)$$

where $g_n \equiv g(k_n)$ is the Galilean coefficient.

Similarly to Fig. 4, Fig. 6 shows the evolution of $u_y(x,t)$ for the same times as in Fig. 4. The solid lines and the symbols ($\times$) represent theoretical and numerical results, respectively. Shocks move from left to right with a constant velocity $V_x=0.08$. Figures 6(a), 6(b), and 6(c) show the results for the normal LBE scheme without interpolation, the scheme with second-order central interpolation, and the scheme with second-order upwind interpolation, respectively. In Figs. 6(b) and 6(c), the dashed lines are the results obtained by setting $g_n=1$ in Eq. (61). Clearly, the effect of $g(\mathbf{k})$ is significant. For the LBE scheme with central interpolation, the results in Fig. 6(b) with $g(\mathbf{k})=1$ underpredict the overshooting at the leading edge of the shock and overpredict the overshooting at the trailing edge, whereas the results in Fig. 6(c) for the LBE scheme with upwind interpolation overpredict the overshooting at the leading edge of the shock and underpredict the overshooting at the trailing edge.

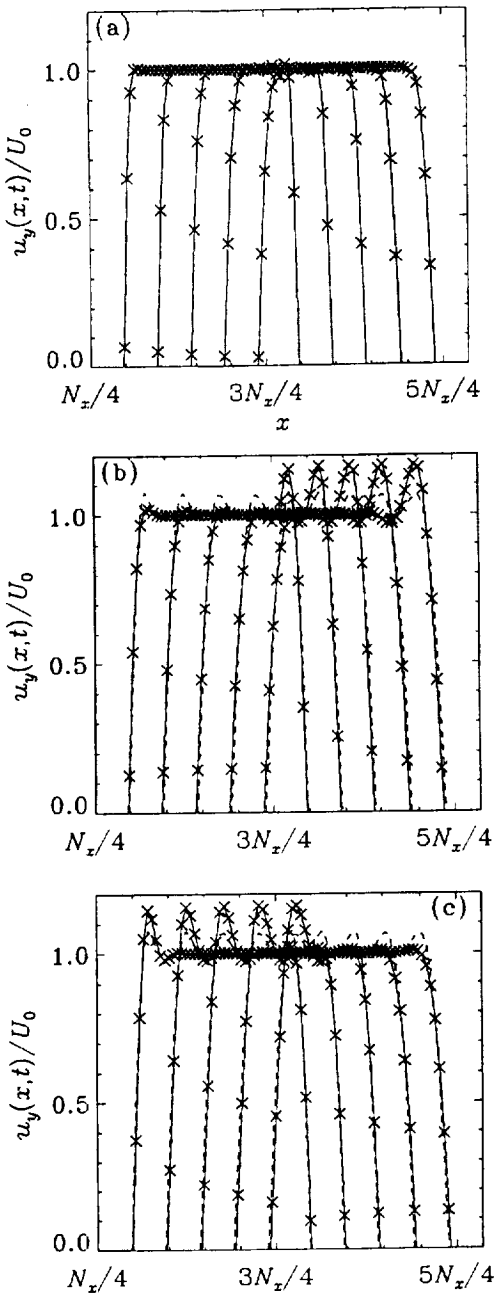

FIG. 6. Decay of discontinuous shear wave velocity profile $u_y(x,t)$ with a constant streaming velocity $V_x=0.08$. The solid lines and symbols ($\times$) are theoretical [Eq. (61)] and numerical results, respectively. The dashed lines in (b) and (c) are obtained by setting $g_n=1$ in Eq. (61). LBE model (a) with no interpolation, (b) with central interpolation and $r=0.5$, (c) with upwind interpolation and $r=0.5$.

VIII. CONCLUSION AND DISCUSSION

In this paper, a generalized nine-velocity LBE model based on the generalized LBE model of d'Humières [27] is presented. The model has the maximum number of adjustable parameters allowed by the discrete velocity set. The values of the adjustable parameters are obtained by optimizing the hydrodynamic properties of the model through the linear analysis of the LBE evolution operator. The linear analysis also provides the generalized hydrodynamics of the LBE model, from which dispersion, dissipation, isotropy, and stability of the model can be easily analyzed. In summary, a systematic and general procedure by which to analyze the LBE models is described in detail in this paper. Although the model studied in this paper is relatively simple, the proposed procedure can be readily applied to analyze more complicated LBE models.

The theoretical analysis of the model is verified through numerical simulation of various flows. The theoretical results closely predict the numerical results. The stability of the model is also analyzed and compared with the BGK LBE

model. It is found that the mechanism of separate relaxations for the kinetic modes leads to a model which is much more stable than the BGK LBE model.

The proposed model is a Galerkin type of scheme. In comparison with the BGK LBE model, the proposed model requires the transformations between the discrete velocity space V and the moment space M back and forth in each step in the evolution equation. However, the extra computational cost due to this transformation is only about 10–20 % of the total computing time. Thus, the computational efficiency is comparable to the BGK LBE model. Our analysis also shows that the LBE models with interpolation schemes have enormous numerical hyperviscosities and anisotropies due to the interpolations.

We also find optimal features of the proposed nine-velocity model: it is difficult to improve the model by simply adding more velocities. For instance, we found that adding eight more velocities $(\pm 1,\pm 2)$ and $(\pm 2,\pm 1)$ would not improve the isotropy of the model. However, our analysis does not provide any *a priori* knowledge of an optimal set of discrete velocities. That problem can only be solved by optimization of the moment problem in velocity space [24]. It is also worth noting that the values of all but two (α_3 and γ_4) of the adjustable parameters in our model coincide with the corresponding parameters in the BGK LBE model. The main distinction between our model and the BGK LBE model is that our model has the freedom to allow the kinetic modes to relax differently, whereas in the BGK LBE model, all kinetic modes relax at the same rate. This mechanism severely affects the stability of the BGK LBE schemes, especially when the system is strongly overrelaxed.

It should be mentioned that the procedure we propose here can be applied to analyze the linear stability of spatially nonuniform flows, such as the Couette flow, Poiseuille flow, or lid-driven cavity flow. For spatially nonuniform flows, the lattice Boltzmann equation is linearized over a finite domain including boundary conditions. This leads to an eigenvalue problem with many more degrees of freedom than was needed in the analysis of this paper. Standard Arnoldi techniques [47] allow us to determine parts of the spectrum of the linearized collision operator, in particular to study the flow stability. This analysis enables us to understand the observation that some flows are much more stable than what is predicted by the linear analysis of spatially uniform flows. For instance, in plane Couette flow with only two nodes along the flow direction, the only possible values of k along the same direction are 0 and π, which are far from the value of k at which the bulk instability occurs. Namely, the reciprocal lattice $\mathbf{k}$ is not large enough to accommodate the possible unstable modes. Furthermore, in the direction perpendicular to the flow, although the reciprocal lattice $\mathbf{k}$ can accommodate unstable shear modes, the velocity gradient, alters the stability of the system. (It improves the stability in this particular case.)

One philosophic point must be stressed. We deliberately did not derive the macroscopic equations corresponding to the LBE model in this work; instead, we only analyzed the generalized hydrodynamic behavior of the modes of the linearized LBE evolution operator. We argue that if the hydrodynamic modes behave exactly the same way as those of the linearized Navier-Stokes equations, up to a certain order of $\mathbf{k}$, provided that the Galilean invariance is also assured up to a certain order of $\mathbf{k}$, then we can claim that the LBE model is indeed adequate to simulate the Navier-Stokes equations (up to a certain order of $\mathbf{k}$). There is no distinction between the LBE model and the Navier-Stokes equations up to a certain order of $\mathbf{k}$. Thus, there is no need to use the Chapman-Enskog analysis to obtain the macroscopic equations from the LBE models. On the other hand, we have also shown that, in the limit of $\mathbf{k}=\mathbf{0}$, these two approaches obtain the same results in terms of the transport coefficients and the Galilean coefficient. Nevertheless, it is very difficult to apply the Chapman-Enskog analysis to obtain the generalized hydrodynamics of the LBE models, which is important to LBE numerical simulations of hydrodynamic systems. The stability result obtained by the linear analysis presented in this paper is very difficult for the standard Chapman-Enskog analysis to obtain. Therefore, the proposed procedure by which to analyze the LBE model indeed contains more information and is more general than the low-order Chapman-Enskog analysis. Despite its generality and power, the linear analysis has its limitations. Because it is a local analysis, it does not deal with gradients.

Our future work will extend the analysis to fully thermal and compressible LBE models in three-dimensional space.

ACKNOWLEDGMENTS

P.L. would like to acknowledge support from ICASE for his visit to ICASE in 1999, during which part of this work was done. L.S.L. would like to acknowledge support from CNRS for his visits to Laboratoire ASCI in 1998 during which part of this work was done, and partial support from NASA (Langley Research Center) under the program of Innovative Algorithms for Aerospace Engineering Analysis and Optimization. The authors would like to thank Professor D. d'Humières of Ecole Normale Supérieure and ASCI for many enlightening discussions, and are grateful to Dr. Robert Rubinstein of ICASE for his careful reading of the manuscript, to Dr. M. Salas, the director of ICASE, for his support and encouragement of this work, and to Professor W. Shyy and Professor R. Mei of the University of Florida for their insightful comments.

APPENDIX A: COUPLING BETWEEN DENSITY AND OTHER MODES

To consider the coupling between the density fluctuation $\delta\rho=\rho-\langle\rho\rangle$ and other modes, e, ε, p_{xx}, and p_{xy}, the equilibrium values of these modes are modified as to the following:

$$e^{(\mathrm{eq})}=\alpha_2\rho+\gamma_2(j_x^2+j_y^2)(2-\rho), \tag{A1a}$$

$$\varepsilon^{(\mathrm{eq})}=\alpha_3\rho+\gamma_4(j_x^2+j_y^2)(2-\rho), \tag{A1b}$$

$$p_{xx}^{(\mathrm{eq})}=\gamma_1(j_x^2+j_y^2)(2-\rho), \tag{A1c}$$

$$p_{xy}^{(\mathrm{eq})}=\gamma_3(j_xj_y)(2-\rho), \tag{A1d}$$

where $(2-\rho)$ is used to linearly approximate $1/\rho$ when the averaged density $\rho_0\equiv\langle\rho\rangle=1$. With the above modifications,

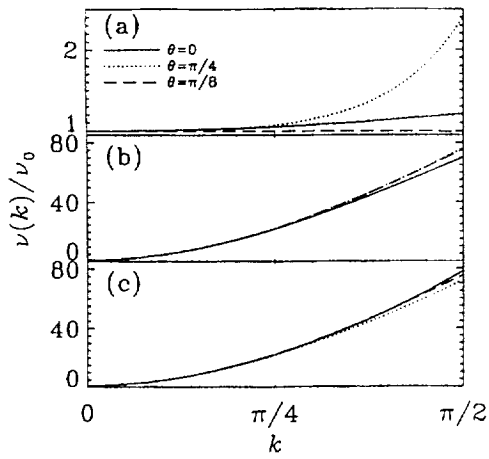

FIG. 7. k dependence of viscosities for various models. The values of the adjustable parameters and the relaxation parameters are the same as in Fig. 1. The solid lines, dotted lines, and dashed lines correspond to $\theta=0$, $\pi/8$, and $\pi/4$, respectively. LBE model (a) with no interpolation, (b) with central interpolation, and (c) with upwind interpolation.

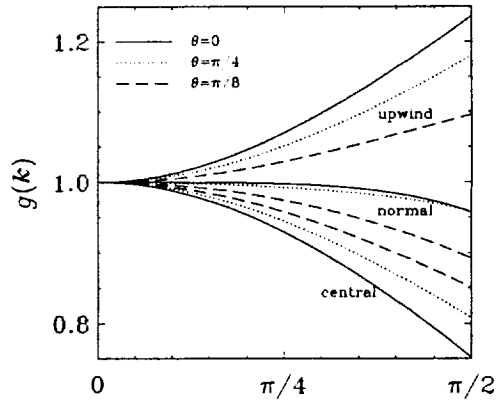

FIG. 8. k dependence of the Galilean coefficient g for various models. Solid lines, dotted lines, and dashed lines correspond to $\theta=0$, $\pi/8$, and $\pi/4$, respectively. The middle three curves are $g(\mathbf{k})$ for the LBE model without interpolation, the lower three for the LBE model with central interpolation and $r=0.5$, and the upper three for the LBE model with upwind interpolation and $r=0.5$.

four elements in the first column of the linearized collision operator C accordingly become

$$C_{12}=s_2\left[\frac{1}{4}\alpha_2-\frac{1}{6}\gamma_2(V_x^2+V_y^2)\right], \tag{A2a}$$

$$C_{13}=s_3\left[\frac{1}{4}\alpha_3-\frac{1}{6}\gamma_4(V_x^2+V_y^2)\right], \tag{A2b}$$

$$C_{18}=-\frac{3}{2}s_8\gamma_1(V_x^2-V_y^2), \tag{A2c}$$

$$C_{19}=-\frac{3}{2}s_9\gamma_3V_xV_y. \tag{A2d}$$

Based on the linearized collision operator with the above changes, the shear and the bulk viscosities at the limit of $\mathbf{k}\rightarrow\mathbf{0}$ are

$$\nu_0=\frac{1}{3}(1-V^2\cos^2\phi)\left(\frac{1}{s_8}-\frac{1}{2}\right), \tag{A3}$$

$$\begin{aligned}\zeta_0=&\frac{1}{12s_2^2}(2-3c_s^2)(2-s_2)\\&-\frac{V\cos\phi}{12c_ss_2s_8}(1-3c_s^2)(3s_2s_8-2s_2-4s_8)\\&+\frac{V^2}{4s_2s_8}[s_2-s_8+2(s_2s_8-s_2-s_8)\cos^2\phi]\\&+\frac{V^3\cos\phi}{4c_ss_2s_8}[s_2-s_8+s_2(s_8-2)\cos^2\phi].\end{aligned} \tag{A4}$$

The sound modes propagate with velocity $V\pm c_s$ (at first order in k). The Galilean coefficient up to $O(k^2)$ is

$$\begin{aligned}g=1+&\frac{k^2}{3s_5s_8^2}[(s_8-2)(s_5-s_8)(s_5s_8-3s_5-3s_8+6)\\&+(\cos^4\theta-\cos^2\theta)]+\frac{k^2V^2}{6c_s^2s_2s_8^2}[(2-s_8)(s_8-s_2)\sin^2\phi\\&+2c_s^2s_2(s_8^2-6s_8+6)\cos^2\phi].\end{aligned} \tag{A5}$$

APPENDIX B: INTERPOLATED LBE SCHEME

Recently, it has been proposed to use interpolation schemes to interpolate $\{f_\alpha\}$ from a fine mesh to a coarse mesh in order to improve the spatial resolution calculations for a limited cost in total number of nodes [43,44]. Obviously, the interpolation schemes create additional numerical viscosities. The Chapman-Enskog analysis shows that any second- or higher-order interpolation scheme does not affect the viscosities in the limit $\mathbf{k}\rightarrow\mathbf{0}$ on the fine mesh. A problem with much greater importance in practice is to calculate the viscosity at finite $\mathbf{k}$. To our knowledge, no such analysis is now available in the literature.

In the interpolated LBE schemes, the advection step is altered by the interpolation scheme chosen, while the collision step remains unchanged. The advection on a fine mesh combined with interpolation on a coarse mesh is the reconstruction step on the coarse mesh. Therefore, to obtain the modified linearized evolution operator L, only the advection operation A must be changed. In what follows, we shall consider a coarse mesh with lattice constant δ_x, and time step δ_t. The lattice constant of a underlying fine mesh is $r\delta_x$, with $r\leqslant 1$. Effectively, the hopping velocities of particles are reduced by a factor of r on coarse mesh. Therefore, dimensional analysis suggests that the sound speed is reduced by a factor of r, and the viscosities are reduced by a factor of r^2 in the limit $\mathbf{k}=\mathbf{0}$. However, the dimensional analysis does not provide any information about the quantitative effects of interpolation when $\mathbf{k}$ is finite. We shall analyze the effects of some commonly used second-order interpolation schemes in

the LBE methods. For simplicity, we shall only deal with a uniform mesh with square grids.

1. Central interpolation

The reconstruction step with second-order central interpolation is given by the following formula:

$$f_\alpha(\mathbf{r}_j)=\frac{r(r-1)}{2}f_\alpha^*(\mathbf{r}_j-\delta\mathbf{r}_\alpha)+(1-r^2)f_\alpha^*(\mathbf{r}_j)+\frac{r(r+1)}{2}f_\alpha^*(\mathbf{r}_j+\delta\mathbf{r}_\alpha), \tag{B1}$$

where f_α^* is the post-collision value of f_α, i.e.,

$$f_\alpha^*\equiv f_\alpha+\Omega_\alpha(f), \tag{B2}$$

and

$$\delta\mathbf{r}_\alpha=\frac{1}{r}\mathbf{e}_\alpha. \tag{B3}$$

The advection operator in this case becomes

$$\mathrm{A}=\mathrm{diag}(1,A,C,B,D,AC,CB,BD,DA), \tag{B4}$$

where

$$A=\frac{r(r+1)p}{2}+(1-r^2)+\frac{r(r-1)}{2p}, \tag{B5a}$$

$$B=\frac{r(r+1)}{2p}+(1-r^2)+\frac{r(r-1)p}{2}, \tag{B5b}$$

$$C=\frac{r(r+1)q}{2}+(1-r^2)+\frac{r(r-1)}{2q}, \tag{B5c}$$

$$D=\frac{r(r+1)}{2q}+(1-r^2)+\frac{r(r-1)q}{2}, \tag{B5d}$$

where $p=e^{ik_x}$ and $q=e^{ik_y}$. With the new phase factors, we find new results at orders 1 and 2 in k. The speed of sound and the Galilean coefficient are multiplied by r and the viscosity coefficients are multiplied by r^2.

At higher order in $\mathbf{k}$, dispersion effects due to lattice arise, leading to differences between solutions of the standard Navier-Stokes equations and the flows computed using the LBE technique.

As in Eq. (53), we find that the advection coefficient for shear waves can be made isotropic to second order in $\mathbf{k}$ by choosing

$$s_5=3r^2\frac{(2-s_8)}{(3r^2-s_8)}, \tag{B6}$$

which improves Eq. (53), since we can choose s_8 close to 2 while maintaining s_5 reasonably far away from 2 (between 1 and 3/2) by taking r^2 close to 2/3.

2. Upwind interpolation

The upwind direction in the LBE method is relative to the particle velocity $\mathbf{e}_\alpha$ (the characteristics) rather than the flow velocity $\mathbf{u}$. Therefore, the interpolation stencil is static in time. Second-order upwind interpolation leads to

$$f_\alpha(\mathbf{r}_j)=\frac{r(r-1)}{2}f_\alpha^*(\mathbf{r}_j-2\,\delta\mathbf{r}_\alpha)+r(2-r)f_\alpha^*(\mathbf{r}_j-\delta\mathbf{r}_\alpha)+\frac{(1-r)(2-r)}{2}f_\alpha^*(\mathbf{r}_j), \tag{B7}$$

where $\delta\mathbf{r}_\alpha$ is defined in Eq. (B3). Accordingly, the phase factors in the advection operator given by Eq. (B4) become

$$A=\frac{(1-r)(2-r)}{2}+\frac{r(2-r)}{p}+\frac{r(r-1)}{2p^2}, \tag{B8a}$$

$$B=\frac{(1-r)(2-r)}{2}+r(2-r)p+\frac{r(r-1)p^2}{2}, \tag{B8b}$$

$$C=\frac{(1-r)(2-r)}{2}+\frac{r(2-r)}{q}+\frac{r(r-1)}{2q^2}, \tag{B8c}$$

$$D=\frac{(1-r)(2-r)}{2}+r(2-r)q+\frac{r(r-1)q^2}{2}, \tag{B8d}$$

where $p=e^{ik_x}$ and $q=e^{ik_y}$.

Again, the third-order term (g_1) in $\mathbf{k}$ for the shear mode is anisotropic unless the following relation is satisfied:

$$s_5=r^2\frac{(2-s_8)}{(3r^2-3rs_8+2s_8)}. \tag{B9}$$

For s_8 and s_5 in the usual range (s_8 near 2 and s_5 between 1 and 3/2), the preceding equation leads to a complex value of r. It should be pointed out that due to the commutativity of propagation along x and y axes, one could apply different interpolation formulas along each axis, according to the physics of flow. For instance, a large stretch of grid can be applied in the direction along which flow fields do not change much in space, whereas in the other orthogonal direction, a normal grid (without interpolation) or even a refined grid [45] can be used, so that the aspect ratio of the meshes is large enough to be appropriate to the flow.

Figure 7 shows the $\mathbf{k}$ dependence of the normalized shear viscosity $\nu(\mathbf{k})/\nu_0$ for the LBE model with and without interpolation schemes. Three orientations of $\mathbf{k}$ are chosen: $\theta=0$ (solid line), $\pi/8$ (dotted line), and $\pi/4$ (dashed line). Figures 7(a), 7(b), and 7(c) show the $\nu(\mathbf{k})/\nu_0$ for the LBE model with no interpolation, with second-order central interpolation scheme and $r=0.5$, and with second-order upwind interpolation scheme and $r=0.5$, respectively. It should be stressed that interpolation schemes do create an enormous amount of numerical viscosity at $k=\pi/2$: Both the central and the upwind interpolation schemes increase the shear viscosity at $k=\pi/2$ by almost two orders of magnitude, whereas without

interpolation, the corresponding increase for the LBE scheme is at most only a factor of about 2.5 (in the direction $\theta=\pi/8$). In all cases, the viscosity displays significant anisotropy at $k=\pi/2$.

Similarly to Fig. 7, Fig. 8 shows the $\mathbf{k}$ dependence of the Galilean-coefficient $g(\mathbf{k})$. The three curves in the middle of the figure corresponding to the LBE model without interpolation. The lower three curves, $g(\mathbf{k})\leq 1$, correspond to the LBE scheme with the central interpolation, and the upper three curves, $g(\mathbf{k})\geq 1$, correspond to the LBE scheme with the upwind interpolation. Again, interpolations have a significant effect on Galilean invariance.

One common feature observed in Figs. 7 and 8 is that the transport coefficients of a model along the direction of $\theta=\pi/8$ is far from those along the directions $\theta=0$ and $\theta=\pi/4$. This is related to the fact that for the square lattice, the wave vector $\mathbf{k}$ along the direction $\theta=\pi/8$ is not a reciprocal vector of the underlying lattice.

[1] G. McNamara and G. Zanetti, Phys. Rev. Lett. **61**, 2332 (1988).
[2] H. Chen, S. Chen, and W. H. Matthaeus, Phys. Rev. A **45**, R5339 (1992).
[3] Y. H. Qian, D. d'Humières, and P. Lallemand, Europhys. Lett. **17**, 479 (1992).
[4] R. Benzi, S. Succi, and M. Vergassola, Phys. Rep. **222**, 145 (1992).
[5] S. Chen and G. D. Doolen, Annu. Rev. Fluid Mech. **30**, 329 (1998).
[6] X. Shan and H. Chen, Phys. Rev. E **47**, 1815 (1993).
[7] X. Shan and H. Chen, Phys. Rev. E **49**, 2941 (1994).
[8] X. He, X. Shan, and G. D. Doolen, Phys. Rev. E **57**, R13 (1998).
[9] L.-S. Luo, Phys. Rev. Lett. **81**, 1618 (1998).
[10] X. He, S. Chen, and R. Zhang, J. Chem. Phys. **152**, 642 (1999).
[11] X. He, R. Zhang, S. Chen, and G. D. Doolen, Phys. Fluids **11**, 1143 (1999).
[12] D. Qi, J. Fluid Mech. **385**, 41 (1999).
[13] L. Giraud, Ph.D. thesis, Université Paris VI, 1997.
[14] L. Giraud, D. d'Humières, and P. Lallemand, Europhys. Lett. **42**, 625 (1998).
[15] U. Frisch, B. Hasslacher, and Y. Pomeau, Phys. Rev. Lett. **56**, 1505 (1986).
[16] S. Wolfram, J. Stat. Phys. **45**, 471 (1986).
[17] U. Frisch, D. d'Humières, B. Hasslacher, P. Lallemand, Y. Pomeau, and J.-P. Rivet, Complex Syst. **1**, 649 (1987).
[18] S. Hou, Q. Zou, S. Chen, G. D. Doolen, and A. C. Cogley, J. Chem. Phys. **118**, 329 (1995).
[19] L.-S. Luo, Int. J. Mod. Phys. C **8**, 859 (1997).
[20] X. He and G. D. Doolen, J. Chem. Phys. **134**, 306 (1997).
[21] X. He and G. D. Doolen, Phys. Rev. E **56**, 434 (1997).
[22] F. Toschi, G. Amati, S. Succi, R. Benzi, and R. Piva, Phys. Rev. Lett. **82**, 5044 (1999).
[23] X. He and L.-S. Luo, Phys. Rev. E **55**, R6333 (1997).
[24] X. He and L.-S. Luo, Phys. Rev. E **56**, 6811 (1997).
[25] T. Abe, J. Comput. Phys. **131**, 241 (1997).
[26] M. Junk, J. Comput. Phys. **151**, 947 (1999).
[27] D. d'Humières, in *Rarefied Gas Dynamics: Theory and Simulations*, Prog. Astronaut. Aeronaut. Vol. 159, edited by B. D. Shizgal and D. P. Weaver (AIAA, Washington, D.C., 1992).
[28] L.-S. Luo, H. Chen, S. Chen, G. D. Doolen, and Y.-C. Lee, Phys. Rev. A **43**, 7097 (1991).
[29] L.-S. Luo, Ph.D. thesis, Georgia Institute of Technology, 1993.
[30] P. Grosfils and P. Lallemand, Europhys. Lett. **24**, 473 (1993).
[31] P. Grosfils, J.-P. Boon, R. Brito, and M. H. Ernst, Phys. Rev. E **48**, 2655 (1993).
[32] S. P. Das, H. J. Bussemaker, and M. H. Ernst, Phys. Rev. E **48**, 2655 (1993).
[33] O. Behrend, R. Harris, and P. B. Warren, Phys. Rev. E **50**, 4586 (1994).
[34] P. L. Bhatnagar, E. P. Gross, and M. Krook, Phys. Rev. **94**, 511 (1954).
[35] J. O. Hirschfelder, C. F. Curtiss, and R. B. Bird, *Molecular Theory of Gases and Liquids* (Wiley, New York, 1954).
[36] X. He and L.-S. Luo, J. Stat. Phys. **88**, 927 (1997).
[37] L. D. Landau and E. M. Lifshitz, *Fluid Mechanics*, 2nd ed. (Pergamon, Oxford, 1987).
[38] Y. H. Qian and Y. Zhou, Europhys. Lett. **42**, 359 (1998).
[39] M. R. Swift, W. R. Osborn, and J. M. Yeomans, Phys. Rev. Lett. **75**, 830 (1995).
[40] M. R. Swift, E. Orlandini, W. R. Osborn, and J. M. Yeomans, Phys. Rev. E **54**, 5041 (1996).
[41] J. D. Sterling and S. Chen, J. Comput. Phys. **123**, 196 (1995).
[42] R. A. Worthing, J. Mozer, and G. Seeley, Phys. Rev. E **56**, 2246 (1997).
[43] X. He, L.-S. Luo, and M. Dembo, J. Comput. Phys. **129**, 357 (1996).
[44] X. He, L.-S. Luo, and M. Dembo, Physica A **239**, 276 (1997).
[45] O. Filippova and D. Hänel, J. Comput. Phys. **147**, 219 (1998).
[46] Y. H. Qian and Y. Zhou, Phys. Rev. E **61**, 2103 (2000).
[47] Y. Saad, *Numerical Method for Large Eigenvalue Problems* (Manchester University Press, Manchester, U.K., 1993).

AIAA 2001-2666
Assessment of the Multi-Relaxation-Time and Single-Relaxation-Time Models in the Lattice Boltzmann Equation Method

Renwei Mei, Dazhi Yu, and Wei Shyy

University of Florida
Gainesville, FL, USA

15th AIAA CFD Conference
11-14 June 2001 / Anaheim, CA

Assessment of the Multi-Relaxation-Time and Single-Relaxation-Time Models in the Lattice Boltzmann Equation Method

Renwei Mei*, Dazhi Yu**, and Wei Shyy†

Department of Aerospace engineering, Mechanics and Engineering Science
University of Florida, Gainesville, FL 32611-6250 USA

ABSTRACT

In solving high Reynolds number flow problems with geometrical discontinuities using the method of lattice Boltzmann equation, the following paradox exits. On the one hand, the density field is required to be nearly constant for the nearly incompressibility condition to be satisfied and the pressure near the geometric discontinuity is linearly proportional to the local density field. On the other hand, the shear stress and the pressure are singular near the geometry singularity, such as sharp corners. This often results in undesirable, strong local spatial oscillations which contaminate the solution for the flow field away from the singular points. The recent work by Lallemand & Luo [7] suggests that the use of a multi-relaxation-time model can improve the computational stability and reduce the undesirable dispersion. However the difference was considered to be largely of higher order. In this paper we report detailed comparison and assessment of the performance of these two LBE models: single-relaxation-time (SRT) and multi-relaxation-time (MRT) for various flows with geometric and flow singularities. Computational results for the pressure, viscous stresses, vorticity, and flow velocity in regions of large gradient show that MRT model significantly reduced the extent of the spatial oscillation near the geometric singular points and improved the quality of the flow field at high Reynolds number. The difference between the solutions of the two models are on the leading order in such cases.

1. BACKGROUND

The method of lattice Boltzmann equation (LBE) solves the microscopic kinetic equation for particle distribution function $f(x, \xi, t)$, where ξ is the particle velocity, in phase space (x, ξ) and time t, from which the macroscopic quantities (velocity and density) are obtained through moment integration of $f(x, \xi, t)$. Because the solution procedure is explicit, easy to implement, and parallelize, the LBE method has increasingly become an attractive alternative computational method for solving fluid dynamics problems in various systems [1-4]. The most widely used lattice Boltzmann model equation is the following single-relaxation-time LBGK model [5],

$$f_\alpha(x_i + e_\alpha \delta t, t + \delta t) - f_\alpha(x_i, t) = -\frac{1}{\tau}[f_\alpha(x_i, t) - f_\alpha^{(eq)}(x_i, t)] \qquad (1)$$

where $f_\alpha(x, t)$ and $f_\alpha^{(eq)}(x, t)$ are the distribution function and the equilibrium distribution function of the α-th discrete velocity ξ_α, respectively, τ is the dimensionless relaxation time and e_α is a discrete velocity vector.

The 9-velocity (or 9-bit) LBE model on the 2-D square lattice (Fig. 1), denoted as the D2Q9 model, has been widely used for simulating 2-D flows. For athermal fluids, the equilibrium distributions is of the following form [6]

$$f_\alpha^{(eq)} = \rho w_\alpha [1 + \frac{3}{c^2} e_\alpha \cdot u + \frac{9}{2c^4}(e_\alpha \cdot u)^2 - \frac{3}{2c^2} u \cdot u] \qquad (2)$$

where w_α is a weighting factor and e_α is a discrete velocity, $c = \delta x/\delta t$ is the lattice speed, and δx and δt are the lattice constant and the time step, respectively. The discrete velocities for the D2Q9 models are

$$e_\alpha = \begin{cases} (0,0,0), & \alpha = 0, \text{ rest particle} \\ (\pm 1,0)c, (0,\pm 1,)c, & \alpha = 1,3,5,7 \\ (\pm 1,\pm 1)c, & \alpha = 2,4,6,8. \end{cases} \qquad (3)$$

and the values of the weighting factor w_α are

$$w_\alpha = \begin{cases} 4/9, & \alpha = 0 \\ 1/9, & \alpha = 1,3,5,7 \\ 1/36, & \alpha = 2,4,6,8. \end{cases} \qquad (4)$$

---

* Professor. ** Graduate student. † Professor and Chair, Fellow AIAA.

The density and velocity can be computed as

$$\rho = \sum_\alpha f_\alpha = \sum_\alpha f_\alpha^{(eq)} , \tag{5}$$

$$\boldsymbol{u} = \frac{1}{\rho}\sum_\alpha \boldsymbol{e}_\alpha f_\alpha = \frac{1}{\rho}\sum_\alpha \boldsymbol{e}_\alpha f_\alpha^{(eq)} . \tag{6}$$

The speed of sound of the above LBE models is $c_s = c/\sqrt{3}$ and the equation of state is that of an ideal gas so that

$$p = \rho c_s^2 . \tag{7}$$

The viscosity of the fluid is

$$\nu = (\tau - \tfrac{1}{2}) c_s^2 \delta t . \tag{8}$$

With this choice for the viscosity, Eq. (1) is formally a second order method for solving incompressible flows [6]. Physical and computational stability requires that $\tau > 1/2$. Equation (1) is usually solved in two steps:

collision step: $f_\alpha^*(x_i, t+\delta t) = f_\alpha(x_i, t)$

$$-\frac{1}{\tau}[f_\alpha(x_i,t) - f_\alpha^{(eq)}(x_i,t)], \tag{9a}$$

streaming step: $f_\alpha(x_i + e_\alpha \delta t,\ t + \delta t) =$

$$f_\alpha^*(x_i, t+\delta t) , \tag{9b}$$

which is known as the LBGK scheme [4,5]. In the above, * denotes the post-collision values. It is noted that the collision step is completely local, and the streaming step is uniform and requires little computational effort, which makes Eq. (1) ideal for parallel implementation. The simplicity and compact nature of the LBGK scheme, however, necessitate the use of square lattices of constant spacing ($\delta x = \delta y$), and consequently lead to the unity of the local Courant-Fridrich-Levy (CFL) number, because $\delta t = \delta x$.

In attempting to obtain solutions for high Reynolds number flows using the LBE method, we found that the solution field for (p, u, v) often exhibit spatial oscillations in regions of large gradient such as stagnation point and sharp convex corners. Especially near a sharp convex corner, because the pressure and the vorticity are singular locally, a large gradient in the density or pressure field exists. Since there usully is insufficient resolution near the corner, the large gradient is often accompanied by spatial oscillations. Depending on the geometry, such spatial oscillation can propagate into the flow to contaminate the macroscopic variables in a large region of interest. The spatial oscillation may adversely affect the computational stability and convergence rate.

Recently, Lallemand and Luo [7] performed detailed analyses on the dispersion, dissipation, and stability characteristics of a generalized lattice Boltzmann equation model proposed by d'Humieres [8]. It was found that by the use of multiple relaxation times in the generalized lattice Boltzmann equations, better computational stability can be achieved over the standard LBGK scheme due to the separation of the relaxations of the various kinetic modes in the generalized lattice Boltzmann equation model--hereinafter referred as the multi-relaxation-time (MRT) model. It is also found in Ref. [7] through the linearized analysis on the MRT model for various simple flows that the MRT model gives the same results, to the second order accuracy, as the single-relaxation-time (SRT) LBGK model does. It seems that these two models are equivalent in the long wavelength limit for macroscopic variable of interest and the difference is a high order effect based on their linear analysis. Such high order differences, however, can be hardly detected in simple linear flows.

Many fluid flow problems posses complicated geometries and mathematical singularities. Since a singularity often affects numerical solutions in high wavenumbers, it is expected that the results of the MRT model be noticeably different from that of the SRT model, at least locally near the geometric singularity. For convection-dominated problems, such local difference in the solution behavior may also lead to difference in the solutions over a larger scale. It is important to understand how the solution based on MRT model behaves in such flows in comparison with the standard LBGK model.

The present paper reports detailed comparison and assessment of the performance of these two LBE models for various flows with geometric and flow singularities. A brief background on the MRT model will be described first. Computational results for the pressure, viscous stresses, vorticity, and flow velocity in regions of large gradient will be compared between the MRT and SRT models under otherwise identical computational and physical parameters for: 1) Stokes first problem; 2) steady uniform flow over a cascade of zero-thickness, finite length flat plates; 3) steady uniform flow over a cascade of finite-thickness, semi-infinite length plates; 4) and steady lid-driven cavity flow. The flow in the Stokes first problem is singular at t=0. The flow in a lid-driven cavity has two singular corners at the intersection of the moving wall and stationary walls in which the viscous stresses have non-integrable singularities. The flows over a plate and a step have singularities in the pressure and stresses, but they are weaker than in the lid-driven cavity flow. These flows with varying degree of singularities allow for a detailed assessment of the two LBE models. The computational results clearly demonstrate that the MRT model has much better behavior in flows involving large gradients than the SRT LBGK model.

2. MULTI-RELAXATION MODEL

In Ref. [7], a new set of variables $\underline{R} = (\rho, e, \varepsilon, j_x, q_x, j_y, q_y, p_{xx}, p_{xy})^T$ are introduced and $\underline{R}$ is related to the set of $\underline{F} = (f_0, f_1, f_2, f_3, f_4, f_5, f_6, f_7, f_8)^T$ as follows,

$$\underline{R} = \begin{pmatrix} \rho \\ e \\ \varepsilon \\ j_x \\ q_x \\ j_y \\ q_y \\ p_{xx} \\ p_{xy} \end{pmatrix} = \begin{pmatrix} 1 & 1 & 1 & 1 & 1 & 1 & 1 & 1 & 1 \\ -4 & -1 & 2 & -1 & 2 & -1 & 2 & -1 & 2 \\ 4 & -2 & 1 & -2 & 1 & -2 & 1 & -2 & 1 \\ 0 & 1 & 1 & 0 & -1 & -1 & -1 & 0 & 1 \\ 0 & -2 & 1 & 0 & -1 & 2 & -1 & 0 & 1 \\ 0 & 0 & 1 & 1 & 1 & 0 & -1 & -1 & -1 \\ 0 & 0 & 1 & -2 & 1 & 0 & -1 & 2 & -1 \\ 0 & 1 & 0 & -1 & 0 & 1 & 0 & -1 & 0 \\ 0 & 0 & 1 & 0 & -1 & 0 & 1 & 0 & -1 \end{pmatrix} \begin{pmatrix} f_0 \\ f_1 \\ f_2 \\ f_3 \\ f_4 \\ f_5 \\ f_6 \\ f_7 \\ f_8 \end{pmatrix} = \underline{\underline{M}}\,\underline{F} \tag{10}$$

where $\underline{\underline{M}}$ is the 9x9 matrix transforming $\underline{F}$ to $\underline{R}$. In the vector $\underline{R}$, ρ is the fluid material density, e is the energy, ε is related to the square of the energy, j_x and j_y are the momentum density (or mass flux), q_x and q_y correspond to the energy flux, and p_{xx} and p_{xy} correspond to the diagonal and off-diagonal component of the viscous stress tensor. One of the inherent disadvantage of the standard LBGK model is that everything is relaxed in the same manner as given by Eq. (9a). In reality, because the mass and momentum are conserved during the molecular collision, there should be no relaxation for the conserved quantities such as mass and momentum. The MRT model can take this difference into consideration in the design of the model. In lieu of Eq. (9a), the collision procedure is carried out as follows,

$$e^* = e - s_2(e - e^{eq}), \tag{11a}$$

$$\varepsilon^* = \varepsilon - s_3(\varepsilon - \varepsilon^{eq}), \tag{11b}$$

$$q_x^* = q_x - s_5(q_x - q_x^{eq}), \tag{11c}$$

$$q_y^* = q_y - s_7(q_y - q_y^{eq}), \tag{11d}$$

$$p_{xx}^* = p_{xx} - s_8(p_{xx} - p_{xx}^{eq}), \tag{11e}$$

$$p_{xy}^* = p_{xy} - s_9(p_{xy} - p_{xy}^{eq}) \tag{11f}$$

where * denotes the post-collision state and the equilibrium values were chosen to be

$$e^{eq} = -2\rho + 3(u^2 + v^2), \tag{12a}$$

$$\varepsilon^{eq} = \rho - 3(u^2 + v^2), \tag{12b}$$

$$q_x^{eq} = -u, \tag{12c}$$

$$q_y^{eq} = -v, \tag{12d}$$

$$p_{xx}^{eq} = u^2 - v^2, \tag{12e}$$

$$p_{xy}^{eq} = uv \tag{12f}$$

Before the streaming step, Eq. (9b), is carried out, one needs to transform the post-collision values, $\underline{R}^*$, back to $\underline{F}^*$ by using

$$\underline{F}^* = \underline{\underline{M}}^{-1}\underline{R}^* \tag{13}$$

In writing the code, Eq. (13) can be combined with Eq. (11) to obtain a single expression

$$\underline{F}^* = \underline{F} - \underline{\underline{M}}^{-1}\underline{\underline{S}}(\underline{R} - \underline{R}^*) \tag{14}$$

where $\underline{\underline{S}}$ is the diagonal matrix:

$$\underline{\underline{S}} = diag(0, s_2, s_3, 0, s_5, 0, s_7, s_8, s_9). \tag{15}$$

The streaming step in the MRT model is carried out exactly in the same manner for each component as in the standard LBGK model based on Eq. (9b)

In Ref. [7], it was shown that for the MRT model to give the same shear viscosity as given by Eq. (8) for the SRT model, one needs to set

$$s_8 = s_9 = 1/\tau. \tag{16}$$

It is much more flexible to chose the rest of the relaxation parameters: s_2, s_3, s_5, and s_7. In general, these four parameters can be chosen to be slightly larger than 1. In this study, we set $s_2 = s_3 = s_5 = s_7 = 1.2$ for simplicity. Very little difference is observed in the flow field if a value of 1.1 is used for (s_2, s_3, s_5, s_7). It is worth commenting here that by setting $s_2 = s_3 = s_5 = s_7 = s_8 = s_9 = 1/\tau$, the SRT model is recovered.

3. RESULTS AND DISCUSSIONS

To effectively demonstrate the difference between the solutions obtained from the SRT model and the MRT model, we compare various macroscopic variables in regions of large gradient. Four cases are considered. They are: i) Stokes first problem; ii) steady uniform flow over a cascade of zero-thickness, finite length flat plates at Re=1000; iii) steady uniform flow over a cascade of finite-thickness, semi-infinite length plates at Re=400 based on the inlet velocity and the thickness of the plate; and iv) steady lid-driven cavity flow at Re=1000. In all the simulations, the initial density is set to be ρ_0=1. The results for the density (and thus pressure) are presented only in terms of the deviation from ρ_0 or some upstream reference value. The results of the SRT model are obtained by running the same MRT code with $s_2 = s_3 = s_5 = s_7 = s_8 = s_9 = 1/\tau$. Obviously, the relative performance between different LBE models depends on many factors including the solution characteristics, types of variables under investigation, and grid resolution. No exhaustive comparison will be made. Instead, we have chosen reasonable grid size in all cases to contrast the behavior of the two models.

3.1 Stoke first problem

For an infinitely long wall to move impulsively with a velocity U at t=0$^+$, the exact solution for the wall shear stress is given by

$$\tau_{xy,w} = -\frac{\mu U}{\sqrt{\pi \nu t}} \tag{17}$$

where μ is the dynamics viscosity of the fluid. Fig. 2 shows the relative error of the LBE solutions for the wall shear stress,

$$E = \frac{|\tau_{xy,w}^{LBE} - \tau_{xy,w}^{exact}|}{|\tau_{xy,w}^{exact}|}. \tag{18}$$

The results are obtained using the relaxation time $\tau=1/s_8=0.55$. Near t=0, there is not enough spatial resolution for the stokes layer of the thickness $\sqrt{\nu t}$. Hence as illustrated in Fig. 2 substantial oscillations are present near t=0. Clearly, the error in the MRT model is smaller than the SRT error for t<100 when the near-wall velocity gradient is large. Eventually, the effect of singularity diminishes and the two solutions approach each other.

3.2 Flow over a cascade of zero-thickness, finite length flat plate

The schematic of the flow is shown in the insert of Fig. 3a. Symmetry condition is imposed at y= ± H. The plate is placed half-way between two gridlines so that the standard bounce-back condition can be used to update the wall condition for f_α's. A zeroth order extrapolation is used at the downstream exit plane for f_α's. A constant uniform velocity condition is imposed at the inlet, x/L= -2. The plate length is 40 in lattice unit (by taking δx=1). The relaxation time controlling the shear viscosity is set to be τ=0.512 and the Reynolds number based on the length is $Re=UL/\nu$ =1000. The free stream velocity is thus U=0.1 and H/L=2 so that there 80 lattices from the plate to the symmetry line.

Fig. 3a compares the density deviation, ρ-1, as a function of y at x/L =0.0125, which is half grid away from the leading edge, based on the MRT model and the SRT model under otherwise identical conditions. Due to the singularity in the flow at the leading edge, it is inevitable to have large gradients in the pressure, stresses, and vorticity near the leading edge at high Re. When there is insufficient numerical resolution, an unphysical spatial oscillation develops near the leading edge. However, MRT model is seen to be much more effective in suppressing the spatial oscillation for ρ or p near the leading edge. Fig. 3b compares ρ-1 as a function of y at x/L=0.5125 under the same condition. Surprisingly, the solution based on the SRT model still possesses a substantial level of spatial oscillations even in the middle of the plate for the whole cross-section while the solution from the MRT model has become sufficiently smooth. Fig. 3c shows the viscous normal stress, τ_{xx}, normalized by $\mu U/L$, as a function of y at x/L = 0.5125. Similar level of oscillations is observed in the SRT based solution. In this work, the viscous stresses are obtained using the non-equilibrium part of the distribution function as,

$$\tau_{ij} = (1-\frac{1}{2\tau})\sum_{\alpha=1}^{8}[f_\alpha(x,t) - f_\alpha^{(eq)}(x,t)](e_{\alpha i}e_{\alpha j} - \frac{1}{2}e_\alpha \cdot e_\alpha \delta_{ij}). \tag{19}$$

Hence no finite difference is employed for the evaluation of the viscous stresses. Fig. 3d compares the dimensionless viscous shear stress, τ_{xy}, as a function of y at x/L = 0.5125. Again, the oscillations in the SRT based solution are noticeable outside the viscous boundary layer.

To develop a further, quantitative understanding of the performance of the two models for flow over a flat plate, the streamwise variation of various macroscopic quantities near the plate y/L =0.0125, which is half-grid above the plate, are also examined. Fig. 4a shows the variation of the pressure coefficient

$$C_p = \frac{p - p_\infty}{\rho_0 U^2/2}, \tag{20}$$

at y/L =0.0125 as a function of x for solutions based on these two models where p_∞ is the pressure at the centerline of the inlet. It is noted that the singularity at x=0 resulted in oscillation in C_p for about 4-5 grid points after the leading edge in the MRT model. However, C_p in the SRT based solution continues to oscillate across the entire plate. Fig. 4b shows variation of the viscous normal stress, τ_{xx}, normalized by $\mu U/L$, at y/L =0.0125. The superiority of the MRT model over the SRT model can be clearly observed in regions before and after the leading edge. Fig. 4c compares the dimensionless wall vorticity, $\partial u/\partial y$, normalized by U/L, between the two models. Little oscillation is observed for the MRT based solution while the SRT based solution continues to show oscillatory behavior up to x/L =0.4, which cannot be considered as the local region of the leading edge.

3.3 Flow over a cascade of finite thickness, semi-finite length plates

The insert in Fig. 5a shows the schematic of the flow. In this study, H/h=4 is used. Symmetry conditions are imposed at the symmetry lines at y=± $H/2$. There are 40 grids from y=-h/2 to y=h/2 so that there are a total of 160 lattices between the symmetry

lines. The free stream velocity, U, is imposed at an upstream section x/h=-2 or 80 to the left of the plate. The downstream exit location is at x/h=8 and a zeroth order extrapolation is employed. The Reynolds number, $Re=hU/\nu$ (= 400 in this study) is based on the inlet velocity U and the thickness of the plate h. The solid walls of the plate are all located half-way between the grids so that the bounce-back condition is used to handle the no-slip condition at the solid walls. We used a relaxation time τ =0.506 that is very close to 0.5 in this case. There are 40 lattices (h=40) across the thickness of the plate; this corresponds to U=0.02 for Re=400.

Fig. 5a shows the streamwise variation of the x-component velocity at y/h=0.5125. For x>0, this corresponds to half a grid above the plate. Away from the convex corner, the approaching flow slows down along y/L=0.5125 due to the blockage by the plate. Very close to the corner, the fluid element feels the turning of the flow direction. According to the classical potential flow description, the flow accelerates around such a convex corner. After the corner (x=0), the no-slip condition causes the near-wall flow to slow down immediately. Thus a sharp drop in the velocity is observed. After a short distance the flow separates to form a slender bubble. While the MRT based solution is reasonably smooth, the SRT based solution exhibits significant oscillations before and after the corner for $|x|/h$<0.2.

Fig. 5b shows the variation of the pressure coefficient C_p at y/L=0.5125. The spatial oscillation in the MRT based solution is rather local and is of small amplitude. The gradual increase of the pressure after the corner reflects the influence of the separation bubble. Further downstream, the pressure starts to decrease linearly as one would expect for a channel flow. The oscillation in the SRT based solution exists for $|x|/h$ ~1 and it shows clearly that the influence of the corner singularity is not local in the SRT based solution.

Fig. 5c compares the variation of the dimensionless shear stress at y/h=0.5125. While the MRT based solution shows no sign of oscillation in the upstream region of the corner, the SRT based solution shows a rather strong oscillation in the viscous shear stress all the way up to x/h ~-0.6. Right after the corner, the shear stress drops sharply due the geometric singularity. The insufficient resolution for the corner singularity resulted in oscillatory behavior in the shear stress downstream of the corner in the SRT based solution. However, the MRT based solution again shows very little oscillation after the corner. Fig. 5d compares the wall vorticity between the two models right after the corner. No oscillation is observed in the MRT model, but the SRT model shows visible oscillation up to x/h=0.5.

3.4 Lid-driven cavity flow

The insect in Fig. 6a shows the coordinate system for the flow inside the cavity. The first line of the grid in the fluid region is at a distance $\Delta\delta x$ from the wall. In this study, Δ=0.3 is used. The boundary condition for $\Delta\neq$0.5 is based on that given in Ref. [9] for curved geometries. The height of the cavity is $H/\delta x$=64+2Δ. With τ =0.52 and Re=1000, the velocity of the moving wall needs to be U=0.1032.

The velocity field is discontinuous at the two corners on the moving wall. Thus the flow singularity is stronger than in the previous two cases where the velocity is continuous near the convex corner. Fig. 6a compares the x-component velocity as a function of y at x/H=0.00464 which is on the first grid away from the left vertical wall. Oscillations are observed in both SRT based and MRT based velocity profiles due to insufficient resolution for the singularity. However, the oscillation in the MRT solution has smaller amplitude and is limited to a region of 5-6 girds. The oscillation in the SRT solution has larger amplitude and propagates further into the flow field. Fig. 6b shows the vertical component of the velocity as a function of y at x/H= 0.00464. Again, the SRT solution has a much larger amplitude and larger region of the oscillation. Fig. 6c compares the velocity profiles of the x-component of the two solutions at the centerline (x/H=0.5) in the lower half of the cavity with a finite difference solution based on the vorticity-stream-function formulation. It is worth noting that the MRT based solution is noticeably more accurate than the SRT based solution even in regions where one considers far away from the singularities.

As a final comment, by taking advantage of many zero elements in $\underline{\underline{M}}^{-1}\underline{\underline{S}}$ and recognizing various common factors in the expressions for the vector $\underline{\underline{M}}^{-1}\underline{\underline{S}}(\underline{R}-\underline{R}^{*})$, the algorithm for the collision step in the MRT model can be coded quite efficiently. For the entire computation of the collision, streaming, and the evaluation of macroscopic variables, the code for the MRT model takes only about 10% more CPU time per time step than an SRT code does. However, this extra 10% work is greatly compensated by the improved convergence of the MRT model in suppressing efficiently the transient oscillation associated with the high-frequency pressure (acoustic) waves, the much improved quality of the results, and the reduced demand for higher resolution.

4. CONCLUSIONS

Based on the detailed examination of the flow fields in various cases, it is clear that the MRT model

has substantial advantages over the SRT model in handling the geometric singularities. While the linear analysis given in Ref. [7] shows that the difference between the SRT model and MRT model mainly lies in the higher order term or for the high wavenumber components, the present simulations in more complicated flows demonstrate that the difference between the two models can be non-local. The difference is substantially larger than just higher order. The MRT model in general provides smoother variations of the macroscopic quantities and has much smaller regions of the oscillation near a singularity. Since the spatial oscillation is often accompanied by the high frequency pressure (acoustic) waves in transient simulations, the MRT model also offers a better convergence toward steady state as well. The MRT model is strongly recommended. The quantitative comparisons will obviously depend on the grid resolution, and the agreement between the two models is expected to be improved as the grid is refined. However the present study has clearly established differences, in actual computational terms, between the single- and multi- relaxation time models.

5. ACKNOWLEDGEMENTS

This work is supported by NASA Langley Research Center. R. Mei also acknowledges partial support of Alcoa Foundation, the Engineering Research Center (ERC) for Particle Science & Technology at the University of Florida, the National Science Foundation (EEC-9402989), and Industrial partners of the ERC.

6. REFERENCES

[1] H. Chen, S. Chen, and W. H. Matthaeus, Recovery of the Navier-Stokes equations using a lattice-gas Boltzmann method, *Phys. Rev. A* **45**, R5339-R5342 (1992).

[2] Y. H. Qian, D. d'Humières, P. Lallemand, Lattice BGK models for Navier-Stokes equation, *Europhys. Lett.* **17**, 479-484 (1992).

[3] R. Benzi, S. Succi, and M. Vergassola, The lattice Boltzmann equation: Theory and applications, *Phys. Rep.* **222**, 145-197 (1992).

[4] S. Chen and G. D. Doolen, Lattice Boltzmann method for fluid flows, *Ann. Rev. Fluid Mech.* **30**, 329-364 (1998).

[5] P. L. Bhatnagar, E. P. Gross, and M. Krook, A model for collision processes in gases. I. Small amplitude processes in charged and neutral one-component system, *Phys. Rev.* **94**, 511-525 (1954).

[6] X. He and L.-S. Luo, Theory of the lattice Boltzmann method: From the Boltzmann equation to the lattice Boltzmann equation, *Phys. Rev. E* **56**, 6811-6817 (1997).

[7] Lallemand, P. & Luo, L.-S., Theory of the lattice Boltzmann method: dispersion, dissipation, isotropy, Galilean invariance, and stability, *Phys. Rev. E.***61**, 6546-6562 (2000).

[8] d'Humieres, D., Generalized lattice Boltzmann equations, in Rarefied Gas Dynamics: Theory and Simulations, Prog. in Astro. Aero., Vol. 159, ed. By D. Shizgal and D.P. Weaver, AIAA, Washington, D.C. (1992).

[9] Mei, R., Luo, L.-S. & Shyy, W., An accurate curved boundary treatment in the lattice Boltzmann method, *J. Computational Physics,* **155**, 307-330 (1999).

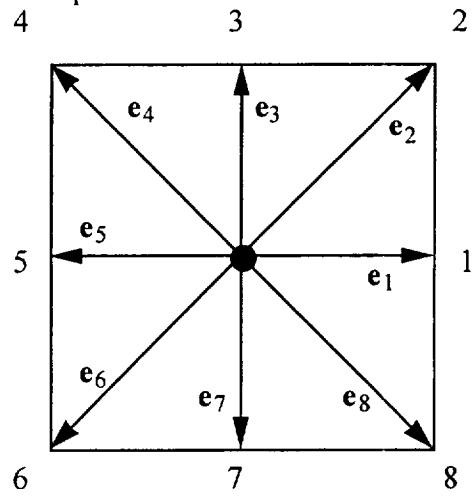

Fig. 1 A 2-D, 9-bit (or 9-speed) lattice.

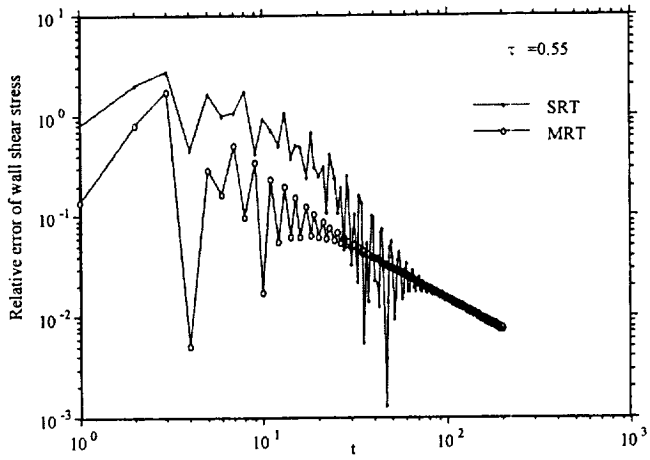

Fig. 2 Comparison of the relative error in the evolution of the wall shearstress for Stokes first problem between the SRT and MRT models.

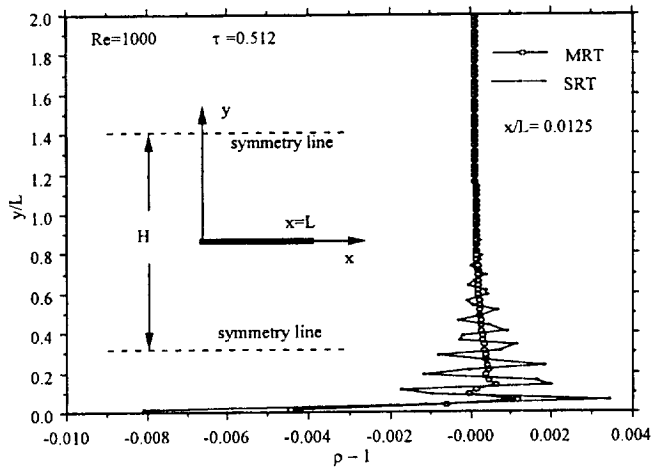

Fig. 3a Comparison of the density profiles near the leading edge (x/L=0.0125) between the SRT model and MRT model at Re=1000.

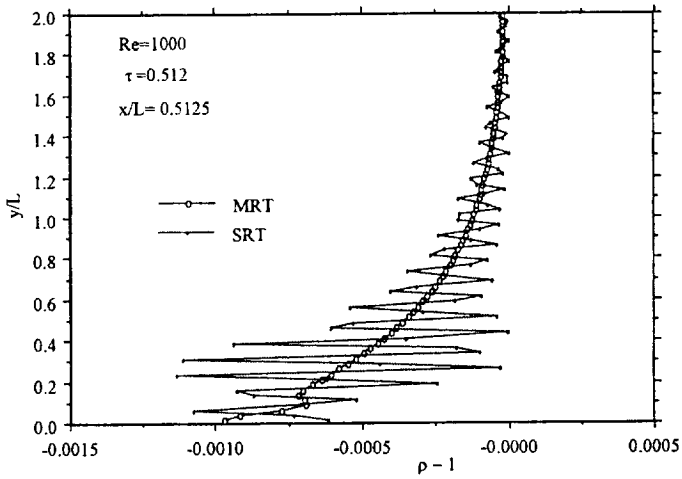

Fig. 3b Comparison of the density profiles at x/L=0.5125 between the SRT model and MRT model at Re=1000.

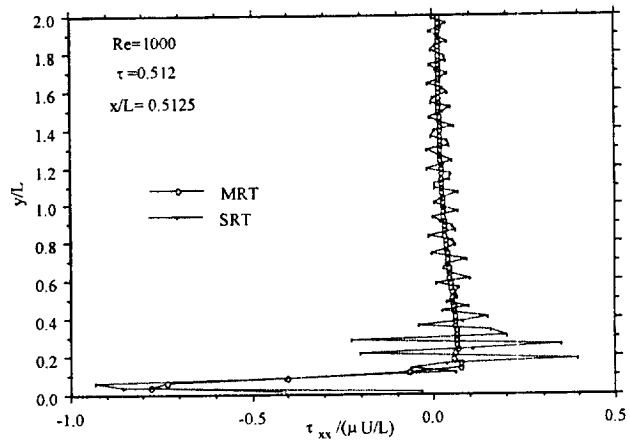

Fig. 3c Comparison of the viscous normal stress profiles at x/L=0.5125 between the SRT model and MRT model at Re=1000.

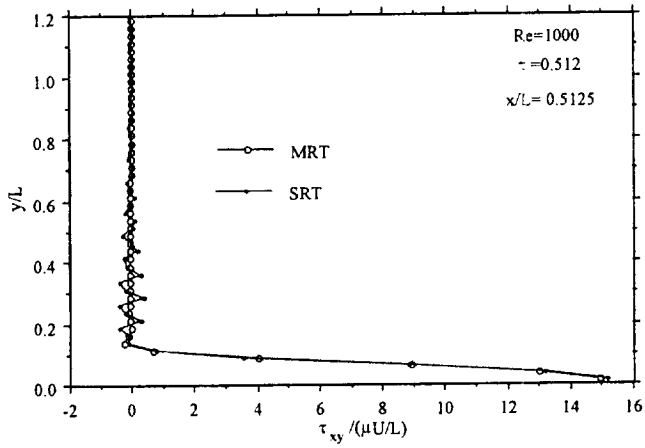

Fig. 3d Comparison of the viscous shear stress profiles at x/L=0.5125 between the SRT model and MRT model at Re=1000.

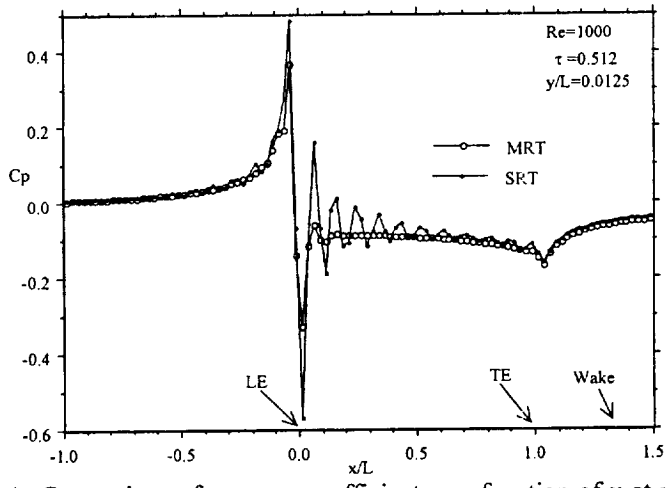

Fig. 4a Comparison of pressure coefficient as a function of x at y/L=0.0125 between the SRT model and MRT model.

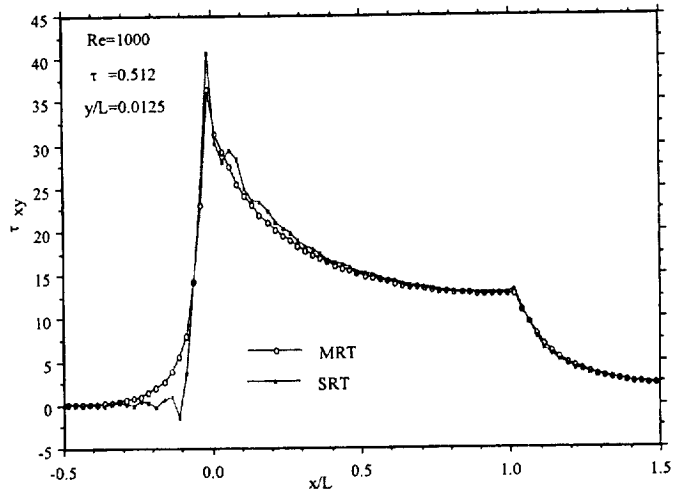

Fig. 4b Comparison of viscous shear stress as a function of x at y/L=0.0125 between the SRT model and MRT model.

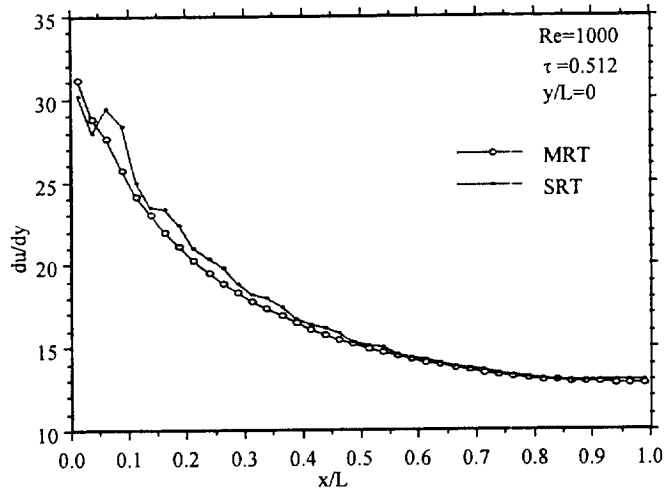

Fig. 4c Comparison of wall vorticity as a function of x between the SRT model and MRT model.

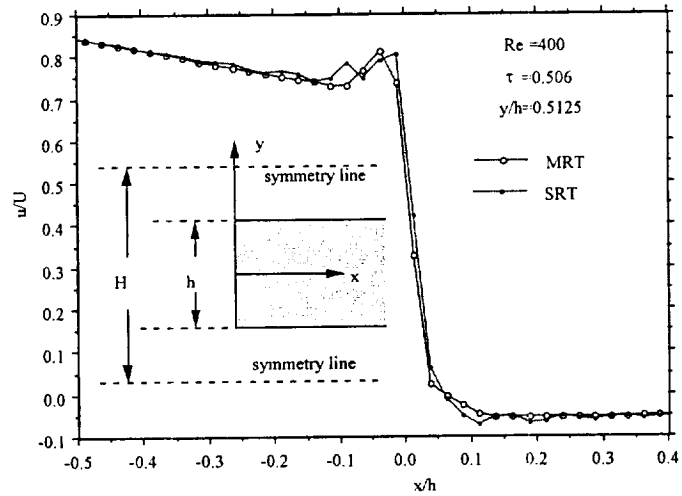

Fig. 5a Streamwise variation of the x-component velocity at y/h=0.5125 at Re=400.

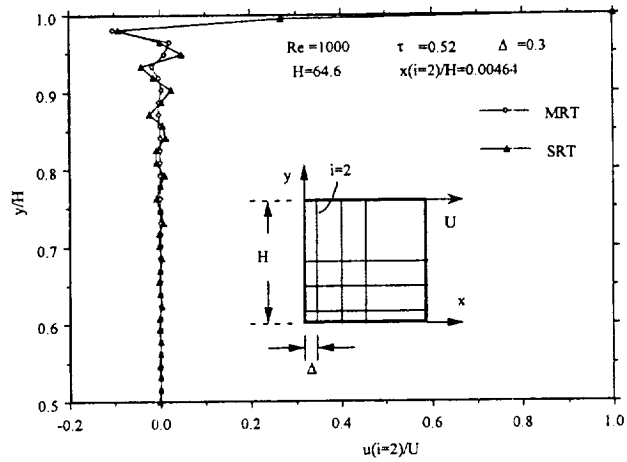

Fig. 6a Comparison of the velocity profiles of x-component at $x=\Delta$ (i=2).

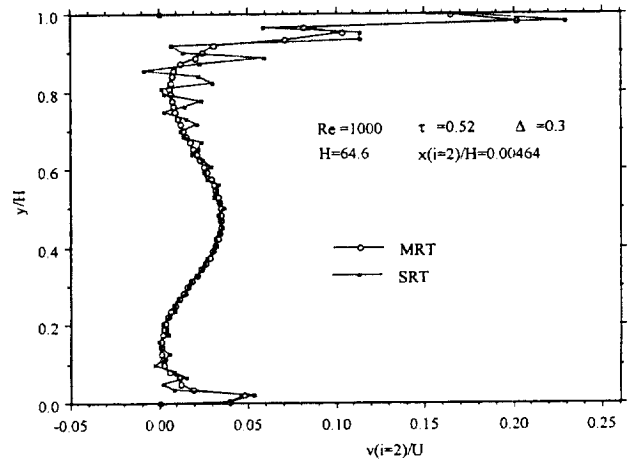

Fig. 6b Comparison of the velocity profiles of y-component at $x=\Delta$ (i=2).

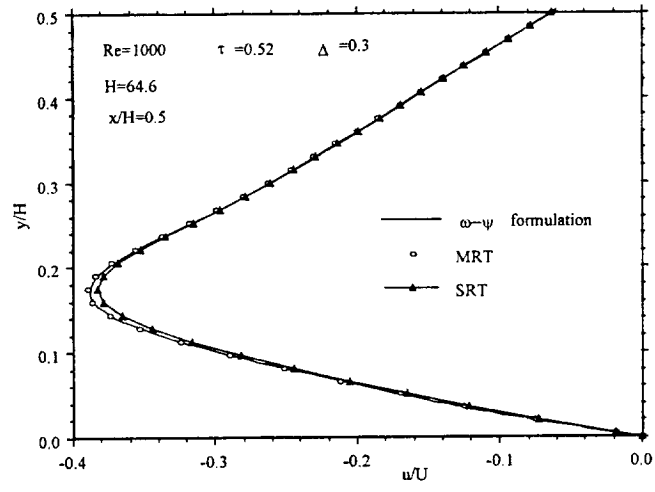

Fig. 6c Comparison of the velocity profiles of x-component at x/H=0.5 in the lower Region of the cavity.

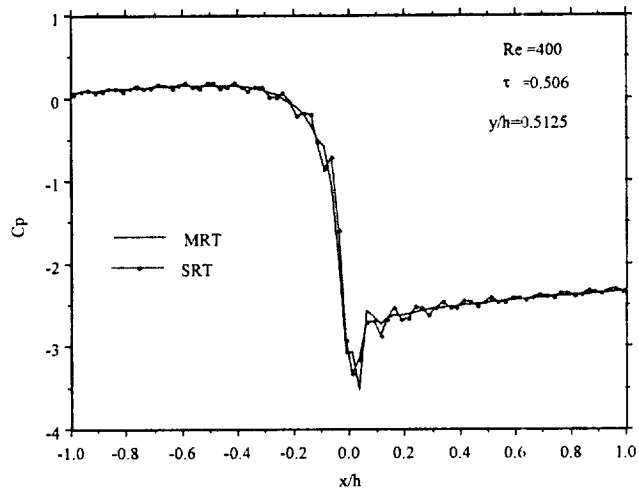

Fig. 5b Streamwise variation of the pressure coefficient Cp at y/L=0.5125.

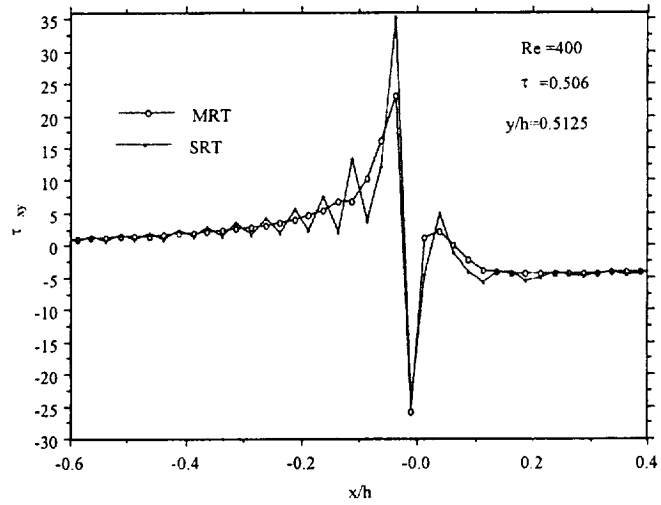

Fig. 5c Streamwise variation of the dimensionless shear stress τ_{xy} at y/L=0.5125.

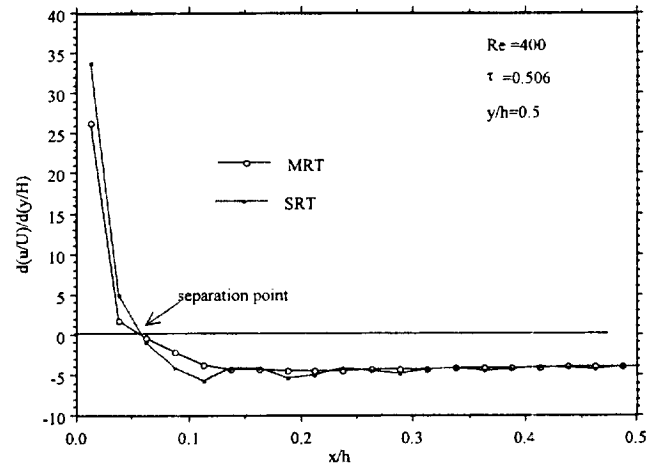

Fig. 5d Dimensionless wall vorticity after the corner of the step at Re=400.

Finite Difference-Based Lattice Boltzmann Method for Inviscid Compressible Flows

Weiping Shi[1], Wei Shyy[2] and Renwei Mei[2]

[1]Department of Mathematics, Jilin University, Changchun 130023, China 130023

[2]Department of Aerospace Engineering, Mechanics & Engineering Science, University of Florida, Gainesville, Florida 32611-6250

Email: shiwp@public.cc.jl.cn wei-shyy@ufl.edu rwm@aero.ufl.edu

ABSTRACT

A finite difference-based lattice Boltzmann model, employing the 2-D, 9-speed square (D2Q9) lattice for the compressible Euler equations, is presented. The model is constructed by allowing the particles to possess both kinetic and thermal energies. Such a lattice structure can represent both incompressible and compressible flow regimes. In the numerical treatment, to attain desirable accuracy, the total-variation-diminishing (TVD) scheme is adopted with either the minmod function or a second-order corrector as the flux limiter. The model can treat shock/expansion waves as well as contact discontinuity. Both one- and two-dimensional test cases are computed, and the results are compared with the exact as well as other reported numerical solutions, demonstrating that there is consistency between macroscopic and kinetic computations for the compressible flow.

1. INTRODUCTION

The lattice Gas Automata (LGA) model was originally presented by Frisch, Hasslacher and Pomeau[1] as an alternative to traditional methods for simulating the Navier-Stokes equation. The classical LGA employs a set of Boolean variables to represent the particle distribution. The development of LGA was obstructed by two fundamental difficulties: the dependence of convection on density and the dependence of pressure on velocity. Furthermore, this and similar models suffer from statistical noise and non-Galilean invariance. The lattice Boltzmann Methods (LBM) developed by Qian [2], and He and Luo [3] overcome these difficulties. In LBM, real numbers are used to represent the ensemble-averaged particle distribution function. LBM has attracted much attention as a novel method for simulation fluid flows, including viscous flows, multiphase fluids, magneto-hydrodynamics, reaction-diffusion systems, and flows through porous media [4].

In the LBM model, the velocity space is discretized into a finite number of discrete values, and most models are constrained to zero Mach number flows. In this work, we focus on the LBM simulation of inviscid compressible flows with discontinuities. Recently, several authors have presented LBM models for compressible flows based on different approaches. For example, Hu [5] proposed a LBM model based on the hexagonal lattice. In this model, the particles possess one of the three energy levels, with a total of 13-bit in the model. Note that for the incompressible flow, only 7-bit are required with the same lattice structure. Similar to Hu's model, Yan [6] presented a 17-bit model with three energy levels and three

speeds on a square lattice. Sun [7,8] formulated an adaptive LBM model in which a particle possesses two different kinds of velocity, one is the *migrating velocity*, relating to the transport (or displacement) of a particle, and the other is the *phase velocity*, related to the momentum of a particle. Palmer [9], on the other hand, developed a lattice Boltzmann algorithm by modeling another scalar field distribution for internal energy. Suffice it to say that by creating an enlarged lattice structure, the thermal energy and the compressibility effect,can be treated. However, such an approach results in a more complicated model with a large number of bits, meaning that the number of equations and the computing time will increase.

In this paper, based on the 2-D, 9-velocity square lattice (D2Q9) model, we propose an LBM model for simulating compressible flows. We do not increase the velocity set in each lattice, but instead revise the energy definition of particles, assuming that besides kinetic energy, the particles also possess thermal energy. The specific heat ratio γ can be chosen freely, and the internal energy of gas can vary in a wide range, so the present model can be used to simulate varying Mach number flows. To improve stability and accuracy, we employ the finite difference-based LBM, previously reported in Mei and Shyy [10], to evolve the particle distribution function. In section 2, we formulate a finite difference-based LBM model, including derivation to ascertain the equilibrium distribution function. The Euler equations are recovered from the present LBM to the first order in time. Section 3 is about the computational procedure. Section 4 presents three numerical tests of one dimensional flow, and the results are compared with the exact

solutions and numerical results based on other schemes. A two-dimensional numerical test of pressure pulse propagation is also presented.

2. CONSTRUCTION OF THE LATTICE BOLTZMANN MODEL

As illustrated in Fig. 1, the model presented in this paper is based on the D2Q9 lattice. We redefine the energy levels ε_A, ε_B and ε_C, respectively, for the rest particles and two kinds of particles with different speed. The particle distribution function at node $\boldsymbol{r}$ and time t is represented by $f_\alpha(\boldsymbol{r},t)$. We define the mass, momentum and total energy at each node as

$$\rho = \sum_\alpha f_\alpha \tag{1}$$

$$\rho u_i = \sum_\alpha f_\alpha e_{\alpha i} \tag{2}$$

$$\frac{1}{2}\rho u^2 + \rho E = \sum_\alpha (\frac{1}{2}|e_\alpha|^2 + \varepsilon_\alpha) f_\alpha \tag{3}$$

where i=1, 2 for 2 dimension, α=0,...,8; $\mathbf{e}_\alpha$ is the velocity vector of particles(see Fig.1). E is the internal energy of per unit mass.

$\mathbf{e}_\alpha = c(\cos(\alpha-1)\pi/4, \sin(\alpha-1)\pi/4)$ for α=1, 3, 5, 7

$\mathbf{e}_\alpha = \sqrt{2}\, c(\cos(\alpha-1)\pi/4, \sin(\alpha-1)\pi/4)$ for α=2, 4, 6, 8,

and $\boldsymbol{e}_0$=0.

where c is the speed parameter. We will use the following velocity moment tensors[11] to aid the derivation of the LBM.

$$\left.\begin{aligned} \sum_{\alpha=1,3,5,7} e_{\alpha i} e_{\alpha j} &= 2c^2\delta_{ij} \\ \sum_{\alpha=2,4,6,8} e_{\alpha i} e_{\alpha j} &= 4c^2\delta_{ij} \end{aligned}\right\} \tag{4}$$

$$\left.\begin{aligned} \sum_{\alpha=1,3,5,7} e_{\alpha i} e_{\alpha j} e_{\alpha k} e_{\alpha m} &= 2c^4 \delta_{ij} \\ \sum_{\alpha=2,4,6,8} e_{\alpha i} e_{\alpha j} e_{\alpha k} e_{\alpha m} &= 4c^4 \Delta_{ijkm} - 8c^4 \delta_{ijkm} \end{aligned}\right\} \tag{5}$$

where $\delta_{ijkm}=1$, if i=j=k=m, otherwise $\delta_{ijkm}=0$, $\Delta_{ijkm}=(\delta_{ij}\delta_{km}+ \delta_{ik}\delta_{jm}+ \delta_{im}\delta_{jk})$ and all the odd order moment tensors equal zero. Furthermore,the particles belong to one of three energy levels. $\varepsilon_\alpha=\varepsilon_A$ for $\alpha=0$; $\varepsilon_\alpha=\varepsilon_B$ for $\alpha=1,3,5,7$; $\varepsilon_\alpha=\varepsilon_C$ for $\alpha=2,4,6,8$.

The evolution of the distribution function can be written as the BGK-type Lattice Boltzmann equation [2,3].

$$\frac{\partial f_\alpha}{\partial t} + e_{\alpha i} \frac{\partial f_\alpha}{\partial x_i} = -\frac{1}{\tau \Delta t}(f_\alpha(r,t) - f_\alpha^{eq}(r,t)) \tag{6}$$

($\alpha=0,1,...,8$)where τ is the single-relaxation time, f_α^{eq} is the local equilibrium distribution chosen to satisfy the macroscopic gas dynamic equation. The right-hand side of Eq.(6) represents the simplified collision operator representing the changes of f due to collisions of particles. Eq.(6), after being multiplied by 1, e_α and $e_\alpha^2/2+\varepsilon_\alpha$ respectively, summed up for all $\alpha=0,...,8$, in addition to considering Eq. (1) to Eq. (3), yields

$$\frac{\partial \rho}{\partial t} + \frac{\partial \rho u_i}{\partial x_i} = 0 \tag{7}$$

$$\frac{\partial \rho u_i}{\partial t} + \frac{\partial}{\partial x_j}(\sum_\alpha e_{\alpha i} e_{\alpha j} f_\alpha) = 0 \tag{8}$$

$$\frac{\partial}{\partial t}(\frac{1}{2}\rho u^2 + \rho E) + \frac{\partial}{\partial x_i}[(\frac{1}{2}e_\alpha^2 + \varepsilon_\alpha) e_{\alpha i} f_\alpha] = 0 \tag{9}$$

In order to recover the gas dynamic equation, besides the conservation of mass, momentum and energy,

$$\sum_{\alpha} f_{\alpha}^{eq} = \rho \tag{10}$$

$$\sum_{\alpha} f_{\alpha}^{eq}\ e_{\alpha i} = \rho u_i \tag{11}$$

$$\sum_{\alpha} (\frac{1}{2} | e_{\alpha} |^2 + \varepsilon_{\alpha}) f_{\alpha}^{eq} = \frac{1}{2} \rho u^2 + \rho E \tag{12}$$

the equilibrium distribution function must satisfy the following momentum and energy flux conditions [5].

$$\sum_{\alpha} f_{\alpha}^{eq} e_{\alpha i} e_{\alpha j} = \rho u_i u_j + p\delta_{ij} \tag{13}$$

$$\sum_{\alpha} f_{\alpha}^{eq} (\frac{1}{2} | e_{\alpha} |^2 + \varepsilon_{\alpha}) e_{\alpha i} = (\frac{1}{2} \rho u^2 + \rho E + p) u_i \tag{14}$$

The pressure p can be obtained from the equations of state and energy of prefect gas.

$$p = (\gamma - 1)\rho E \tag{15}$$

where γ is the ratio of specific heat of gas.

We assume that f_{α}^{eq} has the same functional expression as that in the incompressible D2Q9 LBM [2,3]

$$\left.\begin{array}{ll} f_{\alpha}^{eq} = D_0 \rho + D_3 \rho u^2 & \alpha = 0 \\ f_{\alpha}^{eq} = A_0 \rho + A_1 \rho u_i e_{\alpha i} + A_2 \rho u_i u_j e_{\alpha i} e_{\alpha j} + A_3 \rho u^2 & \alpha = 1,3,5,7 \\ f_{\alpha}^{eq} = B_0 \rho + B_1 \rho u_i e_{\alpha i} + B_2 \rho u_i u_j e_{\alpha i} e_{\alpha j} + B_3 \rho u^2 & \alpha = 2,4,6,8 \end{array}\right\} \tag{16}$$

Substituting Eq.(16) into Eqs.(10)-(14), we obtain ten linear algebraic equations for determining the coefficients A_i, B_i, D_i. Considering Eq. (4), (5), and note that Eq. (10)-(14) are equations of power of ρ and u, so all terms to each order of ρ can be collected.

Specifically, form Eq. (10) we have

$$4A_0 + 4B_0 + D_0 = 1 \tag{17}$$

$$2c^2 A_2 + 4c^2 B_2 + 4A_3 + 4B_3 + D_3 = 0 \tag{18}$$

From Eq. (11) we have

$$2c^2 A_1 + 4c^2 B_1 = 1 \tag{19}$$

From Eq. (12) we have

$$c^4 A_2 + 2c^2 \varepsilon_B A_2 + 2c^2 A_3 + 4\varepsilon_B A_3 + 4c^2 B_2 + 4c^2 \varepsilon_C B_2 + 4c^2 B_3 + 4\varepsilon_C B_3 + \varepsilon_A D_3 = \frac{1}{2} \tag{20}$$

$$2c^2 A_0 + 4\varepsilon_B A_0 + 4c^2 B_0 + 4\varepsilon_C B_0 + \varepsilon_A D_0 = E \tag{21}$$

From Eq. (13) and consider Eq. (15) we have

$$8c^4 B_2 = 1 \tag{22}$$

$$2c^4 A_2 - 8c^4 B_2 = 0 \tag{23}$$

$$2c^2 A_3 + 4c^4 B_2 + 4c^2 B_3 = 0 \tag{24}$$

$$2c^2 A_0 + 4c^2 B_0 = (\gamma - 1)E \tag{25}$$

From Eq. (14) and consider Eq. (15) we have

$$(c^4 + 2c^2 \varepsilon_B) A_1 + (4c^4 + 4c^2 \varepsilon_C) B_1 = \frac{1}{2} u^2 + \gamma E \tag{26}$$

To determine these coefficients from Eq.(17), (21) and (25) we have

$$B_0 = \frac{E[2 - \gamma - (\gamma - 1)(\frac{2\varepsilon_B}{c^2} - \frac{2\varepsilon_A}{c^2})] - \varepsilon_A}{4(\varepsilon_C - 2\varepsilon_B + \varepsilon_A)} \tag{27}$$

$$A_0 = -2B_0 + (\gamma - 1)\frac{E}{2c^2} \tag{28}$$

$$D_0 = 1 - (4A_0 + 4B_0) \tag{29}$$

From Eqs.(19) and (26) we have

$$B_1 = \frac{\frac{1}{2}u^2 + \gamma E - \frac{1}{2}c^2 - \varepsilon_B}{2c^2(c^2 + 2\varepsilon_C - 2\varepsilon_B)} \tag{30}$$

$$A_1 = -2B_1 + \frac{1}{2c^2} \tag{31}$$

$$B_2 = \frac{1}{8c^4} \tag{32}$$

$$A_2 = \frac{1}{2c^4} \tag{33}$$

From Eqs.(18) and (24) we have

$$B_3 = \frac{\varepsilon_A - \varepsilon_C}{8c^2(\varepsilon_C - 2\varepsilon_B + \varepsilon_A)} \tag{34}$$

$$A_3 = -2B_3 - \frac{1}{4c^2} \tag{35}$$

$$D_3 = -\frac{3}{2c^2} - 4A_3 - 4B_3 \tag{36}$$

Here we note that if the energy levels ε_A, ε_B, ε_C and c are chosen to be constants, then A_2, B_2, A_3, B_3, D_3 are constants also. However, A_0, B_0, D_0, A_1, B_1 are functions of macroscopic variables E and u.

Choosing time step Δt as the small perturbation parameter ε, we use the multiscale technique and Chapman-Enskog expansion

$$\frac{\partial}{\partial t} = \frac{\partial}{\partial t_0} + \varepsilon\frac{\partial}{\partial t_1} + \varepsilon^2\frac{\partial}{\partial t_2} + \ldots \tag{37}$$

$$f_\alpha = f_\alpha^{eq} + \varepsilon f_\alpha^{(1)} + \varepsilon^2 f_\alpha^{(2)} + \ldots \tag{38}$$

The macroscopic dynamic equations of mass, momentum and energy can be derived from Eqs. (6)-(15)

$$\frac{\partial \rho}{\partial t}+\frac{\partial \rho u_i}{\partial x_i}=R_1+O(\varepsilon^2) \tag{39}$$

$$\frac{\partial \rho u_i}{\partial t}+\frac{\partial(\rho u_i u_j+p\delta_{ij})}{\partial x_j}=R_2+O(\varepsilon^2) \tag{40}$$

$$\frac{\partial}{\partial t}(\frac{1}{2}\rho u^2+\rho E)+\frac{\partial}{\partial x_i}(\frac{1}{2}\rho u^2 u_i+\rho E u_i+p u_i)=R_3+O(\varepsilon^2) \tag{41}$$

where

$$R_1=0 \tag{42}$$

$$R_2=\varepsilon\tau\frac{\partial}{\partial x_j}[\frac{\partial}{\partial t_0}(\rho u_i u_j+p\delta_{ij})+\frac{\partial}{\partial x_k}(\sum_\alpha f_\alpha^{eq} e_{\alpha i} e_{\alpha j} e_{\alpha k})] \tag{43}$$

$$R_3=\varepsilon\tau\frac{\partial}{\partial x_j}[\frac{\partial}{\partial t_0}(\frac{1}{2}\rho u^2 u_j+\rho E u_j+p u_j)+\frac{\partial}{\partial x_k}(\sum_\alpha f_\alpha^{eq}(\frac{1}{2}|e_\alpha|^2+\varepsilon_\alpha)e_{\alpha j} e_{\alpha k})] \tag{44}$$

In summary, with the present lattice Boltzmann formulation, the macroscopic Euler equations are recovered to the first-order in time.

3. COMPUTATIONAL PROCEDURES

In the BGK model, the evolution equation of particle distribution function is often cast in the form of

$$f_\alpha(x+c_\alpha\Delta t,t+\Delta t)-f_\alpha(x,t)=-\frac{1}{\tau}(f_\alpha(x,t)-f_\alpha^{eq}(x,t)) \tag{45}$$

Eq.(45) recovers the NS equations in the nearly incompressible flow limit. The most frequently adopted BGK model, with Δt=1, separates the evolution process into two steps: collision and streaming. The resulting scheme is based on the first-order upwind scheme, and contains substantial numerical viscosity. For incompressible, viscous flow computations, the numerical viscosity is subtracted from the prescribed viscosity to convert the scheme to the second-order center

difference one. Without physical viscosity, the smearing effect of the first-order upwind treatment is retained because the central difference scheme, along with the explicit Euler time stepping, is intrinsically unstable when the viscous effect diminishes. To improve the solution accuracy, modern concept based on the total variation diminishing (TVD) can be incorporated, as will be presented below.

In the present LBM, there are seven parameters, c, ε_A, ε_B, ε_C τ, Δx, and Δt. The ratio of specific heats γ can also be chosen according to Eq. (15), which, in turn, directly affects the lattice model. If we let $\varepsilon_A=\varepsilon_B=\varepsilon_C=0$ see Eq. (12), then our model becomes the incompressible LBM model. It is noted that c must be greater than the maximum speed of the fluid flow; otherwise it can cause a negative distribution function.

In the following, we first present the finite difference schemes of Eq.(6), based on alternative methods to treat the flux terms. There are also different strategies for handling the collision term, as will be presented after the convection scheme.

(i) LBM1: The minmod method

Utilizing the well known *minmod* scheme[12]the discretized form of convection term of Eq.(6) can be written as

$$e_{\alpha i}\frac{\partial f_\alpha}{\partial x_i} \equiv \frac{\partial}{\partial x_i}F_\alpha$$
$$= \frac{1}{\Delta x}[F_\alpha(I+\frac{1}{2},J)-F_\alpha(I-\frac{1}{2},J)]+\frac{1}{\Delta y}[F_\alpha(I,J+\frac{1}{2})-F_\alpha(I,J-\frac{1}{2})] \quad (46)$$

where $F_\alpha = e_{\alpha i} f_\alpha, F_\alpha(I+\frac{1}{2},J)$ and $F_\alpha(I,J+\frac{1}{2})$ is the flux of

f_α at the boundaries of each cell. For the advection velocity $e_{\alpha x}>0$, we interpolate the flux F_α to the boundaries of each cell, using the *minmod* limiter to estimate the fluxes [12]:

$$F_\alpha(I+\frac{1}{2},J) = F_\alpha(I,J)+\frac{1}{2}\min \mathrm{mod}[\Delta_{backx}F_\alpha(I,J),\Delta_{fwdx}F_\alpha(I,J)] \tag{47}$$

α=1,2,8,

where $\Delta_{fwdx}F_\alpha(I,J) = F_\alpha(I+1,J) - F_\alpha(I,J)$,

$\Delta_{backx}F_\alpha(I,J) = F_\alpha(I,J) - F_\alpha(I-1,J)$, and for the advection velocity $e_{\alpha x}<0$, we interpolate the flux F_α as

$$F_\alpha(I-\frac{1}{2},J) = F_\alpha(I,J)-\frac{1}{2}\min \mathrm{mod}[\Delta_{backx}F_\alpha(I,J),\Delta_{fwdx}F_\alpha(I,J)] \tag{48}$$

α=4,5,6

Using the same interpolation along the *y* direction we have

$$F_\alpha(I,J+\frac{1}{2}) = F_\alpha(I,J)+\frac{1}{2}\min \mathrm{mod}[\Delta_{backy}F_\alpha(I,J),\Delta_{fwdy}F_\alpha(I,J)] \tag{49}$$

α=2,3,4

$$F_\alpha(I,J-\frac{1}{2}) = F_\alpha(I,J)-\frac{1}{2}\min \mathrm{mod}[\Delta_{backy}F_\alpha(I,J),\Delta_{fwdy}F_\alpha(I,J)] \tag{50}$$

α=6,7,8,

where $\Delta_{fwdy}F_\alpha(I,J) = F_\alpha(I,J+1) - F_\alpha(I,J)$,

$\Delta_{backy}F_\alpha(I,J) = F_\alpha(I,J) - F_\alpha(I,J-1)$.

(ii) LBM2: Harten's second-order flux-correction scheme

Instead of the *minmod* scheme, we have also implemented a second-order flux-correction scheme proposed by Harten [12]. Specifically, Harten suggested the following flux correction:

$$F_{\alpha x}(i,j) = c_{\alpha x} f_\alpha(i,j) + \frac{1}{2}(1+\omega\theta_{\alpha x}(i,j))\,|\,c_{\alpha x}\,|\,(1-\frac{\Delta t}{\Delta x}|\,c_{\alpha x}\,|)\times$$
$$\times \min\mathrm{mod}[f_\alpha(i+1,j)-f_\alpha(i,j), f_\alpha(i,j)-f_\alpha(i-1,j)] \qquad (51)$$

where $\omega \geq 0$ is a user-adjustable parameter and

$$\theta_{\alpha x}(i,j) = \frac{|\,f_\alpha(i+1,j)-2f_\alpha(i,j)+f_\alpha(i-1,j)\,|}{|\,f_\alpha(i+1,j)-f_\alpha(i,j)\,|+|\,f_\alpha(i,j)-f_\alpha(i-1,j)\,|} \qquad (52)$$

is a *shock switch.* We interpolate the flux $F_{\alpha x}$ to the boundaries of each cell:

$$F_\alpha(i+\frac{1}{2},j) = \frac{1}{2}[F_{\alpha x}(i+1,j)+F_{\alpha x}(i,j) - \frac{|\,F_{\alpha x}(i+1,j)-F_{\alpha x}(i,j)\,|}{|\,f_\alpha(i+1,j)-f_\alpha(i,j)\,|}(f_\alpha(i+1,j)-f_\alpha(i,j))] \qquad (53)$$

Similar to the correction of flux along x-direction, we have flux correction of y-direction.

$$F_{\alpha y}(i,j) = c_{\alpha y} f_\alpha(i,j) + \frac{1}{2}(1+\omega\theta_{\alpha y}(i,j))\,|\,c_{\alpha y}\,|\,(1-\frac{\Delta t}{\Delta y}|\,c_{\alpha y}\,|)\times$$
$$\times \min\mathrm{mod}[f_\alpha(i,j+1)-f_\alpha(i,j), f_\alpha(i,j)-f_\alpha(i,j-1)] \qquad (54)$$

where

$$\theta_{\alpha y}(i,j) = \frac{|\,f_\alpha(i,j+1)-2f_\alpha(i,j)+f_\alpha(i,j-1)\,|}{|\,f_\alpha(i,j+1)-f_\alpha(i,j)\,|+|\,f_\alpha(i,j)-f_\alpha(i,j-1)\,|} \qquad (55)$$

and interpolate the flux $F_{\alpha y}$ to the boundaries of each cell:

$$F_\alpha(i,j+\frac{1}{2}) = \frac{1}{2}[F_{\alpha x}(i,j+1)+F_{\alpha y}(i,j) - \frac{|\,F_{\alpha y}(i,j+1)-F_{\alpha y}(i,j)\,|}{|\,f_\alpha(i,j+1)-f_\alpha(i,j)\,|}(f_\alpha(i,j+1)-f_\alpha(i,j))] \qquad (56)$$

As to the treatment of the source term, similar to the approach of Mei and Shyy [10] the left-hand-side in Eq. (6) can be treated by a 3-level second-order scheme

$$-\frac{1}{\tau}(f_\alpha - f_\alpha^{eq})\Big|^{n+1} = -\frac{1}{\tau}[f_\alpha^{n+1} - (2f_\alpha^{eq,n} - f_\alpha^{eq,n-1})] \tag{57}$$

The extrapolation for f_α^{eq} ensures that the relaxation term is at the (n+1)st time step. Finally, the discretized from of Eq.(6) can be expressed as

$$\frac{f_\alpha^{n+1} - f_\alpha^n}{\Delta t} + \frac{1}{\Delta t}[F_\alpha(I+\frac{1}{2},J) - F_\alpha(I-\frac{1}{2},J)] + \frac{1}{\Delta y}[F_\alpha(I,J+\frac{1}{2}) - F_\alpha(I,J-\frac{1}{2})]$$
$$= -\frac{1}{\tau}[f_\alpha^{n+1} - (2f_\alpha^{eq,n} - f_\alpha^{eq,n-1})] \tag{58}$$

4. RESULTS AND DISCUSSIONS

In this section, three well-known one dimensional test problems are calculated. A system of 200×6 lattices has been used in the one-dimensional test, and a two – dimensional problem is also presented.

I. 1-D: Sod Test

The initial condition is

$$(\rho_L, u_L, p_L)=(1,0,1) \qquad -0.5<x<0$$

$$(\rho_R, u_R, p_R)=(0.125,0,0.1) \qquad 0<x<0.5$$

The numerical results using LBM *minmod* method and LBM Harten scheme are compared with the exact solution (Fig.2 and Fig.3). The solution contains the

formation of a shock wave and a contact discontinuity. As expected, Harten's second order flux-correction scheme can resolve the discontinuity with fewer points while exhibiting some oscillations in the contact discontinuity region. The width of the sharp gradients in the LBM solutions are compared to those obtained by numerical methods. For the detailed information of the macroscopic solution, see *e.g*, Ref[13]. To evaluate the performance quantitatively, Table 1 lists the L_1 norm error in velocity, pressure and density fields of the two tests flows, along with that of the macroscopic method utilizing the Roe scheme. Figure 4 illustrates the L_1 norm error versus the lattice density. As expected, the first-order accuracy is attained for flows with discontinuities. The present LBM solutions are very competitive in comparison with other well-known approaches based on the macroscopic formulation.

II. 1-D: Lax Test

The initial condition is

$$(\rho_L, u_L, p_L)=(0.445,0.698,3.528) \qquad -0.5<x<0$$

$$(\rho_R, u_R, p_R)=(0.5,0.0,0.571) \qquad 0<x<0.5$$

Using LBM *minmod* method, Fig.5 shows the density, pressure, velocity and internal energy profiles of both LBM and exact solutions. Again, the results are reasonable, with noticeable variations in velocity and pressure profiles in the contact discontinuity region. Figure 6 shows the comparison with the LBM flux-correction solutions; sharper solution profiles are observed. However, there are also more pressure variations around the contact discontinuity.

III. 1-D: Roe Test

The Roe test with the following initial condition:

$$(\rho_L, u_L, p_L)=(1,-1,1.8) \quad -0.5<x<0$$

$$(\rho_R, u_R, p_R)=(1,1,1.8) \quad 0<x<0.5$$

The numerical results and exact solutions of LBM *minmod* method are shown in Fig.7. Similar to other macroscopic schemes, the LBM results exist error in the middle of the density and energy profiles. Again, as demonstrated in Fig. 8, the LBM flux-correction method produces solutions of similar shapes but with sharper gradients. As well known in the macroscopic-based method, the numerical solutions exhibit a bump in energy and density profiles.

IV. 2-D: Propagation of a Circular Pressure Pulse

The computational domain [0,1]×[0,1] is divided into 100×100 square lattices with $\Delta x=\Delta y=0.01$ and time step $\Delta t=0.0001$. The initial conditions for pressure and velocities are $\rho=1$, $u=v=0$ everywhere, with a circular pressure pulse assigned at the center (0.5, 0.5):

$p=1+0.5\times\mathrm{sech}(z)$, where $z=50\times\sqrt{(x_{i,j}-x_{50,50})^2+(y_{i,j}-y_{50,50})^2}$

The evolution of pressure at the center point (0.5, 0.5), with time is compared between the present LBM and an implicit Lagrangian method, as shown in Fig. 9. Good agreement is observed. The figure depicts that the pressure at the center drops rapidly below 1 and then recovers gradually. Fig.10 shows the density, u-velocity and pressure of the solution based on the minmod method at

t=0.2, in half of the domain. Fig.11 shows the corresponding solutions based on Harten's second-order flux-correction scheme. These results agree with each other, as well as those of Ref.14].

5. CONCLUDING REMARKS

In our computations, we find that the numerical accuracy and stability are not sensitive to τ. But the value c, ε_A, ε_B and ε_C must be chosen carefully, to ensure the numerical stability. We also employ the second order upwind difference scheme for discretizing the convection term of Eq.(6),but the numerical result exists strong oscillation near the discontinuities.

Here we chose ε_A <0 to ensure that p and E satisfy the state equation Eq.(15) to ensure physical realizability. Comparing with the macroscopic gas dynamic equation, Eq.(6) is easer, the convection term is the linear function of f_α. On the other hand, the choice of the parameters in the compressible lattice Boltzmann model needs more investigation. As indicated in the model derivation and the case studies, there is a lack of a clear guidance to select the most appropriate combinations. Nevertheless, the parameters chosen here do support the numerical computation to maintain physical realizability.

The theoretical derivation of the lattice Boltzmann equations and the prescription of the corresponding lattice structure offer a framework to develop numerical techniques for flow simulations. Solution accuracy and computational efficiency are determined by the specific schemes adopted to solve the equation. The present model can simulate flows over a wide range of Mach numbers and the

shocks are well captured. Although the model is based on square lattice for 2-D, it can be easily applied to hexagonal lattice and 3-D cubic lattices, as well as employed on curvilinear coordinates and non-uniform grids. As already pointed out in Section 1, in comparison to other lattice models proposed for compressible flow simulations, the present lattice structure, by allowing the particles to possess both kinetic and thermal energies, is simpler in number of discrete energy levels. Furthermore, in contrast to the incompressible flow model, the present numerical scheme benefits more from more sophisticated discretization schemes, such as those based on the TVD concept, which can reduce the numerical viscosity at the expense of added computing cost.

As is well stated in the literature, LBM, being simple in structure, utilizing only linear operators, and obviously parallelizable, is an attractive approach for gas dynamics problems.

ACKNOWLEDGMENTS

This research was carried out at the Computational Thermo-Fluid Laboratory, Department of Aerospace Engineering, Mechanics & Engineering Science, University of Florida, while the first author was a visiting scholar. This work was supported by the National Natural Science Foundation of China (grant No. 19702005), and NASA Largley Research Center.

REFERENCES

[1] U. Frisch, B. Hasslacher and Y. Pomeau, Lattice-Gas Automata for the Navier-Stokes Equation. *Phys. Rev. Lett*, 56. pp. 1505-1508 (1986).

[2] Y.H. Qian, D. d'Humieres, and P. Lallemand, Lattice BGK Models for Navier-Stokes Equation. *Europhys Lett*, 17(6), pp. 479-484(1992).

[3] X. He and L.-S. Luo, A priori derivation of the lattice Boltzmann equation, *Phys. Rev. E,* 55, R6333-R6336 (1997).

[4] S. Chen and G. D. Doolen, Lattice Boltzmann method for fluid flows, *Ann. Rev. Fluid Mech.* 30, pp. 329 (1998).

[5] S. Hu, G. Yan and W. Shi, A Lattice Boltzmann Model for Compressible Perfect Gas. *ACTA Mechanica Sinica* (English Series), 13, No.3, pp. 218-226(1997).

[6] G. Yan, Y. Chen and S. Hu, Simple Lattice Boltzmann Model for Simulating Flows with Shock Wave. *Phys. Rev. E.* 59, pp. 454-459(1999).

[7] C. Sun, Lattice-Boltzmann Models for High Speed Flows. *Phys. Rev. E.* 58, pp7283-7287(1998).

[8] C. Sun, Simulations of Compressible Flows with Strong shocks by an Adaptive Lattice Boltzmann Model. *J. Comput. Phys.* 161. pp. 70-84(2000).

[9] B. J. Palmer and D. R. Rector, Lattice Boltzmann Algorithm for Simulating Thermal flow in Compressible Fluids. *J. Comput. Phys.* 161, pp. 1-20(2000).

[10] R. Mei and W. Shyy, On the Finite Difference-Based Lattice Boltzmann Method in Curvilinear Coordinates. *J. Comput. Phys.* 143, pp. 426-448(1998).

[11] S. Hou, q. Zou, S. Chen, G. Doolen, Simulation of Cavity Flow by the Lattice Boltzmann Method. *J. Comput. Phys.* 118, pp. 329-347 (1995).

[12] C. B. Laney, *Computational Gasdynamics.* (Cambridge University Press, Cambridge, United Kingdom. 1998).

[13] H. Nessyahu and E. Tadmor, Non-oscillatory Differencing for Hyperbolic Conservation Laws. *J. Comput. Phys.* 87,pp. 408-463(1990).

[14] F. Liu, A. C. Mcintosh and J. Brindley, An Implicit Lagrangian Method for Solving One- and Two-Dimensional Gasdynamic Equations. *J. Comput. Phys.* 111, pp. 112-133 (1994)

Table 1

Sod test and Lax test numerical L_1 norm errors. FDLBM compared with the Roe schemes come from Ref.[13]

	Sod's test t=0.1644			Lax's test t=0.16		
	Density	Velocity	Pressure	Density	Velocity	Pressure
LBM1(minmod)	0.00859	0.02752	0.00855	0.03051	0.01228	0.00762
LBM2(flux-correction)	0.00617	0.02165	0.00630	0.02241	0.00963	0.00584
ROE	0.00836	0.01145	0.00666	0.02827	0.02192	0.02655

Here LBM1 is based on the minmod method to interpolate the convection term of Eq. (6), and LBM2 is based on Harten's second-order flux-correction scheme. Total of 200 lattices in space are employed.

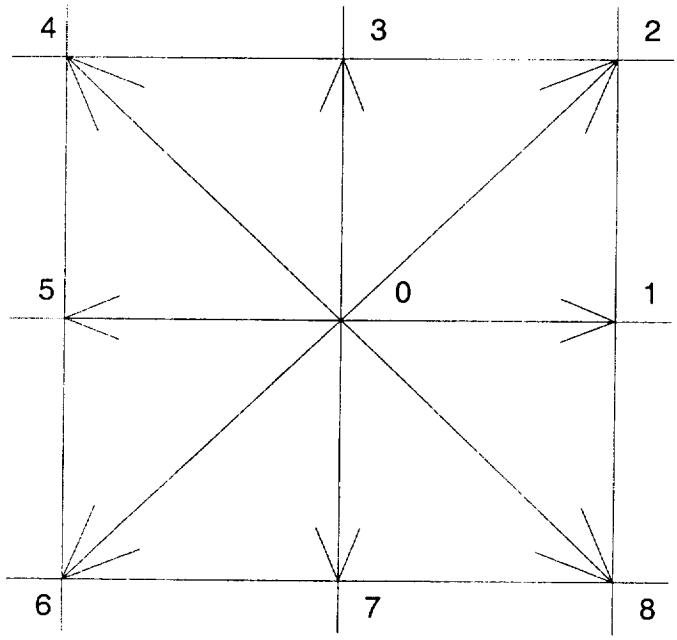

Fig. 1. A square lattice 9-velocity model: D2Q9